Interiors of giant planets : from Juno to Plato

Saburo Howard

UNIVERSITÉ CÔTE D'AZUR

ÉCOLE DOCTORALE
SCIENCES FONDAMENTALES ET APPLIQUÉES

THÈSE DE DOCTORAT

Intérieurs des planètes géantes : de Juno à Plato

Saburo Howard

Laboratoire J.-L. Lagrange, Observatoire de la Côte d'Azur

Présentée en vue de l'obtention du grade de docteur en
Sciences de la Planète et de l'Univers
de l'Université Côte d'Azur

Dirigée par Tristan Guillot — Soutenue le 3 Octobre 2023

Devant le jury composé de :

Florian Debras	*Chargé de recherche, IRAP, Toulouse*
Agnès Fienga	*Astronome, Observatoire de la Côte d'Azur*
Ravit Helled	*Full professor, University of Zürich*
Stéphane Mazevet	*Directeur de recherche, Observatoire de la Côte d'Azur*
Christoph Mordasini	*Full professor, University of Bern*
Ronald Redmer	*Full professor, University of Rostock*
Diana Valencia	*Associate professor, University of Toronto*
Tristan Guillot	*Directeur de recherche, Observatoire de la Côte d'Azur*

OBSERVATOIRE DE LA CÔTE D'AZUR
UNIVERSITÉ CÔTE D'AZUR

cnes

Intérieurs des planètes géantes : de Juno à Plato
Interiors of giant planets: from Juno to Plato

Rapporteurs

Christoph Mordasini
Full professor, University of Bern

Ronald Redmer
Full professor, University of Rostock

Examinateurs

Florian Debras
Chargé de recherche, IRAP, Toulouse

Agnès Fienga
Astronome, Observatoire de la Côte d'Azur

Ravit Helled
Full professor, University of Zürich

Stéphane Mazevet
Directeur de recherche, Observatoire de la Côte d'Azur

Diana Valencia
Associate professor, University of Toronto

Abstract

Interiors of giant planets: from Juno to Plato

Studying the interiors of planets is essential to gain profound comprehension of the processes that drive planetary formation. The present internal structures of planets reflect their origins and evolutionary paths. Jupiter, the largest planet in our Solar System, is of particular significance as it is believed to have formed first, offering insights into the early stages of our system. Understanding Jupiter's interior is also relevant in light of the discovery of over 5 000 exoplanets, many of which being gas giants.

The Juno mission, orbiting Jupiter since 2016, has changed our view of Jupiter's interior and revealed its complexity. By measuring extremely accurately the planet's gravity field, it has provided tight constraints for models of its internal structure. Matching these constraints in addition to atmospheric measurements of composition and surface temperature has proven challenging for interior models. Thus, the primary goal of this thesis was to investigate solutions that reconcile the various observations of Jupiter.

Throughout this work, I conducted Markov chain Monte Carlo calculations to explore a wide range of plausible interior models for Jupiter. First, by examining the heavy element distribution in the interior, the envelope of Jupiter was found to be inhomogeneous. However, the models required invoking a warmer interior than expected. Furthermore, I showed that uncertainties in the equation of state are an important part of the analysis. In particular, non-ideal mixing effects due to interactions between hydrogen and helium must be considered and I thus developed an equation of state table to incorporate those effects. The constructed table, along with uncertainties in the equation of state, was then taken into account when calculating interior models. Specific emphasis was placed on determining the extent of the dilute core, a region above the central core and where heavy elements are gradually mixed in the hydrogen-helium envelope. The size of the dilute core holds major importance to understand the origin and evolution of Jupiter. Previous models pointed to solutions with very extended dilute cores, in tension with evolution models including mixing in the planetary interior. I have identified alternative solutions, featuring less extended dilute cores, in better agreement with evolution models and with interior models of Saturn. But still, our models could not fully satisfy the high heavy element abundance measured in Jupiter's atmosphere. One potential solution is the presence of an inward-decrease of the heavy element abundance. To investigate such hypothesis, constraints on the properties of the accreted material responsible for the atmosphere's enrichment were considered. This scenario is however found to be unlikely. We must conclude that the interior of Jupiter remains mysterious.

What we learn on Jupiter must be applied to exoplanets (or has direct consequences for our comprehension of giant exoplanets). In a few years only, Plato will provide accurate measurements of the radii, masses and also ages of many planetary systems.

Understanding the interior structure and evolution of giant planets enables us to infer their bulk compositions from these measurements. I showed that including non-ideal mixing effects in the equation of state can affect the calculated radii by up to 6%, therefore affecting the inferred composition potentially significantly. I used evolution models to constrain newly discovered transiting giant planets, with particular emphasis for systems of giant planets. In these systems, the planets must have the same age, therefore allowing a more precise comparison of their composition. This is important in order to understand their formation pathways. Demographic statistics on a sufficiently large sample of exoplanets will contribute to advancements also in the understanding of our solar system.

Keywords Giant planets, Jupiter, exoplanets, interiors, composition, equation of state

Intérieurs des planètes géantes: de Juno à Plato

Etudier l'intérieur des planètes est crucial pour comprendre les processus qui régissent la formation des planètes. Leur structure interne actuelle reflète leur origine et évolution. Jupiter, la plus grande planète de notre système solaire, est particulièrement importante. Elle est l'une des premières à s'être formée et est donc une relique de la genèse de notre système. Bien comprendre son intérieur est fondamental, d'autant plus que plus de 5 000 exoplanètes ont été découvertes, parmi lesquelles de nombreuses sont des géantes de gaz.

La mission Juno, en orbite autour de Jupiter depuis 2016, a changé notre vision de sa structure interne et a révélé sa complexité. En mesurant avec une extrême précision le champ de gravité de la planète, elle a fourni des contraintes strictes pour les modèles de structure interne. Cependant, réconcilier ces contraintes en plus des mesures atmosphériques de composition et de température de surface est complexe. Ainsi, l'objectif principal de ma thèse est de trouver des modèles de Jupiter en accord avec les diverses observations.

Tout au long de ma thèse, j'ai réalisé des calculs MCMC (Markov chain Monte Carlo) afin d'explorer un large ensemble de modèles d'intérieur. Tout d'abord, en examinant la distribution des éléments lourds, il a été constaté que l'enveloppe de Jupiter est inhomogène. Toutefois, ces modèles requièrent un intérieur plus chaud que prévu. De plus, j'ai montré que les incertitudes liées à l'équation d'état sont importantes. En particulier, les effets de mélange non idéaux dus aux interactions entre hydrogène et hélium doivent être pris en compte. J'ai donc développé une table d'équation d'état pour incorporer ces effets. Cette table, en plus des incertitudes liées à l'équation d'état, a été utilisée lors des calculs de modèles d'intérieur. Une attention particulière a été portée sur la détermination de l'étendue du noyau dilué, une région au-dessus du noyau central où les éléments lourds sont graduellement mélangés dans l'enveloppe d'hydrogène et d'hélium. La taille du noyau dilué est importante pour comprendre l'origine et l'évolution de Jupiter. Les modèles précédents indiquaient des solutions avec des noyaux dilués très étendus, en désaccord avec les modèles d'évolution tenant compte du mélange dans l'intérieur planétaire. J'ai identifié des solutions alternatives, présentant des noyaux dilués moins étendus, en meilleure concordance avec les modèles d'évolution et avec les modèles internes de Saturne. Cependant, nos modèles ne peuvent pas satisfaire pleinement l'abondance élevée en éléments lourds mesurée dans l'atmosphère. Une solution potentielle serait une diminution en profondeur de l'abondance en éléments lourds. Pour étudier cette hypothèse, les contraintes sur l'accrétion à l'origine de l'enrichissement de l'atmosphère ont été prises en compte. Cependant, ce scénario s'est avéré peu probable. L'intérieur de Jupiter reste donc mystérieux.

Ce qu'on apprend sur Jupiter doit être appliqué aux exoplanètes. Dans quelques années, Plato fournira des mesures précises des rayons, masses et âges de nombreux systèmes

planétaires. Comprendre la structure interne et l'évolution des planètes géantes nous permet d'inférer leur composition globale à partir de ces mesures. J'ai montré qu'inclure les effets de mélange non idéaux dans l'équation d'état affecte les rayons calculés jusqu'à 6%, ce qui peut impacter significativement la composition déduite. J'ai utilisé des modèles d'évolution pour contraindre des planètes géantes en transit récemment découvertes, en mettant l'accent sur les systèmes multiples. Dans ces systèmes, les planètes ont le même âge, ce qui permet une comparaison plus précise de leur composition, et ainsi mieux contraindre leurs processus de formation. Des analyses démographiques sur un échantillon suffisamment grand d'exoplanètes contribueront à mieux comprendre la formation de ces planètes et de notre système solaire.

Mots-clés Planètes géantes, Jupiter, exoplanètes, intérieurs, composition, équation d'état

Summary

English version:

Studying the interiors of planets is important for understanding how they form and evolve. Jupiter, the largest planet in the solar system, gives us valuable insights into the early stages of planet formation. The Juno mission has revealed the fascinating complexity of Jupiter and challenged our understanding of its internal structure. Through my research, I have learnt more about these topics, especially by studying models constrained by Jupiter's gravitational field. I have also looked at exoplanets, which are planets outside our solar system. Applying what we learn on Jupiter to exoplanets is important. By studying planets, whether they are close by or far away, we expand our knowledge and gain a better comprehension of our own solar system and the vast universe beyond.

Version française:

L'étude de l'intérieur des planètes nous aide à comprendre comment elles se forment et évoluent. Jupiter, la plus grande planète du système solaire, est une véritable fenêtre sur les premières phases de notre système. La mission Juno a révélé la complexité fascinante de Jupiter et remis en question ce que nous savions de sa structure interne. Mes recherches ont contribué à une meilleure compréhension de ces aspects en calculant notamment des modèles contraints par le champ de gravité de Jupiter. De plus, dans le cadre de mes travaux, j'ai également consacré du temps à l'étude des exoplanètes, ces planètes situées au-delà de notre système solaire. Appliquer ce qu'on apprend sur Jupiter aux exoplanètes est important. L'étude des planètes, qu'elles soient proches ou éloignées, élargit notre vision et nous permet de mieux comprendre notre système solaire ainsi que les mondes lointains qui peuplent l'univers.

List of publications

Bloot S., Miguel Y., Bazot M., Howard S. (2023). **Exoplanet interior retrievals: core masses and metallicities from atmospheric abundances.** Monthly Notices of the Royal Astronomical Society, Volume 523, Issue 4, pp.6282-6292

Hobson M. et al. includes Howard S. (2023). **TOI-199 b: A well-characterized 100-day transiting warm giant planet with TTVs seen from Antarctica.** Submitted to AASJ.

Howard S. and Guillot T. (2023). **Accounting for non-ideal mixing effets in the hydrogen-helium equation of state.** Astronomy and Astrophysics, Volume 672, id.L1, 7 pp. 10.1051/0004-6361/202244851

Howard S., Guillot T., Bazot M., Miguel Y., Stevenson D. J., Galanti E., Kaspi Y., Hubbard W. B., Militzer B., Helled R., Nettelmann N., Idini B., Bolton S. (2023). **Jupiter's Interior from Juno: Equations of State Uncertainties and Dilute Core Extent.** Astronomy and Astrophysics, Volume 672, id.A33, 25 pp. 10.1051/0004-6361/202245625

Howard S., Guillot T., Markham S., Helled R., Müller S., Stevenson D. J. (2023). **On the hypothesis of an inverted Z gradient inside Jupiter.** submitted to Astronomy and Astrophysics

Korth J., Gandolfi D., Subjak J., Howard S. et al. (2022). **TOI-1130: A photodynamical analysis of a hot Jupiter in resonance with an inner low-mass planet.** Accepted in Astronomy and Astrophysics 10.48550/arXiv.2305.15565

Miguel Y., Bazot M., Guillot T., Howard S. et al. (2022). **Jupiter's inhomogeneous envelope.** Astronomy and Astrophysics, Volume 662, id.A18, 16 pp. 10.1051/0004-6361/202243207

Psaridi A. et al. includes Howard S. (2023). **Three Saturn-mass planets transiting F-type stars revealed with TESS and HARPS.** Accepted in Astronomy and Astrophysics 10.48550/arXiv.2303.15080

Sha L. et al. includes Howard S. (2023). **TESS spots a mini-Neptune interior to a hot Saturn in the TOI-2000 system.** Monthly Notices of the Royal Astronomical

Society, Advance Access 10.1093/mnras/stad1666

Trifonov T. et al. includes Howard S. (2022). **TOI-2525 b & c: A pair of massive warm giant planets with a strong TTV signal revealed by TESS.** The Astronomical Journal, Volume 165, Issue 4, id.179, 23 pp. 10.3847/1538-3881/acba9b

Vowell N. et al. includes Howard S. (2023). **HIP 33609 b: An Eccentric Brown Dwarf Transiting a V = 7.3 Rapidly Rotating B Star.** The Astronomical Journal, Volume 165, Issue 6, id.268, 13 pp. 10.3847/1538-3881/acd197

Acknowledgment

Trois ans se sont écoulés et je tiens à exprimer ma gratitude envers les personnes qui m'ont accompagné tout au long de ce périple. Tout d'abord, je souhaite remercier Tristan, mon directeur de thèse, pour m'avoir donné l'opportunité de réaliser ce projet de recherche. Son accompagnement et sa gentillesse ont été précieux. Son savoir et sa vivacité d'esprit m'ont souvent laissé sans voix et furent à chaque fois une leçon d'humilité.

Parmi mes proches collaborateurs, je remercie Michaël. Ses passages à Nice et sa disponibilité malgré la distance ont été essentiels pour le bon déroulement de ma thèse. Un grand merci également à Yamila, pour sa bonne humeur constante et sa facilité à collaborer avec elle. Je tiens à exprimer ma reconnaissance envers Ravit, pour sa bienveillance et l'opportunité de travailler avec elle pendant mon postdoc. Mes remerciements vont aussi à Dave, son regard aiguisé a eu un impact important sur mes travaux de recherche. Je souhaite exprimer ma reconnaissance à Eli et Yohai pour leur invitation en Israël, une semaine inoubliable qui restera gravée dans mes souvenirs. Leur générosité et leur accueil chaleureux ont rendu ce séjour exceptionnel. Enfin, un sincère remerciement à Maayan, Maria et tous les autres étudiants de leur groupe, que je considère comme des amis plus que des collègues.

J'aimerais aussi exprimer ma reconnaissance envers les personnes de l'observatoire, du laboratoire Lagrange et de l'équipe TOP. Tout particulièrement, je souhaiterais remercier, en premier lieu, mes camarades. Parmi eux, les anciens, qui m'ont accueilli chaleureusement et facilité mon intégration. Je tiens à remercier Adrien, toujours présent à l'observatoire lors de ma première année, en période de pandémie. Un grand merci à Nico, pour tous ces moments de rire et sa simplicité qui ont rendu chaque jour plus agréable. Max, sa maturité et son second degré ont amélioré mes journées à l'observatoire. Camille, notamment pour avoir partagé avec moi le semi-marathon et le marathon en relais. Du bureau d'en face, je tiens à exprimer ma gratitude envers Julia. Sa présence bienveillante, ses conseils et nos échanges sur nos expériences de thèse ont été d'une grande aide. Je remercie également Gabriele. Sa jeunesse, sa fougue, son dynamisme, m'ont permis de prendre du recul ; j'ai apprécié son humour incisif ainsi que ses arrêts décisifs. Je tiens à remercier aussi mes cadets. Fabiola, pour son altruisme, son extrême gentillesse et pour être si avenante. Marjorie, pour son enthousiasme, sa simplicité et pour être si conciliante. Philippine, pour son recul sur la thèse, son amour du confort mais aussi sa capacité de prise d'initiative. Marie, pour sa présence, sa capacité à discuter facilement et son authenticité. Tristan, pour sa fraternité, sa bonté et ses opinions. J'en oublie sûrement d'autres, mais merci encore à Jason, Niels, Vincent et Rahul pour ces bons moments passés ensemble. Merci aussi à Chrysa avec qui j'ai partagé le bureau pendant ces trois ans.

Mes remerciements vont aussi vers Guy, pour tous ces cours de Japonais, son authenticité et ces déjeuners à la bonne franquette. Un merci particulier à F-X, Jean-Pierre et Olivier pour avoir été à mes côtés lors de mes deux nuits d'observation à Calern. Un sincère remerciement à Rose, pour sa douceur, ses conseils motivants et sa simplicité. Merci à Philippe, Sophie, Christine, pour leur présence et bienveillance. Je remercie également ceux avec qui j'ai eu la chance d'enseigner: Marie, Sylvie, Marianne, Marie-Gabrielle, Thierry, Ulrich, Samira. Enfin, Little remercie Khaled, un personnage au fort caractère, un camarade unique avec qui les échanges taquins étaient sans limite. Sa présence a apporté une touche de légèreté et de bonne humeur dans notre quotidien.

Je tiens à remercier aussi mes coéquipiers du foot à Villefranche, notamment Jeff, Kilian, Sylvain, Fabrice, Alexis et d'autres que j'oublie. Merci surtout aux guerriers de Sophia : Arnaud, Gab, Tristan, Nico, Marco, Alberto, Adrien, Thibaud, Hugo, Laurent. On les gagnera un jour ces jeux. Je me dois de remercier d'autres grands du foot, qui ont été là pour moi quasi chaque week-end: Jurgen, Alisson, Adrian, Caoimhin, Virgil, Joe, Andy, Trent, Joël, Nat, Neco, Fabinho, Georginio, Millie, Naby, Hendo, Ox, Shaq, Curtis, Harvey, Bobby, Sadio, Mo, Takumi, Divock, Kostas, Rhys, Thiago, Diogo, Ibou, Luis, Stefan, Cody, Darwin.

Je tiens à remercier Johann, qui m'a donné le goût pour la recherche en 2018. Sans mon stage à l'Onera, je ne serais sûrement pas là aujourd'hui. Merci également à Dominique, un des meilleurs professeurs que j'ai eus, qui m'a donné l'opportunité de pénétrer le milieu de l'astrophysique. Parmi ceux qui m'ont inspiré, je remercie aussi Tommy, Stevie, Tyler, Barney et Taishi.

Plus personnellement, je tiens à remercier mes proches. D'abord mes amis, ceux de toujours. Eliot, je te remercie pour ton omniprésence, ta loyauté, ta bonté, je ne connais personne qui correspond mieux à la définition d'un ami. Jean-Baptiste, merci pour ton authenticité, ta fraternité et ta capacité à t'amuser. Paul, merci pour ton humour, ta détermination et ta légèreté. Votre impact sur ma thèse est non-négligeable. Ces moments ensemble, hors du temps, m'ont toujours permis de décompresser et de m'éloigner des tracas de la thèse. Merci Benjamin, pour ces échanges toujours plein d'autodérision, ton pragmatisme et ton intelligence.

Un sincère merci à Caroline, pour ta loyauté, pour être si dévouée et pour ta tendresse, notamment dans les derniers instants.

Enfin, j'aimerais remercier ma famille. Tout d'abord mes grand-mères, qui ont toujours souhaité le meilleur pour moi, et mes grand-pères, qui j'espère seraient fiers du chemin parcouru. Je remercie mon frère. Ton amour, ta joie de vivre, ton rire, ton dynamisme, ta présence, sont une source de motivation. Je remercie mes parents, pour leur éducation, leur amour, leur temps. Vous êtes les plus grands édificateurs de la personne que je suis aujourd'hui. Je vous suis infiniment reconnaissant.

Table of Contents

List of Figures

List of Tables

List of Algorithms

List of Abbreviations

CEPAM	**C**ode d'**E**volution **P**lanétaire **A**daptatif et **M**odulaire
CD21	**C**habrier **D**ebras 2021
CMS	**C**oncentric **M**aclaurin **S**pheroid
CMS19	**C**habrier **M**azevet **S**oubiran 2019
DFT	**D**ensity **F**unctional **T**heory
EOS	**E**quation **O**f **S**tate
H	**H**ydrogen
He	**H**elium
HG	**H**oward **G**uillot
IWG	**I**nterior **W**orking **G**roup
MCMC	**M**arkov **C**hain **M**onte **C**arlo
MD	**M**olecular **D**ynamics
MGF16	**M**iguel **G**uillot **F**ayon 2016
MH13	**M**ilitzer **H**ubbard 2013
MLS22	**M**azevet **L**icari **S**oubiran 2022
NIE	**N**on **I**deal **E**ffects
PBE	**P**erdew **B**urke **E**rnzerhof
PhD	**P**hilosophiae **D**octor
PIMC	**P**ath **I**ntegral **M**onte **C**arlo
QMC	**Q**uantum **M**onte **C**arlo
REOS	**R**ostock **E**quation **O**f **S**tate
SCvH95	**S**aumon **C**habrier **v**an **H**orn 1995
SR18	**S**chöttler **R**edmer 2018
ToF	**T**heory of **F**igures
TOI	**T**ess **O**bject of **I**nterest
vdW	**v**an **d**er **W**aals
XC	e**X**change and **C**orrelation

Chapter 1

Introduction

Contents

1.1 Motivation

In Roman mythology, Jupiter is the king of the gods. His sister and wife, Juno, despite occasional tumultuous relationships [Homer], is the goddess of marriage and well-known for her fidelity. It is since 2016 that the Juno spacecraft has started its dance with Jupiter. Her love for Jupiter is such that she will continue her dance until 2025. Throughout this dance, Juno has provided valuable information about her partner. As mere mortals, we seek to learn more about these planets named after divinities. Figure. 1.1 shows a high-resolution image captured by the Juno spacecraft. A reason why we study a planet like Jupiter is to understand where we come from. Our Earth formed within the solar system after Jupiter, and the latter had a significant influence on the history of our system. Besides, planets are what they eat, and Jupiter's meal consisted of primordial gas. Therefore, it is crucial to understand Jupiter and its internal composition to understand the conditions under which our Earth could have been created. Two times more massive than the sum of all the other planets of the solar system, Jupiter is an enigmatic object, whose internal structure remains hidden behind coloured clouds and strong winds. Using the gravity data from Juno, we can build models of the interior of Jupiter and infer its internal structure. I will not go in the details now but a quick look at the radius and the mass of the giant planets of our solar system (see, e.g., Figure 3 of Stevenson [1982]) already informs us about the bulk composition of these planets. Jupiter and Saturn are mainly made of a mixture of hydrogen and helium while Uranus and Neptune seem to be much more enriched in heavy elements. Throughout this thesis, heavy elements will refer to any element that is heavier than hydrogen and helium. A good understanding of Jupiter and the other giant planets from our solar system is necessary, also to tackle the field of exoplanets. Extensive and precise data on solar system planets have led to quite remarkable constraints on their structures. These should be considered when studying exoplanets. Inversely, demographic statistics on a sufficiently large sample of exoplanets will contribute to advancements in the understanding of our solar system.

The exoplanet discovery era began in 1995 [Mayor and Queloz, 1995] and more than 5 000 confirmed exoplanets have now been discovered. Yet, hundreds of billions of stars are in our galaxy and it is currently believed that more than half of the stars host at least one planet on average [Fressin et al., 2013]. Among the discovered exoplanets, our system remains highly unique (see Fig. 1.2 showing the mass of the discovered exoplanets as a function of their semi-major axis, compared to the planets of our solar system). So far, many planets found are close to their star. Giant planets were initially thought to form farther away, beyond the so-called ice line, where there is enough solid material to accrete and form a core that can subsequently attract gas. These giant planets, located very close to their star and known as hot Jupiters, could have migrated inward. Could it be that we exist because Jupiter and Saturn did not migrate as close? Migration also occurred in the solar system and one scenario proposed a decade ago

FIGURE 1.1: Jupiter's southern hemisphere seen by Juno. Credit: NASA/JPL-Caltech/SwRI/MSSS. JunoCam. Image processing by Kevin M. Gill.

[Walsh et al., 2011] suggested that Jupiter migrated inward, but Saturn, with the right mass ratio, entered in resonance with Jupiter, causing migration to reverse and move outward, leaving a confined disk in the center that gave birth to the rocky planets. Therefore, the diversity of outcomes from processes like migration is illustrated by our solar system, which represents one of the possible evolutionary paths. The planets of our solar system should be seen not as templates but as opportunities to understand the physical mechanisms which are universal. Nevertheless, the few thousand discovered exoplanets are subject to observational biases that favour detections of large planets close to their star. Future observations of more temperate planets may reveal planets and systems similar to ours.

Our solar system continues to appear quite singular so far, making it an invaluable subject of study. But one may thus wonder if there is life elsewhere. Are we alone in the Universe? This question, perhaps equally philosophical than scientific, was addressed by Epicurus in 305 BC [Epicurus]. He stated that there are an infinite number of worlds similar to ours and an infinite number of different worlds. This plurality of worlds was also supported by Giordano Bruno [Bruno G., 1584]. Following in the footsteps of Copernicus and heliocentrism, Bruno believed that Earth is rather ordinary and defended the idea of the plurality of worlds at the cost of his life. In 1610, Galileo Galilei discovered Jupiter's four largest moons through his telescope and concluded that their motion around Jupiter suggests that Earth is probably not the center of the Universe [Galilei, 1610]. However, the concept of the plurality of worlds has faced reluctance. Bibring J. P. [2019] questions the purpose of searching for life elsewhere because even

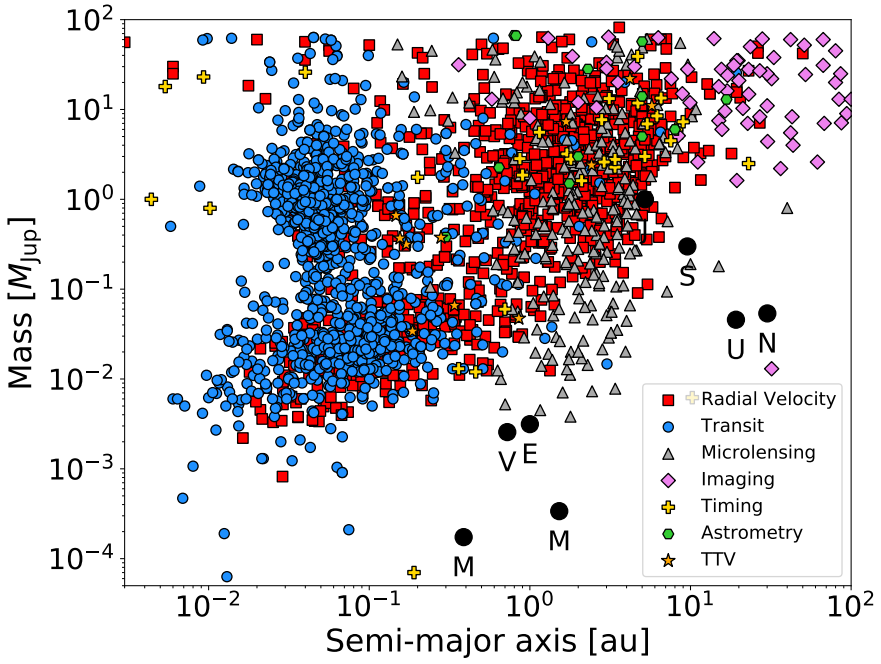

FIGURE 1.2: Mass vs. semi-major axis of confirmed exoplanets. The legend shows the different methods of detection. Planets of the solar system are shown with the first letter of their name. Data is coming from exoplanet.eu.

though the governing physical laws may be the same, the effects (e.g., collisions) can take very diverse directions. The notion that there are identical worlds everywhere might be illusory, and Earth and life may be unique cases. Moreover, our solar system has shown a rich diversity so far, considering the planets, their moons (particularly Jupiter, whose moons can exhibit very different characteristics such as volcanism, craters, and potential subglacial oceans). The presence of water on Earth, which is likely to be necessary for life according to the concept of habitability, required a giant impact that can explain the formation of the Moon [Budde et al., 2019]. There is currently no observation proving or disproving the existence of life elsewhere.

1.2 Exploring giant planets with space missions

Giant planets have been and continue to be observed from Earth. Galileo was the first to point his telescope towards Jupiter in 1610. However, humans are now constructing space missions and sending spacecraft into space to approach these planets. In the 1970s, the first probes created by humans flew towards the outskirts of the solar system and passed by Jupiter. Pioneer 10 sent the first postcard from the planet during a flyby in 1973. With its counterpart Pioneer 11, they paved the way for future missions to explore the outer solar system, including Voyager 1 and Voyager 2. At the end of the 1970s, the two Voyager spacecraft also conducted flybys of Jupiter. They notably measured its gravitational field [Campbell and Synnott, 1985] and provided valuable radio-occultation

measurements that are still useful today [Lindal et al., 1981, Gupta et al., 2022]. Both spacecrafts have now exited the solar system and travel through the interstellar medium. In 1988, the Galileo mission was launched and entered in orbit around Jupiter in 1995. This marked the first time that a spacecraft orbited a planet in the outer solar system. Galileo also deployed a probe that undertook a suicide dive into Jupiter's atmosphere (entry site: 6.57°N, 5.02°W) down to a depth corresponding to a pressure of 22 bar. For approximately an hour, it transmitted invaluable information about the properties of the atmosphere [Seiff et al., 1998, von Zahn et al., 1998]. The high concentration of heavy elements measured by the Galileo entry probe had a significant impact on planet formation theories. Cassini and New Horizons, designed to study Saturn and Pluto respectively, also conducted flybys of Jupiter in 2000 and 2007. In 2011, the Juno mission [Bolton et al., 2017] was launched, and it entered in orbit around Jupiter in 2016. Its polar orbit enabled precise measurements of the planet's gravitational field using Doppler tracking [Iess et al., 2018]. The main objectives of the Juno mission include determining the planet's internal structure, the presence of a core, and the abundance of water. The Juno mission has unveiled the complexity of Jupiter and highly influenced the modelling of giant planet interiors.

Nonetheless, the study of giant planets has not only been limited to missions dedicated to Jupiter. The Cassini mission [Spilker, 2019], mentioned earlier, improved our comprehension of Saturn. In addition to provide accurate measurements of the planet's gravity field, it detected wave features within its rings, offering supplementary constraints on Saturn's interior. On the other hand, Uranus and Neptune never had their dedicated mission [Guillot, 2022]. An orbiter to Uranus could improve our understanding of the currently poorly constrained interiors of the icy giants.

Concerning exoplanets, the Kepler mission (2009-2018) [Borucki et al., 2010] stands out as the most prolific in terms of discoveries so far. Alongside the TESS (Transiting Exoplanet Survey Satellite) mission [Ricker et al., 2015], which took over in 2018, these missions primarily employ the transit method to detect exoplanets. A new era of exoplanet characterization has begun with the launch of the JWST (James Webb Space Telescope) during Christmas 2021. JWST is meant to characterize exoplanets and provide spectra that enables the determination of atmospheric properties. Additionally, the PLATO (PLAnetary Transits and Oscillations of stars) [Rauer et al., 2014] mission aims to detect and characterize diverse types of planets. Notably, it will examine multiple planet systems and provide precise measurements of radii and masses. This information will shed light on the mechanisms governing planetary formation. Furthermore, since the mission also focuses on stars, we will get information about the age of these systems, a crucial parameter for understanding their evolution.

1.3 History of the modelling of the interior of Jupiter

I am here going to narrate a story of how the study of the internal structure of Jupiter evolved through time, in the last century. This is a personal and non-exhaustive summary of the main milestones of the field. I will ineluctably omit some works and hope that my predecessors will not hold it against me.

Almost 100 years ago, in 1924, Sir Harold Jeffreys tried to make some conclusions about the internal structure of the gas giants of the solar system [Jeffreys, 1924]. Linking the moment of inertia of Jupiter with its ellipticity (which depends on the ratio of the polar and equatorial radii, and can be obtained directly from observations but also from the motions of the natural satellites), he could derive the normalised moment of inertia of Jupiter and found it to be 0.265. A homogeneous planet would have given a value of 0.4. Jeffreys then assumed that the moment of inertia of the planet must be larger than it would be if the entire planet had the density of its outer region (surface). He could hence get the following constraint on the density of the outer region of Jupiter and Saturn:

$$\frac{C}{Ma^2} > 0.4\frac{\rho_s}{\rho}, \tag{1.1}$$

C being the moment of inertia, M the mass of the planet, a its equatorial radius, ρ_s the surface density and ρ the bulk density. Comparing the obtained value of ρ_s to the density of the lightest chemical elements, Jeffreys found that the outer regions of the gaseous planets should be made of hydrogen and helium. This led him to build a model where Jupiter is made of an inner layer of rock, surrounded by a layer of ice and an outer layer of hydrogen and helium which is thin (only 9% of the total radius). A representation is shown on Fig. 1.3. This is probably the best constraints that could be obtained when the only available observational data were the mean density and the moment of inertia.

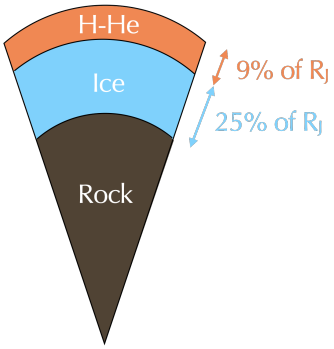

FIGURE 1.3: Jupiter in 1924. Depiction of the interior model of Jupiter proposed by Sir Harold Jeffreys [Jeffreys, 1924].

In the following decades, interest about hydrogen has grown and the need for a better understanding of the equation of state of hydrogen began to be seen as an important path towards a good comprehension of the gas giants. The state of the art of the equation of state of hydrogen will be preserved for Chapter 3. After his good friend Rupert Wildt

[DeMarcus, 1977] reported the preponderance of hydrogen inside Jupiter [Wildt, 1947], Wendell Carden DeMarcus provided an important contribution to models of the interior of the planet [Demarcus, 1958]. Using the theory of figures (detailed in Chapter 2), he could get a sharper inequality than Jeffreys. This could be achieved using the influence of Jupiter's gravity field on the motions of its natural satellites. DeMarcus therefore proposed a jovian model made of a central dense core (representing 2% of Jupiter's mass) surrounded by an envelope of hydrogen and helium. Hydrogen represents about 78% of the mass while helium represents about 20% of the mass. The fraction of helium is increasing with depth as it was believed that elements heavier than hydrogen are more concentrated towards the center of the planet. Overall, the chemical composition of Jupiter would hence be very similar to the Sun's. It is worth to mention that at that time models assumed a relatively cold interior. The presence of internal heat source was only discovered in 1966 [Low, 1966] and only then were the giant planets thought to be fluid, not solid.

Following the work of DeMarcus, James Peebles also proposed a picture of the gas giants that is very close to the Sun's in terms of chemical composition. His paper from 1964 [Peebles, 1964] appears as a singularity among all his contributions in the field of cosmology, but the last section may expose the true motivations of the author. Peebles had the intuition that the interiors of the gas giants were hotter than previously thought. Thus, using a digital computer, he proposed models of Jupiter and Saturn with the novelty of an envelope made of a homogeneous mixture of hydrogen and helium surrounding the central dense core, and with a deep convective atmosphere. The subsequent infrared observations of Jupiter [Low, 1966] showed that the planet emits more energy than it receives from the Sun and convection appears as a the main mechanism to transport heat from the interior. Therefore, William Bill Hubbard put forward the interior of the giant planets to be mostly convective, suggesting models [Hubbard, 1968, 1969] in line with the ones of Peebles. A portrayal of the overall conception of the internal structure of Jupiter at the beggining of the 1970's is shown on Fig. 1.4, accounting for the existence of metallic hydrogen hypothesized from 1935 [Wigner and Huntington, 1935] (more details in Chapter 3).

From the 70's began the era of space missions that visited Jupiter. Flybys of spacecraft improved the accuracy on the measurement of the gravity field, leading to better constraints on the models. On the other hand, differentiation of helium within the interior was suggested [Smoluchowski, 1967, Salpeter, 1973]. Helium was found to be soluble in molecular hydrogen but immiscible in metallic hydrogen [Stevenson and Salpeter, 1977b] that exists in Jupiter's deep interior. Helium droplets form and fall (called "helium rain"), releasing some energy, which can explain the observed excess luminosity of Saturn. In the case of Jupiter, with the success of homogeneous evolution calculations, it is believed that helium differentiation has not or just started [Stevenson and Salpeter, 1977a]. This was confirmed by the measurement of a depletion of helium in Jupiter's

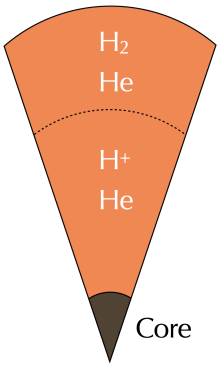

FIGURE 1.4: Jupiter at the beggining of the 1970's. Overall conception of the interior of Jupiter at this time. It consists of a central dense core surrounded by a homogeneous envelope of hydrogen and helium. The chemical composition is almost similar to the Sun's.

atmosphere by the Galileo probe in 1995 [von Zahn et al., 1998]. Thus, "three-layer" models were proposed by the community as shown on Fig. 1.5. A myriad of those models have been built (e.g. Guillot [1999]) and are still applicable today [Miguel et al., 2022]. They notably aim at determining the distribution of heavy elements (heavier than hydrogen and helium) and the mass of the inner core. Fortney et al. [2007] showed how the mass of the core evolved in the community since the 70's, I extended the figure until today (see Fig. 1.6). We can see that after Juno's arrival at Jupiter, in 2016, models have the tendency to favour low mass cores. This is due to the redefinition of the conception of the core inside Jupiter. Thanks to the outstanding accuracy of Juno's measurements, models indicated the presence of a "dilute core" in the interior of the planet [Wahl et al., 2017]. Instead of a pure heavy elements core separated from the hydrogen-helium envelope by a sharp discontinuity, we now believe that Jupiter harbours a region where the heavy elements are gradually mixed in the envelope (see Chapter 4 for more details). Jupiter could still have a central compact core of a few earth masses, but not necessarily, and it would be nested in this dilute core region (that is actually a region still dominated by hydrogen and helium, the mass fraction of heavy elements Z being around 10-20%). This idea was not new and Stevenson already mentioned a "partially disseminated core" back in the 80's [Stevenson, 1982, 1985] but the Juno mission allowed to corroborate this hypothesis. Most interior models now include such dilute or fuzzy core [Debras and Chabrier, 2019, Militzer et al., 2022, Miguel et al., 2022, Howard et al., 2023] as shown on Fig. 1.7.

Additional historical details can be found in notable reviews such as [Hubbard, 1973, Stevenson, 1982, Guillot, 2005, Stevenson, 2020]. Many challenges remain and interior models are to be improved. Among those challenges, the extent of the dilute core and the high metallicity in Jupiter's atmosphere still require to be further investigated, and this thesis is an attempt to make progress on these topics. I finally stress that two major ingredients of the study of the interiors of giant planets are accurate gravitational moments and a good understanding of hydrogen at high-pressure. While major

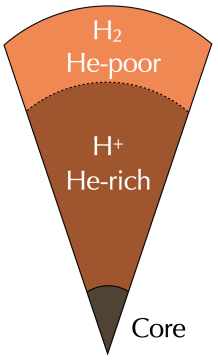

FIGURE 1.5: Jupiter in the 2000's. The standard "three-layer" model of Jupiter. This picture of Jupiter emerged in the 70s and remained until very recently. Because of helium phase separation, it consists of a core surrounded by an envelope made of a helium-rich layer of metallic hydrogen and a helium-poor layer of molecular hydrogen.

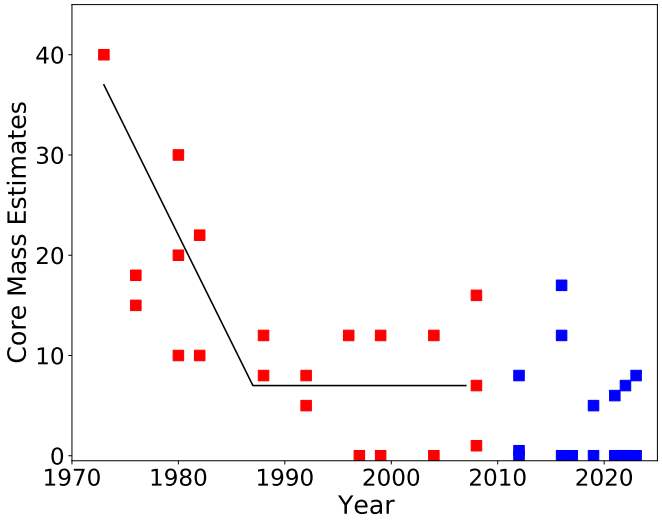

FIGURE 1.6: Jupiter's core mass, as derived by many different authors, at various times since the early 1970s. Adapted from Fortney and Nettelmann [2010] and extended after 2010 (values taken from Nettelmann et al. [2012], Leconte and Chabrier [2012], Hubbard and Militzer [2016], Miguel et al. [2016], Wahl et al. [2017], Debras and Chabrier [2019], Nettelmann et al. [2021], Militzer et al. [2022], Miguel et al. [2022], Howard et al. [2023]).

improvement on the accuracy of the gravitational moments was made possible thanks to space missions, progress has also been made on the equation of state but we will see that there are still uncertainties on this matter today and further experiments and simulations would be important.

1.4 Towards exoplanets

Over the past three decades, the discovery of exoplanets has fueled a growing interest towards a better understanding of these far other worlds. Unfortunately, our comprehension of exoplanets remains limited compared to the planets of our own solar system,

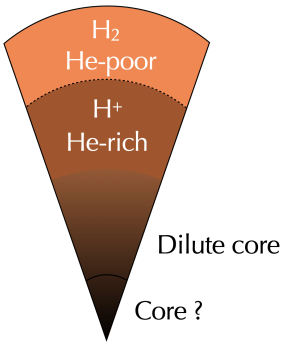

FIGURE 1.7: Jupiter today. The "dilute core" model of Jupiter. Instead of a pure heavy elements core separated from the hydrogen-helium envelope by a sharp discontinuity, we now believe that Jupiter harbours a region where the heavy elements are gradually mixed in the envelope.

mostly due to the lack of precise and diverse measurements. However, the large number of exoplanet samples remains a significant advantage in this field of study. New exoplanets are being detected on a daily basis, primarily by the transit technique where a planet affects the received light of the star when passing in front of it, or the radial velocity technique which calculates the perturbation of the planet on the movement of its host star. Combining both methods can provide the radius and the mass of exoplanets. But their bulk composition can be inferred only with the use of models, constrained by the radius and mass measurements.

Current models for exoplanets are far from being as sophisticated as those developed for planets within our solar system. Typically, exoplanet models represent giant planets simply by a core of heavy elements surrounded by a homogeneous envelope of hydrogen and helium (e.g., Thorngren et al. [2016]). These models rely on various assumptions, notably the equation of state [Howard and Guillot, 2023]. Improving our modelling is key and this is why working on solar system planets which offer accurate and extensive data is important.

Accurate ages of systems (that Plato will provide) help constrain models of exoplanets and atmospheric measurements reduce their degeneracy [Müller and Helled, 2023a]. So far, current instruments (e.g., JWST) try to observe species present in the atmosphere of those exoplanets. These traces are of particular interest because they can provide information about the formation processes. Figure 1.8 shows how JWST is revolutionizing the field of atmospheric characterization of exoplanets, by providing broad-wavelength spectra. Making the link between atmospheric abundances and planetary formation is a primary objective. It is challenging though, as the measured atmospheric composition may not be representative of the bulk metallicity of the planet. Indeed, Jupiter for instance has shown inhomogeneity in its interior [Miguel et al., 2022] and also in its atmosphere [Li et al., 2017]. Applying our knowledge of Jupiter to the study of exoplanets is crucial (see, e.g., Bloot et al. [2023]). The solar system and exoplanet communities

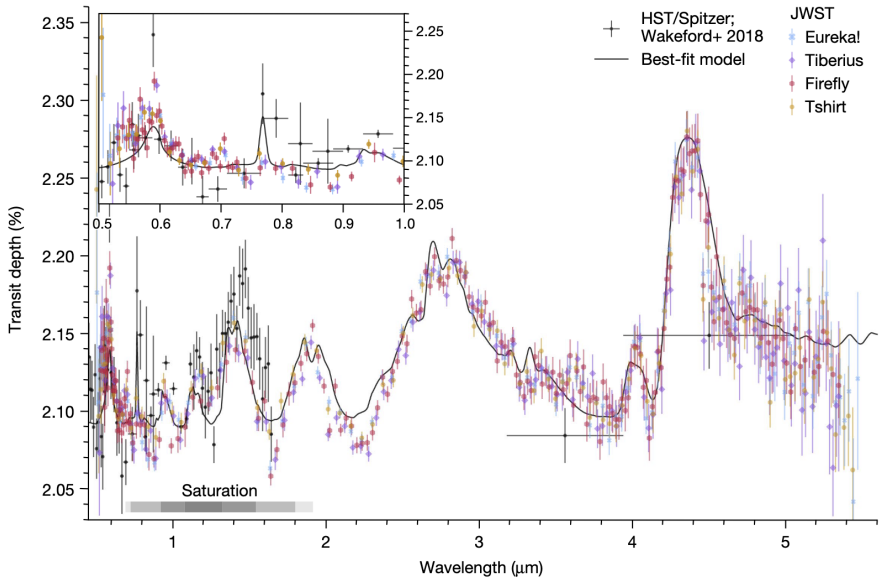

FIGURE 1.8: WASP-39 b transmission spectrum, taken from Rustamkulov et al. [2023]. While only two data points between 2 and 6 microns were previously available Wakeford et al. [2018], JWST provided data on a much wider range of wavelengths.

working side by side would benefit for both fields. Lessons learnt from accurate observations and sophisticated modelling on planets of the solar system lead the way in the study of exoplanets. Analyses of large samples of exoplanets could also identify trends that may help the comprehension of our nearby giant planets.

Many unresolved questions stand in the field of exoplanet (see, e.g., Nettelmann and Valencia [2021]). Among them is the intriguing observation of the inflation of many highly irradiated giant exoplanets: their measured radius is larger than expected [Thorngren and Fortney, 2018, Fortney et al., 2021]. In contrast, warm exoplanets are not subject to such inflation that is not yet fully understood. Further observations of these warm exoplanets will enable valuable comparisons with solar system planets [Müller and Helled, 2023b]. A more in-depth discussion will take place in Chapter 6.

1.5 Outline of the thesis

One of the primary objectives of this thesis is to investigate models of Jupiter that reconcile the various observations of the planet. This implied to give careful consideration to the equation of state. Additionally, I worked on several giant exoplanets and explored the implications of my research on Jupiter for a better understanding of exoplanets. Chapter 2 presents how we make models of giant planets, from observational constraints to theoretical aspects. Chapter 3 focuses on the equation of state, a key ingredient in the modelling of giant planets. It includes the paper from Howard and Guillot [2023] about non-ideal mixing effects. These chapters form the basis for studying

giant planets. Chapter 4 sums up the approach that I used to study Jupiter's interior, especially the statistical method. Chapter 5 presents the results I obtained on Jupiter's interior. It includes (i) my contribution to Miguel et al. [2022] about the inhomogeneity of Jupiter's envelope, (ii) how to account for uncertainties in the equation of state, (iii) the paper from Howard et al. [2023] about the extent of the dilute core and (iv) the paper in preparation about the hypothesis of an inward-decrease of the heavy element abundance. Chapter 6 then presents my work on exoplanets and my contributions to several discovery papers. Chapter 7 is the conclusion, with some future prospects. A quick summary of the main points of this thesis can be found in the Abstract.

Chapter 2

Modelling the interior and evolution of giant planets

Contents

Before presenting any models of Jupiter or extra-solar giant planets, it is necessary to provide a description of how we model giant planets. During my PhD, I mostly focused on interior models of Jupiter (see Chapter 5) but I also had the opportunity to calculate some evolution models for exoplanets (see Chapter 6). The current chapter mostly focuses on Jupiter but the presented methodology can be applied to any giant planet. This chapter hence starts with a summary of the observational data we have on Jupiter, which are invaluable to help constrain interior models. Concerning exoplanets, we have less data and this data is obviously less accurate. I then describe how to build a numerical model and tackle the theoretical aspects. The description of equations of state, a major ingredient of the models, will be described in Chapter 3.

2.1 Observational constraints

Observations are the first constraints that we get on the internal structures of planets. Because modelling the interior of a planet requires an important number of parameters, they reduce the degeneracy of the problem. This section about observational constraints will mainly focus on Jupiter, which was the major object of interest of my thesis. For other giant planets, I refer the reader to reviews such as Guillot [2005], Helled and Guillot [2018], Miguel and Vazan [2023].

2.1.1 Mass, radius

Prior to space missions, the mass of Jupiter has been measured through its gravitational influence on the motions of its satellites and on small bodies [Klepczynski et al., 1971]. With the flybys of the Pioneer and the Voyager missions, the mass of Jupiter could then be derived by analysing the Doppler shift of the radio signals of the spacecrafts [Null, 1976, Campbell and Synnott, 1985]. Accounting for the gravitational perturbations caused by Jupiter's moons and fitting their model to the observed Doppler shift data, these authors could obtain a value of the product GM. The most recent value of GM comes from Juno [Durante et al., 2020] and is equal to $126686534.1 \pm 8.4\,\mathrm{km^3/s^2}$. The precision has thus increased as the uncertainty on GM was of 101 $\mathrm{km^3/s^2}$ at the time of Pioneer and Voyager [Folkner et al., 2017]. The mass of Jupiter can then be inferred choosing a value for the gravitational constant G. We will use the value employed by Bill Hubbard of $G = 6.6738480 \times 10^{-11}\,\mathrm{m^3/kg/s^2}$, which is included in the range given by Mohr et al. [2012]. This yields a value of $M_\mathrm{J} = 1.8982532 \times 10^{27}\,\mathrm{kg}$, which is about $317.85\,M_\oplus$.

The equatorial radius of Jupiter has been measured via a stellar occultation [Hubbard and van Flandern, 1972]. Using precise astrometry and analysing the variations of the brightness of the stars during the occultation, the size and the shape of the planet can

be derived. But the equatorial radius currently used in Jupiter models comes from radio occultations of the Pionner and Voyager spacecrafts [Lindal et al., 1981]. The pressure-altitude profile, combined with the knowledge of the gravity field enables an estimate of the radius of the planet. Performing multiple radio occultations allows a more comprehensive understanding of the size and the shape of Jupiter. The value of the equatorial radius given by Lindal et al. [1981] is 71492 ± 4 km. The extension of the Juno mission will bring opportunities of radio occultations as well as JUICE (Jupiter Icy Moons Explorer) [Smirnova et al., 2022] and should provide a more accurate constraint on Jupiter's equatorial radius (see also Galanti et al. [2023]).

As we here talk about mass and radius, it is inevitable to broach density. The bulk density of Jupiter is about $1.326\,\mathrm{g.cm^{-3}}$ while it is $0.687\,\mathrm{g.cm^{-3}}$ for Saturn. Figure 2.1 compares Jupiter and Saturn to theoretical mass-radius relationships for planets mainly composed of hydrogen and helium. This already gives some hints about the internal composition of the gas giants of our solar system. They are mostly made of these light elements but they must also include some heavy elements, with Saturn being slightly more enriched than Jupiter. The reason why Jupiter has almost the same size as Saturn while being about three times more massive is that the gravity is stronger and material is hence more compressed.

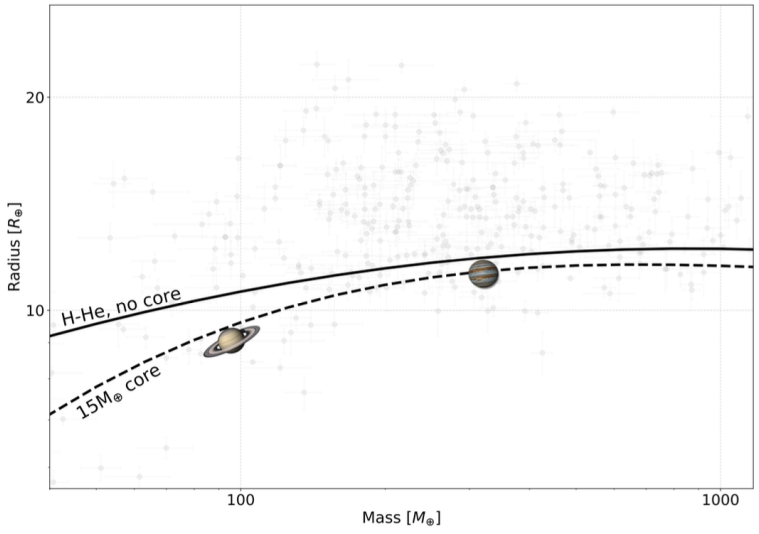

FIGURE 2.1: The mass-radius relation of H-He-dominated planets. Taken from Helled et al. [2022a]. The solid and dotted lines show the relation for pure H-He planets and planets including a $15\,M_\oplus$ core, respectively.

2.1.2 Rotation, winds

Rotation periods of giant planets have first been measured by following the movement of visible features of their atmosphere. For instance, Williams [1896] followed the drift of nine specific currents in Jupiter's atmosphere to estimate its rotation rate. However,

the rotation periods are now usually obtained by measuring the rotation period of the magnetic field. In the middle of the 1950's, radio emissions from Jupiter have been discovered. The motion of charged particles in the magnetosphere, tied to the rotation of the planet, generates these radio emissions. Looking at the periodicity of these emissions leads to the planet's rotation (see e.g. Higgins et al. [1997]). The measurement of the planet's rotation through the rotation of its magnetic field may be a more representative measurement of the global rotation of the planet [Hubbard, 1973]. Indeed, the motion of electronically conducting material, i.e. metallic hydrogen which dominates in the deep interior, is responsible of generating the magnetic field. Therefore, the rotation period of Jupiter is $9^{h}55^{m}29.71^{s}$ [Riddle and Warwick, 1976, Seidelmann and Divine, 1977]. Every three years, a "Working Group on Cartographic Coordinates and Rotational Elements" gathers to make decisions about the rotation periods to adopt [Davies et al., 1986, Archinal et al., 2011] but the adopted value is relatively steady.

As mentioned above, the rotation period of the magnetic field of a giant planet is representative of the rotation of the deep interior. Nevertheless, observing Jupiter, one can see a latitudinal banded structure with an alternation of light zones and dark belts (see Fig. 1.1 in Chapter 1). These bands are linked to eastward and westward zonal winds or jets [Fletcher et al., 2020a], that rotate differentially. Tracking the motions of the clouds enables to retrieve the speed of the winds. But the depth of these jets and the level from where Jupiter rotates as a solid body, have been a major question [Ingersoll, 1990]. Earth-based observations, then from Voyager 1 and 2 [Ingersoll et al., 1979, 1981] and from Cassini [Porco et al., 2003] allowed to derive the zonal winds profile, which remained constant over time and exhibited only slight asymmetry about the equator. The Juno mission confirmed that Jupiter's interior rotates uniformly (as a solid body) with an upper region exhibiting differential rotation [Iess et al., 2018]. The depth of the winds was a matter of debate [Kong et al., 2018] but could be constrained and is thought to be about 3000 km beneath cloud deck [Kaspi et al., 2018, Guillot et al., 2018]. Figure 2.2 shows the zonal winds of Jupiter at the different latitudes. Jupiter's upper region rotates on cylinders and the winds must project in a direction parallel to the spin axis with a radial decay [Galanti et al., 2021].

2.1.3 Gravity field

Because of their rotation, giant planets deviate from a perfectly spherical shape. This departure from sphericity affects the gravity field of the planet. Scrutinising the trajectory of a spacecraft (like Juno) around a planet and estimating the influence of the gravitational pull of this planet can tell about its density distribution. The so-called gravitational moments reflect the slightly perturbed spherical shape of the planet and are nowadays measured with flybys of spacecrafts. This subsection will only present the

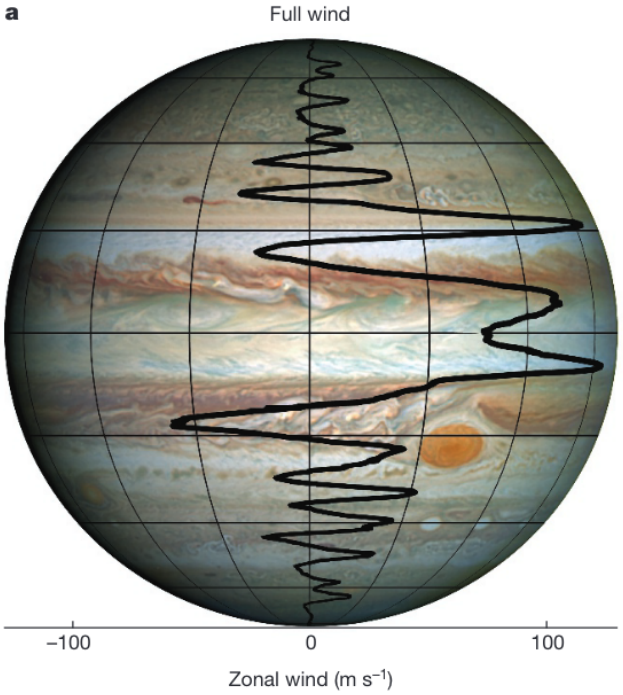

FIGURE 2.2: Jupiter's asymmetric zonal velocity field. Taken from Kaspi et al. [2018].

available measurements of these gravitational moments. A section is dedicated to the theoretical aspects of these precious gravitational moments (see Section 2.5).

If a planet was perfectly spherical, all the gravitational harmonics would be equal to zero. However, giant planets of our solar system have been observed to be oblate. The oblateness $((R_{\rm eq} - R_{\rm pol})/R_{\rm eq})$ was found to be 0.065 for Jupiter and slightly larger for Saturn (see Stevenson [1982] and references therein). This automatically means that the gravitational moments of these planets are not zero. The low-order even gravitational moments (J_2, J_4) were primarily obtained before the era of space missions, thanks to the motion of the natural satellites. More historical details can be found in Chapter 1. Then, higher order harmonics could be measured and the accuracy of the measurements only increased with spacecraft data. Figure 2.3 shows, for Jupiter, the evolution of the accuracy on J_4 and J_6, from the Pionner and Voyager missions [Campbell and Synnott, 1985], through Galileo [Jacobson, 2003], Cassini and New Horizons [Jacobson, 2009] and finally to Juno [Folkner et al., 2017, Iess et al., 2018, Durante et al., 2020]. We have now reached an outstanding level of accuracy that can strongly constrain interior models of Jupiter. The uncertainty of the Juno measurements is actually smaller than the uncertainty on the differential rotation. The latter hence dictates the level of accuracy that interior models need to reach. The latest values of Jupiter's even gravitational moments are given by Durante et al. [2020] and summarized in Table 2.1. We have here tackled only even gravitational harmonics which represent the significant part of the gravitational signature of Jupiter and allow to constrain the internal density distribution. Odd gravity harmonics and their signification will be discussed in Subsection 2.5.3.

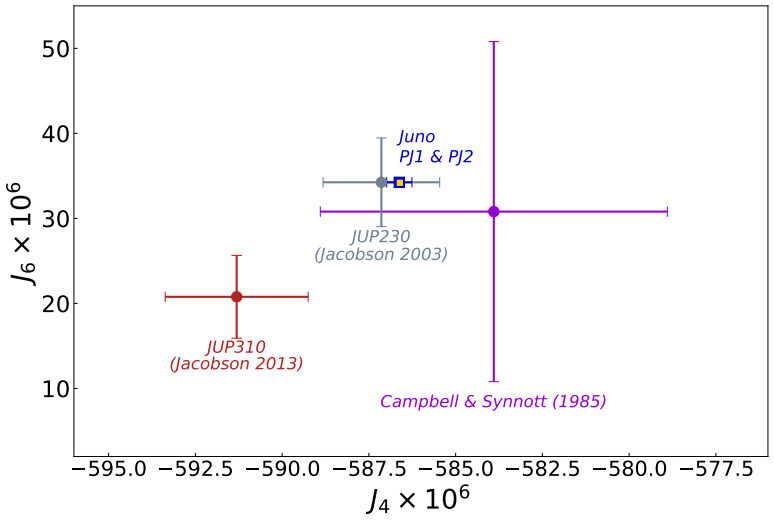

FIGURE 2.3: Improvement of the accuracy of the measurements of the gravitational moments. J_6 vs. J_4. The purple errorbar corresponds to the values obtained after the Pioneer and Voyager missions [Campbell and Synnott, 1985]. The grey errorbar corresponds to the measurement after Galileo [Jacobson, 2003]. The red errorbar corresponds to the one after the Cassini and New Horisons missions [Jacobson, 2009]. The blue errorbar corresponds to the measurement after the two first perijoves of Juno [Folkner et al., 2017]. The yellow dot corresponds to the values after the third and sixth perijoves [Iess et al., 2018].

TABLE 2.1: Even gravitational moments measured by Juno. Taken and adapted from Durante et al. [2020].

	Value	Uncertainty
$J_2(\times 10^6)$	14696.5735	0.0017
$J_4(\times 10^6)$	-586.6085	0.0024
$J_6(\times 10^6)$	34.2007	0.0067
$J_8(\times 10^6)$	-2.422	0.021
$J_{10}(\times 10^6)$	0.181	0.065
$J_{12}(\times 10^6)$	0.062	0.19

We finally stress, although a bit prematurely, that the gravitational moments provide direct information of the outer regions of giant planets. Indeed, Fig. 2.4 shows the contribution functions of the even gravitational moments up to order 6, which peak at the outer part of Jupiter's envelope because of their dependence to r^{2n}. These contribution functions have been calculated according to Zharkov and Trubitsyn [1974] and the calculation of gravity harmonics will be discussed in Section 2.5. This means that interior models can only infer indirectly the deeper structure of the interior of giant planets.

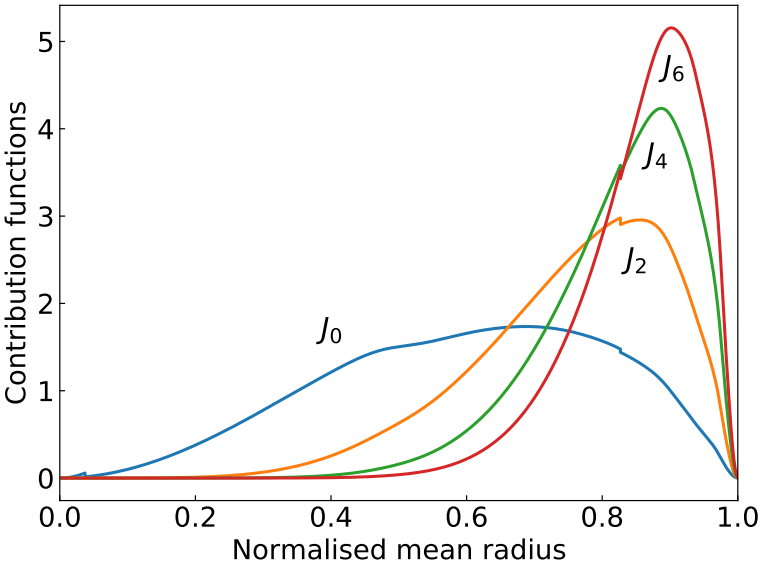

FIGURE 2.4: Contribution functions of the gravitational moments of Jupiter. J_0 corresponds to the mass of the planet. Calculated from [Zharkov and Trubitsyn, 1974], using one model from Howard et al. [2023]. The discontinuities correspond to the boundaries i) between the core and the envelope and ii) between the helium-rich and helium-poor regions of the envelope.

2.1.4 Atmospheric measurements

The definition of the atmosphere of a giant planet is not as evident as for a solid planet. For giant fluid planets like Jupiter or Saturn, the boundary between the atmosphere and the interior is loosely defined. As a person who is mainly interested by the interior of the planet, we arbitrarily set the outer boundary of our models at 1 bar, which is the pressure at the surface of the Earth. Above this pressure level, the mass is negligible and will not affect the gravitational moments (which depend on the density distribution) that interior models try to satisfy. This is hence a good outer limit for us.

Measurements from Earth and from space have provided information on Jupiter's atmosphere, down to tens or hundreds of bars. Interior modellers generally assumed that the properties of the atmosphere like its composition can be extended to the whole or a part of the envelope because of convective mixing. However, processes like phase separations [Stevenson and Salpeter, 1977a], how the interior is mixed [Stevenson, 1985] or even the presence of a radiative region [Guillot et al., 1994] in the interior could hinder the assumption that the atmosphere is representative of the envelope of a planet. We here summarize observational data on two aspects of the atmosphere of Jupiter: its temperature profile and its chemical composition.

Radio occultations, previously mentioned as they were used to derive the radius of Jupiter, can also be used to estimate the temperature profile of the atmosphere. The radio signal from the spacecraft passes through the atmosphere which affects the signal and bends it. The degree of bending of the signal depends on the atmosphere properties

and can be quantified by the refractivity of the material present in the atmosphere. The refractivity can be related to the density which leads to the pressure profile if assuming hydrostatic equilibrium. Using the ideal gas law, it is then possible to retrieve the temperature profile, which will be dependent on the assumed composition of the atmosphere. The temperature at the 1 bar level was found to be $165 \pm 5\,\mathrm{K}$ from Voyager missions [Lindal et al., 1981]. Then, the Galileo mission dived into Jupiter's atmosphere down to a depth of 22 bars [Seiff et al., 1998] and provided an in-situ measurement of $T_{1\mathrm{bar}} = 166.1 \pm 0.8\,\mathrm{K}$. But unfortunately, it was thought that the Galileo probe dropped into a hot-spot [Orton et al., 1996], namely a very particular region which is relatively dry. Thus was raised the question of the representativity of the temperature measurement at 1 bar over the whole range of latitudes and longitudes. A recent reassessment of the radio occultations from Voyager [Gupta et al., 2022], taking benefit of the atmospheric composition measurements of Galileo (because the derivation of the temperature profile requires the independent knowledge of the mean molecular mass), could provide new estimates of the thermal profile of Jupiter's atmosphere (see Fig. 2.5). This reassessment of the Voyager radio occultations, which spanned a broader range of latitudes, longitudes but also times than the Galileo probe, yielded 1 bar temperatures of $170.3 \pm 3.8\,\mathrm{K}$ at 12°S and $167.3 \pm 3.8\,\mathrm{K}$ at 0°N. This indicates a potential variation of up to almost 9 K at the 1 bar level between the latitudes of 12°S (Voyager 1 Ingress) and 7°N (Galileo hot-spot). Furthermore, Voyager suggested that Jupiter's atmosphere was adiabatic around the 1 bar level, with a temperature lapse rate of about $2\,\mathrm{K/km}$. Galileo confirmed the close to adiabatic behaviour of the atmosphere down to ~ 16 bars, and indicated a potential sub-adiabat below, down to 22 bars (see Seiff et al. [1998], Magalhães et al. [2002]).

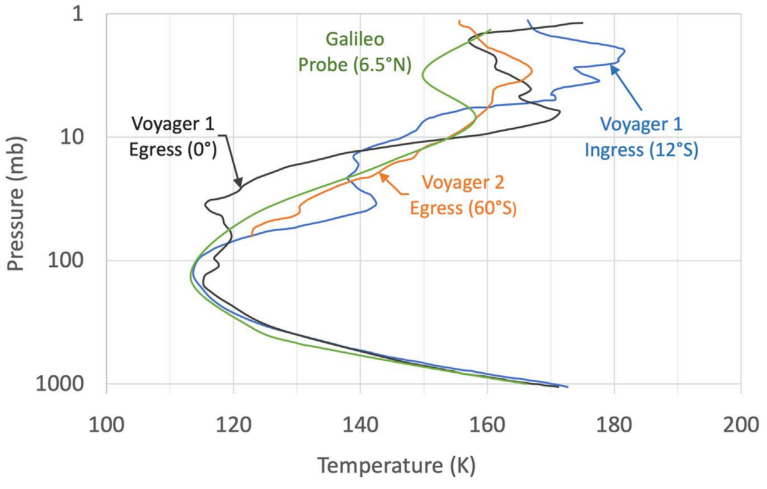

FIGURE 2.5: Updated temperature profiles of Jupiter derived from radio occultation observations by the Voyager 1 ingress and egress and the Voyager 2 egress, compared to the Galileo probe measurements. The Voyager 2 radio occultations could not probe deep enough to the 1 bar level. Taken from Gupta et al. [2022].

The composition of the atmosphere of Jupiter is believed to be hydrogen and helium

dominated, in proportions close to cosmic. The occultation of β Scorpii, the same event used to derive Jupiter's equatorial radius [Hubbard and van Flandern, 1972], led to the conclusion that the atmosphere is a hydrogen and helium mixture with a mass fraction of helium of $Y = 0.28^{+0.24}_{-0.28}$ [Elliot et al., 1974]. The analysis of the Voyager data [Gautier et al., 1981] then provided estimates of the helium atmospheric content through two methods: examining pressure-induced absorption of $H_2 - He$ collisions in infrared spectra from Voyager IRIS (Infrared interferometer spectrometer and radiometer) and then combining them with the radio occultation data [Lindal et al., 1981]. The following values of the helium mass fraction were obtained: $Y = 0.19 \pm 0.05$ and $Y = 0.21 \pm 0.06$. The in-situ measurement of the Galileo probe is the most reliable and yielded: $Y/(X + Y) = 0.238 \pm 0.005$ [von Zahn et al., 1998], a commonly employed value in today's interior models. The Galileo value is greater (the mass fraction of heavy elements was assumed to be 1.9%) than what was suggested by Voyager. On another note, the bulk helium content in Jupiter's interior is expected to be constant through the planet's evolution. A depletion of the helium fraction in the atmosphere compared to the initial bulk helium fraction would mean that the helium fraction in the deep interior must be enhanced. We believe that Jupiter formed by accreting gas from the protosolar nebula. The hydrogen to helium ratio of the atmosphere of Jupiter is hence compared to the Sun's. But because of gravitational settling in the Sun, the protosolar hydrogen to helium ratio relies on measurements of the Sun's photosphere as well as evolution models of the Sun. The protosolar abundances are regularly estimated [Bahcall et al., 1995, Lodders et al., 2009, Serenelli and Basu, 2010]. Table 4 from Asplund et al. [2021] lists several values of the protosolar abundance of helium but also of heavy elements and gives their values: $Y_{\text{proto}} = 0.2725$ and $Z_{\text{proto}} = 0.0154$. Models of Jupiter are thus dependent on the assumed value of Y_{proto}. Concerning heavy elements, infrared spectra from Voyager 1 and 2 [Hanel et al., 1979b,a] already detected among several species water, methane, ammonia, phosphine and germane. The abundances of heavy elements have mainly been measured by the Galileo entry probe [Niemann et al., 1998, Mahaffy et al., 2000, Atreya et al., 2003, Wong et al., 2004] which reported condensible species (H_2O, CH_4, NH_3, H_2S) and noble gases (He, Ne, Ar, Kr, Xe). Water was found to be substantially depleted. But this water measurement is thought to be only representative of the Galileo hot-spot. On the contrary, noble gases are expected to be less subject to spatial variations because they are chemically unactive. However, neon is found to be highly depleted as it is trapped in helium droplets which sink in the deep interior [Wilson and Militzer, 2010]. Besides, the concentration of condensible species was found to be still increasing beneath the cloud level. This behaviour was confirmed by the Juno Microwave Radiometer (MWR) [Li et al., 2017] which showed latitudinal variations and a well-mixed distribution of ammonia from only 50 bars, down to a few hundred bars. Currently, MWR loosely constrained the water abundance in the equatorial region (between 1 and 5 times the protosolar value) [Li et al., 2020]. Disequilibrium species (carbon monoxide, phosphine, germane and arsine) have also been measured [Grassi

et al., 2020] and can help constrain the heavy element content of Jupiter's atmosphere [Cavalié et al., 2023]. Figure 2.6 shows the measured abundances of the four giant planets of the solar system. Figure 2.7 shows the abundances of the major constituents of Jupiter's atmosphere and provides estimates of the atmosphere metallicity to account for in interior models, which is between 2 and 4 times the protosolar value. Finally, isotopic ratios which have mostly been measured by Galileo can be useful to constrain the origin of Jupiter (see Table 3 of Guillot et al. [2022]).

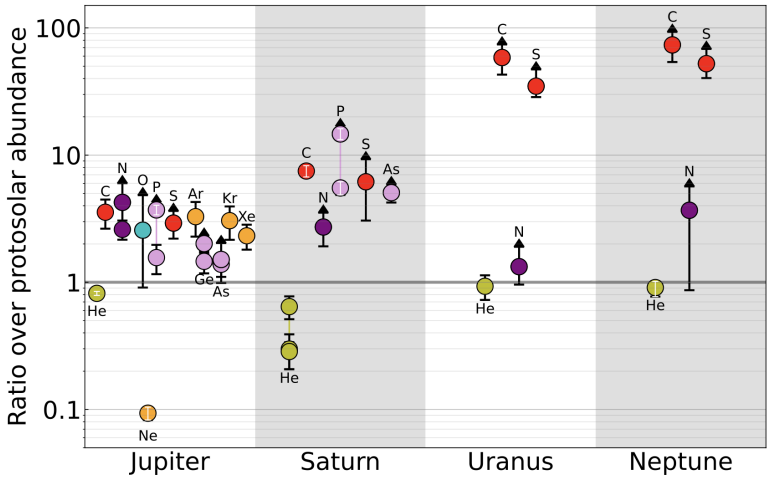

FIGURE 2.6: Elemental abundances of He, C, N, O, P, S, Ne, Ar, Ge, As, Kr and Xe in protosolar units in Jupiter, Saturn, Uranus and Neptune. Taken from Guillot et al. [2022].

2.1.5 Luminosity

The luminosity of a planet conveys key information about its current amount of energy and one can try to understand how the energy is transported from the deep interior to the surface but also how the planet evolved to a state with such luminosity. The luminosity of a planet comes from the reflected light received from the host star and from a potential internal heat. It is measured by observations essentially in the infrared wavelengths.

Öpik [1962] already suggested that Jupiter has an internal heat source, due to an effective temperature of the planet that would be larger than its equilibrium temperature. Before I continue, I need to define the concepts of effective and equilibrium temperatures. The effective temperature $T_{\rm eff}$ is the temperature of the planet considering it is a blackbody that emits the same radiated power:

$$L = 4\pi\sigma R^2 T_{\rm eff}^4. \tag{2.1}$$

The equilibrium temperature $T_{\rm eq}$ corresponds to the effective temperature in the case where the planet has no internal heat source. The intrinsic luminosity $L_{\rm int}$ would hence

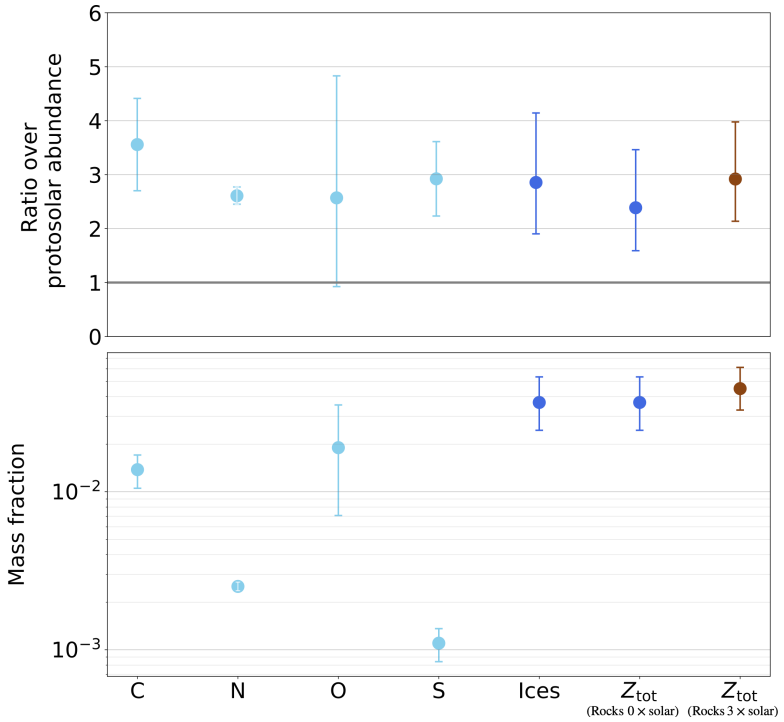

FIGURE 2.7: Abundances of heavy elements in the atmosphere of Jupiter. Here, 'ices' refers to the metallicity of the atmosphere considering only ices (CH_4, NH_3, H_2O and H_2S). Two values of Z_{tot} are shown, which correspond to the metallicity of the atmosphere considering ices (volatiles) and assuming either no rocks (refractories) or an enrichment of three times the protosolar value for rocks. Abundances of methane and hydrogen sulfide are taken from Wong et al. [2004], and ammonia and water abundances are taken from Li et al. [2020]. Protosolar abundances are taken from Asplund et al. [2021]. The protosolar mass fraction of heavy elements is 0.0154. For ices, we calculated the protosolar value considering C, N, O, S, and Ne and included additional elements with the value from Lodders et al. [2009]. Concerning rocks, we only considered Mg, Si, and Fe. **Figure taken from Howard et al. [2023].**

be 0 and the planet is heated only by the luminosity it receives from its star. It is defined as:

$$L_{\rm int} = 4\pi\sigma R^2 (T_{\rm eff}^4 - T_{\rm eq}^4). \tag{2.2}$$

We note that the equilibrium temperature requires the knowledge of the power irradiated by the star as well as the Bond albedo of the planet (see, e.g., Hubbard [1980]).

Infrared observations from Low [1966] definitely confirmed that Jupiter emits more energy than it receives from the Sun. These ground-based observations agreed with a telescope embedded in an aircraft which provided a few years later observations on a wider range of wavelengths [Aumann et al., 1969]. A new measurement of Jupiter's Bond albedo from the Voyager IRIS instrument could better constrain the energy balance (defined as the ratio of the emitted energy to absorbed solar energy), see Hanel et al. [1981] for a summary of the measurements of the effective temperature of Jupiter. The energy balance of Jupiter was assessed by Voyager [Pearl and Conrath, 1991] but the most recent data come from Cassini [Li et al., 2018] and I summarize it in Table 2.2.

TABLE 2.2: Energy balance of Jupiter. The mean radius of Jupiter was taken from [Guillot, 2005].

Energy balance	2.132
Emitted power $[10^{23}\,\mathrm{erg.s^{-1}}]$	86.55
Absorbed solar power $[10^{23}\,\mathrm{erg.s^{-1}}]$	40.61
Intrinsic power $[10^{23}\,\mathrm{erg.s^{-1}}]$	45.94
Intrinsic flux $[\mathrm{erg.s^{-1}.cm^{-2}}]$	7485
Effective temperature [K]	125.6
Equilibrium temperature [K]	103.9
Bond albedo	0.503

The excess of luminosity due to an internal heat supply has two possible explanations, both being gravitational energy sources. The first is heat acquired during the early stages of the formation of Jupiter, in the collapse phase. The second is energy acquired from the differentiation of helium in the envelope, with helium sinking in the deep interior. An excess of luminosity is also found in Saturn and Neptune (not in Uranus so far) and helium differentiation is thought as the most plausible explanation of Saturn's luminosity excess. Measurements of a depletion of helium (see Subsection 2.1.4) in the atmosphere would hence bring support to this explanation. More details about the evolution of giant planets will be discussed in Section 2.4.

2.1.6 Exoplanets data

Concerning other solar system giant planets, a lot of data is also available for Saturn, thanks to the Cassini mission. But Uranus and Neptune are still poorly understood given that no missions really visited them in depth. About exoplanets, observations consist mostly in measurements of radius and mass. This is essentially done with the transit and radial velocity techniques. Age is also important to constrain evolution models and is obtained if we know the age of the star. We are now also getting constraints on the atmosphere properties and the present species by spectroscopy (i.e. JWST). More details will be discussed in Chapter 6.

2.2 Basic equations

Giant planets are governed by the same equations as for a star, without including terms corresponding to nuclear fusion (see e.g. Kippenhahn et al. [2013]). For instance, Jupiter would have needed to be about 13 times more massive to start nuclear reactions [Burrows et al., 1997]. First, assuming no rotation and spherical symmetry, the interior structure and evolution of giant planets can be modelled by the equations of hydrostatic

equilibrium, conservation of mass, conservation of energy and an equation for energy transport:

$$\text{Hydrostatic equilibrium: } \frac{\partial P}{\partial r} = -\rho g \tag{2.3}$$

$$\text{Mass conservation: } \frac{\partial m}{\partial r} = 4\pi r^2 \rho \tag{2.4}$$

$$\text{Energy transport: } \frac{\partial T}{\partial r} = \frac{\partial P}{\partial r}\frac{T}{P}\nabla_T \tag{2.5}$$

$$\text{Energy conservation: } \frac{\partial L}{\partial r} = 4\pi r^2 \rho \left(\dot{\epsilon} - T\frac{\partial S}{\partial t}\right) \tag{2.6}$$

where P is pressure, r is the radius, ρ is the density, $g = Gm/r^2$ is the gravitational acceleration (G being the gravitational constant), m is the mass, T is the temperature, $\nabla_T = \frac{\mathrm{dln}T}{\mathrm{dln}P}$ is the temperature gradient, L is the intrinsic luminosity, $\dot{\epsilon}$ is a term corresponding to sources of energy such as nuclear reactions (generally assumed to be zero for a planet like Jupiter) and S is the specific entropy.

The hydrostatic equilibrium equation is a particular case of the equation of conservation of momentum. Here, magnetic field and viscosity are neglected. We will see further that this equation becomes more complex when accounting for the rotation of a planet. The gravitational acceleration actually derives from the gravitational potential V, which is obtained as a solution of the Poisson equation $\Delta V = 4\pi G\rho$. Whether hydrostatic equilibrium is a valid assumption is a legitimate question. Hydrostatic equilibrium is a state where gravity is balanced by the forces of pressure inside a planet. It implies that no significant change in the size, shape or other properties of the planet will be observed and the planet will remain in this stable state for an extended period of time. It is thought that giant planets are fluid and dynamical processes occur on a much slower timescale than the hydrostatic timescale. The latter reads: $\tau_{\mathrm{hydro}} \approx \frac{1}{2}(G\bar{\rho})^{-1/2}$ [Kippenhahn et al., 2013]. The value of τ_{hydro} for Jupiter is about 28 minutes. It seems rather small but dynamical processes like convection occur much slower. Besides, a comparison of the observed oblateness of a planet (obtained from observations of the apparent flattening) to its dynamical oblateness (obtained from measurements of J_2 and J_4) can assess the assumption of hydrostatic equilibrium and a good agreement between both values is found for Jupiter (see Stevenson [1982]). Thus, hydrostatic equilibrium is overall a good assumption for Jupiter and giant planets.

The mass conservation equation describes how the mass is distributed inside the planet. The energy transport equation describes how temperature varies in the interior. It depends on the temperature gradient ∇_T which depends on how heat is transported in the interior. This will discussed more in detailed in the following section. The energy conservation equation describes the distribution of heat, i.e. how the energy flux varies in the interior. This equation is time-dependent, it also describes how the intrinsic luminosity evolves as the planet ages. The evolution of giant planets will be more detailed in Chapter 6. Equation 2.6 is hence used in evolution models ; in static models

the luminosity is fixed to its present-day measured value. It is important to distinguish static and evolution models. Static models refer to interior or structure models at a specific age (usually today) where the luminosity as well as the temperature profile are given. On the other hand, evolution models simulate the contraction and cooling of planets and show how the properties of planets such as their radius or thermal profile evolve with time. They can provide additional constraints by matching the current observed structure of a planet. For Jupiter, I have mostly been working with static models during my PhD.

In order to solve this set of equations, we need an equation of state $\rho(P,T)$ to link the different physical parameters (discussed in the next chapter) and to define the temperature gradient ∇_T (discussed in the next section). We also need to assume a structure (like three-layer, see Chapter 1) for our model and assume a chemical composition. One must keep in mind that we try to infer the internal composition by solving an inverse problem: models matching best the data will be considered as the best picture of the interior of the planet.

For more information about how to make models of giant planets, I refer the reader to Guillot [1999, 2005], Fortney et al. [2010], Guillot and Gautier [2015], Miguel and Vazan [2023].

2.3 Heat transport in giant planets

How heat is transported through the interior of giant planets is essential to understand. We have seen in the previous subsection that we need to define the temperature gradient to build an interior model. Three mechanisms can explain how heat is transported through the interiors of giant planets: conduction, radiation or convection. It is hence important to assess which process is the main mechanism at work in these planets. This section borrows again ideas from Kippenhahn et al. [2013].

In Jupiter, but not only, an excess of luminosity has been observed (see Subsection 2.1.5). The internal heat somehow needs to be transported from the deep interior to the surface. Let's define the conductive, radiative and adiabatic gradients which are the temperature gradients (how temperature evolves with pressure in the interior) if heat is transported by conduction, radiation or convection, respectively:

$$\nabla_{\rm cond} = \left(\frac{{\rm dln}T}{{\rm dln}P}\right)_{\rm cond}, \quad \nabla_{\rm rad} = \left(\frac{{\rm dln}T}{{\rm dln}P}\right)_{\rm rad}, \quad \nabla_{\rm ad} = \left(\frac{{\rm dln}T}{{\rm dln}P}\right)_{\rm ad}. \tag{2.7}$$

We here assume that in a convective medium, a parcel of fluid that rises or descends would do it fast enough so that it does not exchange heat with its surroundings. This process would thus be isentropic. Evaluating and comparing these gradients would

tell what is the main mechanism that drives heat. Indeed, the lowest gradient would correspond to the most efficient way to transport heat.

2.3.1 Conduction, radiation, convection

The mean free path $l = 1/(\kappa\bar{\rho})$ (κ is the mean absorption coefficient or opacity and $\bar{\rho}$ is the mean density of the medium) of transporting particles in planets is expected to be small compared to the planets radius. Radiation can then be handled as a diffusive process, in the form of a Fick's law. The energy density radiation $U = aT^4$, with $a = 7.57 \times 10^{-15}\,\mathrm{erg.cm^{-3}K^{-4}}$ being the radiation density constant, can replace the number density in the Fick's law. Therefore:

$$\nabla U = 4aT^3\nabla_T, \tag{2.8}$$

and the diffusion coefficient reads:

$$D = \frac{1}{3}cl, \tag{2.9}$$

with c the speed of light. The radiative flux hence reads:

$$F_{\mathrm{rad}} = -k_{\mathrm{rad}}\frac{dT}{dr}, \tag{2.10}$$

with:

$$k_{\mathrm{rad}} = \frac{4ac}{3}\frac{T^3}{\kappa_{\mathrm{rad}}\bar{\rho}}. \tag{2.11}$$

Similarly, the conductive flux can be defined as:

$$F_{\mathrm{cond}} = -k_{\mathrm{cond}}\frac{dT}{dr}, \tag{2.12}$$

with:

$$k_{\mathrm{cond}} = \frac{4ac}{3}\frac{T^3}{\kappa_{\mathrm{cond}}\bar{\rho}}. \tag{2.13}$$

Using the luminosity $L = 4\pi r^2 F$, we can write:

$$\frac{dT}{dr} = -\frac{3}{16\pi ac}\frac{\kappa\bar{\rho}L}{r^2T^3}. \tag{2.14}$$

Assuming hydrostatic equilibrium, the radiative gradient reads:

$$\nabla_{\mathrm{rad}} = \left(\frac{\mathrm{dln}T}{\mathrm{dln}P}\right)_{\mathrm{rad}} = \frac{P}{T}\left(\frac{dT}{dP}\right)_{\mathrm{rad}} = \frac{P}{T}\left(\frac{(dT/dr)}{(dP/dr)}\right)_{\mathrm{rad}} \tag{2.15}$$

It finally yields for both the radiative and conductive gradients:

$$\nabla_{\mathrm{rad}} = \frac{3}{16\pi acG}\frac{\kappa_{\mathrm{rad}}\bar{\rho}L}{mT^4}, \quad \nabla_{\mathrm{cond}} = \frac{3}{16\pi acG}\frac{\kappa_{\mathrm{cond}}\bar{\rho}L}{mT^4}. \tag{2.16}$$

But for simplicity, because we treated radiation and conduction in a similar manner, we will define only one radiative gradient that will be equal to:

$$\nabla_{\rm rad} = \frac{3}{16\pi acG}\frac{\kappa\bar{\rho}L}{mT^4}. \tag{2.17}$$

with $1/\kappa = 1/\kappa_{\rm rad} + 1/\kappa_{\rm cond}$.

Convection corresponds to the transport of heat by movements of fluids. The hot parcels of fluids tend to rise while the cold parcels of fluids tend to sink. This is an efficient mechanism to mix different materials as large-scale movements of fluids may be engendered. In a convective medium, the temperature gradient corresponds to the adiabatic gradient that can directly be calculated from an equation of state:

$$\nabla_{\rm ad} = \left(\frac{{\rm dln}T}{{\rm dln}P}\right)_{\rm S}. \tag{2.18}$$

2.3.2 Criteria for convective stability

Before evaluating these gradients, we here define the stability criteria that would tell if convection occurs in a medium or if it will be inhibited. To derive a criterion, let's assume the simple problem of a parcel of fluid that is raised adiabatically (without exchanging heat with its surroundings) from a position r to a new position $r + \Delta r$ ($\Delta r > 0$). Figure 2.8 illustrates the situation.

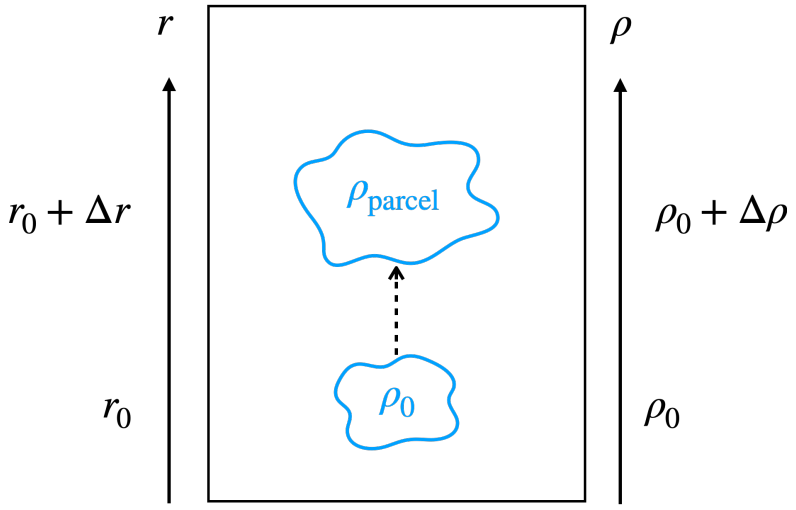

FIGURE 2.8: Schematic of a parcel of fluid raised adiabatically.

The difference in density between the parcel and its surroundings will be:

$$D\rho = \left[\left(\frac{d\rho}{dr}\right)_{\rm parcel} - \left(\frac{d\rho}{dr}\right)_{\rm surr}\right]\Delta r, \tag{2.19}$$

$(d\rho/dr)_{\text{parcel}}$ is the change of density of the parcel when being lifted by Δr and $(d\rho/dr)_{\text{surr}}$ is the density gradient in the surroundings. If the parcel, at its new position, is less dense than its new surroundings, $D\rho < 0$ and the radial component of the buoyancy force $K_r = -gD\rho$ is positive so the parcel will continue to rise, leading to an unstable situation. Nonetheless, if $D\rho > 0$ and the parcel of fluid is denser than its new surroundings, the buoyancy force will be oriented downwards and the parcel will sink back to its initial position, leading to a stable situation. The stability criterion is thus given by $D\rho > 0$:

$$\left(\frac{d\rho}{dr}\right)_{\text{parcel}} > \left(\frac{d\rho}{dr}\right)_{\text{surr}} \tag{2.20}$$

An equation of state $\rho(P, T, \mu)$ could switch from density to temperature in this equation. If we write the differential form of the equation of state, we get:

$$\frac{d\rho}{\rho} = \alpha\frac{dP}{P} - \delta\frac{dT}{T} + \phi\frac{d\mu}{\mu}, \tag{2.21}$$

where:

$$\alpha = \left(\frac{\text{dln}\rho}{\text{dln}P}\right), \quad \delta = -\left(\frac{\text{dln}\rho}{\text{dln}T}\right), \quad \phi = \left(\frac{\text{dln}\rho}{\text{dln}\mu}\right). \tag{2.22}$$

Injecting Eq. 2.21 in Eq. 2.20, removing the pressure related terms because we assume pressure balance, we get:

$$-\left(\frac{\delta}{T}\frac{dT}{dr}\right)_{\text{parcel}} + \left(\frac{\phi}{\mu}\frac{d\mu}{dr}\right)_{\text{parcel}} > -\left(\frac{\delta}{T}\frac{dT}{dr}\right)_{\text{surr}} + \left(\frac{\phi}{\mu}\frac{d\mu}{dr}\right)_{\text{surr}}. \tag{2.23}$$

We assume that the chemical composition of the parcel of fluid does not change during its adiabatic rise ($d\mu = 0$) and we multiply Eq. 2.23 by $-(P)dr/dP$ (pressure height scale) to obtain:

$$\delta\frac{P}{T}\left(\frac{dT}{dP}\right)_{\text{parcel}} > \delta\frac{P}{T}\left(\frac{dT}{dP}\right)_{\text{surr}} - \phi\frac{P}{\mu}\left(\frac{d\mu}{dP}\right)_{\text{surr}} \tag{2.24}$$

Keeping in mind that the parcel of fluid rises adiabatically and that the temperature gradient is equal to ∇_{rad} if the transport of energy is done by radiation or conduction, we finally get the Ledoux criterion:

$$\nabla_{\text{rad}} < \nabla_{\text{ad}} + \frac{\phi}{\delta}\nabla_\mu, \tag{2.25}$$

where $\nabla_{\text{rad}} = (\text{dln}T/\text{dln}P)_{\text{surr}}$, $\nabla_{\text{ad}} = (\text{dln}T/\text{dln}P)_{\text{parcel}}$ and $\nabla_\mu = (\text{dln}\mu/\text{dln}P)_{\text{surr}}$. In the case of a medium with a homogeneous chemical composition, the composition gradient ∇_μ vanishes and it yields the Schwarzchild criterion:

$$\nabla_{\text{rad}} < \nabla_{\text{ad}} \tag{2.26}$$

In both criteria (which are local), if the left-hand side term is greater than the right one,

then it is unstable and convection should occur. A particular situation can happen when a region is Ledoux stable but Schwarzchild unstable ($\nabla_{\rm ad} < \nabla_{\rm rad} < \nabla_{\rm ad} + \frac{\phi}{\delta}\nabla_\mu$). It leads to a less efficient type of convection, called semi-convection or layered convection (or even double-diffusive convection often used in oceanography). In this case, convective cells separated by diffusive interfaces appear, creating a compositional staircase structure (see hydrodynamic simulations of Rosenblum et al. [2011]).

2.3.3 Adiabatic and non-adiabatic interiors

A rough calculation by [Militzer et al., 2016] shows that the adiabatic gradient in Jupiter's interior is almost two orders of magnitude smaller than the conductive gradient, indicating that convection is expected to be the main mechanism driving heat. A crude estimate of the temperature gradient in the interior showed that it is very similar to the adiabatic one [Guillot et al., 2004]. Besides, the excess of luminosity requires an efficient mechanism to transport heat from the interior to the surface of Jupiter to explain the measured luminosity of the planet. Convection appears as the right candidate and the success of homogeneous and fully convective models decades ago [Hubbard, 1968, 1969] brought support to the idea of an adiabatic interior. Also, homogeneous evolution (in the sense that the composition does not change with time) models (albeit of solar composition) [Hubbard, 1977] could lead to a relatively good agreement between the current luminosity and age of Jupiter, without invoking for instance helium unmixing. Finally, adiabatic temperature profiles were measured by Voyager or Galileo in the atmosphere (see Subsection 2.1.4). Those several arguments justify why Jupiter was thought to be essentially convective. This also led to the idea that compositional atmospheric measurements are representative of the envelope because of efficient mixing due to convection. The high opacity of the H/He mixture due to the pressure and temperature conditions in Jupiter's interior can explain why it is convective (more details can be found in Guillot and Gautier [2015]).

Nevertheless, Stevenson [1985] already questioned the adiabatic assumption that comes along with a homogeneous interior. By a simple analogy with a crystal of salt dropped in a beaker containing water, he suggested that a compositional gradient may inhibit large-scale convection. Leconte and Chabrier [2012] followed this speculation and found models with compositional gradients that lead to semi-convection and thus a superadiabatic temperature profile. Recent Jupiter interior models based on Juno gravity data suggest the presence of a dilute core and hence of a non-adiabatic interior (see, e.g., Debras and Chabrier [2019], Militzer et al. [2022]). But compositional gradients are not the only factors that could prevent from large-scale convection [Guillot et al., 2004]. Condensation effects [Guillot, 1995] or rotation [Fuentes et al., 2023] could inhibit convection. Guillot et al. [1994] also suggested that a radiative window may exist in giant planets (between 1200 and 2900 K for Jupiter and between 1400 and 2600 K for Saturn) due to an opacity

decrease. Due to latent heat release, moist convection, with a moist adiabatic gradient $\nabla_{\rm moist,ad}$ smaller than the standard adiabatic gradient $\nabla_{\rm dry,ad}$, can occur and inhibit convection in hydrogen atmospheres [Guillot, 1995, Leconte et al., 2017]. Last but not least, helium differentiation due to immiscibility [Stevenson and Salpeter, 1977a] can also lead to non-adiabaticity.

2.4 Giant planets evolution

Once giant planets are formed, they undergo a phase of cooling and contraction that can last for billions of years. Giant planets start from a stage where they are hot, luminous and extended. We are interested in how these objects cool and contract and we hence look at the evolution of their radius and luminosity.

We recall the energy balance equation:

$$L = L_{\odot} + L_{\rm int}, \tag{2.27}$$

where $L = 4\pi\sigma R^2 T_{\rm eff}^4$ and $L_{\odot} = 4\pi\sigma R^2 T_{\rm eq}^4$, already presented in Subsection 2.1.5. The intrinsic luminosity that corresponds to the internal heat loss is composed of the gravitational energy E_g and the internal energy E_i:

$$L_{\rm int} = -\frac{dE}{dt} = -\frac{d}{dt}(E_g + E_i), \tag{2.28}$$

which leads to Eq. 2.6 (see Nettelmann [2011] for a demonstration) or:

$$L_{\rm int} = 4\pi\sigma R^2 (T_{\rm eff}^4 - T_{\rm eq}^4) = -\int T \frac{dS}{dt} dm \tag{2.29}$$

This equation is in terms of mass but one just needs to use the equation of conservation of mass to have it in terms of radius. We can integrate over time Eq. 2.29 to follow the evolution of the effective temperature and the radius of the planet. But the integration also requires a relation between $T_{\rm eff}$ and the interior temperature $T_{\rm 1bar}$. Such relation can be obtained from model atmospheres, notably from Graboske et al. [1975], so that Eq. 2.29 is only dependent on $T_{\rm eff}$. For instance, Saumon et al. [1992] adopt:

$$T_{\rm eff} = 0.7 g^{0.134} T_{\rm 1bar}^{0.804}. \tag{2.30}$$

The role of the radiative atmosphere above the convective interior is key and dictates the cooling. Model atmospheres based on opacity tables are crucial to account for the properties of the atmosphere.

The procedure followed in CEPAM [Guillot and Morel, 1995] is described in Guillot et al. [1995]. To generate an evolutionary sequence, we start from a static model at

an age of 0. We provide an initial radius of the planet and the value of $c_1 = dS/dt$ at this age, so that the initial luminosity is significantly higher than the actual value ("significantly" is vague but because the luminosity is inversely proportional to age, the initial conditions have only a weak effect, except for very young objects). We can then obtain the effective temperature with Eq. 2.29. Assuming an initial radius actually prescribes the initial entropy of the planet. We continue with a second static model at an age defined by:

$$\Delta t = \frac{\Delta S}{c_1}, \tag{2.31}$$

where ΔS is the specific entropy difference between both models. We now directly know the temperature of this model as its entropy is set by the increment from the previous static model. We can thus get the luminosity and the radius of this second model. We continue this procedure until we reach the current stage or even the desired future state of the planet. Eventually, the planet should reach a point where its radius remains constant. These calculations focus on the long-term evolution phase and do not account for the formation of the planet.

Concerning Jupiter, homogeneous evolution models, namely with no change of the composition with time, have always been quite correct to predict the age of the planet. Evolution models of Hubbard [1977] yielded an age of 5.1 Gyr. With the improvement of interior models thanks to new observational data from Pioneer and Voyager, Saumon et al. [1992] derived an age of ~ 5.3 Gyr. The cooling time of Jupiter was found to be reduced to 4.2 Gyr when including a radiative region [Guillot et al., 1995]. Fortney and Hubbard [2003] derived an age of 4.7 Gyr thanks to improved model atmospheres from Burrows et al. [1997], in agreement with [Hubbard et al., 1999]. Conversely, for Saturn, homogeneous models predict ages of only about 2-2.7 Gyr [Fortney and Nettelmann, 2010]. It is believed that the H/He phase separation [Stevenson and Salpeter, 1977a] is a source of energy that could explain why Saturn is overluminous. Given the great job of homogeneous models for Jupiter, H/He phase separation has not begun or has just begun. Inhomogeneous evolution models, accounting for phase separation and differentiation of helium, have then been developed (see, e.g., Mankovich and Fortney [2020]). Such differentiation will affect the entropy of the different layers of the planet and hence impact its luminosity.

Another aspect of the evolution of a giant planet is how material mix with time, how it is redistributed. This is not something I have directly been working on during my PhD but literature on this topic will be discussed in Chapter 5 when focusing on the extent of the dilute core.

2.5 The figures of planets (the theory behind gravitational moments)

Because of their rotation, planets are not spherically symmetric. The centrifugal force causes the planet to flatten at the poles and to bulge at the equator, creating a slightly oblate shape. The gravity field of the planet hence deviates from one of a perfectly spherically symmetric planet and offers us information on the composition of the interior. The term "figures" refers to the shape of the planets and more precisely to surfaces of equal potential, that will be detailed right after.

The gravity field of a planet can nowadays be measured by a spacecraft in orbit around the planet. Building a planetary model (see Section 2.2) to calculate (numerically) its gravity field and compare it to the observed one appears as an efficient strategy to indirectly determine the internal structure of a planet. This technique, called gravitational sounding, can be employed with the help of the so-called theory of figures. The theory of figures allows to calculate the gravity field of a planet for a specific density distribution. It is hence possible to solve the inverse problem and infer the density distribution inside a planet.

Only ten years ago, Bill Hubbard developed a new method called CMS (Concentric Maclaurin Spheroid) which leads to a more accurate calculation of the gravitational moments. However, this method is more time-consuming than the theory of figures. We will thus proceed by calibrating the gravitational moments obtained with the theory of figures via some offsets that have been estimated beforehand between both methods. The theory behind both method is presented here, more details about their application in the codes (CEPAM [Guillot and Morel, 1995] and CMS4Cepam) I used will be discussed in Chapter 4.

2.5.1 Theory of figures

Calculating the gravity field is key when studying the interior of giant planets and I could not write my thesis without dedicating a subsection to the theory of figures. The latter has been developed since the beginning of the 19th century. I will here provide a description of the theory. This is essentially a summary of the thorough work from Zharkov and Trubitsyn [1978] which was translated from russian to english by Bill Hubbard. I will here focus only on its application to giant planets. I must admit that I probably do not have the mathematical level of the authors and of other scientists who contributed to the theory of figures. I will however try to be as comprehensive as possible on the depiction of the sequence of steps of the theory. For more mathematical details, I refer the reader to Nettelmann [2011].

Assuming a density distribution $\rho(r)$ inside a rotating planet, the goal of the theory of figures is to find the shape of the planet self-consistently with its gravity field. As already mentioned before, solving the inverse problem would then provide us with the internal composition of the planet.

The first assumption made in the theory is hydrostatic equilibrium. The reliability of this assumption is debated in Section 2.2. This can be written in a more complex form than in Eq. 2.3 because we include rotation now:

$$\frac{\nabla P}{\rho} = \nabla V + \nabla Q = \nabla U, \tag{2.32}$$

where U is the total potential, V and Q the gravitational and centrifugal potentials respectively. It shows that level surfaces of (equal) potential are also level surfaces of pressure and density. The problem consists of finding the level surfaces $r = r(\theta)$ (θ being the colatitude) so that $U(r)$ is constant. This potential will now be expressed and we will see that the gravitational potential, that depends on the density distribution, can be developed as an infinite sum of the so-called gravitational moments. This represents the departure of the planet from perfect sphericity, because of its rotation. The gravitational pull of the planet exerted on for instance a spacecraft hence provides information on the shape of the planet, assuming a density distribution.

i. Expressing the total potential.

The gravitational and centrifugal potentials respectively read:

$$V(r) = G \int \frac{\rho(r')}{|r - r'|} d\tau', \tag{2.33}$$

$$Q(r) = \frac{1}{2}\omega^2 r^2 \sin^2\theta. \tag{2.34}$$

We note that r is the radial component of the position of an arbitrary point in space, while r' corresponds to a point inside the planet. $d\tau'$ is a volume element. ω is the angular velocity of rotation of the planet and G is the gravitational constant. The gravitational potential can then be decomposed in a serie of Legendre polynomials using:

$$\frac{1}{|r - r'|} = \begin{cases} \frac{1}{r}\sum_{n=0}^{\infty}(\frac{r'}{r})^n P_n(t), & \text{if } r > r' \text{ (external).} \\ \frac{1}{r}\sum_{n=0}^{\infty}(\frac{r'}{r})^{-n-1} P_n(t), & \text{if } r < r' \text{ (internal).} \end{cases} \tag{2.35}$$

with $t = \cos(\psi)$, ψ being the angle between the radius vectors r and r'. $P_n(t)$ are the Legendre polynomials:

$$P_n(t) = \frac{1}{2^n n!}\frac{d^n}{dt^n}[(t^2 - 1)^n]. \tag{2.36}$$

The gravitational potential can be written:

$$V(r) = \frac{G}{r} \sum_{n=0}^{\infty} \int \rho(r') P_n(t) (r'/r)^k d\tau', \tag{2.37}$$

with $k = n$ if $r > r'$ and $k = -(n+1)$ if $r < r'$. The potential is divided into an external potential where $r > r'$ and an internal potential where $r < r'$. With $t = \cos(\psi) = \cos(\theta)\cos(\theta') + \sin(\theta)\sin(\theta')\cos(\lambda - \lambda')$ (λ and λ' being the azimuthal components corresponding to r and r' respectively) and using the addition theorem for spherical harmonics, the gravitational potential becomes:

$$V(r) = \frac{G}{r} \sum_{n=0}^{\infty} P_n(\cos\theta) \int \rho(r') P_n(\cos\theta') (r'/r)^k d\tau'. \tag{2.38}$$

This expression is not general. Assuming axisymmetry, the gravitational potential does not depend on longitude and terms that depend on the azimuthal component vanish. A more general formula, valid for solid planets and where the density depends on longitude, can be found in [Zharkov and Trubitsyn, 1978] or in [Iess et al., 2018]. And because of assumed symmetry between the northern and southern hemispheres, the density $\rho(r, \theta)$ is an even function of θ. We obtain:

$$V(r, \theta) = \frac{G}{r} \sum_{n=0}^{\infty} (r^{-2n} D_{2n} + r^{2n+1} D'_{2n}) P_{2n}(\cos\theta), \tag{2.39}$$

with:

$$\begin{cases} D_n = \int_{r>r'} \rho(r') (r')^n P_n(\cos\theta) d\tau', \\ D'_n = \int_{r<r'} \rho(r') (r')^{-n-1} P_n(\cos\theta) d\tau'. \end{cases} \tag{2.40}$$

The non-dimensional coefficients are what we call gravitational moments: $J_n = -D_n/(Ma^n)$, M and a being respectively the mass and the equatorial radius of Jupiter. The reader can finally contemplate the expression for the gravitational moments, that have probably already been mentioned dozens of times in this manuscript.

The external gravitational potential can then be written:

$$V_{\text{ext}}(r, \theta) = \frac{GM}{r} \left[1 - \sum_{n=1}^{\infty} \left(\frac{a}{r} \right)^{2n} J_{2n} P_{2n}(\cos\theta) \right]. \tag{2.41}$$

We can express the centrifugal potential as a function of P_2:

$$Q(r) = \frac{1}{3} \omega^2 r^2 (1 - P_2(\cos\theta)). \tag{2.42}$$

It is now time to introduce the "small" parameter q which is the ratio of the centrifugal to the gravitational accelerations:

$$q = \frac{\omega^2 a^3}{GM}. \tag{2.43}$$

Another formulation exists using the mean radius s instead of the equatorial radius:

$$m = \frac{\omega^2 s^3}{GM}. \tag{2.44}$$

Finally, the total external potential can be expressed as:

$$U_{\text{ext}}(r,\theta) = \frac{GM}{r}\left[1 - \sum_{n=1}^{\infty}\left(\frac{a}{r}\right)^{2n} J_{2n} P_{2n}(\cos\theta) - \frac{1}{3}\left(\frac{r}{a}\right)^3 (1 - P_2(\cos\theta))q\right]. \tag{2.45}$$

We now have the final expression of the total external potential and we seek for level surfaces $r(\theta)$ that satisfy this expression. We recall the equation for the gravitational moments:

$$J_{2n} = -\frac{1}{Ma^{2n}}\int \rho(r')(r')^{2n} P_{2n}(\cos\theta) d\tau'. \tag{2.46}$$

The difficulty is that we need to integrate over the volume to calculate the gravitational moments but the shape of the planet is not known and have to be found as part of a self-consistent solution.

ii. The level surfaces.

The level surfaces, where the potential is constant, differ only slightly from spheres and are called spheroids. They are defined as:

$$r(\theta) = l\left(1 + \sum_{n=0}^{\infty} s_{2n} P_{2n}(\cos\theta)\right). \tag{2.47}$$

s_{2n} are the figure functions and describe the shape of the surface (how they deviate from a sphere). The theory of figures is hence a perturbation theory. l is the mean radius of a level surface, that is the radius of a spheroid defined by:

$$\frac{4\pi}{3} l^3 = \frac{2\pi}{3}\int_{-1}^{1} r^3(\theta) \mathrm{dcos}\theta. \tag{2.48}$$

Injecting Eq. 2.47 in the expression of D_n and D'_n, we can get:

$$D_n(l) = \frac{2\pi}{n+3}\int_0^l \rho(l')dl' \int_{-1}^{1} P_n(\cos\theta)\frac{dr^{n+3}}{dl'}\mathrm{dcos}\theta \tag{2.49}$$

$$D'_n(l) = \frac{2\pi}{2-n}\int_l^{R_{\text{m}}} \rho(l')dl' \int_{-1}^{1} P_n(\cos\theta)\frac{dr^{2-n}}{dl'}\mathrm{dcos}\theta \quad (\text{n} \neq 2) \tag{2.50}$$

$$D'_2(l) = 2\pi\int_l^{R_{\text{m}}} \rho(l')dl' \int_{-1}^{1} P_2(\cos\theta)\frac{d\ln r}{dl'}\mathrm{dcos}\theta, \tag{2.51}$$

with R_m. These expressions only depends on l: by moving from (r, θ) to l, we move from a 2D to a 1D problem. We also provide their dimensionless form, with $\beta = l/R_\mathrm{m}$:

$$\begin{aligned} S_n(\beta) = \frac{3}{4\pi\bar{\rho}l^{n+3}} D_n(l), \quad S'_n(\beta) = \frac{3}{4\pi\bar{\rho}l^{2-n}} D'_n(l) \\ S_n(\beta) = \beta^{-n-3} \int_0^\beta \frac{\rho(z)}{\bar{\rho}} \frac{d(z^{n+3} f_n)}{dz} dz \\ S'_n(\beta) = \beta^{n-2} \int_\beta^1 \frac{\rho(z)}{\bar{\rho}} \frac{d(z^{2-n} f'_n)}{dz} dz, \end{aligned} \tag{2.52}$$

with the following expressions for f_n and f'_n and replacing $\cos\theta$ by μ:

$$\begin{aligned} f_n(z) = \frac{3}{2(n+3)} \int_{-1}^1 P_n(\mu) \left(1 + \sum_{n=0}^\infty s_{2n} P_{2n}(\mu)\right)^{n+3} \mathrm{d}\mu \\ f'_n(z) = \frac{3}{2(2-n)} \int_{-1}^1 P_n(\mu) \left(1 + \sum_{n=0}^\infty s_{2n} P_{2n}(\mu)\right)^{2-n} \mathrm{d}\mu \quad (n \neq 2) \\ f'_2(z) = \frac{3}{2} \int_{-1}^1 P_n(\mu) \ln\left(1 + \sum_{n=0}^\infty s_{2n} P_{2n}(\mu)\right) \mathrm{d}\mu. \end{aligned} \tag{2.53}$$

iii. Solving the system of equations.

On a level surface, the potential does not depend on θ, by definition. We can finally write the potential U as a function of the figure functions.

$$U(l) = \frac{4\pi}{3} G\bar{\rho} l^2 \sum_{n=0}^\infty A_{2n}(l) P_{2n}(l), \tag{2.54}$$

$\bar{\rho}$ being the mean density (considering the volume of the planet calculated using its mean radius) and A_{2n} are complicated coefficients that depend on the figure functions s_{2n}. An expansion of these coefficients to third order ($n = 3$) can be found in Zharkov and Trubitsyn [1978] or to fourth order in Nettelmann [2017]. An expansion to order N truncates in Eqs. 2.54 and 2.47 the terms where $n > N$ to allow a calculation of the gravitational moments up to J_{2N}. Because the potential is constant on a level surface, it cannot depend on θ and the A_{2n} coefficients must be equal to zero except for $n = 0$. We are hence left with a system of equations $A_{2n} = 0$ for $n = 1, ..., +\infty$ that enables us to calculate the figure functions s_{2n}. I recall the expressions of the A_{2n} coefficients, taken from Nettelmann [2017] who gives an expansion to fourth order (the values of f_n can be found in the paper). The current version of CEPAM [Guillot and Morel, 1995]

is actually using the expansion to fourth order of Nettelmann [2017].

$$
\begin{aligned}
A_2 = &\left(-s_2 + \frac{2}{7}s_2^2 + \frac{4}{7}s_2 s_4 - \frac{29}{35}s_2^3 + \frac{100}{693}s_4^2 + \frac{454}{1155}s_2^4 - \frac{36}{77}s_2^2 s_4\right) S_0 \\
&+ \left(1 - \frac{6}{7}s_2 - \frac{6}{7}s_4 + \frac{111}{35}s_2^2 - \frac{1242}{385}s_2^3 + \frac{144}{77}s_2 s_4\right) S_2 \\
&+ \left(-\frac{10}{7}s_2 - \frac{500}{693}s_4 + \frac{180}{77}s_2^2\right) S_4 \\
&+ \left(1 + \frac{4}{7}s_2 + \frac{1}{35}s_2^2 + \frac{4}{7}s_4 - \frac{16}{105}s_2^3 + \frac{24}{77}s_2 s_4\right) S_2' \\
&+ \left(\frac{8}{7}s_2 + \frac{72}{77}s_2^2 + \frac{400}{693}s_4\right) S_4' \\
&+ \frac{m}{3}\left(-1 + \frac{10}{7}s_2 + \frac{9}{35}s_2^2 - \frac{4}{7}s_4 + \frac{20}{77}s_2 s_4 - \frac{26}{105}s_2^3\right)
\end{aligned}
\tag{2.55}
$$

$$
\begin{aligned}
A_4 = &\left(-s_4 + \frac{18}{35}s_2^2 - \frac{108}{385}s_2^3 + \frac{40}{77}s_2 s_4 + \frac{90}{143}s_2 s_6 + \frac{162}{1001}s_4^2\right. \\
&\left. + \frac{16902}{25025}s_2^4 - \frac{7369}{5005}s_2^2 s_4\right) S_0 + \left(-\frac{54}{35}s_2 - \frac{60}{77}s_4 + \frac{648}{385}s_2^2\right. \\
&\left. - \frac{135}{143}s_6 + \frac{21468}{5005}s_2 s_4 - \frac{122688}{25025}s_2^3\right) S_2 + \left(1 - \frac{100}{77}s_2\right. \\
&\left. - \frac{810}{1001}s_4 + \frac{6368}{1001}s_2^2\right) S_4 - \frac{315}{143}s_2 S_6 + \left(\frac{36}{35}s_2\right. \\
&\left. + \frac{108}{385}s_2^2 + \frac{40}{77}s_4 + \frac{3578}{5005}s_2 s_4 - \frac{36}{175}s_2^3 + \frac{90}{143}s_6\right) S_2' \\
&+ \left(1 + \frac{80}{77}s_2 + \frac{1346}{1001}s_2^2 + \frac{648}{1001}s_4\right) S_4' + \frac{270}{143}s_2 S_6' \\
&+ \frac{m}{3}\left(-\frac{36}{35}s_2 + \frac{114}{77}s_4 + \frac{18}{77}s_2^2 - \frac{978}{5005}s_2 s_4 + \frac{36}{175}s_2^3 - \frac{90}{143}s_6\right)
\end{aligned}
\tag{2.56}
$$

$$
\begin{aligned}
A_6 = &\left(-s_6 + \frac{10}{11}s_2 s_4 - \frac{18}{77}s_2^3 + \frac{28}{55}s_2 s_6 + \frac{72}{385}s_2^4 + \frac{20}{99}s_4^2\right. \\
&\left. - \frac{54}{77}s_2^2 s_4\right) S_0 + \left(-\frac{15}{11}s_4 + \frac{108}{77}s_2^2 - \frac{42}{55}s_6 - \frac{144}{77}s_2^3\right. \\
&\left. + \frac{216}{77}s_2 s_4\right) S_2 + \left(-\frac{25}{11}s_2 - \frac{100}{99}s_4 + \frac{270}{77}s_2^2\right) S_4 \\
&+ \left(1 - \frac{98}{55}s_2\right) S_6 + \left(\frac{10}{11}s_4 + \frac{18}{77}s_2^2 + \frac{36}{77}s_2 s_4 + \frac{28}{55}s_6\right) S_2' \\
&+ \left(\frac{20}{11}s_2 + \frac{108}{77}s_2^2 + \frac{80}{99}s_4\right) S_4' + \left(1 + \frac{84}{55}s_2\right) S_6' \\
&+ \frac{m}{3}\left(-\frac{10}{11}s_4 - \frac{18}{77}s_2^2 + \frac{34}{77}s_2 s_4 + \frac{82}{55}s_6\right)
\end{aligned}
\tag{2.57}
$$

$$
\begin{aligned}
A_8 = &\left(-s_8 + \frac{56}{65}s_2s_6 + \frac{72}{715}s_2^4 + \frac{490}{1287}s_4^2 - \frac{84}{143}s_2^2s_4\right) S_0 \\
&+ \left(-\frac{84}{65}s_6 - \frac{144}{143}s_2^3 + \frac{336}{143}s_2s_4\right) S_2 + \left(-\frac{2450}{1287}s_4\right. \\
&\left.+\frac{420}{143}s_2^2\right) S_4 - \frac{196}{65}s_2S_6 + S_8 + \left(\frac{56}{65}s_6 + \frac{56}{143}s_2s_4\right) S_2' \\
&+ \left(\frac{1960}{1287}s_4 + \frac{168}{143}s_2^2\right) S_4' + \frac{168}{65}s_2S_6' + S_8' \\
&+ \frac{m}{3}\left(-\frac{56}{65}s_6 - \frac{56}{143}s_2s_4\right)
\end{aligned}
\tag{2.58}
$$

The potential is given by A_0:

$$
U(l) = \frac{4\pi}{3}G\bar{\rho}l^2\sum_{n=0}^{\infty}A_0(l), \tag{2.59}
$$

$$
\begin{aligned}
A_0 = &\left(1 + \frac{2}{5}s_2^2 - \frac{4}{105}s_2^3 + \frac{2}{9}s_4^2 + \frac{43}{175}s_2^4 - \frac{4}{35}s_2^2s_4\right) S_0 \\
&+ \left(-\frac{3}{5}s_2 + \frac{12}{35}s_2^2 - \frac{234}{175}s_2^3 + \frac{24}{35}s_2s_4\right) S_2 + \left(\frac{6}{7}s_2^2 - \frac{5}{9}s_4\right) S_4 \\
&+ S_0' + \left(\frac{2}{5}s_2 + \frac{2}{35}s_2^2 + \frac{4}{35}s_2s_4 - \frac{2}{25}s_2^3\right) S_2' + \left(\frac{4}{9}s_4\right. \\
&\left.+\frac{12}{35}s_2^2\right) S_4' + \frac{m}{3}\left(1 - \frac{2}{5}s_2 - \frac{9}{35}s_2^2 - \frac{4}{35}s_2s_4 + \frac{22}{525}s_2^3\right)
\end{aligned}
\tag{2.60}
$$

The latest update is from Nettelmann et al. [2021] who provided an expansion to seventh order. The gravitational moments can be obtained by comparing the expression of the external potential including the J_{2n} and the one when the D_{2n} coefficients have been replaced by S_{2n}. We obtain:

$$
J_{2n} = -(R_{\mathrm{m}}/R_{\mathrm{eq}})^{2n}S_{2n}(1) \tag{2.61}
$$

Given the density distribution that we obtain by assuming a certain composition of the interior, we can calculate the figure functions which determine the shape of the planet using an iterative procedure and obtain the gravitational moments.

2.5.2 Concentric Maclaurin Spheroids

Given the high accuracy of the measurements of the gravitational moments expected with Juno, a high accuracy was required to calculate numerically the J_{2n}. Bill Hubbard hence developed the Concentric Maclaurin Spheroid (CMS) theory which leads to a more accurate calculation of the gravitational moments. While the theory of figures is a perturbation method (where the level surfaces are defined by their deviations from the

surface of a sphere), CMS consists of considering the planet as a sequence of spheroids of different densities and applying the superposition theorem to express the gravitational potential. The theory is first introduced in Hubbard [2012] and then extended to a multiple number of layers in Hubbard [2013]. I here present a summary, inspired obviously from Hubbard's papers but also from personal notes of Naor Movshovitz [Naor Movshovitz, 2017].

The subject of interest of CMS is to model a planet by a sequence of spheroids in high enough numbers so that any density distribution can be represented. Each spheroid has a constant density. We can hence start by expressing the external gravitational potential of one spheroid of constant density ρ (from Eq. 2.40):

$$D_n = 2\pi\rho \int_0^{\pi} d\theta \int_0^{r(\theta)} (r')^n P_n(\cos\theta)(r')^2 \sin\theta dr' = \frac{2\pi\rho}{n+3} \int_{-1}^{1} r(\mu)^{n+3} P_n(\mu) d\mu, \quad (2.62)$$

with $\mu = \cos\theta$. Using the non-dimensional radius $\xi(\mu) = r(\mu)/a$, the gravitational moments can be written as:

$$J_n = -\frac{1}{Ma^n} \frac{4\pi\rho a^{n+3}}{n+3} \int_0^1 \xi(\mu)^{n+3} P_n(\mu) d\mu. \quad (2.63)$$

With $M = (4\pi\rho a^3/3) \int \xi(\mu)^3 d\mu$, we get:

$$J_n = -\frac{3}{n+3} \frac{\int_0^1 \xi(\mu)^{n+3} P_n(\mu) d\mu}{\int_0^1 \xi(\mu)^3 d\mu}. \quad (2.64)$$

We now consider a sequence of N spheroids as shown on Fig. 2.9, with the outermost labelled with $i = 0$ and the innermost labelled with $i = N - 1$. In the following, we will replace the index n in Eq. 2.64 by k in order to avoid confusion between n and N.

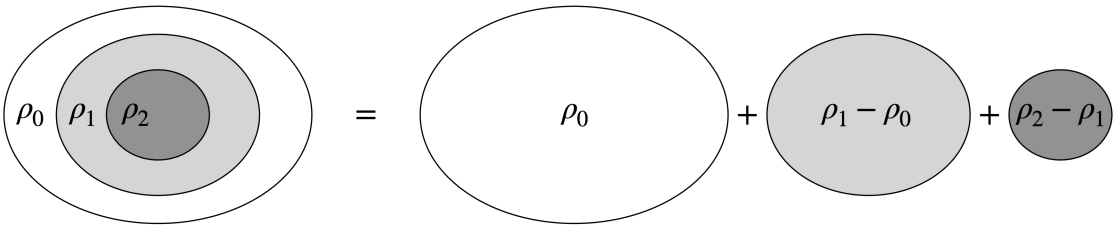

FIGURE 2.9: A sequence of spheroids illustrating the CMS method. Adapted from Hubbard [2013].

Let's go back to the expression of the gravitational potential (Eq. 2.39):

$$V(r,\mu) = \frac{G}{r} \sum_{k=0}^{\infty} (r^{-2k} D_{2k} + r^{2k+1} D'_{2k}) P_{2k}(\mu). \quad (2.65)$$

The potential is linear in density and can hence be expressed, by superposition, as:

$$V_{ext}(r,\mu) = \frac{G}{r}\left(\sum_{i=0}^{N-1}\sum_{k=0}^{\infty} D_{i,2k} r^{-2k} P_{2k}(\mu)\right), \tag{2.66}$$

with:

$$D_{i,2k} = \frac{2\pi\delta\rho_i}{2k+3}\int_{-1}^{1} r_i(\mu)^{2k+3} P_{2k}(\mu) d\mu, \tag{2.67}$$

where $\delta\rho_i = \rho_i - \rho_{i-1}$. Using $M = \sum_{i=0}^{N-1} D_{i,0}$, $\xi(\mu) = r(\mu)/a$ and $Ma_0^{2k} J_{i,2k} = -D_{i,2k}$, we have the expression of the total external gravitational potential:

$$V_{ext}(r,\mu) = \frac{GM}{r}\left(1 - \sum_{i=0}^{N-1}\sum_{k=1}^{\infty} J_{i,2k}\xi_0^{-2k}(\mu) P_{2k}(\mu)\right), \tag{2.68}$$

where:

$$J_{i,2k} = -\left(\frac{3}{2k+3}\right)\left(\frac{\delta\rho_i \int_0^1 \xi(\mu)^{2k+3} P_{2k}(\mu) d\mu}{\sum_{j=0}^{N-1}\delta\rho_j \int_0^1 \xi(\mu)^3 d\mu}\right). \tag{2.69}$$

From the fact that the potential at any point of the surface must be equal to the potential at the equator, we could get an equation that would allow us to calculate the level surfaces $r(\mu)$ or $\xi(\mu)$. This equation and the one just above for the gravitational moments are coupled and an iterative procedure could solve the problem. Nevertheless, because we use the superposition theorem, we need the shape as well as the contribution to the gravitational moments of the internal spheroids. For this purpose, let's focus on a spheroid that corresponds to the level surface j.

On such spheroid of index j, there are three contributions to the gravitational potential: i) the external potential of all the spheroids of index $i \geq j$ (keep in mind that in this case $a_i < a_j$), ii) the external part of all spheroids of index $i < j$ (where $a_i > a_j$) and iii) the internal part of these spheroids of index $i < j$.

i) The potential of a spheroid of index $i \geq j$ is the external potential:

$$V_{i\geq j} = \frac{G}{r_j}\sum_{k=0}^{\infty} D_{i,2k} r_j(\mu)^{-2k} P_{2k}(\mu). \tag{2.70}$$

Let's rewrite it as a function of $\xi_j = r_j/a_0$ and $J_{i,2k} = -D_{i,2k}/Ma_0^{2k}$:

$$V_{i\geq j} = -\frac{GM}{r_j}\sum_{k=0}^{\infty} J_{i,2k}\xi_j(\mu)^{-2k} P_{2k}(\mu). \tag{2.71}$$

A spheroid of index $i < j$ has two parts:

ii) the external part of the sphere of radius r_j included in the spheroid i:

$$V_{i<j,\text{ext}} = \frac{G}{r_j}\frac{4\pi}{3}\delta\rho_i r_j(\mu)^3. \tag{2.72}$$

iii) the internal part, corresponding to the oblate region from r_j to r_i:

$$V_{i<j,\text{int}} = \frac{G}{r_j}\sum_{k=0}^{\infty} r_j(\mu)^{2k+1} P_{2k}(\mu) 2\pi\delta\rho_i \int_{-1}^{1} P_{2k}(\mu)d\mu \int_{r_j(\mu)}^{r_i(\mu)} (r')^{-2k-1}(r')^2 dr'. \tag{2.73}$$

Combining ii) and iii), we get (see [Naor Movshovitz, 2017] for a detailed calculation):

$$\begin{aligned} V_{i<j} &= V_{i<j,\text{ext}} + V_{i<j,\text{int}} \\ &= -\frac{2\pi G\delta\rho_i}{3} r_j(\mu)^2 + 2\pi G\delta\rho_i \int_0^1 r_i(\mu)^2 d\mu + 4\pi G\delta\rho_i r_j(\mu)^2 P_2(\mu) \int_0^1 P_2(\mu)\ln(r_i(\mu))d\mu \\ &\quad + 2\pi G\delta\rho_i \sum_{k=2}^{\infty} r_j(\mu)^{2k} P_{2k}(\mu)\frac{2}{2-k}\int_0^1 P_{2k}(\mu) r_i(\mu)^{2-2k} d\mu. \end{aligned} \tag{2.74}$$

We then can write it as:

$$V_{i<j} = G\sum_{k=0}^{\infty} D'_{i,2k} r_j(\mu)^{2k} P_{2k}(\mu) + G D''_{i,0} r_j(\mu)^2, \tag{2.75}$$

where:

$$D'_{i,2k} = \frac{4\pi}{2-2k}\delta\rho_i \int_0^1 P_{2k}(\mu) r_i(\mu)^{2-2k} \quad , k \neq 1, \tag{2.76}$$

$$D'_{i,2} = 4\pi\delta\rho_i \int_0^1 P_2(\mu)\ln(r_i(\mu))d\mu, \tag{2.77}$$

$$D''_{i,0} = -\frac{2\pi}{3}\delta\rho_i. \tag{2.78}$$

Let's rewrite it as a function of ξ_j, $J'_{i,2k} = -D'_{i,2k}/Ma_0^{-2k+1}$ and $J''_{i,0} = -D''_{i,0}/Ma0^{-3}$:

$$V_{i<j} = -\frac{GM}{r_j}\left(\sum_{k=0}^{\infty} J'_{i,2k}\xi_j(\mu)^{2k+1} P_{2k}(\mu) + J''_{i,0}\xi_j(\mu)^3\right). \tag{2.79}$$

Finally, by combining the three contributions using Eqs. 2.71 and 2.79 and considering all the contribution of every spheroid, we get the total gravitational potential on a level

surface j:

$$V_j(\xi_j,\mu) = \sum_{i=j}^{N-1} V_{i\geq j} + \sum_{i=0}^{j-1} V_{i<j}$$
$$= -\frac{GM}{a_0\xi_j(\mu)}\left(\sum_{i=j}^{N-1}\sum_{k=0}^{\infty} J_{i,2k}\xi_j(\mu)^{-2k}P_{2k}(\mu) + \sum_{i=0}^{j-1}\sum_{k=0}^{\infty} J'_{i,2k}\xi_j(\mu)^{2k+1}P_{2k}(\mu) + \sum_{k=0}^{\infty} J''_{i,0}\xi_j(\mu)^3.\right) \tag{2.80}$$

And I recall the expressions of the coefficients $J_{i,2k}$, $J'_{i,2k}$, $J'_{i,2}$ and $J''_{i,0}$:

$$\begin{aligned}
J_{i,2k} &= -\left(\frac{3}{2k+3}\right)\frac{\delta\rho_i\int_0^1 P_{2k}(\mu)\xi_i(\mu)^{2k+3}d\mu}{\sum_{m=0}^{N-1}\delta\rho_m\int_0^1\xi_m(\mu)^3d\mu},\\
J'_{i,2k} &= -\left(\frac{3}{2-2k}\right)\frac{\delta\rho_i\int_0^1 P_{2k}(\mu)\xi_i(\mu)^{2-2k}d\mu}{\sum_{m=0}^{N-1}\delta\rho_m\int_0^1\xi_m(\mu)^3d\mu}, \quad k\neq 1\\
J'_{i,2} &= -3\frac{\delta\rho_i\int_0^1 P_2(\mu)\ln\xi_i(\mu)d\mu}{\sum_{m=0}^{N-1}\delta\rho_m\int_0^1\xi_m(\mu)^3d\mu},\\
J''_{i,0} &= \frac{1}{2}\frac{\delta\rho_i}{\sum_{m=0}^{N-1}\delta\rho_m\int_0^1\xi_m(\mu)^3d\mu}.
\end{aligned} \tag{2.81}$$

An iterative process is employed as already mentioned. Starting from initial guesses for the above-defined J-coefficients, the shape $\xi_i(\mu)$ of the spheroids are calculated using the implicit expression of the total potential (using Eq. 2.80) at $(\xi_i(\mu),\mu)$ and equated at $(a_i/a_0, 0)$. The J-coefficients are then recalculated with the obtained shape functions. The procedure goes on until a required tolerance is reached. This sums up the basis of the CMS method from Hubbard [2013], more details can be found in the cited paper. I will conclude this subsection by stressing that the CMS theory is still recent. Developments of new theories to improve the calculation of interior models and gravitational moments are valuable (e.g., Basillais and Huré [2023]).

2.5.3 Effects of the winds

Hubbard [1982] already studied the influence of zonal winds rotating differentially on the gravitational signature of giant planets. He even already proposed the idea of calculating interior models assuming solid-body rotation and then add a correction for differential rotation.

If a planet was perfectly spherical, all the gravity harmonics would be zero. The even gravity harmonics and particularly the low-order ones are dominated by the radial density distribution and the shape of the planet, as shown in Subsection 2.5.1 about the theory of figures. They are the main data to constrain the internal mass distribution.

We also saw in Subsection 2.5.1 that the odd gravity harmonics vanish when assuming symmetry about the equator. However, the zonal winds are not hemispherically symmetric (see Subsection 2.1.2) and the odd gravity harmonics are hence not zero. The density distribution inside a giant planet can be decomposed in two parts: a solid-body (or static) component and a dynamical component. Because the gravitational moments are linear in density, we can obtain a contribution to the gravitational moments due to the solid-body rotation and a contribution due to the differential rotation, namely a dynamical contribution. Yet, a fluid planet rotating as a solid-body would have no north-south assymmetry, meaning that the odd harmonics only come from the dynamics. Conversely, the even harmonics have a solid-body component and a dynamical component. Therefore, Kaspi [2013] recommended, in order to infer the wind depth, to measure odd gravity harmonics rather than high-order even gravity harmonics as there will be no need to disentangle the dynamical component to the solid-body component, in addition to the fact that the signature of low-order odd harmonics is greater than the one of high-order even harmonics.

Actually, the winds lead to density anomalies which will perturb the mass distribution and hence the gravitational signature. If they extend deep enough, they will have a major impact on the high-order gravity harmonics [Hubbard, 1999]. They should only be a small perturbation compared to the solid-body contribution but Hubbard [1999] and Kaspi et al. [2010] showed, using a polytrope and the SCvH95 EOS [Saumon et al., 1995] respectively, that the harmonics of order greater than 10 are in fact dominated by the dynamical gravity response rather than the solid-body response.

The wind profile is retrieved from the gravity field data using an inversion technique [Galanti and Kaspi, 2016]. The dynamical component of the density can then be obtained from the thermal wind equation [Kaspi, 2013]:

$$(2\Omega.\nabla)[\widetilde{\rho}u] = \nabla\rho' \times g_0, \tag{2.82}$$

where Ω is the rotation rate, u is the velocity field, $\widetilde{\rho}$ and ρ' are the solid-body and dynamical components of the density respectively, g_0 is the gravity. The dynamical contribution to the gravitational harmonics can then be quantified from this dynamical component of the density. They are noted ΔJ_n.

$$\Delta J_n = -\frac{1}{Ma^n}\int_0^a (r')^{n+2}dr' \int_0^{2\pi} d\phi \int_{-1}^{1} \rho'(r',\mu)P_n(\mu)d\mu. \tag{2.83}$$

Interior models will thus aim at matching $J_{2n}^{\text{static}} = J_{2n}^{\text{Juno}} - \Delta J_{2n}^{\text{differential}}$. Values for $\Delta J_{2n}^{\text{differential}}$ that we use can be found in Miguel et al. [2022] and are listed in Table 2.3.

TABLE 2.3: Dynamical contributions to the even gravitational moments. Taken from Miguel et al. [2022].

	Value	Uncertainty
$\Delta J_2(\times 10^6)$	1.039	0.354
$\Delta J_4(\times 10^6)$	-0.076	0.083
$\Delta J_6(\times 10^6)$	0.016	0.076
$\Delta J_8(\times 10^6)$	0.053	0.062
$\Delta J_{10}(\times 10^6)$	-0.080	0.042

Chapter 3

The importance of the equation of state

Contents

The equation of state (EOS) relates the physical parameters of the interior of a planet such as pressure, temperature, density or entropy. We have seen in Chapter 2 that it is a necessary ingredient to solve the set of equations that make an interior or evolution model (Section 2.2). This chapter could hence have simply been added as a section of the previous chapter. However, the topic of the equation of state was relatively important during my PhD and it deserved its own chapter. Furthermore, Section 3.5 corresponds to the publication of Howard and Guillot [2023]. In this chapter, I will try to make the link between high-pressure physics and planetary sciences, hoping that it can serve as a good introduction for planetary scientists not very familiar with the subject. For a more in-depth description, I refer the reader to reviews like McMahon et al. [2012], Helled et al. [2020a].

3.1 Introduction

3.1.1 Context

Giant planets are often referred as natural laboratories because matter there is subject to conditions that do not exist on Earth. Studying the interiors of giant planets can thus help understanding matter at extreme conditions. But the situation can be seen in both ways. We are here interested in deciphering the internal structures of giant planets and it hence requires a good comprehension of matter at the conditions inside these planets. Inside Jupiter, the pressure and temperature can reach tens of Mbar and several 10^4 K.

The name of gas giants come from the fact that these planets have been formed by accreting gas but their current state is not only made of gas. Indeed, the picture is more complex: they are fluid and hydrogen is for instance expected to transition from a molecular phase to a metallic phase. The interior of Jupiter is actually a place where atoms, molecules, electrons and ions coexist and interact. A particular difficult state to fully understand is the Warm Dense Matter regime. When pressure increases and reaches about the $\sim$Mbar level, with modest temperatures (a few thousand K), interactions between different species become strong. The interior of giant planets is mostly made of hydrogen, but also of helium and a fraction of heavy elements. We will define along the whole manuscript the mass fractions of hydrogen, helium and heavy elements as X, Y and Z, respectively. The additive volume law or linear mixing law (see, e.g., Saumon et al. [1995]) allows to combine EOSs of pure species to model a mixture of these species. It states that an extensive property (e.g., volume or entropy) of a mixture can be calculated by summing each pure specie weighted by their abundance. Figure 3.1 shows the relative contributions in density of the different species for a model of Jupiter taken from Howard et al. [2023]. This model was calculated with the HG23+CMS19 EOS that will be detailed later in this chapter. This shows that hydrogen contributes to almost 90% of the density in Jupiter. Helium is not negligible and represents about

10%. The interactions between hydrogen and helium can reach a contribution of a bit less than 10% at some pressures. The heavy elements contribution remains small, of the order of the percent, except in the very deep interior. This justifies the strong interest on the hydrogen EOS but also shows that helium and interactions between hydrogen and helium should not be omitted.

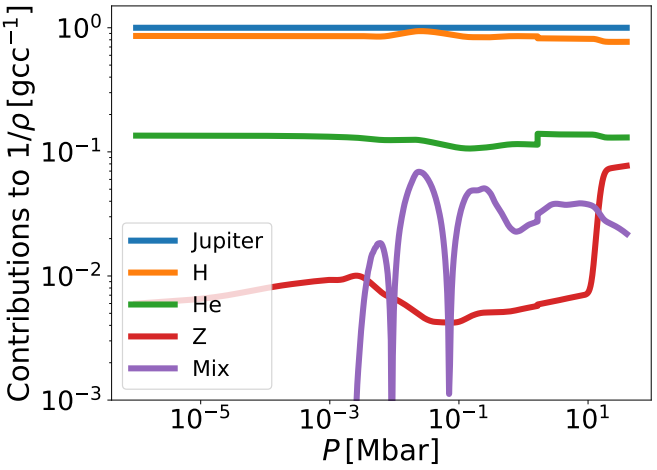

FIGURE 3.1: Relative contributions of hydrogen, helium, heavy elements and hydrogen-helium interactions in the density of Jupiter. The blue curve shows the inverse of the density profile of a state-of-the-art Jupiter model from Howard et al. [2023]. As the density of this model has been computed using the additive volume law that includes the four aforementioned contributions, we quantify each of them. The absolute value of the H-He interactions (noted as "Mix" on the legend) has been taken because this term can sometimes be negative. The discontinuity about ~ 1 Mbar is due to the He phase separation. The increase of the Z contribution at depth is due to the presence of the dilute core.

Models, to satisfy observational constraints, depend on an EOS and the inferred properties are hence dependent on the EOS. Hubbard [1975] showed that a polytrope of index one is a good approximation for the density-pressure relationship inside Jupiter. Nevertheless, with the increasing accuracy of the gravitational moments, more accuracy is needed on the EOS. Fifty years ago, Hubbard's last sentence of his review about interiors of Jupiter and Saturn [Hubbard, 1973] stated that reducing the uncertainty on the EOS at the percent level would be important to discriminate between different models. We still have not reached this level of accuracy and the EOS is still an active field of research to better understand the nature of the interior of giant planets. And many contributions to the study of interiors of giant planets have come along with a new or updated EOS (e.g., Chabrier et al. [1992], Saumon and Guillot [2004], Nettelmann et al. [2012]). A comparison [Militzer and Hubbard, 2009] of the results of two groups [Nettelmann et al., 2008, Militzer et al., 2008] has for instance shown that the EOS can be responsible of huge discrepancies about the inferred internal structure of Jupiter. In this particular case, the nature of the molecular-to-metallic transition (leading to different assumptions considered by modellers: two-layer or three-layer models) was responsible for discrepancies between one group finding massive cores ($14 - 18\,M_{\oplus}$) inside Jupiter

and a second group finding very small cores ($0-7\,M_{\oplus}$). Hence, a proper understanding of the behaviour of hydrogen but also hydrogen-helium mixtures is crucial. And even very recent papers have shed light on the sensitivity of interior models of giant planets to the EOS [Miguel et al., 2016, 2022, Howard and Guillot, 2023, Howard et al., 2023].

3.1.2 Experimental and theoretical means

To calculate an EOS, laboratory experiments can be done but because the conditions inside giant planets are difficult to reproduce, theoretical and numerical calculations are also an important tool. I will here mention what are the different experiments and theoretical means employed to derive EOSs. A non-exhaustive review for hydrogen, helium and mixtures of hydrogen and helium will then follow.

Experiments in laboratories can be static are dynamic. Static ones consist of diamond anvil cells that compress matter, the latter can be heated using lasers. Dynamic experiments use gas gun shocks. The state of the shocked gas is determined by the Hugoniot curve:

$$E(\rho,T)-E_0(\rho,T)=\frac{1}{2}(P(\rho,T)-P_0(\rho_0,T_0))\left(\frac{1}{\rho}-\frac{1}{\rho_0}\right). \tag{3.1}$$

These shock experiments cover only a limited range of pressures and temperatures, they are hence mostly used to benchmark EOSs obtained from other methods. But even static experiments cannot span large ranges of pressure and temperature. Theoretical calculations are thus needed to provide extensive equation of state calculations.

Theoretical calculations have been based on two approaches: the so-called "chemical" and "physical" pictures. The chemical picture considers molecules or atoms that remain distinguished and models their interactions by the use of pair-potentials. These pair-potentials are simply mathematical functions which describe the interactions between particles. Pair-potentials are usually obtained by fitting experimental data. EOS models, within the chemical picture, are based on the free-energy minimisation technique to ensure thermodynamic equilibrium. The Helmholtz free-energy can be defined as $F = k_B T \ln Z$ where k_B is the Boltzmann constant, T is temperature and Z is the partition function. The partition function corresponds to the statistical properties of particles at a thermodynamic equilibrium state. Equilibrium is derived with the particles numbers $\{N\}$ and stoichiometric numbers by minimising $F(T,V,\{N\})$. Approximations are made at the stage of choosing a mathematical model for the free-energy. Different contributions which account for different phenomena are considered in F [Graboske et al., 1969] and non-ideal terms can be included. Once the free-energy is determined, quantities like pressure, entropy and internal energy can be calculated from the derivatives of F (see, e.g, Hummer and Mihalas [1988]). However, when density increases, the chemical picture can hardly provide a good description of the behaviour of matter and is especially not accurate in the molecular-to-metallic transition regime where interactions between

particles become strong. In fact, those semiempirical models are accurate at low densities but fitting pair-potentials simultaneously to different conditions is complicated.

The physical picture focuses on electrons and ions whose interactions are modeled by Coulomb potentials. Collisions between particles are simulated and the behaviour of particles is described by solving the Schrödinger equation and deriving the energy levels occupied by particles. Once thermodynamic equilibrium is reached, properties like pressure or entropy can be obtained. The physical picture appears as a more rigorous method as it should provide an exact description of the behaviour of matter. However, simulations in the framework of the physical picture are time consuming but are now possible with the progress of numerical means. Simulations in the physical picture are often referred as first-principle or ab initio simulations. Among many different methods, two types of calculations are often used for hydrogen and helium: Density function theory molecular dynamics (DFT-MD) and quantum Monte Carlo (QMC). More details about these methods and others can be found in McMahon et al. [2012]. DFT derives the electronic states and MD then derives the forces and the motions of nuclei. DFT evaluates the energy functional of the density and models many-body effects through an exchange and correlation (XC) functional. This XC functional is not exactly known and needs to be approximated. Figure 3.2 shows a snapshot of a DFT-MD calculation, with 220, 18 and 4 atoms of hydrogen, helium and iron, respectively. QMC is a higher level of theory and aims at the wave function using random walks. However, because QMC calculations are computationally expensive, most of the EOSs used in the latest giant planet models rely on DFT-MD calculations so far.

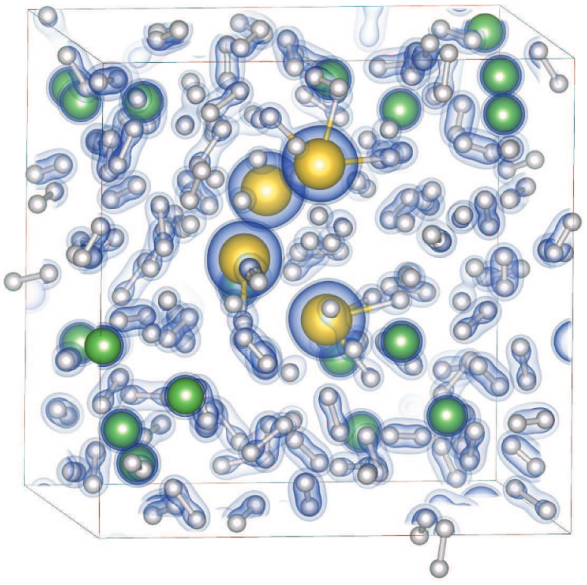

FIGURE 3.2: Snapshot of a DFT-MD calculation, with 220, 18 and 4 atoms of hydrogen, helium and iron, respectively. Taken from Militzer et al. [2016].

3.2 Hydrogen

Hydrogen is the most abundant element in the Universe and also in gas giants such as Jupiter or Saturn. Gas giants were initially thought to be cold. This is only after the discovery of internal heat sources [Low, 1966] that they were believed to be fluid [Hubbard, 1968]. Besides, hydrogen in these planets transitions from a molecular phase (H_2) to a metallic phase (H^+). When pressure increases, molecular hydrogen H_2 dissociates and ionizes, leading to a phase where hydrogen is a good conductor, with free electrons. Actually, the possibility of a metallic form in the phase diagram of hydrogen was suspected almost 100 years ago [Wigner and Huntington, 1935]. Therefore, even if hydrogen is the lightest element in Universe, its phase diagram is not that simple. Hydrogen has been studied with the experimental and theoretical means presented above in Subsection 3.1.2, in the attempt of understanding its phase diagram and providing an accurate EOS. A phase diagram of hydrogen taken from Helled et al. [2020a] is shown on Fig. 3.3.

Diamond anvil cells have been used to compress hydrogen or deuterium (e.g., Loubeyre et al. [2002, 2012], Zaghoo et al. [2016]) and could reach a pressure of about 4 Mbar. Shock experiments have also been conducted [Boriskov et al., 2003, Hicks et al., 2009, Knudson and Desjarlais, 2017] that can help benchmarking theoretical EOSs (see Hugoniot curves from e.g. Miguel et al. [2016], Mazevet et al. [2022]). But so far, extensive EOSs for hydrogen have come from theoretical calculations that could provide data at wide ranges of pressure and temperature, required to model the interior of giant planets. I will now describe briefly EOSs that I have mostly been using. Comparisons of adiabats calculated for these EOSs will be available in Section 3.5.3 and 3.6 to look at the differences between the EOSs.

- SCvH95 [Saumon et al., 1995]

A commonly used EOS is the SCvH95 EOS [Saumon et al., 1995] which is based on the chemical picture described in the previous section. This semi-analytical EOS spans a wide range of pressures ($4 < \log P\,(\mathrm{dyn.cm^{-2}}) < 19$) and temperatures ($2.1 < \log T\,(\mathrm{K}) < 7.06$) and is hence applicable not only to giant planets but also to stars. It accounts for the following species H_2, H, H^+ and e^- and agrees with several experiments. Because of the hard task to properly model the regime of partial dissociation and ionization, a version of this EOS which interpolates between the molecular and metallic phases is available. We also stress that an EOS for helium is provided by Saumon et al. [1995]. Both H and He EOSs can be combined using the additive volume law. However, the Hugoniot curve for SCvH95 does not agree with the most recent shock experiments (see, e.g., Miguel et al. [2016], Chabrier et al. [2019], Mazevet et al. [2022]). Hence this EOS seems today obsolete to study the deep interior of objects like Jupiter but remains useful particularly for low pressure regimes.

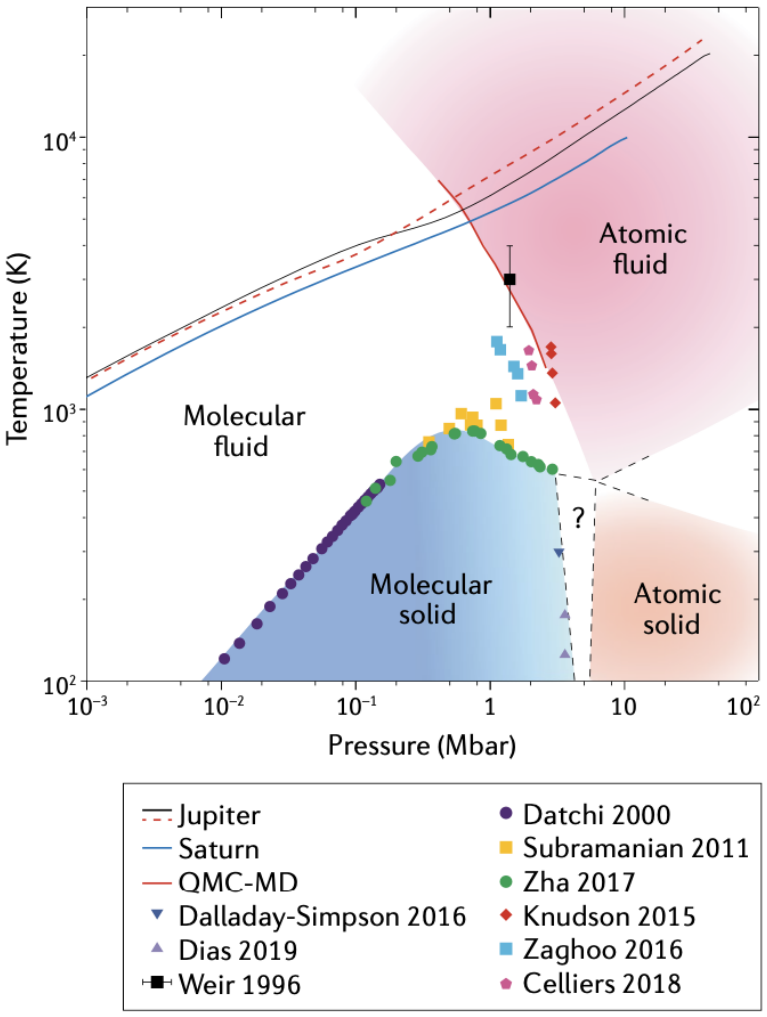

FIGURE 3.3: Phase diagram of hydrogen taken from Helled et al. [2020a]. T-P profiles of Jupiter and Saturn are shown (solid lines for adiabatic interiors and dashed line for non-adiabatic interior). Points show data from experiments and simulations to determine the molecular-to-metallic transition as well as the melting line separating the solid and fluid phases. See the corresponding paper for references therein.

The improvement of numerical means has then led to the use of DFT to provide a more accurate EOS in the warm dense matter regime. Indeed, these first-principle simulations do not rely on the approximations used to account for the interactions between the species considered in the chemical models. Most of these EOSs based on DFT are then combining their results to other EOSs outside of the regime of warm dense matter, typically SCvH95.

- MH13 [Militzer and Hubbard, 2013]

Initially, this EOS was calculated for a hydrogen and helium mixture. It can be considered as a major advance in the field of EOS for giant planets as many models of the interior of giant planets have been using it. It spans a pressure range of

$0.1 < P\,(\text{Mbar}) < 300$ and a temperature range of $1000 < T\,(\text{K}) < 80\,000$. It was obtained by performing DFT-MD simulations, using the PBE (Perdew-Burke-Ernzerhof) functional, on a mixture of 220 H and 18 He atoms which corresponds to a He mass fraction of $Y = 0.245$. Such mixture is close to solar and hence close to Jupiter. This is why it can be considered as a cutting-edge EOS. Because this EOS has been calculated directly for a mixture and not for pure H nor pure He, it takes the non-ideal mixing effects (i.e. the interactions between species) into account. The importance of these mixing effects are discussed in Section 3.5. We will refer to this EOS as MH13* as we constructed it by fitting an adiabat provided by Burkhard Militzer (see Subsection 3.6). Actually, Militzer and Hubbard [2013] provide two tables so that one can derive the EOS from the ab initio data. The first one provides P, E, F and S (pressure, internal energy, free energy and entropy, respectively). The second one provides the Helmholtz free energy from a 2D spline function fitting the ab initio results. From this table, one can calculate P and S thanks to provided derivatives. Nevertheless, using one table or another and depending on interpolation methods, deriving the EOS from the ab initio data can lead to slightly different EOSs (see later in Subsection 3.6). I also stress that Militzer and Hubbard [2013] calculate the entropy with a thermodynamic integration technique described in Militzer [2013]. A strong feature of the MH13* EOS is a higher density in the region of the molecular-to-metallic transition.

- CMS19 [Chabrier et al., 2019]

The CMS19 EOS covers pressures of $1 < \log P\,(\text{dyn.cm}^{-2}) < 23$ and temperatures of $2 < \log T\,(\text{K}) < 8$. It combines three EOSs: i) the SCvH at low pressures, in the molecular phase, ii) the QMD calculations of Caillabet et al. [2011] in the intermediate domain ($\sim$ Mbar), in the pressure ionization regime and iii) the dense plasma model of Chabrier and Potekhin [1998] at high pressures, in the fully ionized regime. The densities at the boundaries between the three combined EOSs are given in Chabrier et al. [2019]. An EOS for He is also provided and can be used to model a mixture of H and He using the additive volume law.

- MLS22 [Mazevet et al., 2022]

The MLS22 EOS can be considered as an update of the CMS19 hydrogen EOS. The difference is that the range of interpolation between QMD calculations in the intermediate pressure regime and the SCvH95 EOS at low pressures has been tightened in order to better fit the latest shock experiments of Knudson and Desjarlais [2017].

- MGF16+MH13 [Miguel et al., 2016]

The MGF16+MH13 EOS has been derived by Miguel et al. [2016] from the ab initio data of Militzer and Hubbard [2013]. The authors have extracted a pure H EOS from the aforementioned DFT-MD simulations on a mixture of H and He (see the paper for more details about how to extract a pure H EOS). Because the MGF16+MH13 EOS is based on the MH13 data, some mixing effects are included in this pure H EOS. Hence, combining this EOS with a pure He EOS accounts for mixing effects but they remain fixed and equal to those calculated by MH13 at $Y = 0.245$. The MHG13+MH13 EOS is built from the table 1 of Militzer and Hubbard [2013] and extends it to a wider range of pressures and temperatures ($4 < \log P\,(\mathrm{dyn.cm}^{-2}) < 19$ and $2.25 < \log T\,(\mathrm{K}) < 7$) by grafting it to the SCvH95 EOS. Grafting the tables of different EOSs is a delicate task: they can have different dimensions, with irregular shapes. We will see some differences, in the pressure domain between the MH13 data and SCvH95, between MGF16+MH13 and the CD21 EOS (see right after) which has been built following the same procedure.

- CD21 [Chabrier and Debras, 2021]

The CD21 EOS has followed the same procedure than Miguel et al. [2016] who built an EOS from the MH13 [Militzer and Hubbard, 2013] data. But Chabrier and Debras [2021] combine it with CMS19 instead of simply SCvH95. The range of pressures and temperatures of CD21 is thus the same as for CMS19. The fact that CD21 and MGF16+MH13 (starting from the same dataset) lead to slightly different EOSs, that are also slightly different from the MH13* EOS used by his father Burkhard Militzer, show that there are uncertainties due to combination of EOS tables and interpolation methods.

Another notable EOS that has not been described here is the REOS [Becker et al., 2014], which also provides a He EOS.

Concerning the dissociation and metallization of hydrogen in the interior of Jupiter, previous experiments [Zaghoo et al., 2016] and theoretical calculations [Morales et al., 2010] suggested a first-order transition. Nonetheless, other experiments [McWilliams et al., 2016] rule out a discontinuous transition. DFT [Tamblyn and Bonev, 2010] and recent QMC [Pierleoni et al., 2016, Mazzola et al., 2018] calculations also favour a continuous process. The location of the molecular-to-metallic transition is currently not precisely determined. Present estimates suggest that it should occur from a few ~ 0.1 or ~ 1 Mbar in Jupiter. Constraining precisely its location would be important because it is linked to the magnetic field of the planet but also because it impacts the modellers' conception of different layers in the planet.

3.3 Helium

Pure helium has also been studied by diamond anvil cells [Loubeyre et al., 1982, Vos et al., 1990] and shock experiments [Eggert et al., 2008, Celliers et al., 2010]. Theoretical

calculations have provided EOSs: SCvH, REOS, CMS19 all provide a He table, in addition to a pure H table. More about simulations on He can be found in Militzer et al. [2016]. Helium is also expected to metallize but at pressures one order of magnitude larger than for hydrogen. The interest has been so far more concentrated on hydrogen but helium is a non negligible component of gas giants. Its contribution, as well as its influence through mixing effects with hydrogen, is definitely important to consider.

3.4 Hydrogen-Helium mixtures

Jupiter is made of a mixture of hydrogen and helium, with a small percentage of heavy elements. The overall hydrogen-to-helium ratio is generally assumed to be protosolar (see Subsection 2.1.4). But around the Mbar level, helium is expected to phase separate [Salpeter, 1973, Stevenson and Salpeter, 1977b,a] as it becomes immiscible in metallic hydrogen. Droplets of helium will form and sink because they are heavier than the surrounding hydrogen. The helium content is hence expected to be slightly depleted in Jupiter's outer region and slightly enhanced deeper. Therefore, calculating EOSs at different mixture compositions is required.

Only a few data is available for EOSs of H-He mixtures. Experiments at room temperatures [Loubeyre et al., 1991] have been conducted. The most recent experiment [Brygoo et al., 2021], which combined static and dynamic compressions, has looked at the optical properties of matter to study demixing in H-He mixtures. This experiment is actually suggesting that He phase separation may occur deeper (up to 5 Mbar in Jupiter) than what is suggested by theoretical calculations. Lorenzen et al. [2009, 2011] performed DFT-MD simulations using the PBE functional to study mixtures for 33 different helium fractions, from 1 to 24 Mbar, and temperatures up to 15 000 K. They however used the approximation of the ideal entropy of mixing. Morales et al. [2009], Morales et al. [2013] also used the PBE functional and studied 12 different mixture compositions up to pressures of 12 Mbar and temperatures of 10 000 K. They calculated the non-ideal entropy of mixing which led to lower demixing temperatures compared to results based on the ideal entropy of mixing. These calculations predicted demixing to happen between 0.8 and 3 Mbar. Nevertheless, more recent DFT calculations Schöttler and Redmer [2018a,b], used the van der Waals density functional (vdW-DF) exchange-correlation functional, also considered the non-ideal entropy of mixing and performed simulations for 31 helium fractions, with pressures of 0.2 to 30 Mbar and temperatures of 1000 to 15 000 K. They found that demixing is occuring to even lower temperatures and it is hence possible that it has not started yet in Jupiter. A more detailed discussion can be found in Schöttler and Redmer [2018a] and also in the appendix of Howard and Guillot [2023] presented in Appendix A. A comparison of the immiscibility curves of the different experiments and simulations will be available in Section 5.5. In a nutshell, these

studies on H-He mixtures mostly focused on the phenomenon of helium demixing and its location.

But extensive calculations at a huge number of pressure-temperature points are required to have a useful EOS for interior models. Experiments and simulations on mixtures allows to avoid the approximation of the additive volume law. We will see in next section that non-ideal mixing effects between H and He are important to consider, something that was already nicely emphasised by Vorberger et al. [2007]. Actually, helium is important to consider because of the phase separation in mixtures but it has also other effects like delaying the metallization of hydrogen (due to helium stabilizing hydrogen), something which has been confirmed by QMC calculations of Mazzola et al. [2018].

So far, the most extensive calculation of a H-He EOS has been done by Militzer and Hubbard [2013] who ran ab initio simulations and provided an EOS for a mixture of $Y = 0.245$. Today, many EOSs have been derived from these ab initio simulations (see Section 3.2). We will present in the next section an EOS (that we call HG23) for the interactions between H and He. It can be combined with pure EOSs of H and He. Schöttler and Redmer [2018b] also provides an EOS but the number of P-T points is lower than for MH13, these authors ran simulations for several compositions instead of focusing on only one single composition. Our HG23 table provides a simple way to calculate H-He EOSs for different compositions.

3.5 Non-ideal mixing effects

This section is directly taken from Howard and Guillot [2023] and emphasises the importance of accounting for interactions between hydrogen and helium in the EOS. In this paper, we build and provide an EOS table for the mixing effects that can be combined to pure H and He EOSs when making use of the additive volume law.

3.5.1 Context

The hydrogen and helium equation of state (hereafter H-He EOS) is crucial in many contexts, but is particularly challenging to model in a high-pressure, low-temperature regime where interactions between molecules, atoms and ions are substantial, near a megabar and at temperatures lower than 10^4 K [e.g. Helled, 2018]. These conditions concern giant planets [Guillot, 2005, Fortney et al., 2010, Militzer et al., 2016] and brown dwarfs in particular [Baraffe, 2014]. With pressures reaching up to terabar (for the most massive and cold brown dwarfs), these objects span a range of thermodynamical conditions that includes low-pressure regimes for which experimental data are available and high-pressure regimes that are reasonably well understood [Helled et al., 2020a], but, with temperatures in the megabar regime ranging from about 5000 K to 20,000 K

[Guillot and Gautier, 2015], they cross this difficult and uncertain regime in parameter space. Understanding their interior structure and evolution requires an accurate EOS relating physical parameters such as pressure, temperature, density and entropy.

Except for the specific case of the hydrogen-helium phase separation [e.g. Brygoo et al., 2021], most of the effort has been invested so far in the analysis of pure systems of either hydrogen or helium. This has been realised by means of laboratory experiments with anvil cells and laser-driven shocks, and theoretically, with approaches such as density functional theory (DFT), path integral Monte Carlo (PIMC) and quantum Monte Carlo (QMC) based on first-principles simulations (see Helled et al. [2020a] for more details). The pure EOSs are usually coupled with the linear mixing rule (also known as the additive volume rule), whose principle is to consider that for extensive variables such as volume and entropy, the value of the mixture is equal to the sum of the pure species weighted by their respective abundances [Saumon et al., 1995]. However, Vorberger et al. [2007] pointed out that in the regime in which hydrogen transitions from a molecular to an atomic fluid, the presence of helium shortens and strengthens the molecular hydrogen bonds, leading to non-linear effects and potentially non-negligible deviations from the linear mixing hypothesis. This implies that in addition to pure EOSs, the behaviour of mixtures should be calculated for all values of the abundances considered. Some DFT simulations have been conducted to study the conditions for a phase separation of hydrogen and helium, but only for a limited range of parameters [Morales et al., 2013, Schöttler and Redmer, 2018b,a] (hereafter called SR18). An extensive DFT calculation for a H-He mixture has been carried out by Militzer and Hubbard [2013] to provide an EOS (the so-called MH13 EOS) that fully accounts for the interactions between hydrogen and helium particles for temperatures between 1000 and 80,000 K and pressures between 0.1 and 300 Mbar. However, it is available only for one specific composition, namely a mixture of 220 hydrogen atoms for 18 helium atoms, corresponding to a helium mass-mixing ratio $Y = 0.245$. Extensions of this table to cover a wider range of pressures and temperatures have been made available by Miguel et al. [2016] and Chabrier and Debras [2021] (CD21, hereafter). However, while these works provide EOSs that in principle can be applied to any mixture of hydrogen and helium, the treatment of non-linear effects remains fixed and equal to that calculated by Militzer and Hubbard [2013] at $Y = 0.245$.

Our work aims to obtain a H-He EOS that includes the hydrogen and helium interactions and remains valid for any hydrogen-to-helium ratio. This EOS should recover the CD21 EOS as well as both the pure end members CMS19-H and CMS19-He [Chabrier et al., 2019], when there is only hydrogen or only helium in the system, respectively. Section 3.5.2 describes how the table is built that contains the contribution of the interactions between hydrogen and helium. Sections 3.5.3 and 3.5.4 are dedicated to applications to Solar System planets and exoplanets, respectively.

3.5.2 Derivation of a table for non-ideal mixing effects

In order to account for the interactions between hydrogen and helium, we make use of the linear mixing rule, but add a term ΔV or ΔS that corresponds to an excess or deficit of volume or entropy, respectively,

$$\frac{1}{\rho_{\rm H-He}} = \frac{X}{\rho_{\rm H}} + \frac{Y}{\rho_{\rm He}} + \Delta V(X,Y), \tag{3.2}$$

$$S_{\rm H-He} = XS_{\rm H} + YS_{\rm He} + \Delta S(X,Y), \tag{3.3}$$

where X and Y are the mass fractions of hydrogen and helium, $\rho_{\rm H}$, $\rho_{\rm He}$ and $\rho_{\rm H-He}$ are the densities of pure hydrogen, pure helium, and the hydrogen-helium mixture, respectively, and $S_{\rm H}$, $S_{\rm He}$, and $S_{\rm H-He}$ are the specific entropies of pure hydrogen, pure helium, and the hydrogen-helium mixture, respectively. The volume of mixing ΔV and entropy of mixing ΔS depend on X and Y, namely the composition of the mixture. All quantities are evaluated at a given pressure P and temperature T. A non-zero volume of mixing results from interactions between hydrogen and helium. The entropy of mixing is the sum of a non-ideal part and an ideal part $\Delta S_{\rm ideal}$, arising even without these interactions. Following Chabrier et al. [2019] [see also Saumon et al., 1995], we write

$$\Delta S_{\rm ideal} = -k_{\rm B}\frac{x_{\rm H}\ln(x_{\rm H}) + x_{\rm He}\ln(x_{\rm He})}{\langle A\rangle m_{\rm H}}, \tag{3.4}$$

where $k_{\rm B}$ refers to the Boltzmann constant, x_i is the number fraction of component i, $m_{\rm H}$ is the atomic mass unit, and $\langle A\rangle = \sum x_i A_i$, A_i being the mass number.

Given the known EOSs for pure hydrogen, for pure helium, and for one mixture of hydrogen and helium with mass mixing ratios $X^* = 1 - Y^*$ and Y^*, respectively, a natural choice is to assume as a first-order approximation,

$$\Delta V(X,Y) = XYV_{\rm mix}; \qquad \Delta S(X,Y) = XYS_{\rm mix}. \tag{3.5}$$

$V_{\rm mix}$ and $S_{\rm mix}$ are then quantities that are independent of X and Y (but vary as a function of P and T). Using Eqs. (3.2) and (3.3), we can hence calculate $V_{\rm mix}$ and $S_{\rm mix}$,

$$V_{\rm mix} = \frac{1}{\tilde{X}\tilde{Y}}\left[\frac{1}{\rho_{\rm H-He^*}} - \frac{X^*}{\rho_{\rm H}} - \frac{Y^*}{\rho_{\rm He}}\right], \tag{3.6}$$

$$S_{\rm mix} = \frac{1}{\tilde{X}\tilde{Y}}\left[S_{\rm H-He^*} - X^*S_{\rm H} - Y^*S_{\rm He} - \Delta S_{\rm ideal}(Y^*) + \Delta S_{\rm ideal}(\tilde{Y})\right]. \tag{3.7}$$

Here we have included a complication that arises when the table for the mixture is calculated for a helium mass-mixing ratio Y^*, but the mixing terms have been evaluated for a different mixing ratio $\tilde{Y}$. In the case that we consider, the CD21 H-He table is given for a helium mass-mixing ratio $Y^* = 0.275$, but includes the non-ideal mixing effects from Militzer and Hubbard [2013], who evaluated the H-He interactions for a

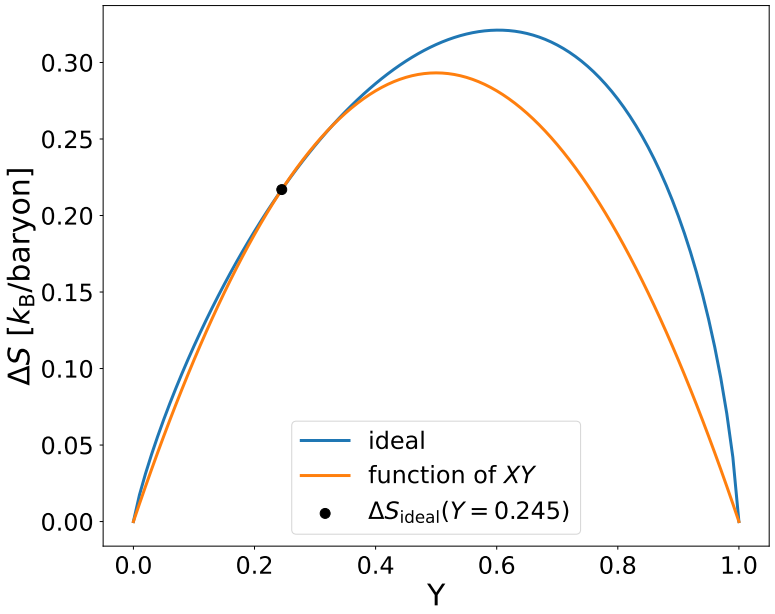

FIGURE 3.4: Comparison of the ideal entropy of mixing (blue curve and Eq. (3.7)) with its first-order approximation, assumed proportional to XY, the product of the mass-mixing ratios of hydrogen and helium (orange curve), calculated as $\Delta S_{\rm ideal}(\tilde{Y})\ XY/(\tilde{X}\tilde{Y})$, with $\tilde{Y} = 0.245$. **Taken from Howard and Guillot [2023].**

mixture with $\tilde{Y} = 0.245$. Equation. (3.7) also accounts for the fact that the CD21 EOS evaluates the ideal entropy of mixing at $Y^* = 0.275$, but the non-ideal entropy of mixing at $\tilde{Y} = 0.245$.

We note that Eq. (3.4) yields a value of $\Delta S_{\rm ideal}$ that is not strictly proportional to XY, in contrast to the assumption used in Eq. (3.5). However, Fig. 3.4 shows that the error made by approximating the ideal entropy of mixing as if it were proportional to XY is small: it is always smaller than $0.1\,k_{\rm B}$/baryon, and when we limit ourselves to compositions such that $Y < 0.4$, the error made is smaller than $0.01\,k_{\rm B}$/baryon. This thus supports our assumption that mixing terms should to first order be proportional to XY.

Using Eqs. (3.6) and (3.7), the H-He table from Chabrier and Debras [2021], and the pure H and He tables from Chabrier et al. [2019], which all use the same $P-T$ grid (pressures from 10^{-11} to 10^{11} Mbar and temperatures from 10^2 to 10^8 K), we can calculate a new table for $V_{\rm mix}$ and $S_{\rm mix}$ for the same set of pressures and temperatures. We stress that this table is valid in the same domain as the EOSs from Chabrier et al. [2019] and Chabrier and Debras [2021], whose limitations concern the regions in which molecular hydrogen and ionised hydrogen become solid as well as the region in which ion quantum effects become important, namely at low T and high P (see Fig.1 and Fig.16 of Chabrier et al. [2019] for the precise locations in the phase diagrams). The table was cleaned as described in Appendix A.2 to avoid spurious numerical effects and is available for download. Combined with the CMS19 tables, it can be used to calculate the internal

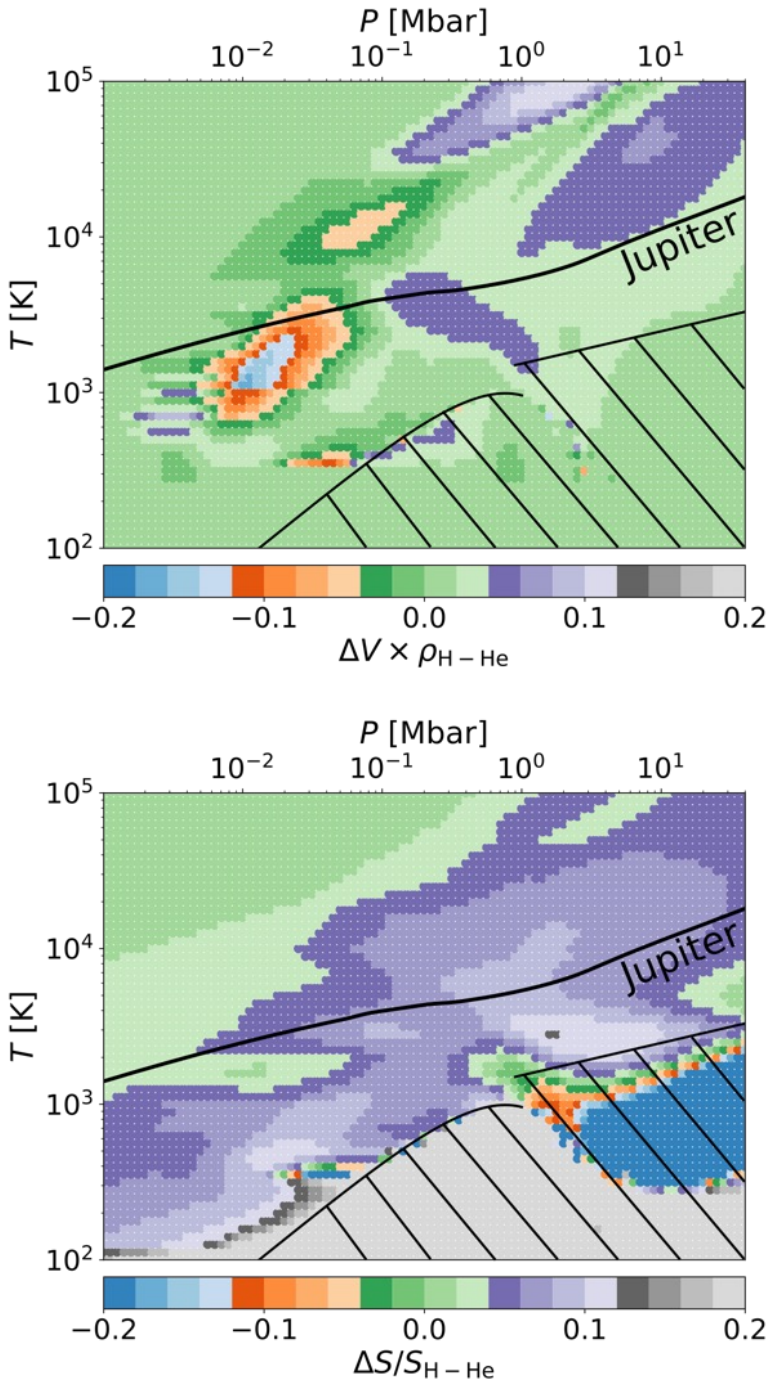

FIGURE 3.5: Relative contributions of the mixing terms ΔV and ΔS to the total specific volume $1/\rho_{\mathrm{H-He}}$ and entropy $S_{\mathrm{H-He}}$, respectively, as a function of pressure and temperature. The solid black line corresponds to the Jupiter adiabat from Miguel et al. [2022]. The values of $\Delta V \times \rho_{\mathrm{H-He}}$ and $\Delta S/S_{\mathrm{H-He}}$ are calculated for $X^* = 0.725$ and $Y^* = 0.275$. The hashed areas correspond to the region in which the mixing volume and entropy are invalid [see Chabrier et al., 2019, for more details]. **Taken from Howard and Guillot [2023].**

structure of giant planets and brown dwarfs of variable compositions and including non-ideal mixing effects. The EOS for any mixture may then be evaluated from the EOSs for the pure elements, Eqs. (3.2) and (3.3), $\Delta V = XYV_{\rm mix}$ and $\Delta S = XYS_{\rm mix}$.

Figure 3.5 shows the relative amplitude of the mixing quantities ΔV and ΔS in a mixture with $Y = 0.245$. A typical Jupiter adiabat passes a region between 0.01 Mbar and 0.04 Mbar, where the non-ideal mixing effects are strongest. In this region, the density of the hydrogen and helium mixture inside Jupiter is denser by almost 10% compared to the density obtained without accounting for the H-He interactions. Around 0.06 Mbar, the sign of ΔV changes and becomes positive (the mixture becomes less dense). Then, ΔV continues to increase to approximately 0.2 Mbar and starts to decrease afterwards.

The variations in ΔV obtained in the $0.1 - 1$ Mbar pressure range for Jupiter conditions are in line with those obtained by Vorberger et al. [2007]. However, we point out that we obtain unanticipated negative contributions (i.e. non-linear mixing terms yielding higher densities) at lower pressures. We note that this low-pressure region, around 0.01 Mbar, is a sensitive area in which EOS tables are combined, possibly yielding interpolation errors.

The bottom panel of Fig. 3.5 shows that the presence of helium yields a mixing term that is small in the classical regime at low pressures and high-enough temperatures, but reaches up to 10% away from it. On the Jupiter adiabat, this increase in ΔS occurs at pressures close to 0.1 Mbar, peaks in the megabar region, and slowly decreases at higher pressures. For temperatures that are about five times lower than on the Jupiter adiabat, we enter the invalidity regime of the EOSs. Results obtained in this regime should not be trusted.

Figure 3.6 shows that in the classical regime, in which $T \gtrsim 10^6\,\mathrm{K}\ (P/\mathrm{Mbar})$, the entropy excess is equal to the ideal value from Eq. (3.4). At lower temperatures, the mixing entropy term increases to up to almost three times the ideal value, except in a small region centred on 10^{-2} Mbar and 2000 K, where we see a decrease to only about 0.5 times the ideal value. Again, this decrease may be due to interpolation issues inherent to the original CMS19 and CD21 tables in a region that combines output from different works. For a typical Jupiter adiabat, ΔS is equal to the classical value up to 5 kbar and then increases to between 1.5 and 2.5 times this value, with a maximum around 0.5 Mbar. It is important to realise that uncertainties on both the pure and mixed EOSs still exist, as shown by a comparison to the SR18 calculations in Appendix A.1.

3.5.3 Application to Solar System planets

After deriving a table containing the mixing terms, we applied it to the cases of Jupiter and Saturn. We first compared adiabats for pure hydrogen-helium mixtures just by integrating the adiabatic gradient starting from 1 bar, 166.1 K (i.e. adapted to Jupiter

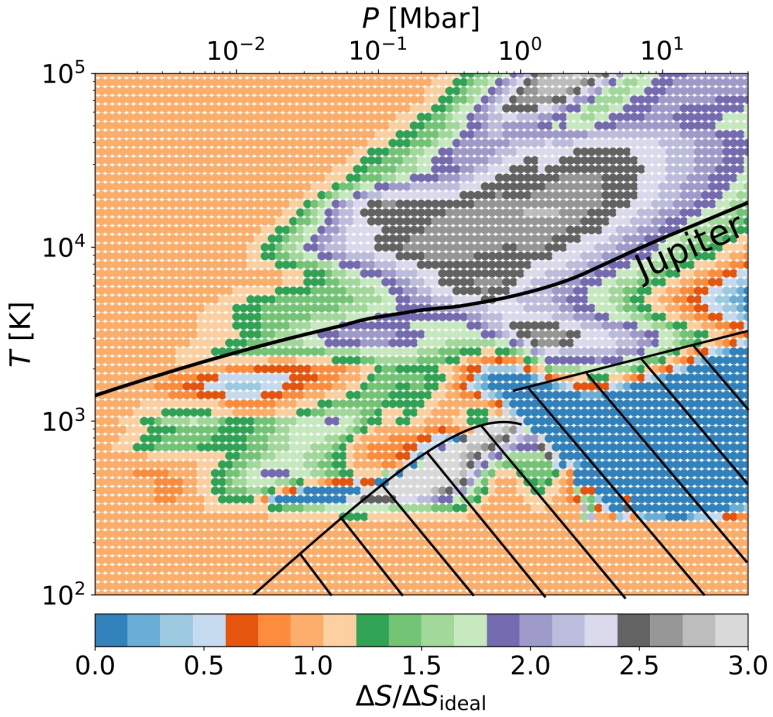

FIGURE 3.6: Ratio of the mixing entropy ΔS and the ideal entropy of mixing ΔS_{ideal} for a mixture of $Y = 0.245$. The hashed area corresponds to the region in which the entropy of mixing is invalid [see Chabrier et al., 2019, for more details]. **Taken from Howard and Guillot [2023].**

conditions). We used a simple homogeneous model, without a compact core and with a uniform helium composition ($Y = 0.245$). For convenience, because in the Jupiter interior $P \propto \rho^2$ [Hubbard, 1975], Fig. 3.7 compares values of $\rho/\sqrt{P}$ obtained for different EOSs. We note that all the new EOSs are much denser than SCvH95 [Saumon et al., 1995] in a wide region, from pressures of about 0.1 to 10 Mbar. The CMS19 [Chabrier et al., 2019] and MLS22 [Mazevet et al., 2022] EOSs do not include the interactions between hydrogen and helium at all. They were obtained using Eqs. (3.2) and (3.3) with the mixing terms ΔV and ΔS both equal to 0 and combining a pure hydrogen table (CMS19-H or MLS22-H) with a pure helium table (CMS19-He or SCvH95-He). They are particularly less dense between 0.01 and 0.1 Mbar but denser at depth than other EOSs. The MGF16+MH13 [Miguel et al., 2016] and CD21 [Chabrier and Debras, 2021] EOSs include the non-ideal mixing effects from Militzer and Hubbard [2013], who evaluated the H-He interactions for a mixture with $\tilde{Y} = 0.245$ and thus are very close to MH13* [Militzer and Hubbard, 2013]. They are also based on Eqs. (3.2) and (3.3) with ΔV and ΔS both equal to 0 ; but the non-ideal mixing effects evaluated at $\tilde{Y} = 0.245$ are included in the pure effective hydrogen table (MGF16+MH13-H or CD21-H; see Chabrier and Debras [2021] for more explanations on how to derive an effective pure H table that accounts for the H-He interactions). While MGF16+MH13-H is combined with SCvH95-He, CD21-H is combined with CMS19-He. Then, based on the table derived in Sect. 3.5.2, we added the mixing terms to the CMS19 and MLS22 EOSs and

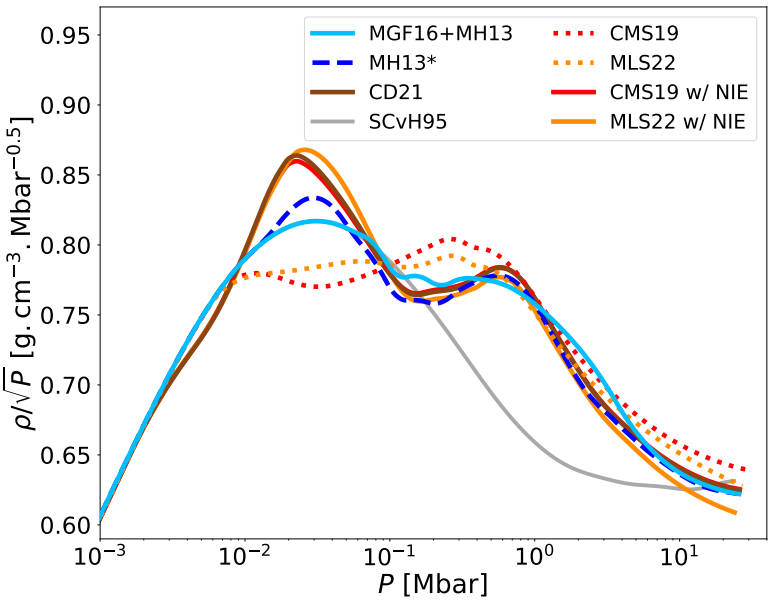

FIGURE 3.7: Adiabats obtained from different EOSs and corresponding to a homogeneous model, without a compact core, with $Y = 0.245$. NIE stands for non-ideal effects. **Taken from Howard and Guillot [2023].**

obtained adiabats (CMS19 w/ NIE and MLS22 w/ NIE) that are closer to the other EOSs that include the non-ideal mixing effects (MGF16+MH13, MH13*, and CD21).

An EOS that does not properly include the interactions between hydrogen and helium tends to underestimate the total amount of heavy elements in Jupiter. A quick test that consists of estimating the amount of heavy elements needed to match the equatorial radius of Jupiter, using a static model, can give a rough estimate of the impact of taking the non-ideal mixing effects into account. Focusing on a model similar to the one used for the adiabats of Fig. 3.7, with $Y = 0.245$, we ran two models: one model with CMS19, and one model with CMS19, including the non-ideal mixing effects. In the first case, we needed to add a compact core of 14.1 $M_\oplus$ to fit the equatorial radius of Jupiter, while we needed to add a compact core of 20.8 $M_\oplus$ in the second case. This shows that using the CMS19 EOS [see Ni, 2019, Nettelmann et al., 2021, Miguel et al., 2022] leads to an underestimation of the amount of heavy elements in Jupiter.

Another issue arises when the helium mixing ratio departs from the value $\tilde{Y} = 0.245$, and particularly, as in Jupiter and Saturn, when the helium abundance varies from the protosolar value due to H-He phase separation [Stevenson and Salpeter, 1977a]. In this case, even EOSs based on Militzer and Hubbard [2013] such as MGF16+MH13 and CD21 continue to evaluate the non-ideal mixing effects at $\tilde{Y} = 0.245$. In order to evaluate the magnitude of this effect, we proceeded as follows. First, we calculated some adiabats (at 1 bar conditions for Jupiter) for several values of Y and for the three EOSs CMS19, CD21, and our new EOS (CMS19 w/ NIE), which is based on the combination of CMS19-H, CMS19-He, and the mixing terms derived in Sect. 3.5.2, using Eqs. (3.2) and (3.3). We then searched for the maximum difference in density between the adiabats

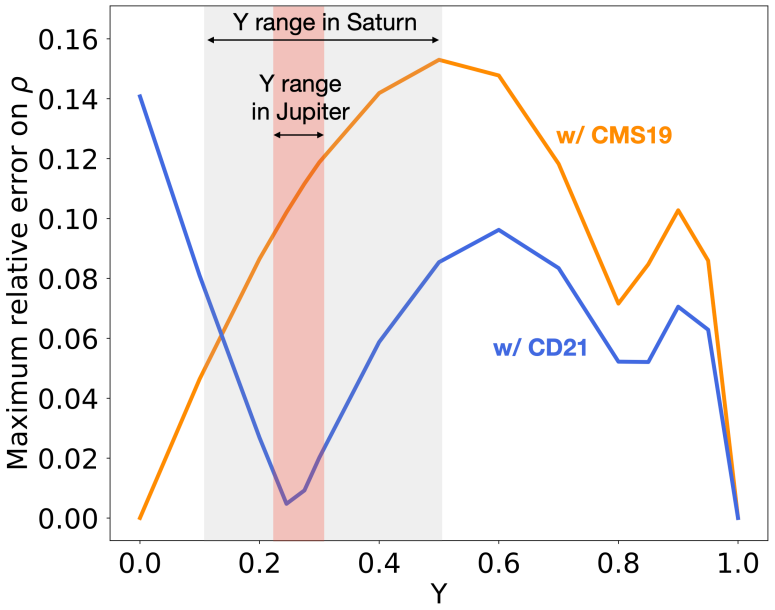

FIGURE 3.8: Comparison in density of our new EOS (this work) based on the non-ideal mixing effects derived in Section 3.5.2 with both CD21 and CMS19, according to the helium mass fraction Y. The shaded red and grey areas correspond to the range of values of Y in Jupiter (taken from models of Miguel et al. [2022]) and Saturn (taken from Mankovich and Fuller [2021]), respectively. **Taken from Howard and Guillot [2023].**

derived for each EOS at every value of Y. Figure 3.8 shows that the maximum deviation between our new EOS and CMS19 reaches a peak near $Y = 0.5$ and is equal to 0 at $Y = 0$ and $Y = 1$ because our new EOS is constructed to recover the pure end members CMS19-H and CMS19-He. With CD21, the maximum deviation reaches a minimum near $Y = 0.245$, which corresponds to the value where the non-ideal mixing effects were estimated. (The minimum is not exactly zero because of the difference between $\tilde{Y} = 0.245$ and $Y^* = 0.275$.) In the case of Jupiter, a relative difference of 12% can exist (for Y close to 0.3) between our new EOS and CMS19. The comparison with CD21 yields a 2.5% difference in density at most. For Saturn, where the range of Y is wider [Mankovich and Fuller, 2021], the effects of the H-He interactions are even stronger. Using CMS19 can lead to a 15% error in density (for $Y = 0.5$), while using CD21 can lead to an error of 8.5%.

3.5.4 Application to exoplanets

So far, we focused on static models to analyse internal structures at a given time. Now, we use CEPAM and a non-grey atmosphere [Guillot et al., 2006, Parmentier et al., 2015] to model the evolution of planets and determine the influence of the H-He interactions during their lifetime. As seen in Sect. 3.5.3, when we do not include non-ideal mixing effects, static models lead to an underestimated amount of heavy elements, thus a denser mixture of hydrogen and helium overall. Hence, static models (with similar quantities

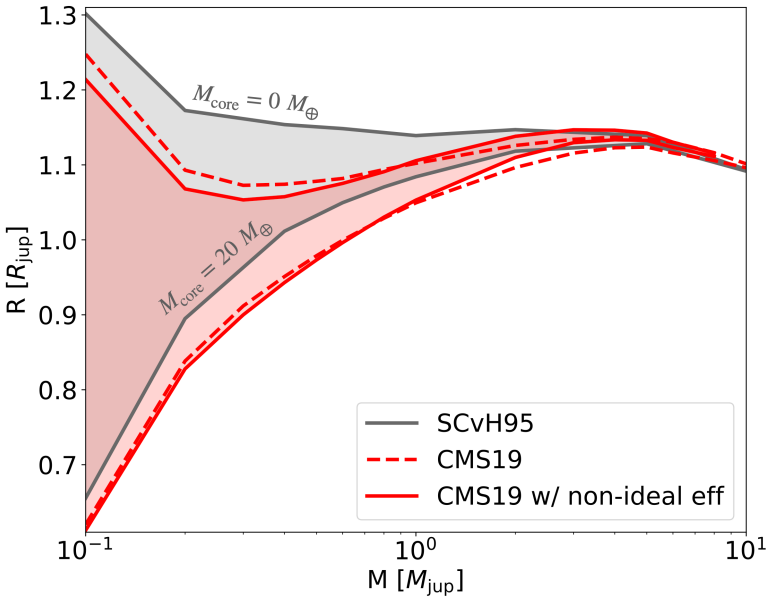

FIGURE 3.9: Evolution models of giant planets for three EOSs: SCvH95, CMS19, and our new EOS (CMS19 w/ non-ideal effect), with T_{eq}=1500 K, taken at 4.5 Gyr. The models consist of a pure rocky core overlaid with a H-He envelope of solar composition. The coloured area for each EOS is bounded by evolution models without a core and with a 20 $M_\oplus$ core. **Taken from Howard and Guillot [2023].**

of heavy elements) will yield a larger radius when accounting for these non-ideal mixing effects. Assuming simple structures consisting of a central rocky core and a surrounding H-He envelope of solar composition ($Y = 0.3$), we calculated evolution models for giant planets with T_{eq}=1500 K. For each EOS, Figure 3.9 shows the mass-radius relation obtained at 4.5 Gyr, bounded by homogeneous models without a core (on top) and with a core of 20 $M_\oplus$ (at the bottom). Static models (for fixed boundary conditions) yield larger radii when non-ideal mixing effects are included, by up to 2% for planets of 1-3 M_{Jup}. When we consider the evolution, the present-day radius results both from the mass-radius relation for static models and from the history of the planet in the $P - T$ diagram. Figure 3.9 shows that the effects are generally in the opposite sense, leading to a change in radius due to non-ideal mixing that is smaller than for purely static models. We find larger radii for planets that are more massive than Jupiter when we use our new EOS (CMS19 w/ NIE) compared to CMS19; and in contrast to static models, we find smaller radii (by up to 2%) for planets that are less massive than Jupiter. The difference can reach 6% at most, at younger ages. Furthermore, we stress that the radii differ significantly (by up to 8%) from those obtained with the SCvH95 EOS, which is commonly used [Fortney et al., 2007]. Because of the accuracy in masses and radii of exoplanets, more careful modelling is needed and improved knowledge of the H-He EOS is important to characterise exoplanets.

3.5.5 Conclusion

In Howard and Guillot [2023], we thus have provided a simple way to account for the interactions between hydrogen and helium in the EOS. We have derived mixing terms (including the non-ideal contribution) to be added to the classically used linear mixing law for density and entropy, respectively. We built a table of these mixing terms as a function of pressure and temperature. This table is to be combined with pure EOSs to derive the properties of any hydrogen and helium mixture. We emphasise that omitting these mixing effects can lead to a relative error in density of up to 15% on the H-He EOS for Jupiter and Saturn, resulting in a serious underestimation of the heavy element reservoir and invalidating the fit to the observed gravitational moments. Even models including these non-ideal mixing effects evaluated for a helium mass-mixing ratio $Y = 0.245$ [Debras and Chabrier, 2019, Miguel et al., 2022, Militzer et al., 2022, Mankovich and Fuller, 2021] have intrinsic errors on the density evaluated to up to 2.5% for Jupiter and 8.5% for Saturn. In addition, when the non-ideal mixing effects are not included, a change of up to 6% in the calculated radii of exoplanets may result. Furthermore, given the differences between EOSs, we stress that uncertainties on the H-He EOS still exist. Our approach provides a way to obtain a self-consistent EOS for different helium abundances. We stress that it relies on EOSs calculated for three compositions only (for $Y = 0$, $Y = 0.245$ and $Y = 1$). Ab initio calculations and high-pressure experiments for $P = 10^{-2} - 10\,\mathrm{Mbar}$ and $T = 1000 - 20,000\,\mathrm{K}$ with other hydrogen-helium compositions, but also including heavy elements, would be highly desirable.

3.6 Uncertainties in the H-He equation of state

This section corresponds to sections 3.1 and 3.2 of Howard et al. [2023]. It compares adiabats calculated with different EOSs and shows the uncertainties on the H-He EOS that exist.

Jupiter being mostly composed of hydrogen and helium, interior models of the planet require the use of an appropriate EOS for these chemical elements. The SCvH95 [Saumon et al., 1995] EOS was commonly applied for studying Jupiter and extrasolar giant planets [Thorngren et al., 2016]. However, in the last decade, with the improvement of shock Hugoniot data analyses and the development of ab initio simulations, new H-He EOSs have emerged [Militzer and Hubbard, 2013, Chabrier et al., 2019, Mazevet et al., 2022]. To compare these EOSs, we derived adiabats for pure hydrogen–helium mixtures ($Y = 0.245$) by simply integrating the adiabatic gradient starting from 1 bar, 166.1 K (i.e. Jupiter's conditions). For the sake of comparison, heavy elements have not been included but they would only slightly affect the adiabats (see Helled [2018]). Table 3.1 details the specifics of the EOSs used to calculate these adiabats. The MGF16+MH13 EOS was

derived by Miguel et al. [2016] from the ab initio simulation data of Militzer and Hubbard [2013]. We built MH13* by fitting an adiabat provided by Burkhard Militzer (private communication), based on the ab initio EOS of Militzer and Hubbard [2013]. We used a polynomial function g to fit the residuals between the MGF16+MH13 adiabat and the one provided by BM. We then perturbed the MGF16+MH13 EOS so that $\rho_{\mathrm{MH13}*} = (1-g)\rho_{\mathrm{MGF16+MH13}}$. The comparison between MGF16+MH13 and MH13* is detailed a bit later. More information about the derivation of CD21 can be found in Chabrier and Debras [2021]. The HG23+CMS19 and HG23+MLS22 EOSs both make use of the tables of the non-linear mixing effects provided in Howard and Guillot [2023]. We note that all these EOSs, except SCvH95, account for the interactions between hydrogen and helium particles. Still, MGF16+MH13, CD21, and MH13* include the non-ideal mixing effects but they remain fixed and equal to that calculated by Militzer and Hubbard [2013] for a single composition ($Y = 0.245$). On the other hand, HG23+CMS19 and HG23+MLS22 include the H-He interactions and remain valid for any composition of the mixture (see Howard and Guillot [2023]). For convenience, as $P \propto \rho^2$ in Jupiter's interior [Hubbard, 1975], Figure 3.10 compares values of $\rho/\sqrt{P}$. The SCvH95 EOS is much less dense than the other, more recent EOSs, ranging from 0.1 to 10 Mbar. (Quantum Monte Carlo simulations [Mazzola et al., 2018] yield even denser hydrogen (between 0.3 and 2.6 Mbar) than found by EOSs obtained from density functional theory.) We find a maximum relative deviation between the different EOSs (except SCvH95) that amounts to 5.5% (around 0.03 Mbar). The discrepancy between the various EOSs gives us an estimate of the uncertainty on the EOS to be accounted for in Jupiter models.

The differences between the EOSs seen in Fig. 3.10 are surprising, because in that parameter space, with the exception of SCvH95, they are all based on the results obtained by the same ab initio calculations from Militzer and Hubbard [2013]. In order to understand where these differences come from, we must examine the way the EOS tables are constructed. Two tables are available in Militzer and Hubbard [2013]. Table 1 provides the thermodynamic quantities obtained from the density functional molecular dynamics (DFT-MD) calculations. This latter was directly used by Miguel et al. [2016] and grafted to the SCvH95 EOS to construct the MGF16+MH13 table. On the other hand, Table 2 from Militzer and Hubbard [2013] provides coefficients for a free-energy fit from which one can calculate all thermodynamic quantities. This free-energy fit is used by Militzer et al. [2022] and forms the basis of the MH13 EOS (similar to our MH13* EOS). Both the CD21 EOS [Chabrier and Debras, 2021] and the nonideal mixing tables of Howard and Guillot [2023] use this EOS and have to interpolate the results with the SCvH95 EOS in the molecular regime. To assess the uncertainty due to the choice of table, but also due to the way we interpolate through the table, we derived adiabats from both Table 1 and Table 2 from Militzer and Hubbard [2013]. To do so, we used a one-dimensional interpolation to evaluate pressure and temperature at a typical value of entropy for Jupiter (7.078061 $k_b\mathrm{el.}^{-1}$), for each density value. This procedure is straightforward for Table 1, but for Table 2 we followed the procedure prescribed by Militzer and Hubbard [2013]

TABLE 3.1: H-He EOSs used in interior models. Concerning the heavy elements, the EOSs used for ices and rocks are respectively those of water and dry sand from Lyon and Johnson [1992].

Name of the H-He EOS	H EOS	He EOS	H-He interactions	Notes/References
MGF16+MH13	MGF16-H	SCvH95-He	Included in the H EOS but fixed at $Y = 0.245$	Derived by Miguel et al. [2016] from Militzer and Hubbard [2013]
MH13*	- -	- -	- -	Adjusted from MGF16+MH13 to fit a $Y = 0.245$ adiabat from Militzer et al. [2022]
CD21	CD21-H	CMS19-He	Included in the H EOS but fixed at $Y = 0.245$	Derived by Chabrier and Debras [2021] from Militzer and Hubbard [2013]
HG23+CMS19	CMS19-H	CMS19-He	HG23	H and He EOSs from Chabrier et al. [2019] and non-ideal mixing effects from Howard and Guillot [2023]
HG23+MLS22	MLS22-H	CMS19-He	HG23	H EOS from Mazevet et al. [2022] and non-ideal mixing effects from Howard and Guillot [2023]
SCvH95	SCvH95-H	SCvH95-He	None	H and He EOSs from Saumon et al. [1995]

before deriving the adiabats. We then tried three different types of interpolation (linear, quadratic, and cubic) when calculating the adiabats. Figure 3.11 shows the different extent in parameter space of the two tables from Militzer and Hubbard [2013] and how different choices, in particular on the order of the interpolation, affect the resulting adiabat. Table 2 is slightly extended compared to Table 1 and provides density and entropy for temperatures between 1000 and 80,000 K, and pressures between 0.1 and 300 Mbar. The maximum deviation between adiabats calculated from Table 1 and Table 2 is of the order of 2%. The order of the interpolation brings a maximum deviation that amounts to 1.3%. These uncertainties lead to the differences between the MGF16+MH13 and the MH13* EOSs. However, at pressures of lower than 0.1 Mbar, there are also discrepancies between both EOSs that are certainly due to the combination of the DFT-MD calculations of Militzer and Hubbard [2013] with the SCvH95 EOS of Saumon et al. [1995]. The construction of an EOS is very sensitive to the merging of several tables, particularly around the regions where the tables are connected. This may explain the high values of

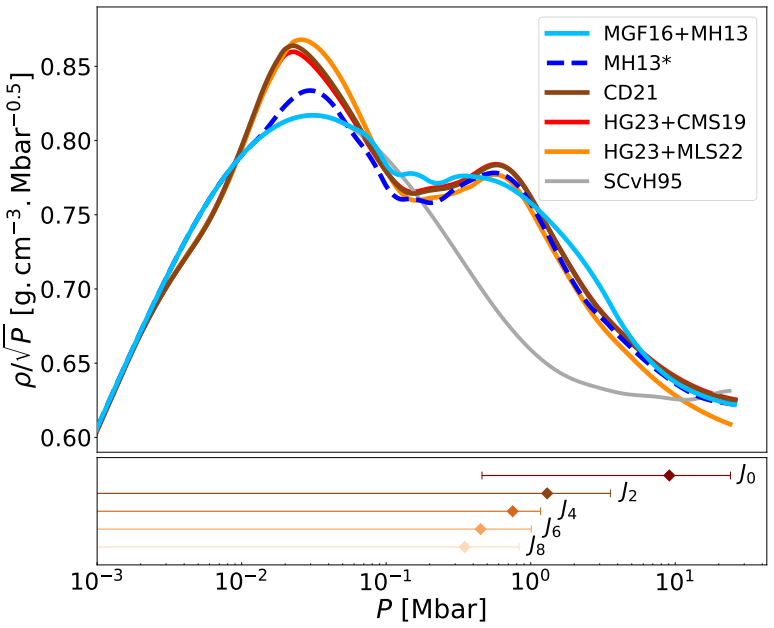

FIGURE 3.10: Adiabats obtained from different EOSs and corresponding to a homogeneous model, with no compact core, with $Y = 0.245$. Table 3.1 lists the details of the EOSs. Below are shown the contribution functions of the gravitational moments of order 0 to 8 centred at their peak. Their extent corresponds to their full width at half maximum (see Guillot [2005] for more details). **Taken from Howard et al. [2023].**

density around 0.03 Mbar and the slightly lower densities at $P < 0.01$ Mbar for CD21, HG23+CMS19, and HG23+MLS22 (see Fig. 3.10). Furthermore, we can see that the points of Table 1 —displayed in Fig. 3.11— are sparse, particularly between 0.1 and 1 Mbar, at densities relevant to the region used to derive a Jupiter adiabat, affecting the accuracy of the interpolation through the table.

3.7 Heavy elements

As shown on Fig. 3.1, the density contribution of the heavy elements in Jupiter is negligible compared to the ones of hydrogen, helium and even the interactions between these species. Besides, we cannot really distinguish with different types (ices, rocks) of heavy elements inside giant planets so far. However, in the future, we may reach a level of accuracy that requires a good understanding of the behaviour of heavy elements. So far, the EOSs I have used for heavy elements are the SESAME [Lyon and Johnson, 1992] ones for water and drysand. More modern ones obvisouly exist now.

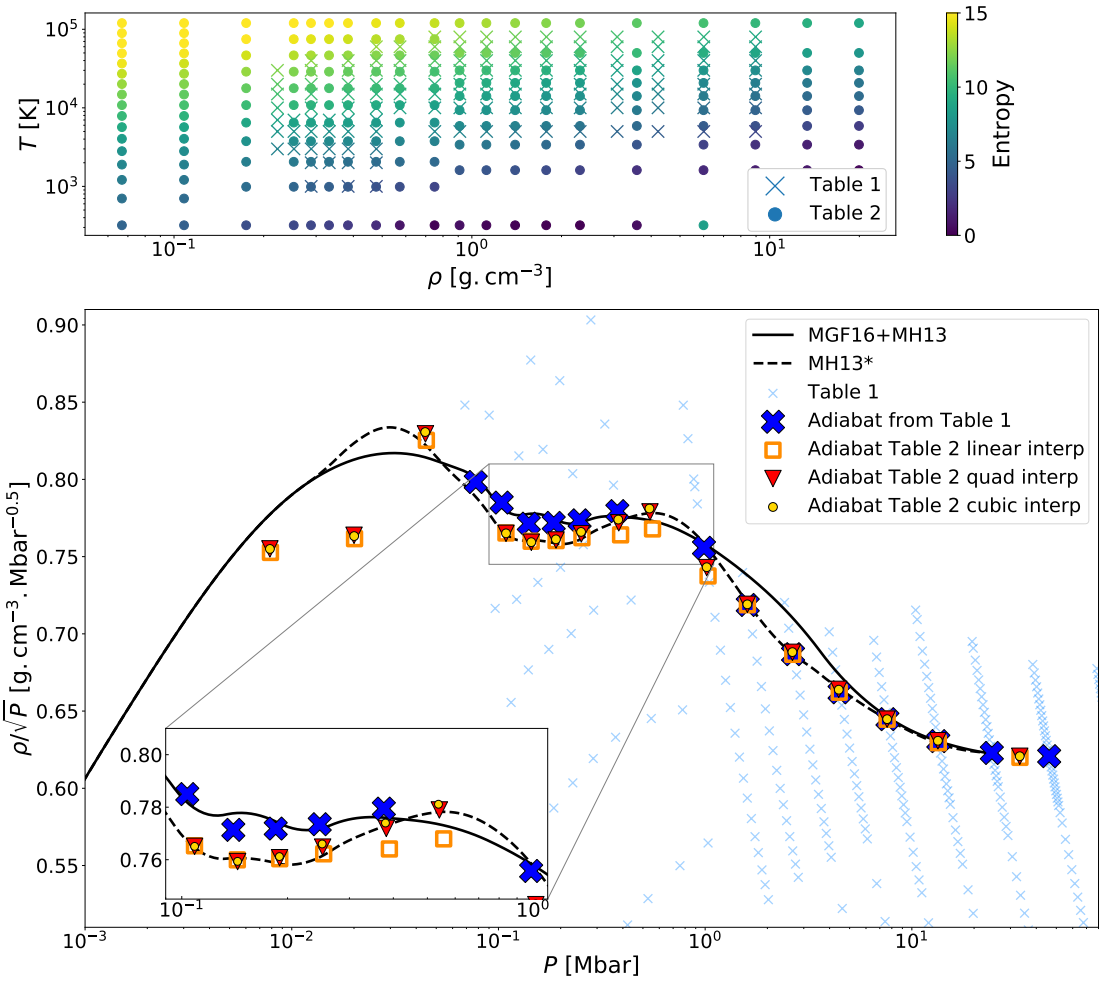

FIGURE 3.11: Comparison between the MH13* and MGF16+MH13 EOSs. *Top panel.* Comparison of Table 1 and Table 2 from Militzer and Hubbard [2013]. *Bottom panel.* Comparison of adiabats obtained with the MH13* and MGF16+MH13 EOSs and of points obtained by direct interpolation of the above tables. The $(P, \rho/\sqrt{P})$ points of Table 1 from Militzer and Hubbard [2013] are shown as blue crosses. The locations at which the entropy is equal to 7.078061 $k_b$el.$^{-1}$ (a typical value of entropy for Jupiter) according to the interpolations in the two tables are shown with different symbols, as labelled. **Taken from Howard et al. [2023].**

Chapter 4

Advancing the methodology: statistical analysis and comparative studies of Jupiter's interior

Contents

We focused in the two previous chapters on how to build interior and evolution models of giant planets. I will present in this chapter the approach that my collaborators and I decided to follow in order to study Jupiter's interior. The next chapter will be dedicated to interior models of Jupiter. During my PhD, I spent a significant part of my first year, at home because of Covid, but more interestingly trying to get familiar with the tools that I then used all along the three years of PhD. More specifically, I learnt how to handle CEPAM [Guillot and Morel, 1995], a code to calculate models of giant planets but also a Markov chain Monte Carlo code (referred as MCMC in the whole manuscript) developed by Michaël Bazot [Bazot et al., 2012]. During this first year of PhD, I also spent time on preliminary analyses that were useful before the calculations that will be presented in the next chapter and that led to the publication of Howard et al. [2023]. It involved many zoom meetings with Yamila Miguel, Michaël Bazot and Tristan Guillot but also with Burkhard Militzer and Bill Hubbard to compare our interior models.

4.1 The statistical approach

The study of Jupiter's interior started a hundred years ago, where single models were built by hand, with no computers. Then, series of models could be proposed [Peebles, 1964], each based on different assumptions. However, the number of models considered was limited to no more than ten (see, e.g., Hubbard [1969], Chabrier et al. [1992]). During the 1990s and 2000's, ensemble of models were proposed, involving the systematic variation of input parameters by small increments. This approach gained popularity and became widely used, allowing researchers to assess the influence of specific parameters and to determine large solution ranges [Guillot, 1999, Saumon and Guillot, 2004, Nettelmann et al., 2008]. It is only very recently that more modern statistical methods have been applied to studying the interiors of giant planets [Mankovich and Fuller, 2021, Miguel et al., 2022, Howard et al., 2023]. This allows to explore a huge number of different possible models but also to assess how plausible they are.

The exquisitely accurate measurements of the gravitational moments by Juno allow us to constrain interior models. The inverse problem of inferring the properties of Jupiter's interior from these measurements can be tackled through a Bayesian approach. This is the approach that we decided to follow in order to study large ensembles of models instead of a quest for one or few plausible or best models. We can hence carry out an extensive exploration of the parameters of the interior.

4.1.1 The MCMC

In recent years, particular interest was given to a branch of the field of statistics called Bayesian inference. The frequentist approach that is based on using data from experiments can be seen, put crudely, as the determination of the frequency of occurence of an event. On the other hand, the Bayesian approach treats probabilities as degrees of belief, rather than as frequencies generated by some process. It provides us with a measurement of our state of knowledge on a particular problem. Moreover, a benefit of the Bayesian framework is that it includes past knowledge (known as prior), for instance from experiments, into the assessment of this problem. We make use of this Bayesian approach and particularly of a Markov chain Monte Carle (MCMC) code to cope with the problem of retrieving the parameters of Jupiter's interior. This section aims to give a brief overview of how MCMC works and we stress that it was mainly inspired by Gregory [2001] and Bazot et al. [2012]. The MCMC code I used all along this work was developed by Michaël Bazot, who took time to help me handle it.

While many articles and lectures directly begin with the theoretical aspects to introduce MCMC, I believe it is useful to provide some intuition first, to give to the non-expert reader an idea of MCMC sampling, before looking at the equations. The goal of MCMC is to sample models around a region of interest, namely to determine the sets of parameters that lead to models in agreement with some observations we have (called data). While Monte Carlo refers to the stochastic aspect, Markov chain refers to the sequence of parameter sets. Thus, the method starts by initialising a number of walkers, that are basically initial random guesses of parameter sets. Each walker then explores independently the parameter space and try to get close to the region of interest. To do so, MCMC are based on algorithms to choose the way walkers are moving in the parameter space. A new position to go is smartly proposed, the algorithm then assesses if it is a good place to go. A chain will correspond to the path followed by a walker. An efficient MCMC code will finally lead to an estimation of the credible range of our model parameters allowed by the data, known as posterior.

Let us now go more in the details and introduce some mathematical considerations. Let $\theta = (\theta_1, ..., \theta_k)$ be the unknown parameters of the interior of the planet and $x = (x_1, ..., x_n)$ be the available data (e.g. measurements of the gravitational moments). The basis of MCMC sampling comes from the Bayes formula:

$$P(\theta|x) = \frac{P(x|\theta)P(\theta)}{P(x)}. \tag{4.1}$$

Our quantity of interest is $P(\theta|x)$, called the posterior. It corresponds to the probability of our model parameters θ given the data x (what we think the parameters are post using data). The prior $P(\theta)$ corresponds to what we think the parameters θ are before using any data. The likelihood, written $P(x|\theta)$ or $\mathcal{L}(\theta, X)$, is how we think the data is

distributed. The nominator is quite easy to calculate. The denominator corresponds to the evidence $P(x)$, which can be computed by integrating over all possible parameter values:

$$P(x) = \int P(x|\theta)P(\theta)d\theta. \tag{4.2}$$

The evidence is a normalisation constant to ensure that the integral of the posterior over the entire parameter space is 1. It is hard to compute but we will see that MCMC does not require to calculate it because it does not depend on θ.

We then define $\mathcal{C}(\theta)$ as the predictions of the data (calculated with CEPAM). The difference between $\mathcal{C}(\theta)$ and x is noted ϵ. Minimizing this error ϵ (coming from instrumental but also model errors) is actually not an easy problem because $\mathcal{C}$ is not an explicit function. MCMC generates samples distributed according to a probability distribution that is linked to the discrepancy between observations and their prediction by $\mathcal{C}(\theta)$. Assuming that the error ϵ_n on each observation x_n is normally distributed, with a standard deviation noted σ_n (uncertainty on x_n), and that errors on different observations are independent, we define the likelihood:

$$\mathcal{L}(\theta, X) = p(\epsilon) = \left(\prod_{n=1}^{N} \frac{1}{(2\pi)^{1/2}\sigma_n} \right) \times \exp\left(-\frac{1}{2} \sum_{n=1}^{N} \left[\frac{\mathcal{C}(\theta) - x_n}{\sigma_n} \right]^2 \right). \tag{4.3}$$

We aim to maximise the likelihood, that is, to minimise the usual $\chi^2 = \sum[(\mathcal{C}(\theta) - x_n)/\sigma_n]^2$ in Eq. 4.3. We can hence compute the posterior $P(\theta|x)$. Note that the output of the MCMC which is the posterior actually refers to a set of samples of posteriors. And since we face a multi-parameters problem, we will often use posteriors to refer to joint posterior probability distributions. MCMC will provide samples randomly distributed according to the targeted distribution of interest by simply evaluating this distribution at a certain number of parameter values.

An important aspect of MCMC algorithms is how to propose new parameter sets to get close to the region of interest where we want to sample models. The point is to make not random guesses but smart guesses for θ to move from a position to another. In the standard Metropolis sampler for instance, the new position is sampled from a normal distribution centred around the current one, with a certain standard deviation (how far we move positions). The algorithm employed here is the Metropolis-Hastings algorithm, which is different from the Metropolis one as it proposes asymmetric jumps to move positions. The sampling depends on an instrumental distribution $q(\theta^*|\theta^{(t)})$, which is a probability distribution used to propose and generate a new set of parameters θ^*, here at iteration t. In our case, we employ a mixture of three distributions: two Gaussian distributions both centred at the current state of the parameters but with different standard deviations, in order to have the possibility to propose small and big jumps to move position and a third uniform distribution to avoid chains to be trapped in potential local minima. Our MCMC follows the Metropolis-Hastings algorithm, recalled

in Algorithm 1. Starting from an initial position (a first guess of the parameter set), a new position is proposed with the instrumental distribution. We then need to assess if this proposed position is a good one to go or if it a better option t stay at the current position. To do so, we compare the posterior probability of the proposed position with the posterior probability of the current position. We thus define an acceptance ratio $p_{\text{accept}} = p_{\text{proposal}}/p_{\text{current}}$ which becomes only the ratio of both posterior probabilities when assuming that the instrumental distribution is symmetrical ($q(\theta^{(t)}|\theta^*) = q(\theta^*|\theta^{(t)})$). The ratio of the posterior probability at the proposed and current states eliminates the need for the evidence term, simplifying the expression to:

$$\frac{\frac{P(x|\theta^*)P(\theta^*)}{P(x)}}{\frac{P(x|\theta^{(t)})P(\theta^{(t)})}{P(x)}} = \frac{P(x|\theta^*)P(\theta^*)}{P(x|\theta^{(t)})P(\theta^{(t)})}. \tag{4.4}$$

If the posterior probability of the proposed position is higher than the posterior probability of the current position, the acceptance ratio p_{accept} will be greater than 1 and $\rho(\theta^{(t)}, \theta^*)$ will be taken as 1 given its definition shown in Algorithm 1. If the posterior probability of the proposed position is lower than the posterior probability of the current position, then p_{accept} will be lower than 1 and the new position will be accepted with such probability. We then draw u from a uniform distribution in [0,1] and accept $\theta^{(t+1)} = \theta^*$ if $u < \rho$. Parameters leading to an increase in posterior probability will hence always be accepted while parameters decreasing the posterior probability will be randomly accepted, depending on the acceptance ratio. This procedure allows regions of high posterior probability to be explored more often.

Algorithm 1 Metropolis-Hastings algorithm. Taken from Bazot et al. [2012].

For $t = 1$, choose an initial value $\theta^{(1)}$. Then, at iteration t:

1. Generate: $\theta^* \sim q(\theta|\theta^{(t)})$
2. Select:

$$\theta^{(t+1)} = \begin{cases} \theta^* & \text{with probability } \rho(\theta^{(t)}, \theta^*), \\ \theta^{(t)} & \text{with probability } 1 - \rho(\theta^{(t)}, \theta^*), \end{cases}$$

where

$$\rho(\theta^{(t)}, \theta^*) = \min\left\{\frac{P(\theta^*|x)}{P(\theta^{(t)}|x)}\frac{q(\theta^{(t)}|\theta^*)}{q(\theta^*|\theta^{(t)})}, 1\right\}.$$

Using a MCMC code appears as an efficient tool to study the problem of Jupiter's interior which is highly degenerate. A wide exploration of a high number of parameters can be performed. We show on Fig. 4.1, for a specific run (dilute core models, MLS22 EOS, from Miguel et al. [2022]) the evolution of the mean value of the parameters and data as the MCMC progresses through multiple iterations (N). It shows the exploration of the parameter space by the walkers (parameter sets). Here, Y_{proto}, Y_{atm} and $Z_{\text{atm,ices}}$ are fixed parameters, which is why they have not been plotted. We can see that the algorithm correctly converged (see the appendix in Bazot et al. [2012] for a discussion about monitoring convergence). In our calculations presented in Chapter 5, we have always removed the first half of the iterations (called burn-in sequence) to discard samples far

from the targeted posterior distribution. The burn-in sequence has not been removed on this figure. However, the MCMC can be computationally expensive as millions of models will be calculated if we consider using hundreds of walkers and running about 10 000 iterations. We therefore need a code that calculates interior models rather fast.

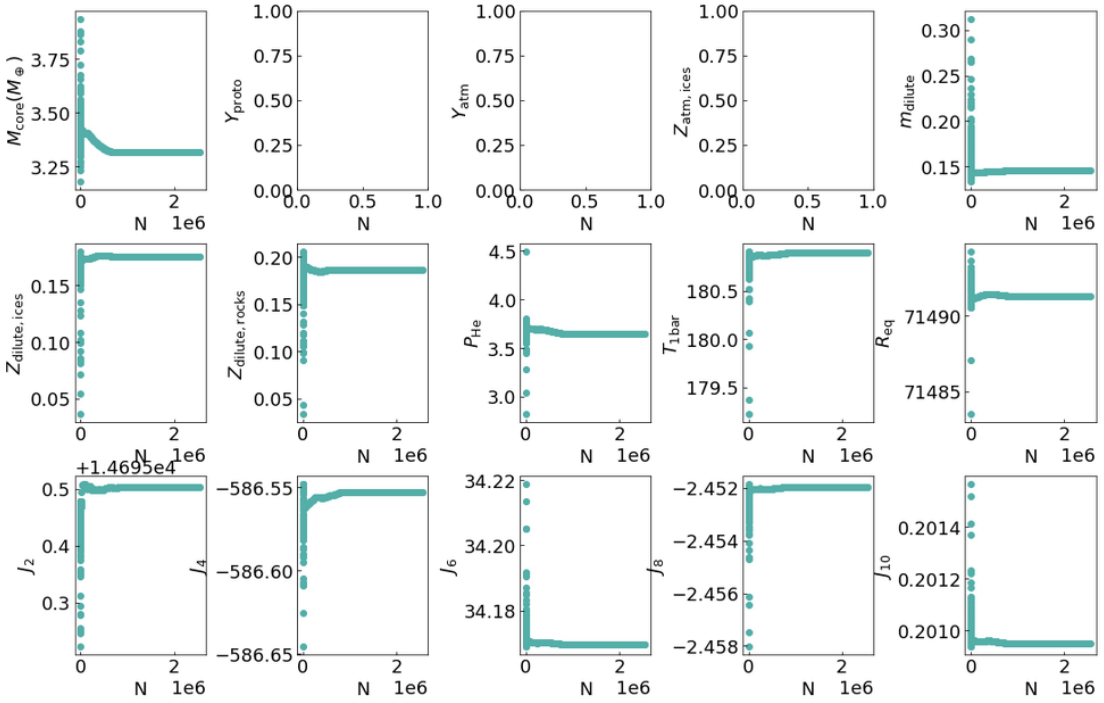

FIGURE 4.1: Evolution of the mean value of the CEPAM parameters and data as the MCMC progresses through millions of iterations (N).

4.1.2 Offsets calculations

To make our MCMC running in a decent amount of time (about $\sim$ 10 hours on Licallo, the supercomputer of the Observatoire de la Côte d'Azur), we need to compute the gravitational moments relatively fast. CEPAM [Guillot and Morel, 1995] calculates the gravitational moments with the theory of figures to order 4 and takes about a few seconds to run a model with 1000 layers. On the other hand, Bill Hubbard has developed a code called CMS4Cepam meant to take the outputted density profile of CEPAM and running CMS [Hubbard, 2013] on it. Running CMS4Cepam takes however about 2 to 3 hours. Running it with the MCMC would not be an efficient strategy. Even with optimised versions of CMS (CMS-planet by Naor Movshovitz or CMS-Weizmann by Maayan Ziv and Eli Galanti), the calculations still takes a few minutes, which is still considerably larger than the computation time of CEPAM. The CMS method is in fact much more time consuming because it explicitly calculates the shapes of the spheroids (see Subsection 2.5.2) to the required level of accuracy. The accuracy of the different methods to compute the gravitational moments can be assessed by comparing them to an exact solution for a polytrope [Wisdom and Hubbard, 2016]. The following text in

this subsection has been taken and adapted from my contribution in subsection 2.3. of Miguel et al. [2022].

Because results calculated with the CMS method are more accurate but more computationally demanding, the runs are made using the theory of figures that allows us to perform many more runs in a shorter time, but we use the accuracy of the CMS method by calibrating the gravity harmonics obtained from the theory of figures to the CMS values [Guillot et al., 2018]. Because the gravity harmonics measured by Juno have reached a very high accuracy, estimating the offsets between both methods is essential.

This calibration is done by assessing offsets ($\delta J_{2n} = J_{2n}(\text{ToF}) - J_{2n}(\text{CMS})$), between the gravity harmonics from the theory of figures and the ones from the CMS method, using a random sample of 100 of our preferred models. We then take these models and perform an optimization procedure, modifying M_{core} and Z_1 to perfectly fit the observational measurements of the equatorial radius R_{eq} and J_2 – to get offsets from the most accurate models – and then compute the offsets for these second set of models using both methods. Figure 4.2 displays the offsets for both sub-samples (models with and without the optimization procedure). Our results show a correlation between the offsets, where δJ_4 and δJ_6 depend strongly on δJ_2. Higher order gravitational moments (δJ_8, δJ_{10}), are less dependent on δJ_2. Thanks to these linear relationships, we can quantify the impact of an offset on J_2 on the offsets of the higher order gravitational moments. We also note that the residuals are very small compared to the error bars of Juno accounting for the differential rotation. We calculate the median value of δJ_2 among the 100 optimised models and calculate the higher order offsets using the linear relationships. Table 4.1 lists the offsets found, where we note that previous offsets from Guillot et al. [2018] almost lie on the linear regression curves, showing that our offsets have changed very slightly and thus our calculations are robust. We show on Fig. 4.3 the gravitational moments obtained using the newly calculated offsets. We have a good agreement between our optimised models either calibrated with these offsets or ran with CMS4Cepam. Moreover, we can see on the top right panel that only a change in the core mass or the molecular envelope metallicity of a few percents can lead to a good fit of the gravitational moments. We believe that our MCMC calculations provide robust results, running millions of models. Our assessment of the offsets is reliable, leading to an effective calibration of our models. And even if the models feature a value of J_2 a bit far from the observational constraint, it does not qualitatively affect the results as only a small correction will be needed. We finally stress that the offsets have been calculated for a specific type (3-layer) of models and with a specific EOS (MGF16+MH13). Other types of models could slightly affect the offsets.

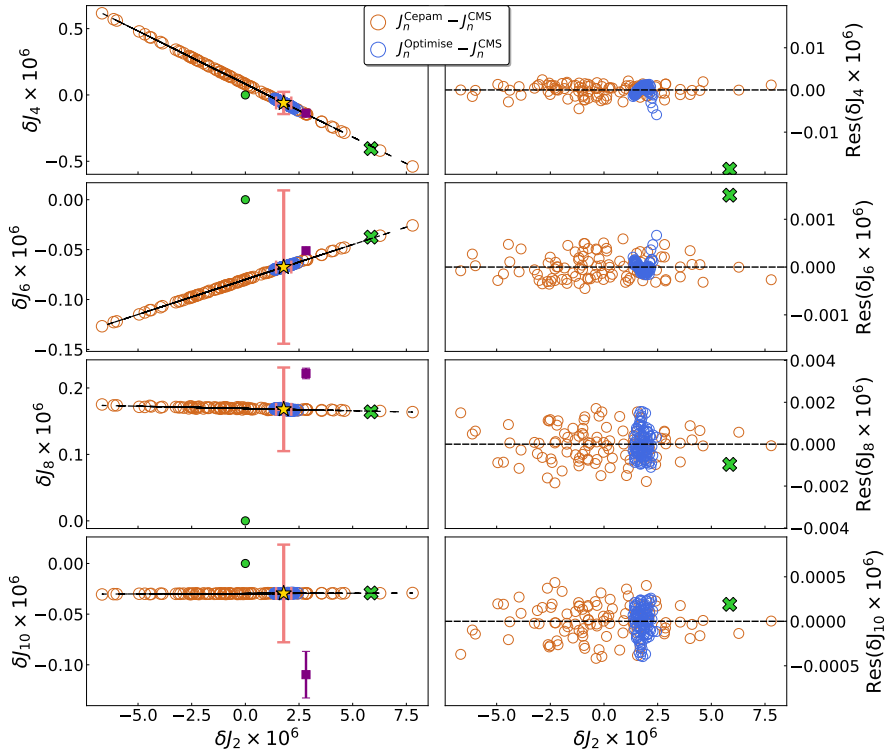

FIGURE 4.2: Offsets between ToF and CMS for two subsamples (MCMC models and optimised models). *Left panels* : Offsets on the gravitational moments. The black dashed line shows the linear fit of our models. The green dot shows the origin. The yellow star corresponds to the linear fit of the optimised models median of ΔJ_2. The pink errorbars shows the uncertainty of the Juno measurements accounting for the differential rotation. The purple errorbars show the uncertainty of the Juno measurements. The green cross shows the former offsets from Guillot et al. [2018]. *Right panels* : Residuals of the linear fit shown on the left panels. **Taken from Miguel et al. [2022].**

TABLE 4.1: Offsets between ToF and CMS. The first column indicates the offsets for a null value of δJ_2, the second (values highlighted) shows offsets estimated after picking the median value of δJ_2 (the new set of offsets used in our calculations), then we show previous offsets calculated in Guillot et al. [2018] and finally the error bars from Juno with and without accounting for differential rotation. **Taken from Miguel et al. [2022].**

	$\delta J_2 = 0$	$\delta J_2 = \text{median}(\delta J_2)$	Guillot+2018	Juno error	Juno w/ diff rot error
$\delta J_2 \times 10^6$	0	**1.78621**	5.8554	0.014	0.35425
$\delta J_4 \times 10^6$	0.0822626	**-0.0604954**	-0.4045	0.004	0.0836
$\delta J_6 \times 10^6$	-0.0799887	**-0.0674861**	-0.0375	0.009	0.0768
$\delta J_8 \times 10^6$	0.16909	**0.167862**	0.1641	0.025	0.0624
$\delta J_{10} \times 10^6$	-0.0297133	**-0.0295843**	-0.0291	0.069	0.0423
$\delta J_{12} \times 10^6$	0.004131	**0.00411681**		0.175	

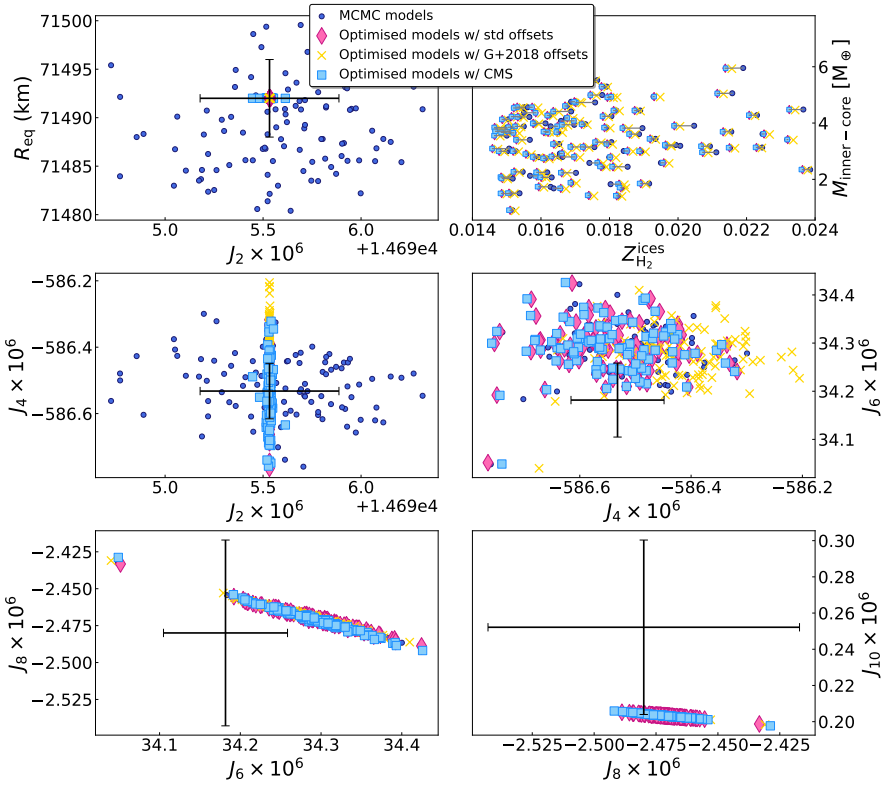

FIGURE 4.3: Results for 4 sets of 100 models : random models from our preferred MCMC runs, optimised models with new offsets, optimised models with former offsets from Guillot et al. [2018] and optimised models with CMS calculation. *Top left panel* : Equatorial radius vs J_2. *Top right panel* : Core mass vs fraction of ices in the molecular hydrogen layer. Grey lines show the pairing between each model and its optimised version. *Middle and bottom panels* : Gravitational moments. The black error bars show the uncertainty of the Juno measurements accounting for the differential rotation. **Taken from Miguel et al. [2022].**

4.2 Comparison with other models

My first contribution to interior models of Jupiter happened during the preparation of Miguel et al. [2022] which will be presented in the next chapter. This paper was prepared in parallel with Militzer et al. [2022]. And with the two groups, we compared our works very often before submitting the two papers. I want to stress here that we came a long way before being able to obtain the models presented in Miguel et al. [2022]. We for instance took time to realise that our models were too far from the constraint on the helium mass fraction measured by Galileo. It seems obvious now but at that time it was not. An important thing to mention is that we struggled to have a good agreement between our results and the ones from Militzer's group (him and Bill Hubbard). Even with the same hypotheses and parameters we still had some discrepancies. We hence made non-negligible efforts trying to understand the source of discrepancy.

Our first hypothesis, comparing density profiles of models, is that the slight discrepancies we were seeing on the calculated gravitational moments were due to a different treatment

of the core. Militzer provided us a model with $M_{\rm core} = 6\,M_\oplus$ and where the compact core is modelled by a single point with a density of $82\,{\rm g.cm^{-3}}$. In CEPAM, we treat the core using several layers. I implemented a core of constant density for the sake of comparison (CEPAM is usually using an empirical EOS to model the density in the core). I then ran models with four different values of density: 20, 30, 60 and $100\,{\rm g.cm^{-3}}$. A routine was also developed to fit the density profile in the envelope of Militzer's model. Figure 4.4 shows the comparison of the resulting density profiles in the region of the compact core. The deviations in terms of J_6 and J_4 are shown on Fig. 4.5. Our models using MGF16+MH13 are between 3 and 6 ppm from the J_4 value of Militzer's model with $M_{\rm core} = 6\,M_\oplus$ (top left corner) and between 0.4 and 0.7 ppm in J_6. When fitting the density profile of Militzer's model, we are closer (between 1 and 4 ppm in J_4 and between 0.1 and 0.4 ppm in J_6) but there is still a gap. We believe that the gap left is due to the treatment of the core that is different between CEPAM and the single layer of Militzer.

This is only when looking at a model with no compact core that we could find a good match between our results fitting Militzer's density profile and Militzer's model. We find an excellement agreement on J_4 and J_6 for this model. We hence believe that the deviations we were initially seeing are due to deviations in the density profile, especially between 0.01 and 1 Mbar. Actually, we initially believed that we were using the same EOS, as the one we were using (MGF16+MH13 but we used to simply call it MH13!) was derived by Miguel et al. [2016] from Militzer and Hubbard [2013]. We did not think that the slight deviations we see on the left panel of Fig. 4.5 could have a significant effect on the gravitational moments. But with the amazing accuracy on the gravitational moments now obtained with Juno, small deviations of the order of a few percents in the important region between 0.01 and a few Mbar are important and could explain the gap in this comparison. We thus finally solved the main discrepancy between our models and the ones of Militzer: it is due to the EOS that is actually slightly different. The comparison between the MGF16+MH13 EOS and the original MH13 EOS used by Militzer (that we then built from the best model of Militzer from Militzer et al. [2022] and called MH13*) was presented in Chapter 3 and can be seen again on Fig. 4.5. We concluded from this comparison that the gravitational moments are very sensitive to the EOS. This motivated the work that will be presented in next chapter where we investigated interior models with several EOSs and also tried to take the uncertainty on the EOS into account.

4.3 Implementation of a dilute core

In the past few years, a new generation of interior models of Jupiter has emerged. Instead of the traditional 3-layer (see, e.g., Guillot [1999], Miguel et al. [2022]) representation (molecular hydrogen, metallic hydrogen, compact core), these new models exhibit a

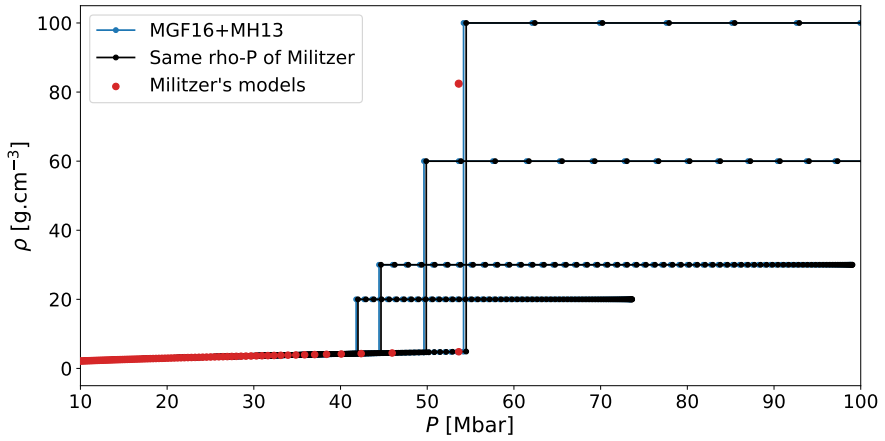

FIGURE 4.4: Comparison of density profiles in the region of the compact core. In red, a model from Militzer with $M_{\text{core}} = 6\,M_{\oplus}$ is shown. Our models are shown either in blue for which we use the MGF16+MH13 EOS or in black for which we fitted the density profile of Militzer's model instead of using our EOS.

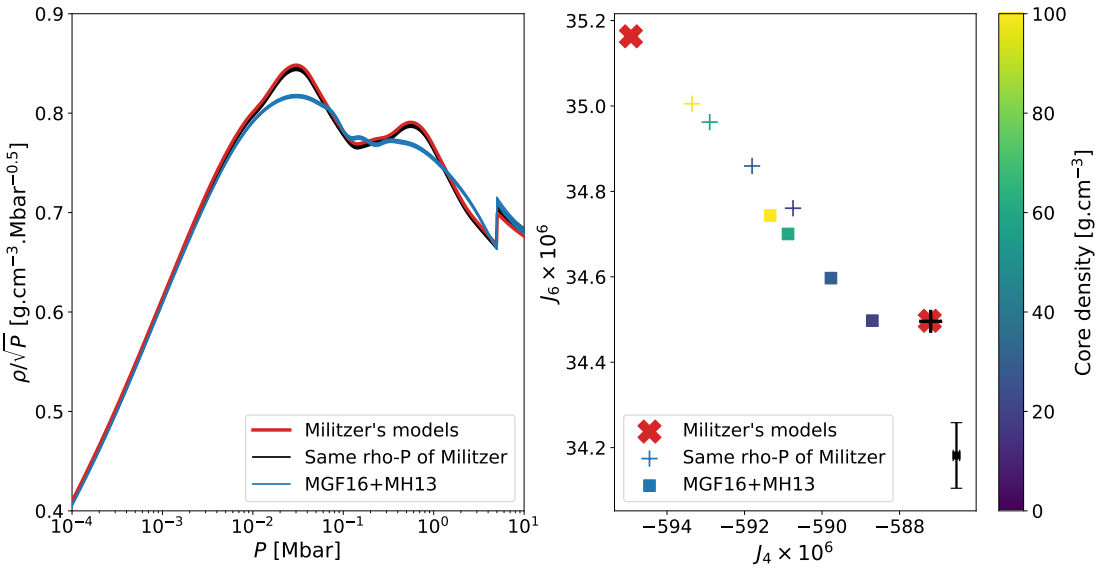

FIGURE 4.5: Comparison of models with the ones of Militzer. *Left panel.* Comparison of $\rho/\sqrt{P}$ as a function of pressure. *Right panel.* Gravitational moments J_6 and J_4 of different models. The red crosses show models of Militzer (with $M_{\text{core}} = 6\,M_{\oplus}$ in the top left corner and $M_{\text{core}} = 0$ for the other cross). The black errorbar shows the Juno measurement accounting for differential rotation.

fourth layer corresponding to a dilute core [Wahl et al., 2017]. In the latter models, heavy elements are gradually distributed from the inner compact core to the envelope of the planet. Hereafter, the envelope will refer to every region of Jupiter except the inner compact core only made of ices and rocks. A schematic comparing both types of models with their layers is shown on Fig. 4.6. Finest and more detailed schematics can be found in Miguel et al. [2022], Miguel and Vazan [2023]. CEPAM already included the possibility to run dilute core models [Guillot et al., 2018] but I implemented a more rigorous way to calculate this kind of models.

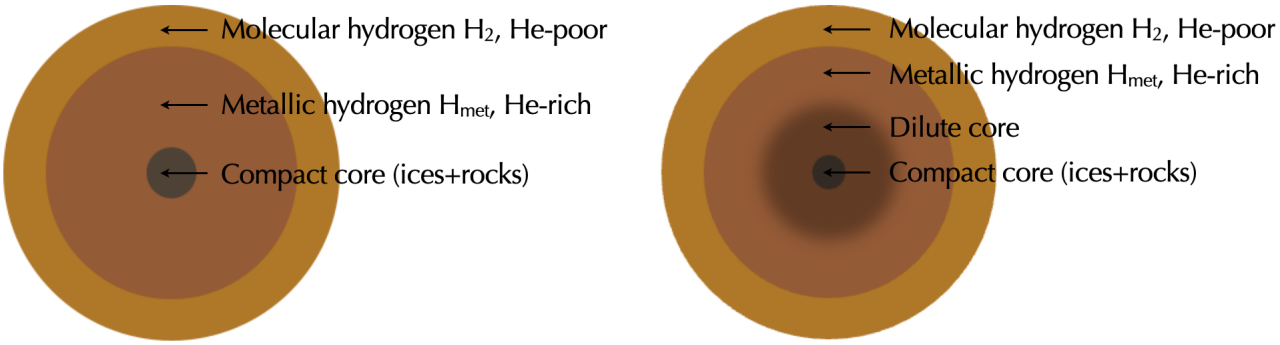

FIGURE 4.6: Schematic of a comparison of 3-layer and dilute core models.

Implementing this dilute core in the models requires to modify the expression of the heavy elements mass fraction Z. In a 3-layer model, $Z_{\mathrm{H_2}}$ and $Z_{H_{\mathrm{met}}}$ are the mass fractions of heavy elements respectively in the molecular hydrogen and the metallic hydrogen layers. In the compact core, this mass fraction of heavy elements is obviously equal to 1 since there is no hydrogen nor helium. In a 3-layer model, the expression of $Z(m)$ is hence given in Eq. 4.5, where m_{core} is the normalised mass of the compact core and m_{He} is the normalised mass at the location of the He phase separation. We have seen in Chapter 3 that the transition from molecular to metallic hydrogen and the He phase separation are two phenomena that occur probably around the same region.

$$Z(m) = \begin{cases} Z_1 = Z_{\mathrm{H_2}} & \text{if } m_{\mathrm{He}} < m < 1 \text{ (region 1)} \\ Z_2 = Z_{\mathrm{H_{met}}} & \text{if } m_{\mathrm{core}} < m < m_{\mathrm{He}} \text{ (region 2)} \\ 1 & \text{if } 0 < m < m_{\mathrm{core}} \end{cases} \tag{4.5}$$

With a dilute core, the expression of $Z(m)$ is given in Eq. 4.6. Z_{dilute} is the maximum mass fraction of heavy elements in the dilute core region, m_{dilute} controls the extent of the dilute core in terms of mass (it corresponds to half of the decay point in the error function) and δm_{dil} is a parameter controlling how steep is the heavy elements gradient.

$$Z(m) = \begin{cases} Z_1 = Z_{\mathrm{H_2}} & \text{if } m_{\mathrm{He}} < m < 1 \text{ (region 1)} \\ Z_2 = Z_{\mathrm{H_{met}}} + \frac{Z_{\mathrm{dilute}} - Z_{\mathrm{H_{met}}}}{2} \left[1 - \mathrm{erf}\left(\frac{m - m_{\mathrm{dilute}}}{\delta m_{\mathrm{dil}}}\right)\right] & \text{if } m_{\mathrm{core}} < m < m_{\mathrm{He}} \text{ (region 2)} \\ 1 & \text{if } 0 < m < m_{\mathrm{core}} \end{cases} \tag{4.6}$$

With this new expression of Z in region 2, it is critical to adjust the value of the helium abundance in order to preserve a protosolar value of $\langle\frac{Y}{X+Y}\rangle = Y_{\text{proto}} = 0.277$ (see Subsection 2.1.4 in Chapter 2) overall in the envelope. Another constraint is the Galileo measurement of $Y_{\text{atm}} = \frac{Y_{\text{H}_2}}{X_{\text{H}_2}+Y_{\text{H}_2}} = 0.238$ [von Zahn et al., 1998]. For the sake of simplicity, let use the quantity $\frac{Y}{X}$ instead of $\frac{Y}{X+Y}$:

$$\alpha = \langle\frac{Y}{X}\rangle, \alpha_1 = \frac{Y_1}{X_1}, \alpha_2 = \frac{Y_2}{X_2} \tag{4.7}$$

It is then easy to retrieve the values of α and α_1 with the constraints :

$$\alpha = \frac{Y_{\text{proto}}}{1-Y_{\text{proto}}}, \alpha_1 = \frac{Y_{\text{atm}}}{1-Y_{\text{atm}}} \tag{4.8}$$

Furthermore, $X + Y + Z = 1$ must always be verified so that:

$$Y_i = \frac{\alpha_i}{1+\alpha_i}(1-Z_i), X_i = \frac{1}{1+\alpha_i}(1-Z_i), i = [1,2] \tag{4.9}$$

Then, to conserve an overall protosolar value of $\langle\frac{Y}{X+Y}\rangle$:

$$\alpha = \langle\frac{Y}{X}\rangle = \frac{\int Y dm}{\int X dm} = \frac{\frac{\alpha_1}{1+\alpha_1}\int(1-Z_1)dm + \frac{\alpha_2}{1+\alpha_2}\int(1-Z_2)dm}{\frac{1}{1+\alpha_1}\int(1-Z_1)dm + \frac{1}{1+\alpha_2}\int(1-Z_2)dm} \tag{4.10}$$

Let write :

$$\begin{aligned} m_{xy_1} &= \int_{m_{\text{He}}}^{1}(1-Z_1)dm \\ &= (1-Z_1)(1-m_{\text{He}}) \end{aligned} \tag{4.11}$$

$$\begin{aligned} m_{xy_2} &= \int_{m_{\text{core}}}^{m_{\text{He}}}(1-Z_2)dm \\ &= (1-Z_{\text{H}_{\text{met}}})(m_{\text{He}}-m_{\text{core}}) - \frac{Z_{\text{dilute}}-Z_{\text{H}_{\text{met}}}}{2}\left[(m_{\text{He}}-m_{\text{core}}) - \int_{m_{\text{core}}}^{m_{\text{He}}}\text{erf}\left(\frac{m-m_{\text{dilute}}}{\delta m_{\text{dil}}}\right)dm\right] \end{aligned} \tag{4.12}$$

It is then possible to express α_2 :

$$\alpha_2 = \frac{\alpha(1+\alpha_1)m_{xy_2} + (\alpha-\alpha_1)m_{xy_1}}{(1+\alpha_1)m_{xy_2} - (\alpha-\alpha_1)m_{xy_1}} \tag{4.13}$$

Finally, the helium abundance in region 2 can be calculated thanks to Eq. 4.9 now that the formula of α_2 is known. This has been implemented in CEPAM so that we have the possibility to calculate interior models with a dilute core, that still preserve the right helium-to-hydrogen ratio in the whole interior.

4.4 Summary

We found a good agreement between our models and those developed by another research group, when employing the same parameterization. Moreover, our recent advancements enable us to run dilute core models, which match better the gravity data from Juno according to recent models [Wahl et al., 2017, Debras and Chabrier, 2019]. The integration of an efficient statistical tool has been crucial in our research, as it allows us to explore a wide range of models within a reasonable timeframe. The use of CEPAM, calibrated with the accuracy of the CMS method, enables fast and reliable calculations. As a result, we now possess a robust foundation to calculate interior models of Jupiter.

Chapter 5

Interior models of Jupiter

Contents

Building upon the methodology presented in the previous chapter, our objective was to constrain the internal structure of Jupiter. This chapter starts with a quick recap on the formation and evolution of Jupiter. It is important to have these aspects in mind to establish the connection with interior models. Then, this chapter follows a relatively chronological order. It starts by presenting my contribution to Miguel et al. [2022], a work which is the result of a close collaboration with Yamila Miguel, Michaël Bazot and Tristan Guillot but also enriched by many fruitful discussions with the Interior Working Group (IWG) of the Juno team. I ran the MCMC simulations and provided the data to Yamila Miguel who led the paper. This paper was developed in parallel with the paper led by Burkhard Militzer [Militzer et al., 2022]. We believe that our paper is particularly noteworthy because it brings a statistical framework to the study of Jupiter's interior. Next, motivated by current uncertainties in the EOS, I focused on how we could account for these in interior models and within the MCMC approach. Meanwhile, we emphasised the importance of accounting for non-ideal mixing effects [Howard and Guillot, 2023]. It led to the publication of Howard et al. [2023] in which we (with several collaborators of the IWG) highlighted the uncertainties associated with the EOS and sought to assess the robustness of solutions linked to it. Our objective was to identify models that not only better satisfied the present-day constraints but also aligned with our understanding of the planet's formation and evolution. This chapter ends with an exploration of the hypothesis on an inverted Z gradient in Jupiter, as previously proposed by Debras and Chabrier [2019]. This investigation may offer insights that help reconcile models with the observed supersolar abundance of heavy elements in the atmosphere (see Fig. 2.7).

5.1 Brief recap on formation and evolution

I provide here a few very basics aspects about the formation and evolution of Jupiter to make the link with the presented interior models that will follow.

5.1.1 Formation

There are two main scenarios to explain how giant planets form: core accretion and disk instability (see Helled et al. [2014] for a review). Disk instablity leads to gravitational fragmentation in the disk and may explain the formation of massive planets. On the other hand, core accretion [Pollack et al., 1996] is seen as the standard scenario to explain the formation of solar system planets. It includes three phases. The first one is the formation of a pure heavy element core by accreting planetesimals (km-sized) or pebbles (cm-sized) [Lambrechts and Johansen, 2012, Johansen and Lambrechts, 2017]. The mass of this core was traditionally assumed to be about ten earth masses in giant planets. Then, the second phase consists in the beginning of accretion of gas while continuing to accumulate solids. A good understanding of the disk is important to understand the

properties of the accreted material on giant planets. The third phase is called runaway gas accretion, where the accretion of gas is rapid. The available gas in the disk will limit the supply to the planets. Heavy elements may be accreted after the whole dissipation of the gas, but only a limited amount [Matter et al., 2009]. Nonetheless, the internal structure may be more complex than a compact core surrounded by an envelope [Helled and Stevenson, 2017]. It could harbour an inner region where the heavy elements are gradually distributed outwards, leading to a composition gradient or dilute core. In the context of the presence of a dilute core, suggested by interior models, its formation could naturally happen when planetesimals or pebbles are simultaneously accreted with gas. Those solids would be dissolved before reaching the central pure heavy element core [Mordasini et al., 2006]. The initial structure of Jupiter is key to determine the evolution and final structure [Vazan et al., 2015, 2018, Müller et al., 2020]. But we need to keep in mind that how a planet like Jupiter formed may not result in a similar interior structure as we observe today. This is why evolution is crucial to consider in order to connect formation and interior models.

5.1.2 Evolution

The evolution of Jupiter is the key phase that links the formation and the present structure. It is important to establish a consistent connection between the formation, the evolution and the current internal structure of the planet. While formation is a process that lasts probably about a few Myr, evolution lasts a few Gyr. Timescales are different. During its evolution, Jupiter is expected to cool and contract. A complete description of a combined formation and evolution model of Jupiter, based on the core accretion scenario and in agreement with the present-day observed characteristics of the planet, can be found in Mordasini et al. [2012]. Recently, there has been renewed interest in a former idea [Stevenson, 1985] that there may be a composition gradient inside Jupiter. Such composition gradient could be primordial [Lozovsky et al., 2017, Helled and Stevenson, 2017]. But it could undergo significant changes as the planet evolves, especially due to convective mixing [Vazan et al., 2016]. Recently, it has been shown that maintaining an extended dilute core is hard as the composition gradient will be progressively eroded. Convection is then mixing efficiently, leading to an enriched and homogeneous outer envelope [Vazan et al., 2018, Müller et al., 2020].

The next sections in this chapter now focus on interior models, that are based essentially on the gravity data measured by Juno and do not include assumptions from the formation or evolution perspectives. We will compare the obtained results with these aspects.

5.2 An inhomogeneous envelope

This section corresponds to my contribution to Miguel et al. [2022]. As previously mentioned, this paper provides a bayesian analysis of interior models of Jupiter. The main goal of our paper was to assess the envelope's homogeneity by looking at the distribution of heavy elements.

In this section, Subsection 5.2.3, which discusses certain choices made in the model setup, was adapted from Howard et al. [2023]. Since both this paper and Miguel et al. [2022] share a similar parameterization and assumptions, it was appropriate to relocate this content here for convenience. Subsections 5.2.5, 5.2.6 and 5.2.8 have directly been taken from Miguel et al. [2022].

5.2.1 Introduction

The interior of Jupiter is important to study to understand its formation. A good comprehension of its present structure can provide hints and help distinguish between different formation pathways. With Juno, the presence of a dilute core inside Jupiter was suggested (see Wahl et al. [2017] and also Debras and Chabrier [2019]). However, these papers essentially proposed a selection of models that best represent the structure of Jupiter. Given the high number of parameters and assumptions made when building interior models, we have adopted a different approach to study Jupiter's interior. We use a MCMC (see Section 4.1) and explore a wide range of possible models. We hence investigate on the one hand conventional three-layer models and on the other hand dilute core models. In addition, we consider several state-of-the-art H-He EOS. Investigating the distribution of heavy elements in the interior and determining whether Jupiter's envelope is homogeneous or not may tell about how heavy elements were accreted, through planetesimals or pebbles.

5.2.2 Parameters of the models and choices of priors

Before presenting the results of this study, it is essential to provide the details of our numerical setup. This information will be relevant throughout the entire chapter as we have maintained nearly the same parameterization for various analyses. We use the MCMC method described in Section 4.1 and we hence need to define some priors. In this section, I provide a description of the parameters used in our interior models, as well as the priors we selected for our calculations. In the next section, I present some preliminary MCMC calculations that guided us in making these choices for the priors. Table 5.1 lists the parameters used in our models.

TABLE 5.1: List of parameters used in our interior models.

Parameter	Description
$M_{\rm core}$	Mass of the compact core
$P_{\rm He}$	Pressure at which He phase separation occurs
$T_{\rm 1bar}$	Temperature at 1 bar
$T_{\rm jump}$	Temperature increase over the He phase separation region
$Y_{\rm proto}$	Protosolar helium mixing ratio
$Y_{\rm atm}$	Helium mixing ratio in the atmosphere
$Z_1^{\rm ice}$	Mass fraction of ices in the molecular hydrogen region
$Z_1^{\rm rock}$	Mass fraction of rocks in the molecular hydrogen region
$Z_2^{\rm ice}$	Mass fraction of ices in the metallic hydrogen region
$Z_2^{\rm rock}$	Mass fraction of rocks in the metallic hydrogen region
$Z_{\rm dilute}^{\rm ice}$	Mass fraction of ices in the dilute core region (only for dilute core models)
$Z_{\rm dilute}^{\rm rock}$	Mass fraction of rocks in the dilute core region (only for dilute core models)
$m_{\rm dilute}$	Extent of the dilute core in terms of mass (only for dilute core models)
$\delta m_{\rm dil}$	Slope of the dilute core (only for dilute core models)

Tables 5.2 and 5.3 recap the priors used in Miguel et al. [2022], for both three-layer and dilute core models (see Fig. 4.6). A fixed value of 0.277 was used for $Y_{\rm proto}$. We used $\frac{Y_1}{X_1+Y_1} = 0.238$, consistent with Galileo and used a protosolar abundance of heavy elements [Lodders et al., 2009] in the atmosphere $Z_1 = 0.0153$ (ices only) (see Section 2.1.4 in Chapter 2). We also mention that an increase in entropy is allowed in the helium-demixing region by including a temperature jump $T_{\rm jump}$. An a posteriori examination of the models shows that this region is convectively stable for values of this parameter lower than approximately 2000 K. In Howard et al. [2023], which will be presented in Section 5.4, almost the same priors have been used, with only a few differences ($Z_1 = 0.02$) and focusing on dilute core models.

TABLE 5.2: Parameters explored in our MCMC calculations for three-layer models. The parameter is given in the first column, the corresponding distribution in the second, and the lower and upper bounds in the third and fourth. When relevant, the mean and the standard deviation of the truncated normal are given in columns five and six. **Taken from Miguel et al. [2022].**

Parameter	Distribution	Lower bound	Upper bound	μ	σ
$M_{\rm core}(M_\oplus)$	Uniform	0	0.075	–	–
$Z_2^{\rm rock}$	Uniform	0	0.5	–	–
$Z_2^{\rm ice}$	Uniform	0	0.5	–	–
$T_{\rm 1bar}$ (K)	Normal	135	215	165	4
$P_{\rm He}$ (Mbar)	Normal	0.8	9	3	0.5
$T_{\rm jump}$ (K)	Uniform	0	2000	–	–

TABLE 5.3: Same as Table 5.2 but for dilute core models. **Taken from Miguel et al. [2022].**

Parameter	Distribution	Lower bound	Upper bound	μ	σ
$M_{\rm core}(M_\oplus)$	Uniform	0	0.075	–	–
$Z^{\rm rock}_{\rm dilute}$	Uniform	0	0.5	–	–
$Z^{\rm ice}_{\rm dilute}$	Uniform	0	0.5	–	–
$m_{\rm dilute}$	Uniform	0	0.6	–	–
$T_{\rm 1bar}$ (K)	Normal	135	215	165	4
$P_{\rm He}$ (Mbar)	Normal	0.8	9	3	0.5
$T_{\rm jump}$ (K)	Uniform	0	2000	–	–

5.2.3 Justification of priors

In this section, we conducted preliminary MCMC calculations to shed light on the reasons behind specific choices we made regarding the priors on the parameters of our MCMC calculations. These calculations justify why we opted to fix $Y_{\rm proto}$ and $Y_{\rm atm}$.

The optimisation problem is characterised by two issues: (1) The constraints on Jupiter's gravitational moments are extremely tight, meaning that only a tiny fraction of the parameter space allows for successful models, and (2) the high density of recent H-He EOSs imply that in most cases, fitting only Jupiter's radius and J_2 value would require nonphysical negative Z_1 or core mass values. In practice, this means that some parameters can be led to values that are significantly offset from their prior.

To assess the influence of the priors, we ran four different simulations (using the MGF16+MH13 EOS) with our MCMC code and focus on three parameters: $Y_{\rm proto}$, $Y_{\rm atm}$, $T_{\rm 1bar}$ and two data: J_4, J_6. In the first run, we set all parameters to vary freely using a Gaussian prior (mean μ, standard deviation σ) centred on the value from observations. In the second, third, and fourth runs, we respectively fix one, two, and three of the aforementioned parameters. We note that the accuracy on the J_{2n} is clearly higher compared to that on the other parameters. σ/μ is equal to 0.01% and 0.2% for J_4 and J_6 (0.0002% for J_2), respectively, while it is equal to 2% for the three other parameters. Figure 5.1 shows the posterior distribution of $Y_{\rm proto}$, $Y_{\rm atm}$, $T_{\rm 1bar}$, J_4, and J_6 for the four different runs. When setting all parameters free, the MCMC code samples models well around the mean values of the J_{2n} measured by Juno (accounting for the influence of differentially rotating winds; see Miguel et al. [2022]). However, $Y_{\rm proto}$, $Y_{\rm atm}$, and $T_{\rm 1bar}$ are at 2σ or 3σ from the mean value of their respective prior. When fixing $Y_{\rm proto}$, the sampled values of J_6 are now at 1σ from the observed mean value and sampled values of $Y_{\rm atm}$ are at 7-8σ from Galileo's measurement. When fixing $Y_{\rm proto}$ and $Y_{\rm atm}$, the J_6 fit is slightly poorer than the previous run. However, $T_{\rm 1bar}$ has now a 4σ difference from the mean value of the prior. Finally, when fixing $Y_{\rm proto}$, $Y_{\rm atm}$, and $T_{\rm 1bar}$, J_4 differs by more than 20σ from Juno's measurement and J_6 differs by 5σ.

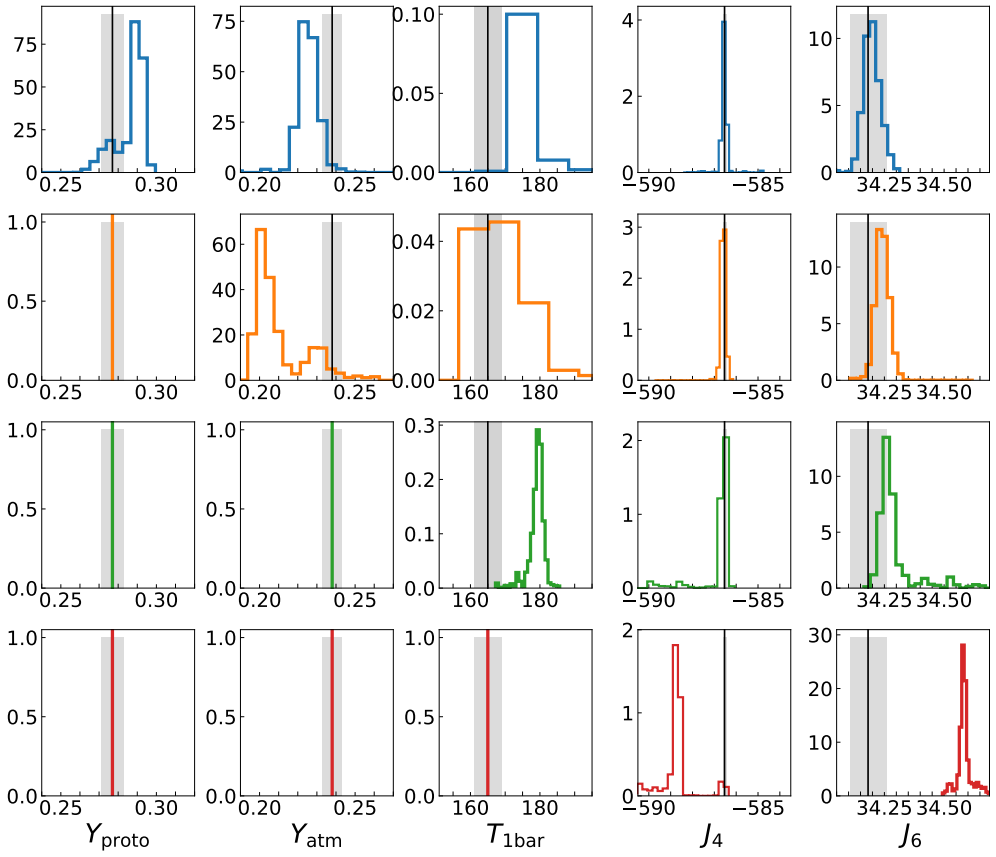

FIGURE 5.1: Posterior distributions of Y_{proto}, Y_{atm}, T_{1bar}, J_4, and J_6 for four different MCMC runs using the MGF16+MH13 EOS. The blue histograms correspond to a run where the four parameters are free. In the orange run, Y_{proto} is fixed. In the green run, Y_{proto} and Y_{atm} are fixed. In the red run, Y_{proto}, Y_{atm}, and T_{1bar} are fixed. When histograms show a black vertical solid line, this indicates that a prior was set and was centred at the value from observations ($Y_{proto} = 0.277 \pm 0.006$, $Y_{atm} = 0.238 \pm 0.005$, $T_{1bar} = 165 \pm 4$ K, $J_4.10^6 = -586.53 \pm 0.0836$ and $J_6.10^6 = 34.18 \pm 0.07682$). The gray areas correspond to the standard deviation of the prior (1 sigma). **Taken from Howard et al. [2023].**

This shows that to satisfy the observational constraints on parameters such as Y_{proto} and Y_{atm}, we need to fix them instead of using a Gaussian prior, because the uncertainties on the gravitational moments dominate. Otherwise, these parameters will be further than 1σ from the observed value. As the observational constraint is looser on T_{1bar} because of the question of latitudinal dependency —which raises the possibility that Jupiter's deep temperature may be higher than the Galileo probe reference value (see Section 2.1.4 in Chapter 2)—, only T_{1bar} will be set as a free parameter in some of the runs presented.

5.2.4 Gravitational moments

Figure 5.2 shows the equatorial radius and the gravitational moments of our models sampled by the MCMC code. For both dilute core and three-layer models, we obtain solutions that match R_{eq} and J_2. Our solutions nicely match J_4 and J_6 except for a

few dilute core models which are within the 2σ range of the observed J_6. While all our models reproduce J_8, their value of J_{10} is at the edge of the 1σ errorbar. We note that the outer metallicity is set to $Z_1 = 0.0153$ ($1 \times$ the protosolar value). More details about the heavy elements distribution will be discussed in the further sections. The corner plots in Appendix B show the posterior distribution of all the parameters in these models.

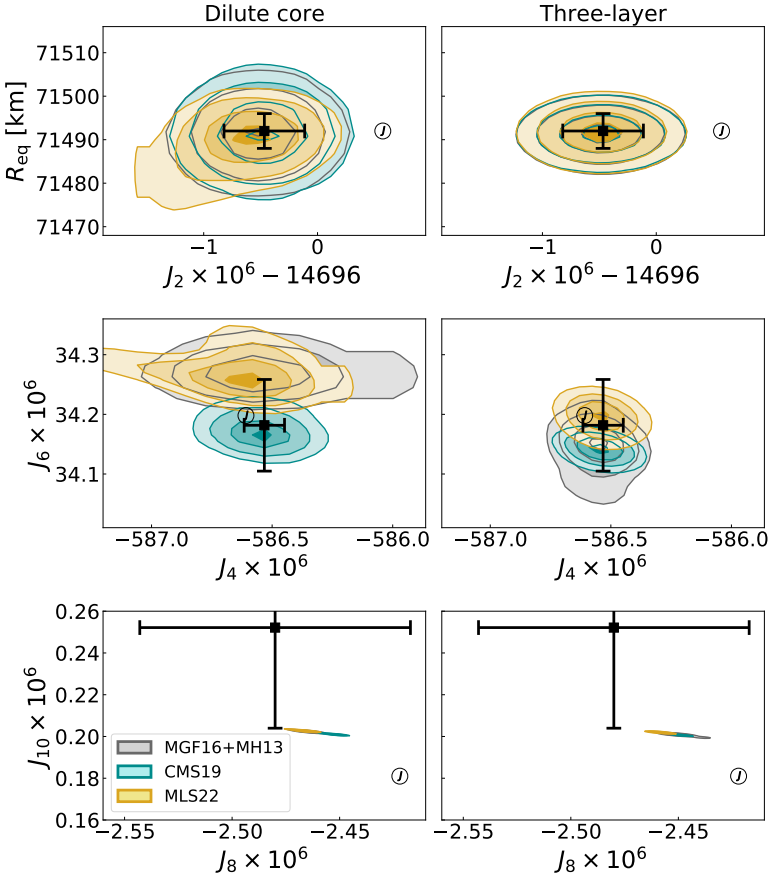

FIGURE 5.2: Equatorial radius and gravitational moments for dilute core and three-layer models, obtained for three different H-He EOSs, MGF16+MH13, CMS19 and MLS22, respectively (see text). *Left panels.* Dilute core models. *Right panels.* Three-layer models. Both types of models use $Z_1 = 0.0153$ (protosolar). The circles with a J correspond to the measurements of the gravitational moments by Juno [Durante et al., 2020]. The black error bars correspond to the gravitational moments corrected by differential rotation (see Subsection 2.5.3 in Chapter 2).

5.2.5 Distribution of the heavy elements

We recall that the structure of dilute core and three-layer models are explained in Chapter 4. When analysing the distribution of heavy elements in the envelope, we considered the envelope to consist of H_2- and $H_{metallic}$- layers for the three-layer models and to consist of H_2- and $H_{metallic}$- dominated layers and dilute core for the dilute core models. We calculated a quantity called ΔZ to assess the inhomogeneity of Jupiter's envelope.

This quantity is defined as $\Delta Z = Z_{\rm dilute} - Z_1$ (i.e. the difference in heavy elements between the H_2- dominated layer and the dilute core region) for dilute core models while it is defined as $\Delta Z = Z_2 - Z_1$ (i.e. the difference in heavy elements between the H_2- and $H_{\rm metallic}$- dominated layers) for three-layer models. A value of ΔZ equal to 0 would indicate a homogeneous envelope. Figure 5.3 shows ΔZ for both type of models. For three-layer solutions, we find that ΔZ is larger than zero for all models calculated with the MGF16+MH13 and MLS22 EOSs. For the CMS19 EOS, we find that the probability of finding models with $\Delta Z > 0$ is 97.6%. Concerning dilute core models, we obtain all models with ΔZ larger than zero, independently of the EOS. Our results robustly demonstrate that Jupiter's envelope is not homogeneous: the external layer of the envelope is depleted of heavy elements compared to the inner part of the envelope. This result is independent of both the models adopted for the interior of the planet and the EOS used. We note, however, that different EOSs lead to different distributions of the heavy elements in the interior of the planet.

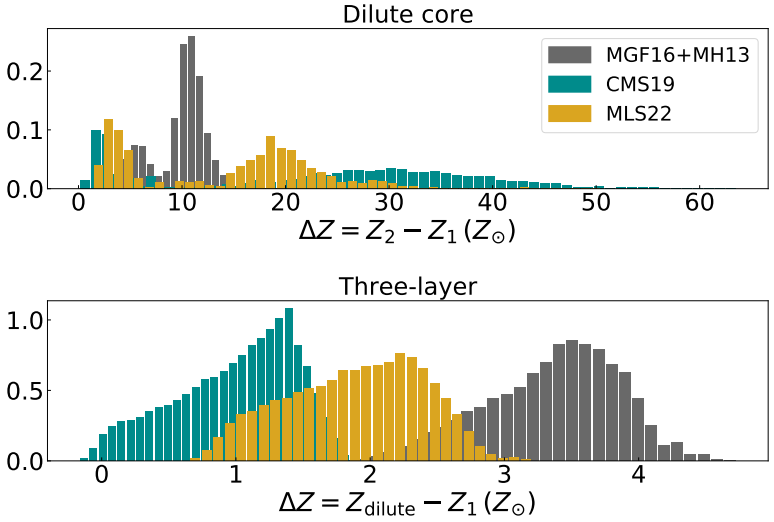

FIGURE 5.3: Histograms of ΔZ for both dilute core and three-layer models. This quantity assesses the inhomogeneity of Jupiter's envelope. Different colours show models calculated with different EOSs. **Adapted from Miguel et al. [2022].**

An analysis of the mass of heavy elements in the different layers for a random sample of 1000 of our models is shown in Figure 5.4. We see that the total mass of heavy elements ($M_{Z_{\rm total}}$) varies between 11 and 30 $M_\oplus$, with differences resulting from the choice of the EOS. Calculations done with the MGF16+MH13 EOS have $18 < M_{Z_{\rm total}} < 30\ M_\oplus$, models with MLS22 have $14 < M_{Z_{\rm total}} < 24\ M_\oplus$ and models with CMS19 have $11 < M_{Z_{\rm total}} < 18\ M_\oplus$, independently of the model of Jupiter adopted (three-layer or dilute core). For the three-layer models, the differences mostly arise from discrepancies of the mass of heavy elements in the $H_{\rm metallic}$-dominated region (M_{Z_2}) that varies between 2 and 23 $M_\oplus$, depending on the EOS. For models with a dilute core, the differences are mostly due to differences in the mass of heavy elements in the dilute core region ($M_{Z_{\rm dilute}}$), that is found to vary between 1 and 25 $M_\oplus$, depending on the EOS adopted

in the calculation. The mass of heavy elements in the H_2-dominated region (M_{Z_1}) is quite similar for models with different EOSs, independently on the model adopted for Jupiter. This is expected given the prior used to match the observational constraints from the Juno and Galileo missions. Regarding the inner core, we find that it varies between 0 and 7 $M_\oplus$ for all models, with its exact value depending on the model adopted for Jupiter's interior. The three-layer models have $M_{\rm core} \simeq 6\ M_\oplus$, independently on the EOS adopted. Conversely, we see two groups of solutions for models with a dilute core: a group with inner core masses between 3 and 6 $M_\oplus$, and another group with small masses up to 2 $M_\oplus$.

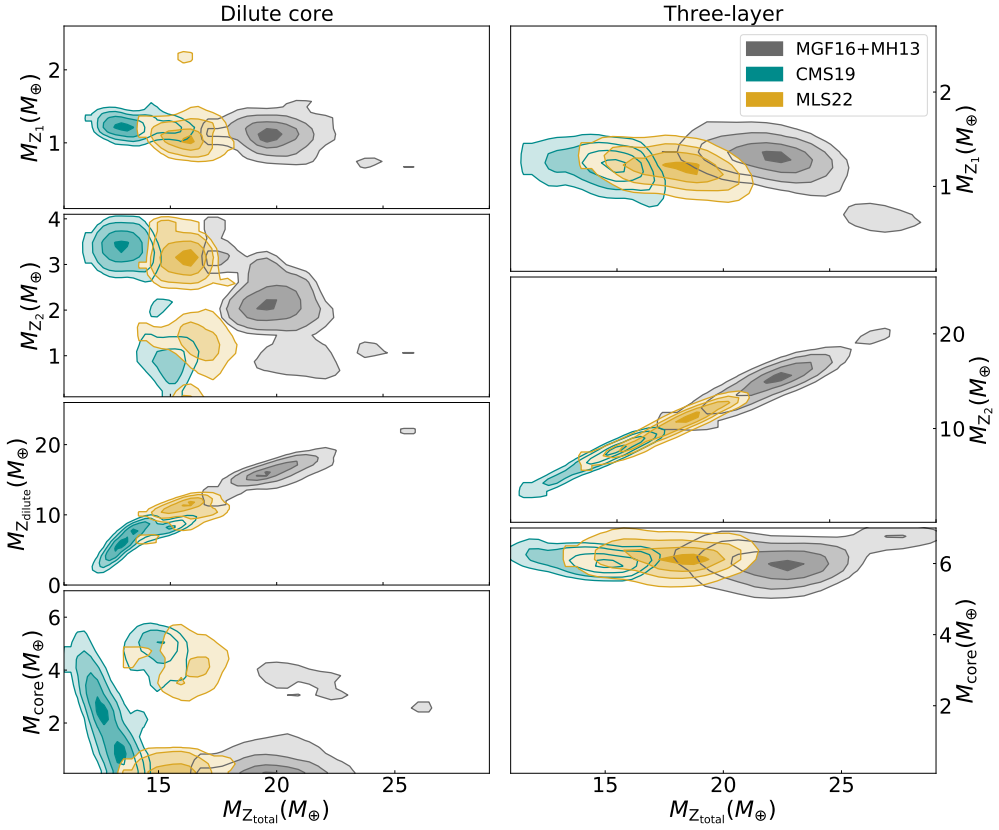

FIGURE 5.4: Mass of heavy elements in the different layers as a function of the total mass of heavy elements in Jupiter for a random sample of 1000 models extracted from our three-layer models (*right panels*) and dilute core models (*left panels*). Left panels indicate (from top to bottom) the mass of heavy elements in the H_2- dominated, $H_{metallic}$- dominated, dilute core and inner core regions, respectively. Right panels indicate (from top to bottom) the mass of heavy elements in the H_2- dominated, $H_{metallic}$- dominated and inner core regions, respectively. **Taken from Miguel et al. [2022].**

In comparison, dilute core models from Wahl et al. [2017], who, using the original MH13 EOS, found a value of $M_{\rm core} + M_{\rm dilute}$ ($M_{\rm dilute}$ being the total mass in the dilute core region) between 10 and 24 $M_\oplus$ and $M_{Z_{\rm total}}$ of 24-27 $M_\oplus$. These results are consistent with our results, even though most of them have sub-solar atmospheric metallicities. Ni [2019] performed four-layer models using the MH13 and CMS19 EOSs. They found a range of $M_{\rm core}$+$M_{\rm dilute}$ of 6.5-27 $M_\oplus$ and $M_{Z_{\rm total}}$ of 24-28 $M_\oplus$ with MH13 and $M_{\rm core}$+$M_{\rm dilute}$ of

3-12 $M_\oplus$ and $M_{Z_{\text{total}}}$ of 8-12 $M_\oplus$ with CMS19. For both EOSs, the results are in good qualitative agreement with ours, even though, in this case again, their optimisation led to sub-solar atmospheric metallicities as opposed to our results where $Z_1 = 1 \times Z_{\text{solar}}$. Debras and Chabrier [2019] imposed the constraint of a minimum atmospheric metallicity of $Z = 0.02$. They found that in order to fit this and all other constraints using the CMS19 EOS, an inward-decrease of the abundance of heavy elements between the H_2- and H_{metallic}-dominated regions was required. We also find these type of solutions when using the CMS19 EOS and three-layer models (Fig 5.3), but since they represent 2.4% of our sample we find this unlikely. The $M_{Z_{\text{total}}}$ found by Debras and Chabrier [2019] are of 25-30 and 40-45 $M_\oplus$ for models without and with inner core, respectively. Our results with CMS19 always led to considerably smaller values. A similar discrepancy with the Debras and Chabrier [2019] study is found by Nettelmann et al. [2021]. Nettelmann et al. [2021] used CMS19 and dilute core models. They found M_{core} of up to 3.8 $M_\oplus$ and $M_{Z_{\text{total}}}$ up to 13 $M_\oplus$, comparable to our results. We note that in Nettelmann et al. [2021] the authors calculate the gravitational harmonics using an expansion of the ToF of seventh order, different from the method used here (Section 2.5). In summary, we have performed a large exploration of the parameter space and we find that our results include most other individual models presented in other works.

5.2.6 A hotter interior than expected

Figure 5.5 shows that our models tend to have temperatures at 1 bar going from ∼169 to ∼188 K for the three-layer models to values between ∼165 and ∼182 K for the dilute core models, depending on the EOS adopted. While these values are high compared to observations by the Galileo probe (166.1 K, Seiff et al. [1998]), it is not clear whether those in situ measurements represent the typical 1 bar temperature on Jupiter because of latitudinal variability, which may exist to a limited extent [Fletcher et al., 2020b]. Furthermore, a reassessment of the Galileo probe data led to an increase of the temperature of ≃4 K [Gupta et al., 2022] and, additionally, the possibility of superadiabaticity in the interior [Leconte et al., 2017, Guillot et al., 2020] could yield a deep entropy corresponding to a temperature a few degrees higher than the measured value at 1 bar. More details can be found in Subsection 2.1.4 of Chapter 2. In all cases dilute core models have temperatures more in agreement with the expectations given the values observed and the uncertainties in this parameter. Regarding the separation pressure for the immiscibility of helium in hydrogen, our values are always close between 2 and 4 Mbar , that are in agreement with the higher limit of numerical calculations [Morales et al., 2013, Schöttler and Redmer, 2018b] and more in agreement with recent laboratory experiments estimations [Brygoo et al., 2021]. Nettelmann et al. [2021] also find that higher temperatures at 1 bar help in reaching higher metallicities in the atmosphere. Their models have separation pressures between the H_2- and H_{metallic}-dominated regions close to 6 Mbar while our models use separation pressures around 3 Mbar.

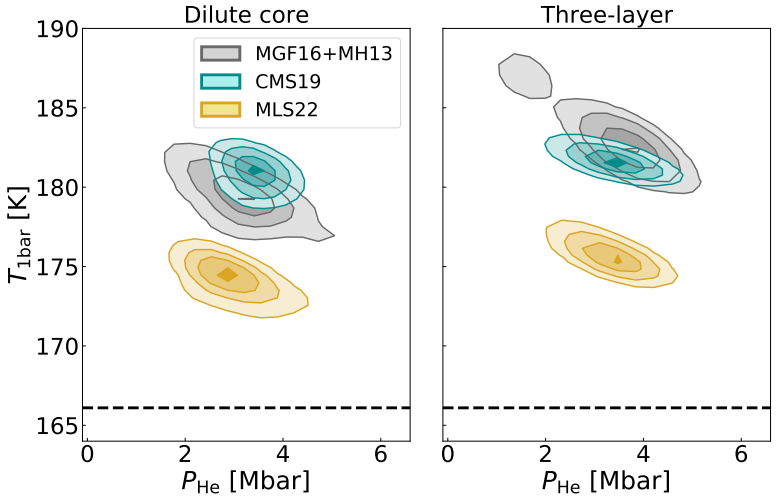

FIGURE 5.5: Temperature at 1 bar vs. helium transition pressures for both dilute core and three-layer models. The black dotted line corresponds to the 1 bar temperature measured by the Galileo probe.

5.2.7 On the importance of a dilute core

A legitimate questioning is if a type (three-layer or dilute core) of model is preferred. A first important difference in our models is that three-layer models have a discontinuity in Z at the location of helium rain ($Z_1 \neq Z_2$) while dilute core models do not have it ($Z_1 = Z_2$). We arbitrarily chose that feature in dilute core models. But because helium rain appears late (after 4 Gyr) in Jupiter's evolution [Mankovich and Fortney, 2020], it is unlikely that a very strong change in composition exists in that region. Our dilute core models hence seem more realistic. Another thinking is that three-layer models can be seen as a particular case of dilute core models where the dilute core extends all the way up to the helium rain region. Of course, this is without considering the thermal structure of the dilute core, its stratification and its entropy composition. Thus, we try to compare both types of model and to assess the preponderance dilute core. Figure 5.6 shows typical distributions of heavy elements in both types of model. We define two useful quantities, $M_{Z,dil*}$ and $M_{Z,env*}$ (detailed in the caption), in order to assess how predominant the dilute core is, but also to provide estimates of the amount of heavy elements that needs to be accreted onto the compact core during the formation of the planet. The name of $M_{Z,dil*}$ is counterintuitive for three-layer models but it is then more simple to show plots using the same quantity of interest.

We compare $M_{Z,dil*}$ for both types of model on Fig. 5.7. We first see that $M_{Z,dil*}$ is larger than zero for almost all models, consistent with an inhomogeneous envelope. We see again the dependence of the distribution of heavy elements to the EOS. $M_{Z,dil*}$ is found to be larger in dilute core models rather than three-layer models. While only one trend is observable for three-layer models, we see two trends for dilute core models. Among these two trends, the first one, with the highest $M_{Z,dil*}$ values, corresponds to

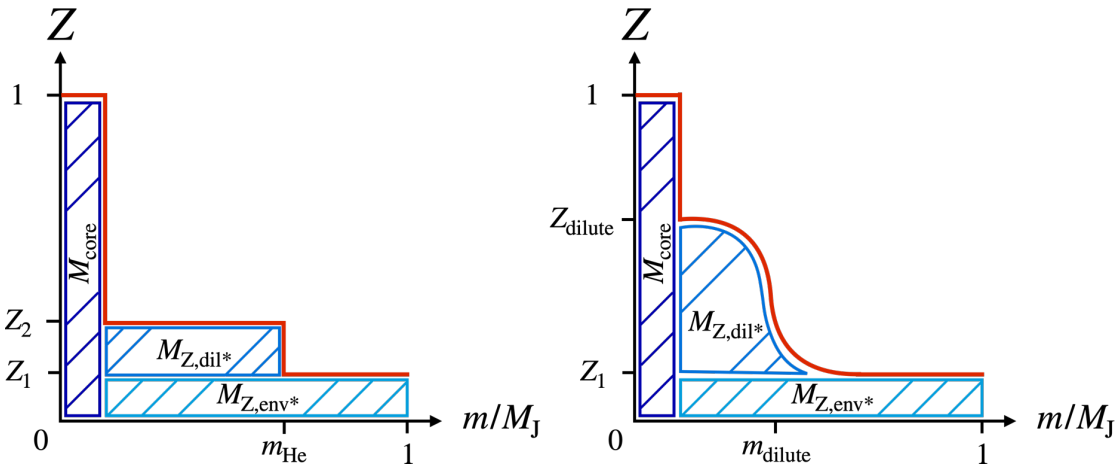

FIGURE 5.6: Distribution of heavy elements for a three-layer and a dilute core models. The three hashed areas correspond to the mass of the compact core $M_{\rm core}$ (only made of heavy elements), $M_{\rm Z,dil*}$ and $M_{\rm Z,env*}$. $M_{\rm Z,dil*}$ is either the mass of heavy elements in the dilute core region excluding the area where $Z < Z_1$ for dilute core models or the mass of heavy elements in the $\rm H_{metallic}$-dominated region excluding the area where $Z < Z_1$ for three-layer models. $M_{\rm Z,env*}$ is then the mass of heavy elements in the rest of the envelope in both cases. **Taken from Howard et al. [2023].**

models with almost no compact core ($M_{\rm core}$ mostly between 0 and 2 $M_\oplus$) and a dilute core which is not very extended ($m_{\rm dilute} < 0.3$ and $Z_{\rm dilute} > 0.15$). The second trend looks more similar to three-layer models. Indeed, these models have $M_{\rm Z,dil*}$ which is only slightly higher than the one of three-layer models. Besides, their compact core have a mass larger than 4 $M_\oplus$, closer to the 6 $M_\oplus$ of almost all three-layer models. Their dilute core is more extended ($m_{\rm dilute} > 0.3$ and $Z_{\rm dilute} < 0.15$), in line with three-layer models if we consider them as models with a dilute core that extends up to the helium rain region. The distinction between both types of model can hence be very thin. For comparison, calculations from Stevenson et al. [2022] propose models with a compact core of 4.5 to 6.2 $M_\oplus$ and a composition gradient extending to approximately 15% of Jupiter's mass. Yet, our results here propose either models with such compact core but with a much more extended dilute core or models with almost no compact core but with a less extended dilute core ($m_{\rm dilute} < 0.3$). We can already see that further work is required to reconcile formation and evolution models with interior models.

To assess the importance of the dilute core region, we compare the involved mass of heavy elements responsible for inhomogeneity ($M_{\rm Z,dil*}$) with the heavy element mass in the rest of the envelope ($M_{\rm Z,env*}$). Figure. 5.8 shows the comparison. $M_{\rm Z,env*}$ is actually almost constant because it is equal to $Z_1(1 - m_{\rm core})$. We see that the majority of our models have $M_{\rm Z,dil*}$ larger than $M_{\rm Z,env*}$, the ratio of the two quantities going up to 4. Moreover, we will see that the results using the CMS19 and MLS22 EOSs should be cautiously interpreted because they do not take mixing effects (see Subsection 3.5 in Chapter 3) into account. $M_{\rm Z,dil*}$ is thus non-negligible at all and this shows the importance of either the dilute core region or the $\rm H_{metallic}$-dominated region with a Z increase for three-layer models. However, considering only the gravity data, it is actually

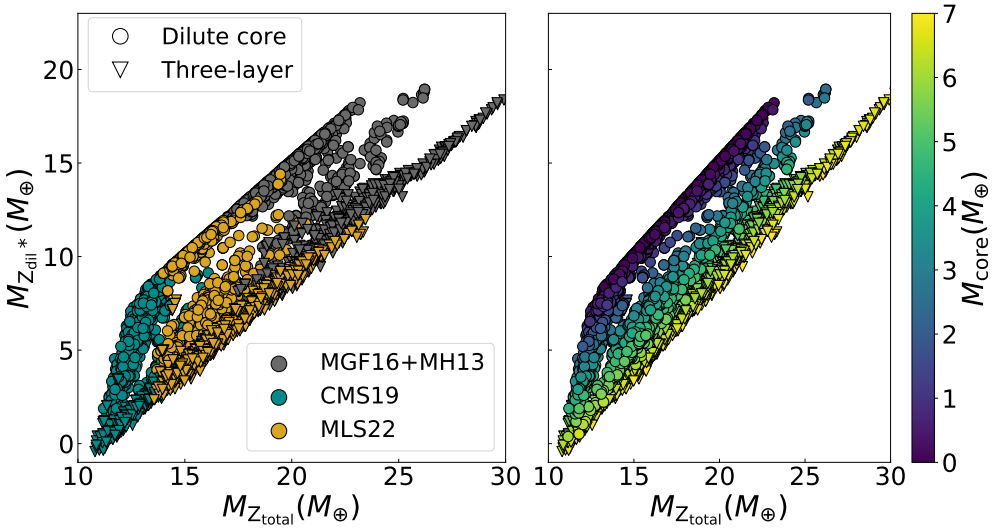

FIGURE 5.7: $M_{Z,dil*}$ (see Fig. 5.6) vs. the total mass of heavy elements, for three-layer and dilute core models, and for three different EOSs.

not easy to discriminate between both types of model. They both fit relatively well the gravitational moments and the differences on other parameters such as T_{1bar} or P_{He} are not big enough to favour one type of model. But again, we do not expect a discontinuity in the Z profile at the location of helium rain, something that is inherent to three-layer models. This is why we focused on models with a dilute core in Howard et al. [2023].

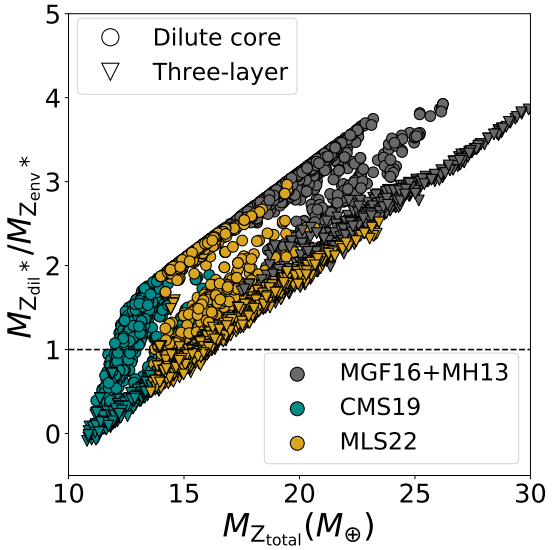

FIGURE 5.8: Ratio of $M_{Z,dil*}$ to $M_{Z,env*}$ (see Fig. 5.6) vs. the total mass of heavy elements, for three-layer and dilute core models, and for three different EOSs. The black dashed line indicates when $M_{Z,dil*} = M_{Z,env*}$

5.2.8 Conclusion

This study comprehensively reproduces observational constraints from the Juno measurements (the even and odd gravity harmonics and water abundance in the atmosphere), along with helium measurements from the Galileo probe, exploring different models for Jupiter's interior and considering all recent EOSs. We show that the gravity constraints point to a deep entropy of Jupiter that corresponds to a 1 bar temperature that is higher than traditionally assumed (i.e. 170–180 K rather than 166 K). We robustly demonstrate that the heavy-element abundance is not homogeneous in Jupiter's envelope. Our results imply that Jupiter continued to accrete heavy elements in large amounts while its hydrogen-helium envelope was growing, contrary to predictions based on the pebble-isolation mass in its simplest incarnation [Lambrechts and Johansen, 2012], favouring instead planetesimal-based or more complex hybrid models [Alibert et al., 2018]. Furthermore, the envelope did not mix completely during the planet's subsequent evolution, not even when Jupiter was young and hot [Vazan et al., 2018]. Our result clearly shows the need for further exploration of nonadiabatic interior models for the giant planets, and it provides a base example for exoplanets: a non-homogeneous envelope implies that the metallicity observed is a lower limit to the planet bulk metallicity. Therefore, metallicities inferred from remote atmospheric observations in exoplanets might not represent the bulk metallicity of the planet. Moreover, we demonstrate that knowledge of the EOS is crucial in determining the mass of heavy elements in the interior of Jupiter, and we put important constraints on Jupiter's inner core, which is found to be up to 7 $M_{\oplus}$, a result that is independent of the interior model and EOS adopted in the calculations.

5.3 Accounting for uncertainties on the equation of state

We have found interior models that fit the gravity data from Juno. However, these models rely on several assumptions. They exhibit an interior that is hotter than expected, regarding the constraints on $T_{1\text{bar}}$ from Galileo and Voyager. Moreover, the mass fraction of heavy elements in the outer envelope is only protosolar while atmospheric measurements suggest a supersolar metallicity. One of our main conclusions is that Jupiter's envelope must be inhomogeneous but we also highlighted how crucial the H-He EOS is for inferring the internal structure of the planet. Uncertainty on the H-He EOS exists (see Section 3.6). Investigating if our lack of knowledge on the EOS is the source of the difficulty to satisfy all observational constraints appears as a promising path of research. The importance of the EOS for Jupiter's interior models had already shown to be of paramount importance [Guillot et al., 1997, Saumon and Guillot, 2004, Miguel et al., 2016] but studies so far used different EOS tables without accounting for intrinsic uncertainties within these EOSs. With the high accuracy of Juno's measurements of the gravitational moments, it is now even more important to employ an accurate EOS to properly infer the internal structure of Jupiter. Missing for instance H-He interactions and not including mixing effects in the EOS can lead to an incorrect determination of the internal composition, as we showed in Howard and Guillot [2023] (see Subsection 3.5 in Chapter 3). We must stress that models presented in Miguel et al. [2022] (also in [Ni, 2019, Nettelmann et al., 2021]) and using the CMS19 or MLS22 EOSs actually do not account for these interactions. In this subsection, we look at how we can include the uncertainty on the H-He EOS in our interior model calculations and from now on, we will only focus on EOSs that take mixing effects into account.

Subsections 5.3.2, 5.3.3 and 5.3.4 are directly taken from Howard et al. [2023] and correspond to the sections 3.3, 3.4 and 4.2 of the latter paper.

5.3.1 An unconstrained modification of the equation of state

In order to account for the uncertainty on the EOS, we want to allow for small modifications of the EOS in our routine. We thus need to implement a way to modify or perturb an EOS when we calculate interior models with CEPAM and then need to include that in our MCMC.

We want to modify an EOS by using an appropriate function so that:

$$\rho_{\text{modif}} = \rho + \delta\rho = \rho(1 + f). \tag{5.1}$$

A simple way to perturb an EOS is to use a Gaussian function, that we define as:

$$f = d\rho \times \exp\left(-\left[\frac{\log_{10}(\mathrm{P}/\mathrm{P}_{\mathrm{modif}})}{\Delta P}\right]^2\right), \tag{5.2}$$

where P_{modif} corresponds to the pressure (in cgs units) at which the density modification is applied, ΔP controls the width of the modification; and $d\rho$ is the amplitude of the density change.

I stress that we here freely modify the EOS. Our only constraints come from the assumed priors on P_{modif}, ΔP and $d\rho$. We do not detail more the chosen priors on these parameters. We will see in the next subsection that we should actually consider a constraint on how we perturb an EOS. The EOS calculations (see Subsection 3.1.2) actually rely on the free energy or a related quantity. The latter must overall be conserved. We in fact have a quite good understanding of the low pressure and high pressure regimes but this is really in the intermediate regime that uncertainties exist most (due to strong interactions between particles in different states). Typically, a reduction of density in this intermediate regime will hence need to be compensated by an increase of density at some point, so that the overall free energy is consistent with the EOS calculations. More details will be discussed in the next subsection. And the chosen priors will also be presented at this stage.

We here quickly present the results we obtained running MCMC runs we this "unconstrained" way to modify the EOS. Figure 5.9 shows, for three-layer and dilute core models, the obtained modified adiabats for a subsample of 100 models extracted from our MCMC calculations. These models nicely match the gravitational moments (see Appendix C). For three-layer models, a density reduction mostly located around 0.3 Mbar is obtained while for dilute core models, a density reduction mostly located around 0.06 Mbar is obtained. The amplitude of this density reduction reaches at most 6%, which is probably of the order of magnitude of the current uncertainty on the EOS. Thus, these results are satisfying and do not require a warmer deep interior as presented in Section 5.2. However, we stress that the heavy element abundance in the outer envelope is only protosolar here and a more important (may be too significant) perturbation of the density profile may be required to fit the measured gravitational moments if we consider supersolar abundances of heavy elements. We present in the next subsection a more rigorous method to modify the EOS.

5.3.2 A thermodynamically consistent modification of the equation of state

With the uncertainty on the EOSs in hand, we want to account for it in our interior models. To do so, we need a function perturbing an EOS. Initially, we simply used a

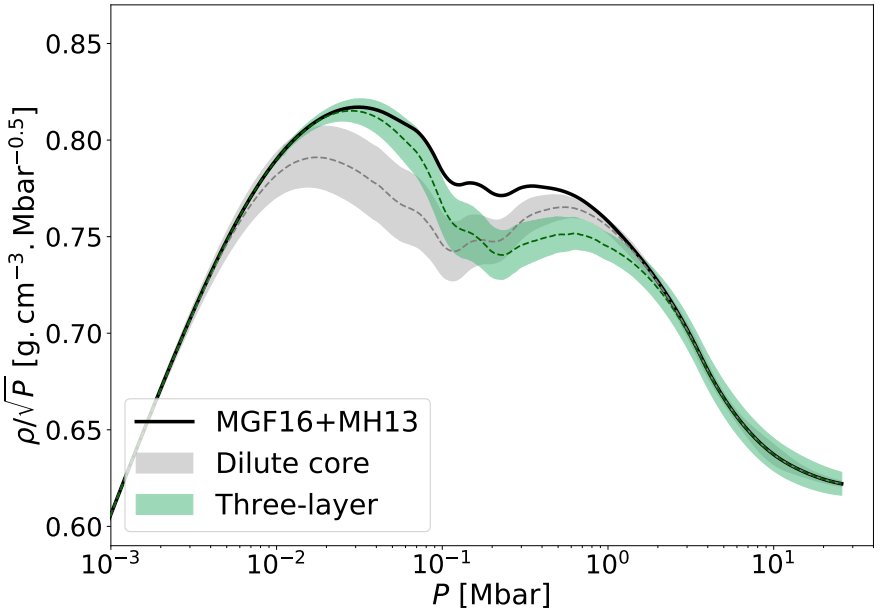

FIGURE 5.9: Adiabats obtained for models with an unconstrained modification of the EOS. The black solid line corresponds to the original MGF16+MH13 EOS. Green shows results obtained with three-layer models. Grey shows results obtained with dilute core models. The dashed lines correspond to the adiabat obtained with the mean values of $P_{\rm modif}$, ΔP, and $d\rho$ of a subsample of 100 models randomly drawn from the MCMC output. We compute the standard deviation (σ) of the 100 adiabats and the envelopes show the adiabats of the 1 σ spread from the mean modified adiabat (dashed line). Here, $T_{\rm 1bar}$ is fixed at 166.1 K.

Gaussian function to perturb the density profile of our models (similarly to Nettelmann et al. [2021]). Nonetheless, an EOS cannot be perturbed freely. Indeed, any variations of the EOS should satisfy the limits of a thermodynamical potential. The Helmholtz free energy, which is usually where an EOS comes from, is relatively well known at low and high density regimes. Low densities correspond to the regime of an ideal gas and the free energy is known from experimental data and statistical mechanics. High densities correspond to the regime well above the metallisation pressure where hydrogen is fully ionised and the free energy here is known from theory and simulations. Here, we use the internal energy because $P = -\left(\frac{dU}{dV}\right)_S$ can lead to an integral constraint on legitimate density changes of the EOS. If we know the internal energy at low and high regimes for a given entropy, that is, $U(\rho_1, S)$ and $U(\rho_2, S)$, respectively, we can obtain an expression of the differences between these two terms, which is to be conserved by perturbations along the adiabat:

$$\Delta U = U(\rho_2, S) - U(\rho_1, S) = \int_{\rho_1}^{\rho_2} \frac{P}{\rho^2} d\rho. \tag{5.3}$$

If $\delta\rho$ corresponds to a slight density modification, then we have

$$\Delta U_{\text{modif. EOS}} - \Delta U_{\text{orig. EOS}} = \int_{\rho_1}^{\rho_2} \frac{P}{(\rho+\delta\rho)^2} d\rho - \int_{\rho_1}^{\rho_2} \frac{P}{\rho^2} d\rho, \tag{5.4}$$

Using the approximation $P \propto \rho^2$, we then get

$$\Delta U_{\text{modif. EOS}} - \Delta U_{\text{orig. EOS}} \propto \int_{\rho_1}^{\rho_2} \frac{\delta\rho}{\rho} d\rho = 0. \tag{5.5}$$

This difference must be 0 if ΔU in Eq. (5.3) is to be conserved. Equation (5.5) provides a constraint on how we are allowed to perturb an EOS. Hence, we need to choose an appropriate function to perturb the EOS while verifying this constraint. This function, denoted f here, comes from the equation

$$\rho_{\text{modif}} = \rho + \delta\rho = \rho(1 + f). \tag{5.6}$$

Therefore, we need to find f so that

$$\int_{\rho_1}^{\rho_2} f d\rho = 0. \tag{5.7}$$

Using again $P \propto \rho^2$ and changing variables, we need to choose an f that satisfies

$$\int_{P_1}^{P_2} f(\log_{10}(\mathrm{P}))\sqrt{\mathrm{P}}\mathrm{d}\log_{10}(\mathrm{P}) = 0. \tag{5.8}$$

We naturally define f as

$$f = K\frac{d\rho}{\sqrt{P}} \exp\left(-\left[\frac{\log_{10}(\mathrm{P}/\mathrm{P}_{\text{modif}})}{\Delta P}\right]^2\right) \operatorname{erf}\left(\frac{\log_{10}(\mathrm{P}/\mathrm{P}_{\text{modif}})}{\Delta \mathrm{P}}\right). \tag{5.9}$$

The function f is composed of a Gaussian and an error function, and includes a division by the square root of the pressure, with $d\rho$ being the amplitude of the density modification. From Eq. (5.5), we infer that to satisfy this integral constraint, a density reduction at a certain pressure will imply a density increase at another pressure. To modify an EOS and obtain this trend, we use the product of a Gaussian and an error function. And to properly satisfy the integral constraint from Eq. (5.5) after changing the integral as a function of the density into an integral as a function of $\log_{10}(\mathrm{P})$, we need to multiply by the square root of the pressure. This function depends on three parameters: P_{modif} corresponds to the pressure (in cgs units) at which the density modification is applied, ΔP controls the width of the modification; and $d\rho$ is the amplitude of the density change. The constant K is in units of square root of pressure divided by density and is set to $K = 1.04 \times 10^6$ $\sqrt{\text{dyn.cm}^{-2}}.\text{g}^{-1}.\text{cm}^3$. Figure 5.10 shows how the integral constraint from Eq. (5.5) is satisfied for two different models. One model simply uses a Gaussian function to modify the density profile and clearly does not respect the integral constraint. On the other hand, the second model, which uses the function f defined above, satisfies this constraint well, because the ΔU difference falls close to zero at high pressures. More precisely, this value at high pressures is not exactly zero due to the perturbation theory approximation applied to Eq. (5.4) where $\delta\rho/\rho$ is assumed

small. But overall, there is a significant difference between how the integral constraint is respected between the two models of Figure 5.10, and the effort of satisfying this constraint must be underlined. We stress that our function f was naturally but arbitrarily chosen; there are certainly other functions that could satisfy Eq. (5.5).

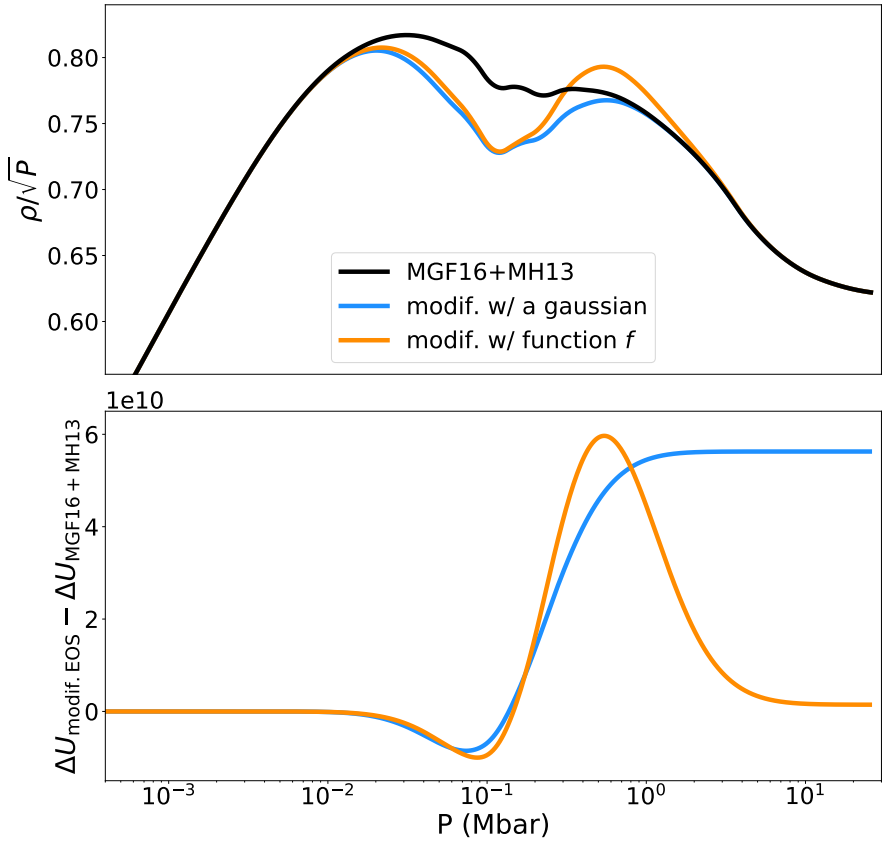

FIGURE 5.10: Comparisons of the ΔU difference for a model modified with only a Gaussian function (blue) and a model modified with the defined function f (see Eq. (5.9)) composed of a Gaussian and an error function (orange). *Top panel.* Comparison of the adiabats ($P_{\text{modif}} = 10^{11}$ dyn.cm^{-2}, ΔP=0.5, $d\rho$=-0.06 for the blue curve & $P_{\text{modif}} = 10^{11.5}$ dyn.cm^{-2}, ΔP=0.6, $d\rho$=-0.05). *Bottom panel.* Difference between the ΔU of the modified models and that of the reference model (MGF16+MH13). **Taken from Howard et al. [2023].**

5.3.3 Priors on the modification of the EOS

For MCMC runs in which we allow modifications of the EOS, we use priors on $d\rho$, P_{modif}, and ΔP, as defined in Eq. (5.9). The priors are either Gaussian or uniform (a more detailed discussion can be found in Section 5.3.4) with boundaries set to avoid physically inconsistent modifications. We set P_{modif} between $10^{11.5}$ and $10^{12.5}$ dyn.cm^{-2} (which correspond to 0.3 and 3 Mbar, respectively), as a preliminary study shows us that a density reduction followed by an increase in the density at higher pressure is preferred over a density increase followed by a decrease. We set ΔP between 0.2 and 0.8 so that low ($< 10^{-2}$ Mbar) and high (> 10 Mbar) pressures are not significantly affected by

the density modification. Allowing P_{modif} and ΔP to surpass the specified boundaries would allow modifications of the EOS that are not consistent with the constraints. The boundaries of $d\rho$ are set to allow a change of amplitude in density that does not exceed 10%. Using a random sampling, Figure 5.11 shows the possible modifications that can be allowed from the original EOSs with the priors and boundaries we chose. When plotting the density according to the pressure, we can see that the differences are small even when we perturb the adiabats. Table 5.4 sums up the priors we chose to run further MCMC simulations.

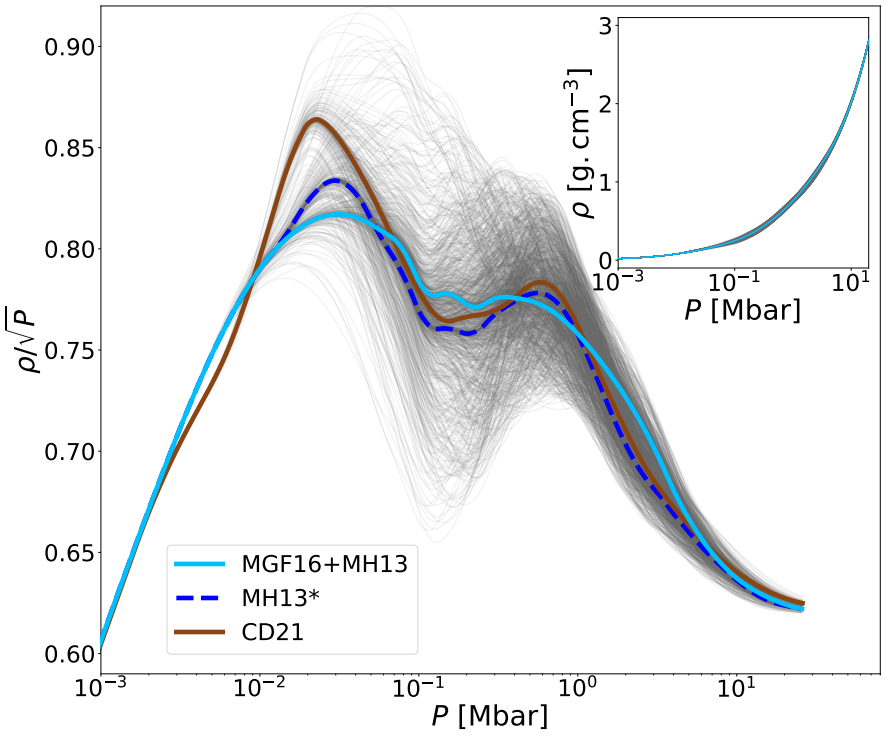

FIGURE 5.11: Possible adiabats (gray lines) that can be obtained when modifying the MGF16+MH13, MH13*, CD21, HG23+CMS19, and HG23+MLS22 EOSs with the chosen priors (see Table 5.4). **Taken from Howard et al. [2023].**

TABLE 5.4: Priors for the parameters used to modify the EOS. **Adapted from Howard et al. [2023].**

Parameter	Distribution	Lower bound	Upper bound	μ	σ
P_{modif} (dyn.cm^{-2})	Uniform	$10^{11.5}$	$10^{12.5}$	–	–
ΔP	Uniform	0.2	0.8	–	–
$d\rho$	Uniform	-0.1	0.1	–	–

5.3.4 Runs with a modified EOS

For MCMC runs in which we allow for modifications of the EOS, we first chose Gaussian priors on P_{modif}, ΔP, and $d\rho$ (see Sections 5.3.2 and 5.3.3). Our goal was to penalise

models with a substantial change of the EOS and favour models with only a slight modification of the EOS; as for the other parameters discussed in the previous section, this led to large deviations of the EOS. Figure 5.12 compares the adiabats of models including EOS modifications, with a uniform prior on P_{modif} and either uniform or Gaussian priors on ΔP and $d\rho$. For the Gaussian priors, the parameters for ΔP were $\mu = 0.5$ and $\sigma = 0.02$, and the parameters for $d\rho$ were $\mu = 0.$ and $\sigma = 0.01$. The difference between $\rho/\sqrt{(P)} - P$ profiles obtained after modification of the EOS is subtle between runs with Gaussian and uniform priors. This slight difference between the modified adiabats leads to a better fit of the data (equatorial radius, gravitational moments) for models obtained with uniform priors. When using Gaussian priors, most of the models are at 2σ or 3σ from the observed equatorial radius and J_4 and are at 4σ to 5σ from the mean value assumed for the prior on P_{He} (see Fig. D.1). As the modified adiabats are very similar and the agreement with the observational constraints is slightly better, we present results obtained with uniform priors.

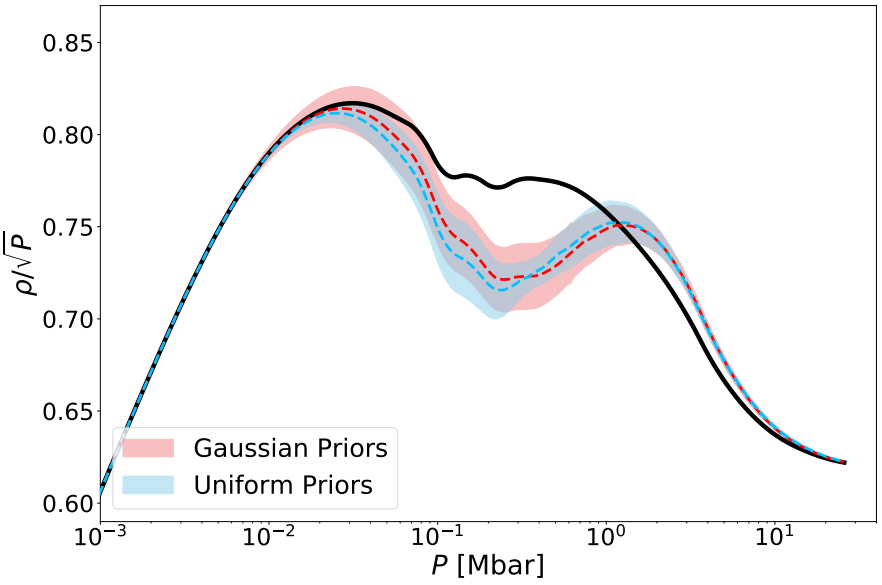

FIGURE 5.12: Adiabats obtained for models with a modification of the EOS. The black solid line corresponds to the original MGF16+MH13 EOS. Red shows results obtained with Gaussian priors on ΔP ($\mu = 0.5$ and $\sigma = 0.02$) and $d\rho$ ($\mu = 0.$ and $\sigma = 0.01$). Blue shows results obtained with uniform priors. The prior on P_{modif} remains uniform in both cases. The dashed lines correspond to the adiabat obtained with the mean values of P_{modif}, ΔP, and $d\rho$ (see Section 5.3.2) of a subsample of 100 models randomly drawn from the MCMC output. We compute the standard deviation (σ) of the 100 adiabats and the envelopes show the adiabats of the 1 σ spread from the mean modified adiabat (dashed line). Here, $T_{1\text{bar}}$ is fixed at 166.1 K. **Taken from Howard et al. [2023].**

As previously mentioned, the modification of the initial MGF16+MH13 EOS is relatively substantial, with a change in density that can reach up to $\sim 11\%$ in amplitude (see Fig.5.12). Figure 5.13 shows the modifications of the EOS for models (using uniform priors) at respectively $T_{1\text{bar}} = 166.1$ K and 174.1 K. At higher Z_1, the modifications of the EOS occur at higher pressures but in any case, the amplitude remains significant

(between 6 and 11%). In addition, these changes to the EOS are likely to be incompatible with Hugoniot data [Knudson and Desjarlais, 2017]. We therefore provide the results with modified EOS as a way to test the robustness of the solutions, but we will generally focus on results using the original EOSs. We show the results of these models with modified EOS in the next section, for convenience, as they were included in Howard et al. [2023]. However, given the significant departures from the original EOSs, we believe that these results should be taken with caution.

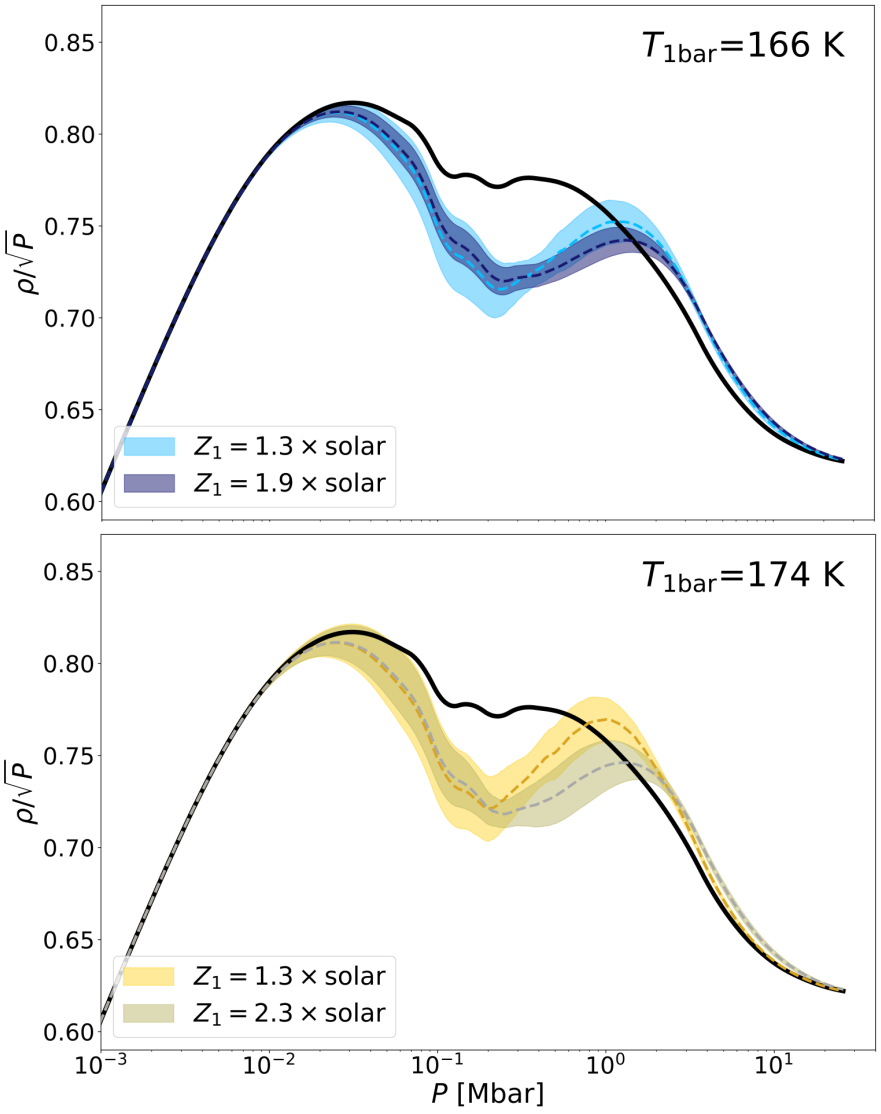

FIGURE 5.13: Adiabats obtained for models with modified EOS. *Top Panel.* T_{1bar} is fixed at 166.1 K. The light blue area shows results for $Z_1 = 0.02$ (1.3 × the protosolar value) while dark blue shows results for $Z_1 = 0.0286$ (1.9 × the protosolar value). *Bottom Panel.* T_{1bar} is fixed at 174.1 K. The yellow area shows results for $Z_1 = 0.02$ (1.3 × the protosolar value) while gray shows results for $Z_1 = 0.035$ (2.3 × the protosolar value). The black solid line corresponds to the original MGF16+MH13 EOS. Other details of the figure can be found in the caption of Fig. 5.12. **Taken from Howard et al. [2023].**

5.4 How extended is the dilute core?

This section corresponds to Howard et al. [2023]. In particular, Section 5.4.1, 5.4.2, 5.4.3, 5.4.4, 5.4.5, 5.4.6 correspond to sections 1, 4.3, 4.4, 4.5, 4.6 and 5 of Howard et al. [2023].

5.4.1 Introduction

Despite the significant improvement to measured gravitational moments provided by Juno [Iess et al., 2018, Durante et al., 2020], the interior of Jupiter remains mysterious. After the two first perijoves of Juno, Wahl et al. [2017] proposed the presence of a dilute core inside the planet: a region above the central compact core where heavy elements are gradually mixed with hydrogen and helium in the envelope. However, most models led to atmospheric abundances that are incompatible with observations. Debras and Chabrier [2019] then looked for models compatible with atmospheric abundances and proposed models that require an inward decrease of the abundance of heavy elements (negative Z gradient). Such scenario will be discussed in Section 5.5. Recently, Militzer et al. [2022] found models with both an atmosphere of protosolar composition of heavy elements and a positive Z gradient, but with large deviations of the gravitational moments requiring specific differential rotation solutions. In Miguel et al. [2022], we found solutions with smaller differential rotation offsets but these required a higher interior entropy than that measured by the Galileo probe.

While all these recent interior models rely on different assumptions, most of them still yield a dilute core inside Jupiter that is very extended. Debras and Chabrier [2019] and Militzer et al. [2022] find dilute cores that respectively reach 65%-75% and 63% of Jupiter's radius. These values correspond to a dilute core that extends up to respectively $\sim 60\% - 75\%$ and $\sim 50\%$ of Jupiter's mass. From the point of view of evolution, Vazan et al. [2018] showed that the outer envelope is mixing efficiently and the outer 60% in mass are of uniform composition after 4.5 Gyr. However, Müller et al. [2020] then modelled the formation of Jupiter using realistic initial entropies and found even more efficient mixing during the planetary evolution where only the inner 20% of the mass is left intact, suggesting that Jupiter's dilute core is not very extended. It has therefore been challenging so far to find agreement over the extent of the dilute core between interior and formation–evolution models of Jupiter, unless an additional process, such as a giant impact, is considered [Liu et al., 2019]. In addition, the gravitational imprint of the dilute core in Jupiter's tidal signal registered by Juno [Idini and Stevenson, 2022a,b] has lead to increased uncertainty over the extent of the dilute core.

Furthermore, constraining the internal structure of Jupiter requires a good understanding of the behaviour of hydrogen and helium at the pressure and temperature conditions

in the planet. Interior models therefore also rely on a key ingredient, which is a hydrogen and helium equation of state (hereafter H-He EOS). Experiments and simulations have been extensively conducted to provide accurate EOSs (see Helled et al. [2020a] and references therein for a review) but some uncertainty remains. In addition, Howard and Guillot [2023] recently emphasised the importance of accounting for H-He interactions when calculating EOSs for interior models. The aim of this study is to estimate how extended Jupiter's dilute core is given the current uncertainty on the H-He EOS.

We ran models for the different EOSs and outer envelope metallicity Z_1. We keep almost the same parameterization as in Miguel et al. [2022]. In the following, we present two types of results: (a) models with the original EOSs, variable $T_{1\,\mathrm{bar}}$ and $Z_1 = 0.02$; and (b) models with modified EOSs, a value of $T_{1\,\mathrm{bar}}$ equal to either the Galileo value of 166.1 K or the upper limit from Gupta et al. [2022], 174.1 K, and values of $Z_1 = 0.02$, 0.029, and 0.035 (1.3 to 2.3 $\times$ protosolar). Our results confirm and extend those of Miguel et al. [2022]. When using the same hypotheses, we obtain the same results as Militzer et al. [2022] (see Appendix D.3), and results that are consistent with those presented by Debras and Chabrier [2019].

5.4.2 Surface temperature $T_{1\mathrm{bar}}$ and helium transition pressure P_{He}

As mentioned at the end of Subsection 5.4.1, we present two sets of models: with original EOSs and with a modification of the EOS. Here, we focus on the 1 bar temperature, which prescribes the entropy inside Jupiter, and on the pressure where helium rain occurs [Stevenson and Salpeter, 1977a]. The latter sets the limit between the molecular hydrogen (helium-poor) and the metallic hydrogen (helium-rich) layers. Figure 5.14 shows the values of these two parameters for the two types of interior models sampled by our MCMC code. Interior models with the original EOSs (and $Z_{\mathrm{atm}} = 0.02$) all yield a 1 bar temperature, which is higher than the value measured by Galileo, which ranges from 171 to 188 K. In particular, with the MGF16+MH13 EOS, we obtain a $T_{1\mathrm{bar}}$ of between 180 and 188 K, while we were obtaining a $T_{1\mathrm{bar}}$ of between 175 and 183 K for $Z_{\mathrm{atm}} = 0.0153$ (protosolar value) in Miguel et al. [2022]. Therefore, a Z abundance of 1.3 $\times$ protosolar instead of 1 $\times$ protosolar in the outer envelope leads to a 5 K increase in $T_{1\mathrm{bar}}$ to fit the J_{2n} (see Section 5.4.3). Only models using MH13* or HG23+MLS22 seem to be in line with the upper end of the temperature provided by Gupta et al. [2022]. Overall, all models present a high 1 bar temperature, which could correspond to a deep entropy in line with a hotter interior due to a potential superadiabaticity [Guillot, 1995, Leconte and Chabrier, 2012]. The models using original EOSs exhibit a helium transition pressure of between 0.8 and 4.5 Mbar, which is in agreement with the values obtained by simulations and experiments (see Lorenzen et al. [2011], Morales et al. [2013], Schöttler and Redmer [2018b], Brygoo et al. [2021]). For all EOSs, we can distinguish two ensembles of solutions: one with high P_{He} corresponding to models with

a compact core of a few earth masses (1-6 $M_\oplus$) and a highly extended dilute core ($m_{\rm dilute}$ between 0.4 and 0.6) and a second one with lower $P_{\rm He}$ corresponding to models with almost no compact core and a less extended dilute core ($m_{\rm dilute}$ between 0.15 and 0.45) (more details in Section 5.4.5). The difference in $T_{\rm 1bar}$ between the two ensembles of solutions is only of 2-3 K. Therefore, accurate constraint of the pressure at which helium rain occurs could help to characterise the dilute core and to determine the atmospheric entropy of Jupiter.

Concerning models with a modification of the EOS, we calculate two subsets of models where we fix $T_{\rm 1bar}$ at 166.1 or 174.1 K. For each temperature, we present results for two values of the abundance of heavy elements in the outer envelope Z_1. At $T_{\rm 1bar} = 166.1$ K, models with $Z_1 = 0.02$ have $P_{\rm He}$ values concentrated between 3 and 4.5 Mbar. With $Z_1 = 0.029$, models tend to high transition pressures, around 6 Mbar, and are far from fitting the observed equatorial radius and gravitational moments (see Section 5.4.3). At $T_{\rm 1bar} = 174.1$ K, we obtain values of $P_{\rm He}$ of between 1.5 and 3.5 Mbar for $Z_1 = 0.02$ and of between 3 and 4.5 Mbar for $Z_1 = 0.035$, which are both close to what is expected.

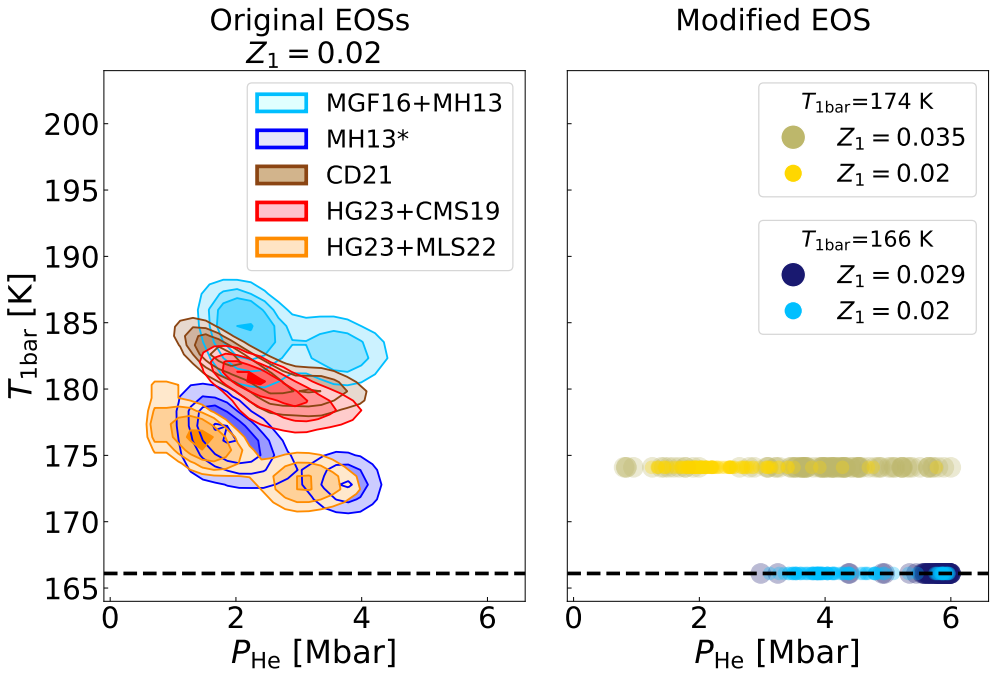

FIGURE 5.14: Temperature at 1 bar vs. helium transition pressures for two types of models. *Left panel.* Models using original EOSs. $Z_1 = 0.02$. *Right panel.* Models with a modification of the EOS. The initial EOS that has been modified is MH13. We present two subsets of models: with $T_{\rm 1bar} = 166.1$ K and $T_{\rm 1bar} = 174.1$ K. The black dotted line corresponds to the 1 bar temperature measured by the Galileo probe. **Taken from Howard et al. [2023].**

5.4.3 Equatorial radius $R_{\rm eq}$ and gravitational moments J_{2n}

Here, we examine the fit of our models to the gravitational moments measured by Juno and accounting for differential rotation. Figure 5.15 shows the equatorial radius and the gravitational moments obtained with our interior models. All models with original EOSs can reproduce the equatorial radius and all the gravitational moments except J_6. We find solutions for MGF16+MH13 that can match J_6 corrected by differential rotation. For the four other EOSs, the sampled values of J_6 are in the 2 - 3 σ range. We can see a correlation between $T_{\rm 1bar}$ and J_6: models using an EOS that yields higher $T_{\rm 1bar}$ present lower values of J_6. With MGF16+MH13, $J_6 \times 10^6$ is between 34.1 and 34.3. With MH13*, CD21 and HG23+CMS19, $J_6 \times 10^6$ is between 34.2 and 34.4. With HG23+MLS22, $J_6 \times 10^6$ is between 34.3 and 34.5. Militzer et al. [2022] found a value of $J_6 \times 10^6$ of 34.47 for $T_{\rm 1bar} = 166.1$ K using their EOS from Militzer and Hubbard [2013].

Concerning models allowing for a modification of the EOS, at $T_{\rm 1bar} = 166.1$ K, we manage to find models matching $R_{\rm eq}$ and all J_{2n} when $Z_1 = 0.02$. However, at $Z_1 = 0.029$, we can no longer fit $R_{\rm eq}$ or J_{2n}. These models have an equatorial radius that is several sigma below the observational constraint but we still retain them to test the robustness of our results. We then set $T_{\rm 1bar}$ to 174.1 K and find models reproducing $R_{\rm eq}$ and all J_{2n}, even for $Z_1 = 0.035$ (2.3 $\times$ protosolar).

5.4.4 Heavy-element distribution

We now compare the distribution of heavy elements in our models. Figure 5.16 shows the heavy elements masses defined in Fig 5.6. Models with original EOSs have a total mass of heavy elements of between 18 and 33 $M_\oplus$ and a compact core of less than 6 $M_\oplus$. These results are in line with those obtained by Miguel et al. [2022]), showing that increasing the Z abundance in the outer envelope from 1 $\times$ protosolar to 1.3 $\times$ protosolar does not lead to a drastic change in the distribution of heavy elements. $M_{\rm Z,dil*}$ is between 10 and 25 $M_\oplus$, which is larger than $M_{\rm Z,env*}$ by up to a factor of 4. Hence, models with no modification of the EOS have most of their heavy elements in the dilute core region rather than in the rest of the envelope.

Allowing for modifications of the EOS generally leads to a lower total mass of heavy elements, mostly between 12 and 20 $M_\oplus$. This is due to modifications of the EOS that make the adiabats (hence the H-He mixture) denser at depth. The mass of the compact core does not exceed 8 $M_\oplus$ for these models. $M_{\rm Z,dil*}$ is similar in all of our four cases: models are concentrated around a region where $M_{\rm Z,dil*} \sim 5 - 7$ $M_\oplus$. However, $M_{\rm Z,env*}$ clearly depends on the value of Z_1. For $Z_1 = 0.02$, $M_{\rm Z,env*}$ is around 6 $M_\oplus$, for $Z_1 = 0.029$, $M_{\rm Z,env*}$ is around 9 $M_\oplus$, and for $Z_1 = 0.035$, $M_{\rm Z,env*}$ is around 11 $M_\oplus$. Therefore, our models with a modified EOS do not lead to a dilute core that is predominant in

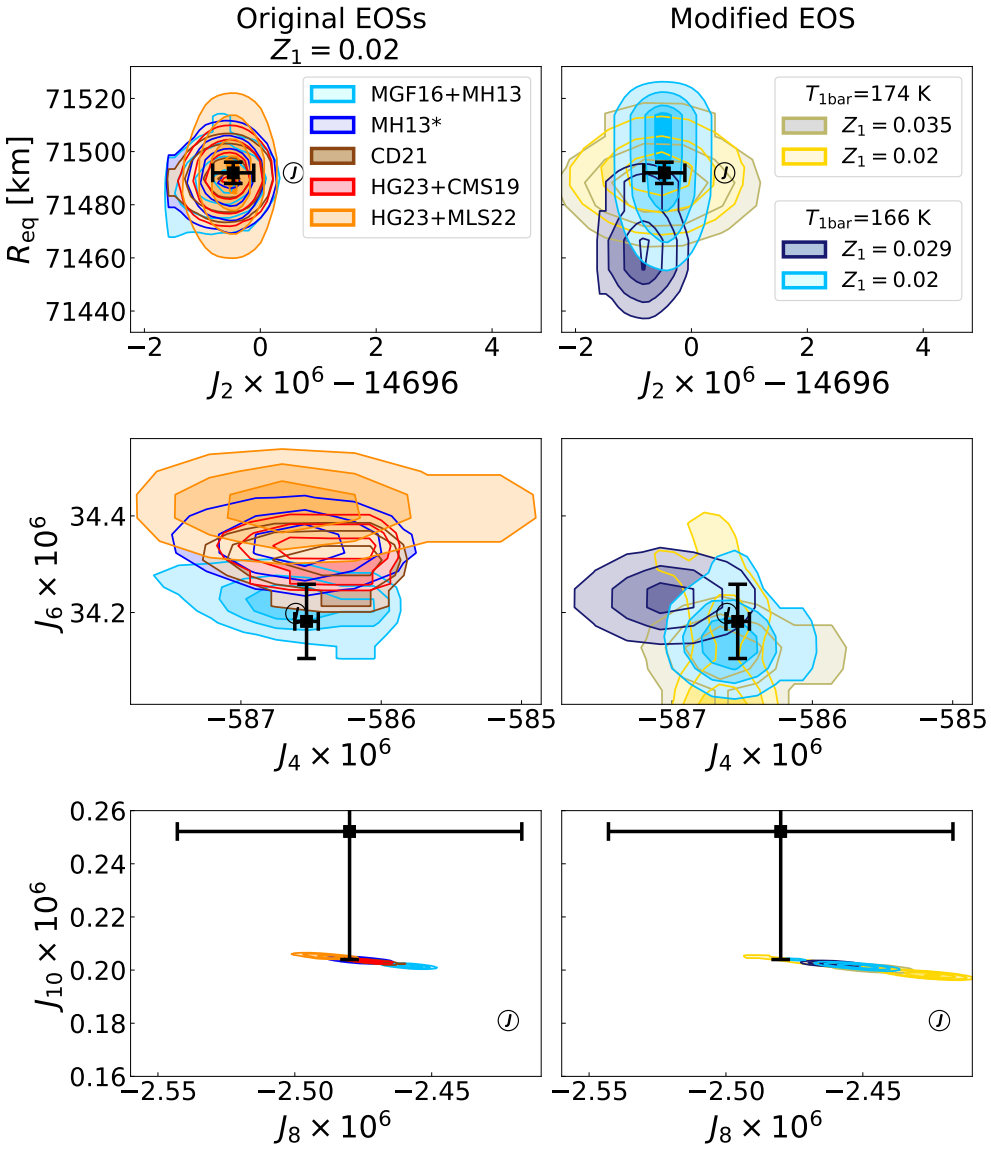

FIGURE 5.15: Equatorial radius and gravitational moments for two types of models. *Left panels.* Models using original EOSs. $Z_1 = 0.02$. *Right panels.* Models with a modification of the EOS. The inital EOS that has been modified is MH13. We present two subsets of models: with $T_{1bar} = 166.1$ K and $T_{1bar} = 174.1$ K. The circles with a J correspond to the measurements of the gravitational moments by Juno [Durante et al., 2020]. The black error bars correspond to the gravitational moments corrected by differential rotation (see 2.5.3). **Taken from Howard et al. [2023].**

heavy elements compared to the rest of the envelope, contrary to what we find for models with original EOSs.

We stress that the total masses of heavy elements inferred here are lower limits: The presence of compositional gradients implies that parts of the interior may be super-adiabatic because it is Ledoux-stable, double-diffusive [see Leconte and Chabrier, 2012], or stable to moist convection [Guillot, 1995, Leconte et al., 2017], meaning that the interior could be warmer and thus retain more heavy elements than calculated here. For

example, Militzer et al. [2022] estimated that a doubling of the central temperature of Jupiter would increase the mass of heavy elements from 25 to 42 $M_\oplus$.

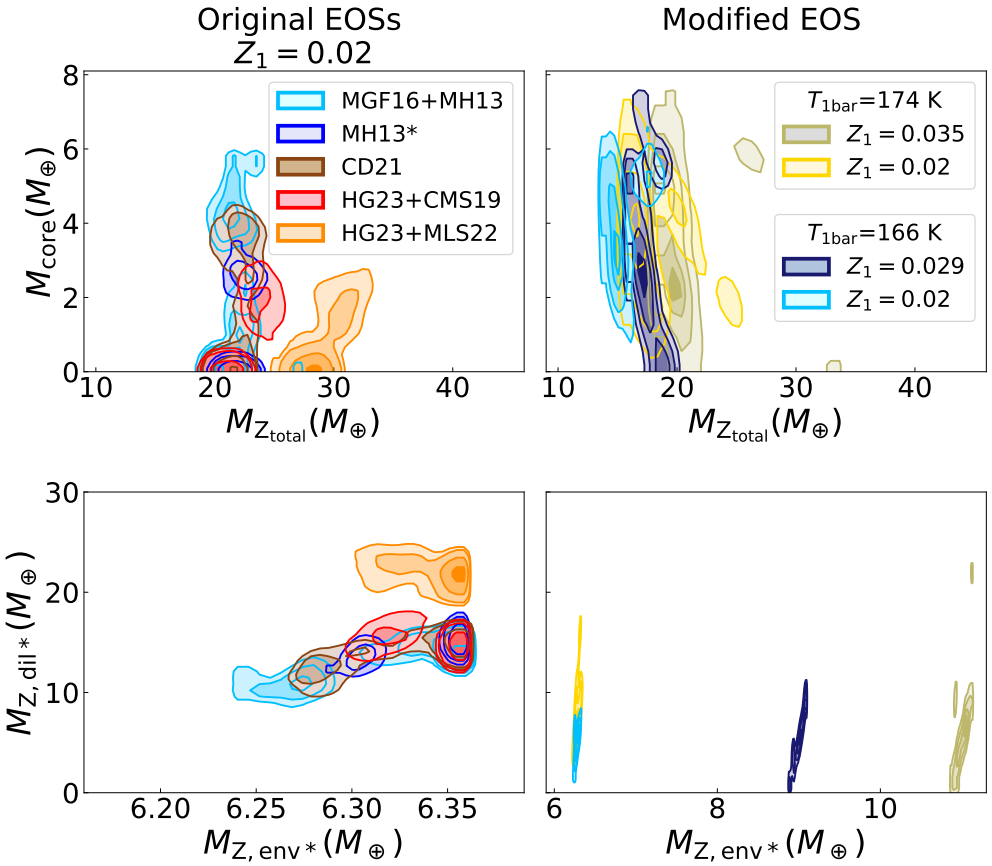

FIGURE 5.16: Masses of heavy elements in our interior models. *Top panels.* Mass of the compact core vs. total mass of heavy elements in Jupiter. *Bottom panels.* $M_{Z,dil*}$ vs. $M_{Z,env*}$ (see Fig. 5.6). **Taken from Howard et al. [2023].**

5.4.5 Dilute core characteristics

A key question is the extent of this dilute core, which connects interior models of Jupiter and formation and evolution models. Recent interior models from Militzer et al. [2022] and Debras and Chabrier [2019] suggest considerably extended dilute cores that respectively reach 63% and 65%-75% of Jupiter's radius. These values correspond to $\sim$ 50% and $\sim$ 60%-75% of Jupiter's mass, respectively, which can be compared to the value of our m_{dilute} parameter. We note that the comparison is not exact because it is affected by the functional form chosen for the dilute core (see Fig. 5.6), but the effect is minor: In our case, the added heavy element mass fraction in the dilute core drops from 50% of its maximal value at $m = m_{\text{dilute}}$ to only 8% at $m_{\text{dilute}} + \delta m_{\text{dil}}$ with $\delta m_{\text{dil}} = 0.075$.

The preferred model from Militzer et al. [2022] would have a value of $m_{\text{dilute}} \sim 0.36$ in our parameterisation. Figure 5.17 shows the values of m_{dilute} found for our models. Using original EOSs, we obtain m_{dilute} of between 0.15 and 0.6 (the dilute core extends

from $\sim 15\%$ to $\sim 60\%$ of Jupiter's total mass). We confirm that we find models with very extended dilute cores as in Debras and Chabrier [2019] and Militzer et al. [2022]. But we are also finding models with relatively narrow dilute cores (down to $\sim 15\%$ of Jupiter's mass). These solutions with relatively small, dilute cores are in better agreement with the mixing and evolution calculations of Müller et al. [2020], which yield a dilute core that does not exceed 20% of Jupiter's mass, resulting in a dilute core that extends only up to Jupiter's inner $\sim 60\ M_\oplus$. This leads to a formation scenario that is consistent for both Jupiter and Saturn [see Guillot et al., 2022], because Saturn is likely to harbour a dilute core that extends to $52-60\ M_\oplus$ of the planet's total mass [Mankovich and Fuller, 2021].

Concerning models with a modification of the EOS, we find a few models with very extended dilute cores but the majority yield $m_{\rm dilute} < 0.15$. We suspect that these results are spurious. The changes in the H-He EOS lead to an increase in density at high pressures that can mimic the effect of a dilute core. As the H-He mixture is denser in the dilute core region, less heavy elements can be added, which leads to these low values of $m_{\rm dilute}$ (and also $M_{\rm Z,dil*}$, see Section 5.4.4).

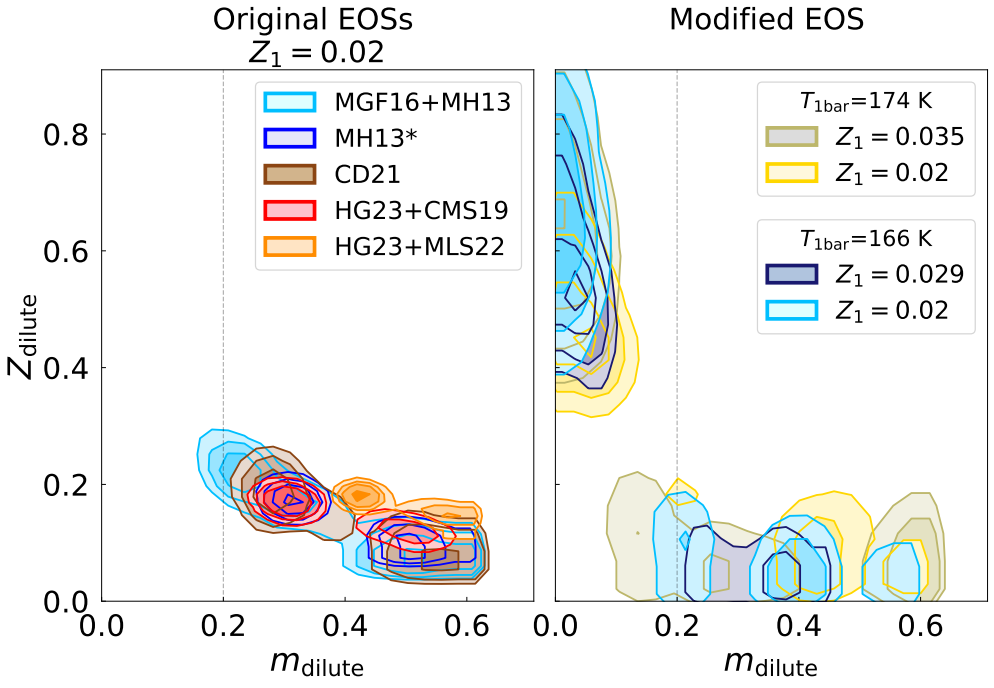

FIGURE 5.17: $Z_{\rm dilute}$ vs. $m_{\rm dilute}$ for two types of models. $Z_{\rm dilute}$ is the maximum mass fraction of heavy elements in the dilute core region while $m_{\rm dilute}$ controls the extent of the dilute core in terms of mass (see Section 4.3 and Fig. 5.6). *Left panel.* Models using original EOSs. $Z_1 = 0.02$. *Right panel.* Models with a modification of the EOS. The initial EOS that has been modified is MH13. We present two subsets of models: with $T_{\rm 1bar} = 166.1$ K and $T_{\rm 1bar} = 174.1$ K. The thin gray dotted line corresponds to $m_{\rm dilute} = 0.2$, which corresponds approximately to the extent of the dilute core of 20% of Jupiter's mass predicted by formation models from Müller et al. [2020]. **Taken from Howard et al. [2023].**

5.4.6 Conclusion

In Howard et al. [2023], we thus have explored a wide variety of interior models of Jupiter constrained by all available observations and using available EOSs. Our models assume the presence of a central dense compact core, a dilute core of variable extent and heavy-element composition, and an outer envelope of uniform Z composition. The helium phase separation is modelled as a jump in helium abundance in the Mbar pressure range.

While high-pressure experiments and ab initio calculations have led to significant improvements, H-He EOSs remain a source of uncertainty when modelling Jupiter's interior. We observe a range in the adiabatic density profiles of up to 5% at pressures ranging from 10 kbar to 10 Mbar. We interpret these variations as resulting from changes between different EOS tables and from different interpolation choices in relatively sparsely populated tables.

An important source of uncertainty results from our poor knowledge of Jupiter's complex atmosphere and the possibility of a higher entropy than generally assumed. By allowing the $T_{1\,\mathrm{bar}}$ parameter to vary [see Miguel et al., 2022], we obtain models that fit all constraints for all EOSs used. The values of $T_{1\,\mathrm{bar}}$ obtained range from 171 K to 188 K, significantly higher than 166.1 K from the Galileo probe [von Zahn et al., 1998], but within $164K - 174K$, which is the range of values obtained by Gupta et al. [2022] from a reanalysis of Voyager's radio occultations. Interestingly, MH13* and HG23+MLS22 (see Table 3.1), the two EOSs that lead to the lowest $T_{1\,\mathrm{bar}}$ values, yield the highest values of J_6, which are slightly outside the range expected from differential rotation. Conversely, the MGF16+MH13 EOS leads to the smallest values of J_6, well within expectations, but the largest values of $T_{1\,\mathrm{bar}}$.

In all cases, we obtain a dilute core of heavy-element mass of between 10 and 25 $M_\oplus$, confirming the result obtained by Miguel et al. [2022] that Jupiter's envelope is inhomogeneous. The range of values is also fully compatible with the results obtained by Militzer et al. [2022] and Debras and Chabrier [2019]. The mass of the compact core ranges between 0 and 6 $M_\oplus$. The total mass of heavy elements that we find ranges from 18 to 33 $M_\oplus$. However, we must stress that, given the possibility of (perhaps significant) superadiabatic regions [see Guillot, 1995, Leconte and Chabrier, 2012, Leconte et al., 2017, and Section 5.4.4], these masses are lower limits.

Our dilute cores are characterised by a global mass fraction of heavy elements of between 0.02 and 0.27 (in addition to the envelope heavy element mass fraction $Z_1 \sim 0.02$) and extend from $\sim 15\%$ to $\sim 60\%$ of Jupiter's total mass. We reiterate that the exact extent of the dilute core will depend on the shape of its compositional gradient. These solutions therefore encompass those of Debras and Chabrier [2019] and Militzer et al. [2022], but also allow for small, dilute cores. These solutions with small, dilute cores are compatible

with the formation–evolution models of Müller et al. [2020], which suggest that the outer 80% in mass should be fully mixed by convection, leaving a primordial dilute core extending only up to Jupiter's inner $\sim 60\ M_\oplus$. This result is also promising, in light of interior models for Saturn, which indicate that a dilute core extends to $52 - 60\ M_\oplus$ of the planet's total mass [Mankovich and Fuller, 2021]. This could lead to a formation scenario that is consistent for both Jupiter and Saturn [see Guillot et al., 2022].

However, there is an important caveat to consider: As pointed out by Wahl et al. [2017] and Debras and Chabrier [2019], and confirmed by all further modelling efforts, interior models of Jupiter constrained by Juno's gravitational moments favour solutions with small values of Z in the outer envelope. While our solutions are calculated by imposing $Z_1 = 0.02$, this represents a bare minimum, given all spectroscopic constraints (see Fig. 2.7). When imposing higher values of Z_1, we find an increasingly more difficult situation, with solutions departing from the constraints on $R_{\rm eq}$ and J_2 and/or modifications to the EOSs that were too important and most likely incompatible with the experimental constraints. Interestingly, a similar situation arises for Saturn [Mankovich and Fuller, 2021], indicating that we may be missing an important physical ingredient.

Several directions of research could lead to significant improvements in our understanding of Jupiter's interior structure and composition. For example, progress in the analysis of Juno microwave radiometer data to infer abundances of ammonia and water as well as temperatures as a function of depth and altitude [Li et al., 2020] will help us to understand heat transport and the composition of the deep atmosphere [see also Stevenson et al., 2022]. Future radio occultations with Juno should further test observational constraints on temperature and shape. Improvements on EOSs, both experimentally and numerically, with particular emphasis on the hydrogen–helium mixture at pressures between 10 kbar and 10 Mbar and near Jupiter's adiabat (temperatures from 1000 K to 20,000 K on this pressure range) would be extremely valuable. Finally, while indications of the presence of normal modes of Jupiter exist [Gaulme et al., 2011, Durante et al., 2022], their identification from dedicated observational efforts [Gonçalves et al., 2019, Shaw et al., 2022] would be an extremely powerful tool for fully constraining the interior structure and composition.

5.5 On the hypothesis of an inverted Z gradient inside Jupiter

We have studied the range of possible solutions with dilute core models, accounting for uncertainties in the EOS. We have found models in better agreement with evolution models and with interior models of Saturn. But still, our models do not fully satisfy the high abundance of heavy elements measured in Jupiter's atmosphere (see Subsection 2.1.4). A potential solution is an inverted Z gradient, namely an inward-decrease of the abundance of heavy element, as previously proposed by Debras and Chabrier [2019]. We investigate this hypothesis in this section. I stress that this will be part of a future paper, which is in preparation.

5.5.1 Introduction

Models of Jupiter's interior, based on Juno gravity data [Durante et al., 2020], struggle to agree with measurements of the atmospheric composition [Li et al., 2020, Wong et al., 2004, Mahaffy et al., 2000]. So far, interior models succeeded to bridge the gap, not without difficulty, by relying on different assumptions: by assuming a warmer interior or by modifying the equation of state [Nettelmann et al., 2021, Miguel et al., 2022, Howard et al., 2023], by optimising the wind profile [Militzer et al., 2022] or by including a decrease of the heavy element abundance Z with depth [Debras and Chabrier, 2019], namely an inverted Z-gradient. Interior models actually favour a low metallicity in the outer envelope (subsolar or solar) while atmospheric measurements from Galileo and Juno suggest a supersolar abundance of heavy elements (around three times the protosolar value, see e.g. Guillot et al. [2022], Howard et al. [2023]). One may ask if the composition measured in the atmosphere is representative of the entire molecular envelope of Jupiter [Helled et al., 2022b].

We discuss in Section 5.5.2 the general concept of an inverted Z-gradient and the constraints it brings in terms of stability and external accretion. We then present two scenarios. First, we assess in Section 5.5.3 the hypothesis of an inverted Z-gradient located where He (helium) phase separates, as already proposed by Debras and Chabrier [2019]. Second, in Section 5.5.4, we present a scenario with a similar inverted Z-gradient but at upper regions, due to a radiative zone.

5.5.2 Inverted Z gradient: stability, formation

Interior models of Jupiter aim to match the measured gravitational moments, that depend on the density distribution of the planet (see, e.g., Zharkov and Trubitsyn [1978]). However, the difficulty of these models to satisfy the gravitational moments indicates

that they seem too dense, especially in outer regions of the envelope (0.1 – 1 Mbar) which have a significant contribution to the gravitational moments. Therefore, an inward-decrease of the heavy element content, in agreement with the supersolar atmospheric measurements but then reduced to solar or subsolar at depth, appears as a promising idea. Such inverted Z-gradient was proposed by Debras and Chabrier [2019], the latter will be discussed in the next section.

Nevertheless, an inverted Z-gradient requires to be stable against convection to be sustained. It can be balanced either by an increase in the helium mass fraction Y or a decrease in temperature, to make sure that the density ρ still increases with depth. We calculate, for Jupiter, the maximum increase in heavy elements that can be afforded by increasing Y or by decreasing temperature. To do so, (i) we calculate $\Delta Z/\Delta Y$ by equating $\rho(Z_j, Y_j)$ and $\rho(Z_{j+1}, Y_{j+1})$ where $\Delta Z = Z_j - Z_{j+1}$ and $\Delta Y = Y_{j+1} - Y_j$ (so that both ΔZ and ΔY have positive values) and (ii) we calculate $\Delta Z/(\Delta T/T)$ by equating $\rho(Z_j, T_j)$ and $\rho(Z_{j+1}, T_{j+1})$ where $\Delta T = T_j - T_{j+1}$ is the temperature difference relative to an isentrope. Here, j refers to the layer where the inverted Z gradient takes place. Densities are calculated using the additive volume law and including non-ideal mixing effects [Howard and Guillot, 2023]:

$$\frac{1}{\rho(P,T)} = \frac{X}{\rho_{\rm H}(P,T)} + \frac{Y}{\rho_{\rm He}(P,T)} + XYV_{\rm mix} + \frac{Z}{\rho_{\rm Z}(P,T)}, \tag{5.10}$$

where $\rho_{\rm H}$, $\rho_{\rm He}$, $\rho_{\rm Z}$ are the densities of hydrogen, helium and heavy elements respectively, X, Y, Z their respective mass fractions and $V_{\rm mix}$ is the volume of mixing. Figure 5.18 shows the results. In the ideal gas regime in Jupiter, we expect $\Delta Z/\Delta Y \sim 0.5$, meaning that the increase in He is required to be at least twice larger than the change in Z. We also expect $\Delta Z/(\Delta T/T) \sim 0.9$. It is not exactly 1 because we here assumed a mixture of hydrogen and helium consistent with Galileo's measurement of Y [von Zahn et al., 1998]. Using ideal gas relationship $\Delta\mu/\mu = \Delta T/T$ and the definition of the mean molecular weight $\frac{1}{\mu} = \frac{X}{\mu_{\rm H}} + \frac{Y}{\mu_{\rm He}} + \frac{Z}{\mu_{\rm Z}}$, we indeed obtain:

$$\Delta Z = \frac{\Delta\mu}{\mu} \times \left(\frac{\mu_{\rm Z}\,\mu_{\rm H}}{\mu_{\rm Z} - \mu_{\rm H}} \left(\frac{X}{\mu_{\rm H}} + \frac{Y}{\mu_{\rm He}} \right) \right) \sim \frac{\Delta T}{T} \times 0.9, \tag{5.11}$$

where $\mu_{\rm H}$, $\mu_{\rm He}$, $\mu_{\rm Z}$ are the molecular weights of hydrogen, helium and heavy elements respectively. The ideal gas regime extends down to the $\sim$kbar level. Deeper, non-ideal effects kick in and for instance a bigger decrease in temperature is required to allow an inverted Z-gradient at deeper regions. One can hence know how much Z can be balanced by an increase in Y or a decrease in temperature, at different levels in Jupiter.

An inverted Z-gradient can be stabilized, but vertical transport of heavy material through the stable region might still occur during the lifetime of Jupiter. We know, for example, that breaking gravity waves [Dörnbrack, 1998] and Kelvin-Helmholtz instabilities in the Earth's stratosphere produce an eddy diffusion coefficient of 10^3 cm^{2}s^{-1} [Massie

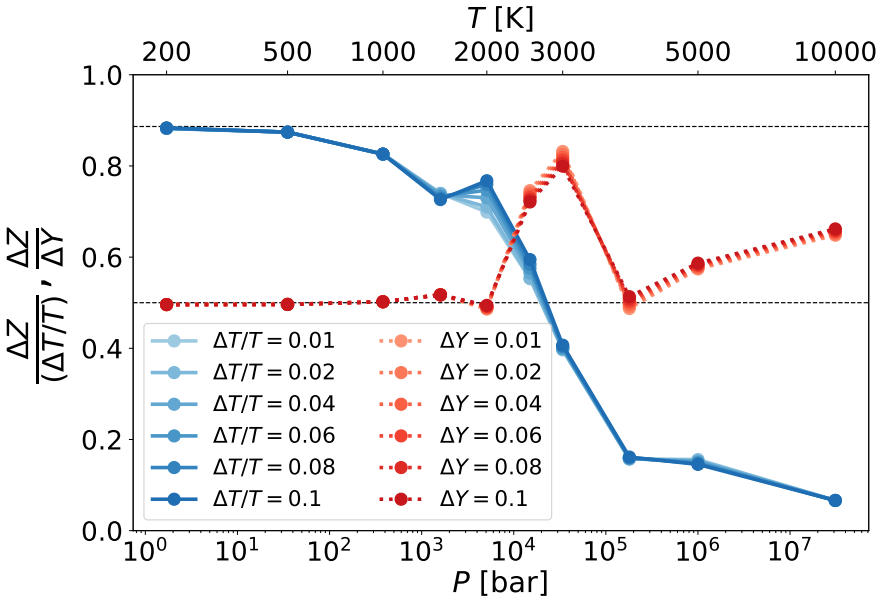

FIGURE 5.18: $\Delta Z/\Delta Y$ and $\Delta Z/(\Delta T/T)$ as a function of pressure and temperature in Jupiter. This shows the maximum increase in heavy elements allowed by increasing Y or by lowering the temperature to ensure stability where the inverted Z-gradient takes place. The horizontal dashed lines show the values of $\Delta Z/\Delta Y$ (*bottom*) and $\Delta Z/(\Delta T/T)$ (*top*) for an ideal gas. We stress that the calculation of ΔZ has here been done using the HG23+CMS19 equation of state [Chabrier et al., 2019, Howard and Guillot, 2023] for H-He and the SESAME-drysand equation of state [Lyon and Johnson, 1992] for heavy elements. The 1 bar temperature was taken at 170 K.

and Hunten, 1981]. We assume an eddy diffusion coefficient K_{zz} of 1 $\mathrm{cm^2 s^{-1}}$ which is three order of magnitude smaller, but two orders of magnitude larger than the lower bound, molecular diffusivity. In the case of the presence of a radiative zone (discussed in Section 5.5.4), we consider a thickness L of 1000 km for the stable layer. We obtain a diffusion timescale of

$$\tau_{\mathrm{mix}} \sim 320\,\mathrm{Myr} \left(\frac{1\,\mathrm{cm^2 s^{-1}}}{K_{zz}}\right) \left(\frac{L}{1000\,\mathrm{km}}\right)^2 . \tag{5.12}$$

Of course, there is a large uncertainty on the eddy diffusion coefficient as well as the thickness of the stable layer, but maintaining this inverted Z-gradient on a billion year timescale is rather challenging. In the case of an inverted Z-gradient located where He phase separates (discussed in Section 5.5.3), the thickness of the stable region may be larger, increasing the diffusion timescale to the order of one to ten billion years.

Furthermore, this inverted Z-gradient implies some constraints on its origin. First, an enrichment from below is ruled out as internal mixing will tend to homogenise the envelope [Vazan et al., 2018, Müller et al., 2020]. The enrichment hence needs to be external in order to establish an inverted Z-gradient . We discuss two important aspects of this external enrichment: the amount and the properties of the accreted material. We show on Fig. 5.19 how much material can be accreted on Jupiter, through impacts from the

destabilized population of the primordial Kuiper belt [Bottke et al., 2023]. The estimate of the collisional history was based on constraints derived from the craters found on giant planet satellites and the size-frequency distribution of the Jupiter Trojans. The figure also shows the pressure level in Jupiter at which the accretion of such amount of material would lead to a region above this level where Z is three times the protosolar value. For instance, within the first 500 Myr after Jupiter's formation, about 2.10^{-3} $M_\oplus$ can be accreted, which can lead to a threefold enhancement relative to solar from the top of the atmosphere down to 1 kbar. The two scenarios that we present in the following sections will have to satisfy this constraint on the possible amount of accreted material. The occurrence of impacts (large impact or cumulative small impacts) to form an inverted Z-gradient and an investigation of the stability of this region over billions of years is presented in Müller [2023] (in preparation).

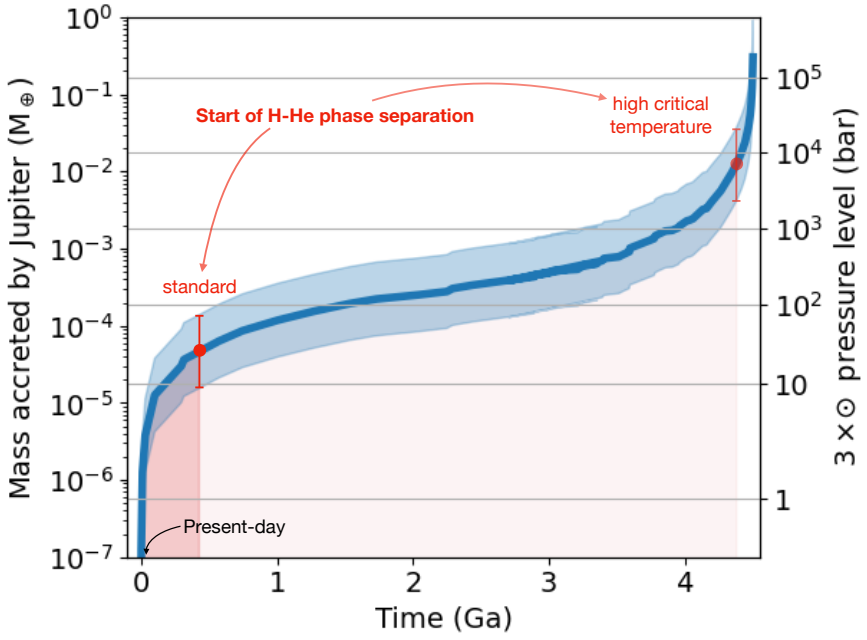

FIGURE 5.19: Accretion of material on Jupiter as a function of time from the present (0) to Jupiter's formation 4.5 Ga ago, based on Bottke et al. [2023]. In the last billion year, Jupiter accreted only about 10^{-4} $M_\oplus$ of material. The y axis on the right displays the pressure level in Jupiter at which the accretion of an amount of material would lead to a region above this level where Z is three times the solar value. The time at which hydrogen-helium phase separation started according either to standard models [e.g., Schöttler and Redmer, 2018b] or to experiments indicating a high critical temperature [Brygoo et al., 2021] are indicated in red. The corresponding error bars correspond to the mass accreted since that time.

Finally, we show in Fig. 5.20 the isotopic ratios of $^{15}N/^{14}N$ and D/H for objects of the solar system. Only Jupiter exhibits a protosolar composition of $^{15}N/^{14}N$ [Guillot et al., 2022] and D/H while all other objects have supersolar isotopic ratios. The inverted Z-gradient hence must have been established early. Otherwise, the enrichment of Jupiter in heavy elements would have been made by objects with very different isotopic composition as we expect the properties of a late accretion of heavy elements to be consistent with the

properties of objects that we can still find in the solar system today. This constitutes an additional constraint, on the properties of the accreted material. The argument about

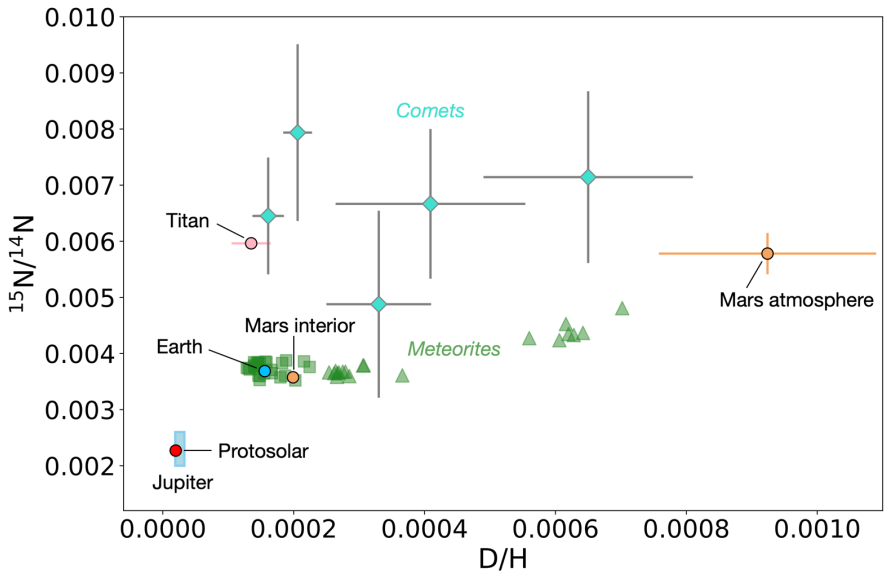

FIGURE 5.20: Isotopic ratios of $^{15}N/^{14}N$ and D/H among objects from the solar system. Adapted and updated from Marty [2012] and Füri and Marty [2015]. Jupiter's data are coming from Galileo [Mahaffy et al., 1998, Owen et al., 2001]. Protosolar values are from Marty et al. [2011], Geiss and Gloeckler [2003]. Earth's data are from Anders and Grevesse [1989], Michael [1988]. Mars' data are from Mathew and Marti [2001] and Wong et al. [2013], Webster et al. [2013] respectively for its interior and its atmosphere. The D/H of the interior is a lower limit as large variations are measured in martian meteorites [Saito and Kuramoto, 2020]. Titan's data are from Niemann et al. [2010], Abbas et al. [2010]. For meteorites, bulk isotopic ratios (*squares*) and values in insoluble organic matter (IOM) (*triangles*) are displayed. Here are shown data for various types of chondrites (CI, CM, CO, CR, CV) from Kerridge [1985], Aléon [2010]. Data for 5 comets (103P/Hartly, C/2009 P1 Garradd, C/1995 O1 Hale-Bopp, 8P/Tuttle and C/2012 F6 Lemmon, from left ro right) are displayed, taken from Bockelée-Morvan [2008], Manfroid et al. [2009], Biver et al. [2016], Shinnaka et al. [2016], Lis et al. [2019] and Bockelée-Morvan et al. [2015] and references therein. We mention that the average $^{15}N/^{14}N$ value for 21 comets has been found to be 0.007 ± 0.001 [Manfroid et al., 2009].

isotopes is however valid only if we consider that the formed inverted Z-gradient involves nitrogen. There is a possibility where the accreted material mostly brought carbon and not nitrogen. In fact, the C/N ratio in comet 67P/Churyumov–Gerasimenko indicates that this ratio is about 29 [Fray et al., 2017] on average from dust particles, implying a deficit in nitrogen. Combining this value to measurements from the cometary gas phase, Rubin et al. [2019] found a C/N ratio of 22 and 26 in 67P considering a dust-to-ice ratio of 1 or 3. The question of the representativity of this C/N ratio value among other comets is an ongoing area of research. The C/N ratio of 67P is in line with comet 1P/Halley [Jessberger et al., 1988] and the lower range of 81P/Wild 2 (although important variations have been measured in 81P particles) [de Gregorio et al., 2011]. It is also compatible with the chondritic value but large variations are observed in UCAMMs (ultracarbonaceous Antarctic micrometeorites) (see Engrand et al. [2023] and references therein). Nevertheless, if the accreted material was depleted in nitrogen, explaining the

formation of an inverted Z-gradient would then require to invoke different processes for different components and lead to a C/N value in Jupiter's atmosphere that is close to protosolar ($\sim$ 4.3, see Table 2 from Guillot et al. [2022]). However, we also note that the composition of the accreted material in both the gaseous and solid phase as well as the accretion rates remain largely unknown and should be explored in detail in future research.

5.5.3 An inverted Z gradient at the helium rain location

One of the only attempts that succeeded to yield a supersolar abundance of heavy elements in the atmosphere ($Z = 0.02$) was from Debras and Chabrier [2019]. These authors included a decrease of heavy elements with depth around where He phase separation takes place. It led to lower values of $|J_4|$ and $|J_6|$ and helped reconciling Juno's measurements. To ensure that denser material does not lie on top of lighter material, the decrease in Z was balanced by an increase in Y. Debras and Chabrier [2019] set the phase separation around 0.1 Mbar in their models, where $\Delta Z \sim 0.015$ and ΔY is between $\sim [0.02 - 0.05]$. Those models hence have ΔZ between $\sim [0.3 - 0.75] \times \Delta Y$, ensuring fairly well stability as Fig. 5.18 shows that ΔZ needs to be smaller than $\sim 0.6 \times \Delta Y$ at this pressure level.

However, one of the main explanations of this inverted Z-gradient is a late accretion of heavy material. This scenario requires such accretion to happen after He demixing occured in Jupiter, so that the accreted heavy material remains above the location of helium rain. We see from Fig. 5.19 that to obtain $Z = 3\times$ protosolar above 0.1 Mbar, an accretion of $\sim 0.15\, M_\oplus$ of heavy elements is required. Accreting this amount of material is more likely to occur during the early phases of the solar system evolution. More realistic values of the pressure at which He phase separates (a few Mbar) indicate that a few $M_\oplus$ of heavy elements are needed, which could not be explained. But the timing of the scenario put forward by Debras and Chabrier [2019] is tricky. We ran simple evolutionary models of Jupiter (with $M_{\rm core} = 10\ M_\oplus$ and a homogeneous envelope of solar composition). The results are shown in Fig. 5.21. We find that He phase separation is expected to occur late in the evolution of Jupiter, i.e. at 4 Gyr according to conventional models (consistent with Mankovich and Fortney [2020]), based on the immiscibility curve of Schöttler and Redmer [2018b]. But He demixing could occur after 100 Myr at the earliest, if we consider the experimental immiscibility curve from Brygoo et al. [2021]. In any case, He demixing is happening relatively late. Such late accretion could not bring more than about $0.01\, M_\oplus$ of heavy material (see Fig. 5.19) and would lead to an enrichment with the wrong isotopic composition as discussed in Section 5.5.2. A way to salvage this scenario would be to assume that Jupiter underwent a giant impact with a Mars-mass object. Such objects are not found in the present-day distribution of planetesimals in the Kuiper belt. It is therefore important to assess the likelihood

of such an impact at different ages. This impact should have occured very late in the evolution of the system, i.e. within the past 500 Myr, according to conventional H-He phase diagrams, making it an extremely low-probability event. Alternatively, it might have occurred earlier, only 100 Myr after the planet's formation if one assumes the high critical demixing temperature obtained experimentally by Brygoo et al. [2021]. In both of these cases, however, the object should have brought little nitrogen or should have been composed of a different composition in comparison to the observed small objects in the solar system.

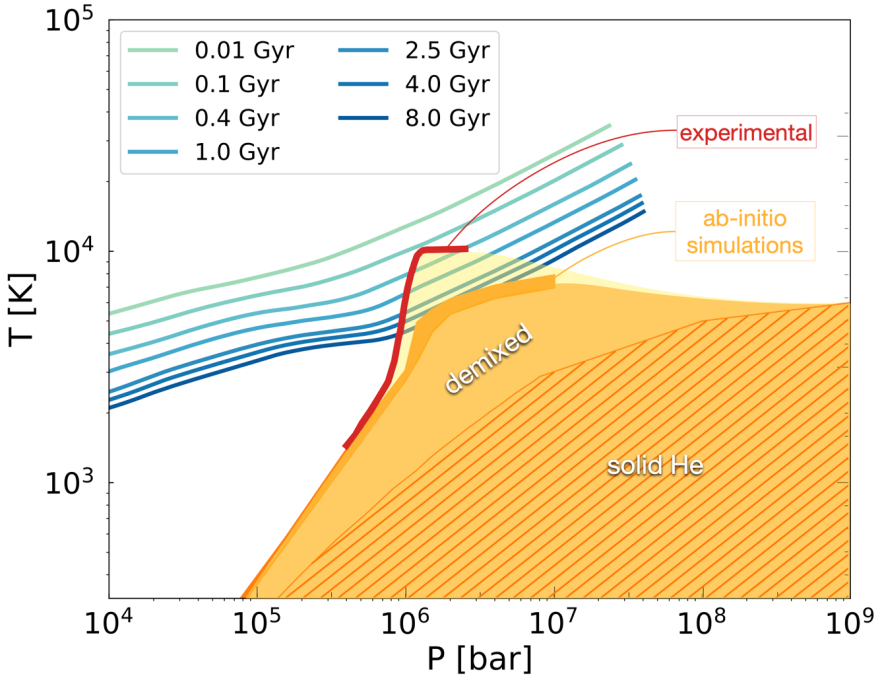

FIGURE 5.21: A sequence in evolutionary time of Jupiter interior profiles superimposed with a miscibility diagram of H-He. Adiabats of Jupiter at ages ranging from 10 Myr to 8 Gyr (top to bottom) are displayed. We show the immiscibility curve of experiments from Brygoo et al. [2021] (red) and of ab-initio simulations from Schöttler and Redmer [2018b] (orange). The hashed region is where He becomes solid.

5.5.4 An inverted Z gradient at uppermost regions, due to a radiative zone

Next, we envision an inverted Z-gradient located at upper regions ($\sim$kbar) and established early (probably less than 10 Myr). Our hypothesis is that the presence of a radiative zone prevents downward mixing. A radiative region could exist in the upper envelope, as suggested by Guillot et al. [1994] (between 1200 and 2900 K) and more recently by Cavalié et al. [2023] (between 1400 and 2200 K). A depletion of alkali metals would bring support to the potential existence of such radiative layer [Bhattacharya et al., 2023]. Accreted heavy material on top of this radiative zone may thus be prevented from mixing with the rest of the envelope below this radiative zone. It should

be noted that the question of the presence of a radiative zone is a separate question of getting a higher Z value above this radiative layer, which is what we focus on here.

First we ask: Can we find interior models with such radiative zone that satisfy the present gravitational moments measured by Juno? To answer this question, we use the opacities from Guillot et al. [1994] to set a radiative region in our models and implement an inverted Z-gradient . Fig. 5.18 shows that an inverted Z-gradient can be stabilized by a sub-adiabatic temperature gradient. Around the $\sim$kbar level, ΔZ needs to be smaller than about $0.7 \times \Delta T/T$. The models that we present here have $\Delta T/T$ of about 10%, allowing an increase of Z of three times the protosolar value ($Z \sim$ 5%, [Asplund et al., 2021]) and hence ensuring stability. We ran MCMC calculations (as in Miguel et al. [2022], Howard et al. [2023]). At first, we could not find interior models fitting the equatorial radius and the gravitational moments of Jupiter. In this case, the radiative zone was extending from 1200 to 2100 K. We then parameterized (arbitrarily multiplying by 5) the opacities and could obtain solutions, with a radiative region extending from approximately 1600 to 2100 K. Thus, the possible location and extent of the radiative zone may be constrained by the gravity data. We find models that reproduce the measured equatorial radius and gravitational moments. Fig. 5.22 shows the gravitational moments J_4 and J_6 obtained with these models for two different equations of state (the full posterior distributions are given in Appendix E for one specific EOS). We find that interior models including a radiative zone can hence satisfy the observed gravitational moments from Juno (at 3 σ in J_6) as well as the compositional constraints on the atmosphere.

To obtain $Z = 3 \times \odot$ above 1 kbar, an accretion of $\sim 2.10^{-3}\, M_\oplus$ of heavy elements is required, which can be done in the first few hundred million years (see Fig. 5.19). The isotopic constraints mentioned in Section 5.5.2 still stand and imply that a late delivery of heavy material above the radiative zone cannot be possible. Therefore, we examine whether the inverted Z-gradient could have been formed early and maintained in Jupiter. To this end, we use again our evolutionary models presented in Section 5.5.3 and Fig. 5.21 and include now a radiative zone using our opacities (multiplied by 5). Figure 5.23 compares the radiative and adiabatic temperature gradients at ages ranging from 1 Myr to 10 Gyr. The radiative zone is located roughly where the radiative gradient is lower than the adiabatic gradient. We see that the radiative region appears around 10 Myr and is progressively shifted to deeper regions. Thus, the initially enriched material above the radiative zone will progressively mix with material of protosolar composition as the radiative zone is shifted to deeper levels. Such behaviour of the radiative zone was already predicted by Guillot [1999]. Considering that the mass above the radiative region at 10 Myr is $\sim 10^{-5}\, M_\mathrm{J}$ and increases to $\sim 3.10^{-4}\, M_\mathrm{J}$ at 4 Gyr, the Z-gradient at 10 Myr must be high enough so that the abundance of heavy elements becomes approximately three times the protosolar value nowadays. If the disk phase does not exceed 10 Myr, it means that above the radiative zone, a Z value of 60 times the protosolar value

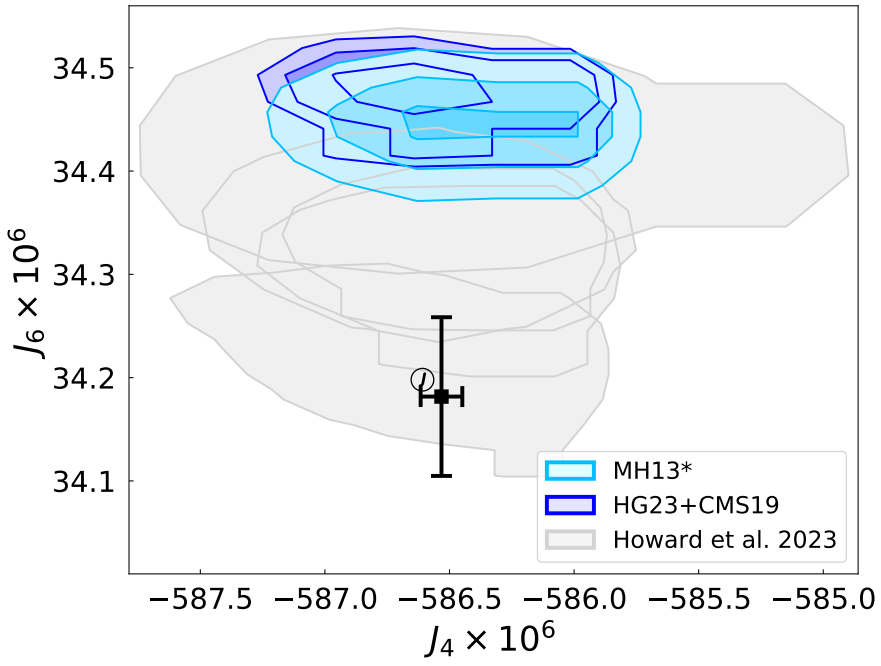

FIGURE 5.22: J_6 vs J_4 of models including a radiative zone (with Z being 3 × the protosolar value above), using the MH13* [Militzer and Hubbard, 2013] or the HG23+CMS19 [Chabrier et al., 2019, Howard and Guillot, 2023] EOS. These models are compared to previous results obtained by Howard et al. [2023] with no radiative zone nor inverted Z-gradient (Z being only 1.3 × the protosolar value in the atmosphere). The full covariations of the parameters of the MCMC calculation using MH13* are given in Appendix E.

($\Delta Z \sim 0.9$) is required at 10 Myr. Keeping such a ΔZ and ensuring stability may be hard since a significant $\Delta T/T$ would be required to prevent mixing (the factor of 0.9 in Eq. 5.11 would even be lower given the increased molecular weight due to a much higher Z value), making the scenario, under the set of our assumptions, rather unlikely. Furthermore, diffusion through the radiative zone is expected after a few hundred million years (see Section 5.5.2), making the scenario even more challenging. However, this behaviour of the radiative zone as the planet evolves is one case corresponding to the use of a specific opacity table and the details of the evolution code. Further investigation of this scenario is therefore required.

5.5.5 Conclusion

The inverted Z-gradient is an appealing idea for interior models to explain both the gravity field and the atmospheric composition of Jupiter. It can be stabilized by either an increase if the helium mass fraction or a decrease in temperature. However, as we show here, such Z-gradient at the location of helium rain, as proposed by Debras and Chabrier [2019], is rather unlikely as it would require to accrete an excessive amount of material, that cannot be justified from collisional evolution models of the solar system. It would also require a late accretion, that isotopic constraints actually do not allow. An

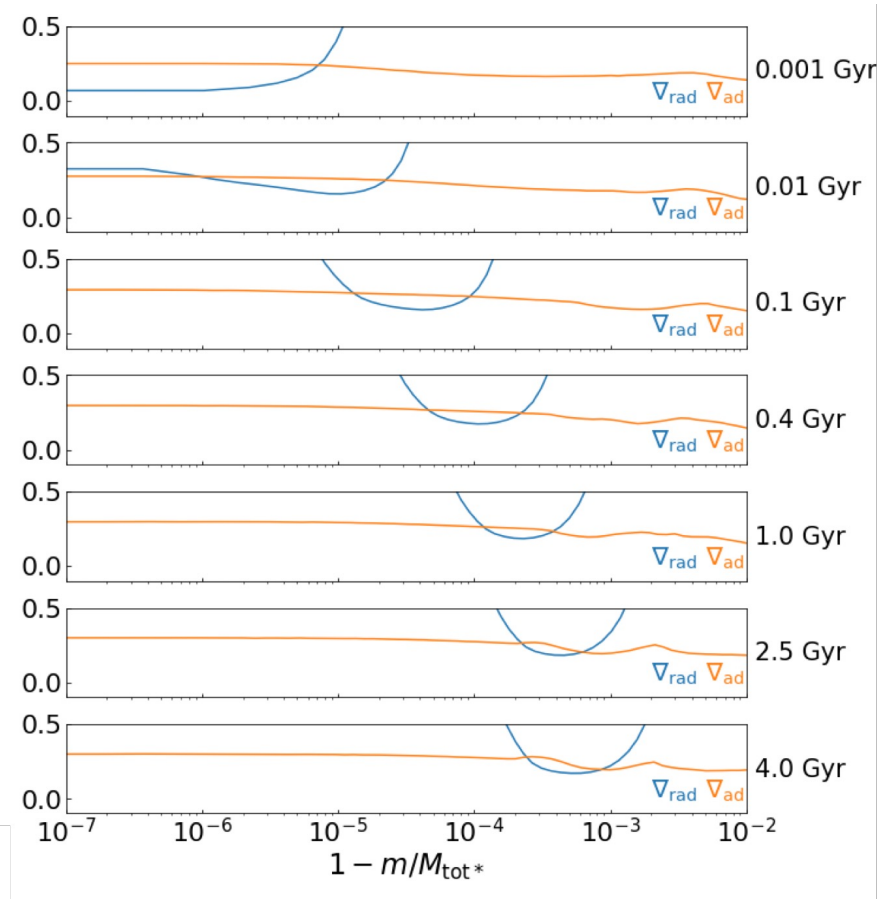

FIGURE 5.23: Comparison of the radiative and adiabatic temperature gradients in Jupiter, at ages ranging from 1 Myr to 10 Gyr. We estimate the minimum value of ∇_{rad} as the approximate upper limit of the radiative region. The evolution models consist of a central core of 10 $M_{\oplus}$ and a homogeneous envelope of solar composition.

inverted Z-gradient , established early and at upper regions ($\sim$kbar), due to a radiative zone, might be a solution. We show here that such a scenario works from the point of view of the present gravity data and enough material may be accreted. Nevertheless, this radiative zone appears around 10 Myr and is shifted to deeper regions with time. Such inward-shift of the radiative zone requires at $\sim$ 10 Myr a significant Z-gradient ($\Delta Z \sim 0.9$ in our case), that is hard to be stabilized. However, our calculations and results rely on a specific (and parameterized) opacity table used here. Updated opacity data could produce a radiative region that occurs at a different location and could undergo a different evolution, which would change the required additional mass that needs to be accreted in order to enrich the outer envelope. Furthermore, despite this work being based on the latest considerations regarding the quantity and properties of the materials responsible for enriching the atmosphere, our knowledge of the materials that Jupiter might have accreted is still incomplete. Yet, in our setup, the hypothesis of a radiative zone that prevents downward mixing is rather unlikely. Alternative scenarios such as an inverted gradient of helium instead of heavy elements as well as further investigation of the topic are required to resolve Jupiter's metallicity puzzle.

5.6 An inverted Y gradient?

If an inverted Z gradient is unlikely, an inverted Y gradient might be a solution. It could allow a significant decrease in the mean molecular weight of Jupiter's outer envelope. Such scenario does not require any additional physical mechanism as He phase separation is a well established phenomenon in Jupiter. An inverted Y gradient can thus appear naturally. The distribution of the mass fraction of helium in such scenario is shown in Fig. 5.24. The presence of a stable region (as in Subsection 5.5.4) would imply that helium demixing has not affected the whole molecular envelope. Consequently, the atmospheric helium abundance, measured by Galileo ($Y/(X+Y) = 0.238$), would not represent the entirety of the molecular envelope. Instead, the depletion of helium beneath the stable region would be more pronounced than expected. This could work as the draining timescale of helium through the stable layer is long (estimated at approximately 1 Gyr, personal communication with Steve Markham) and given the fact that demixing is expected to occur late in the evolution.

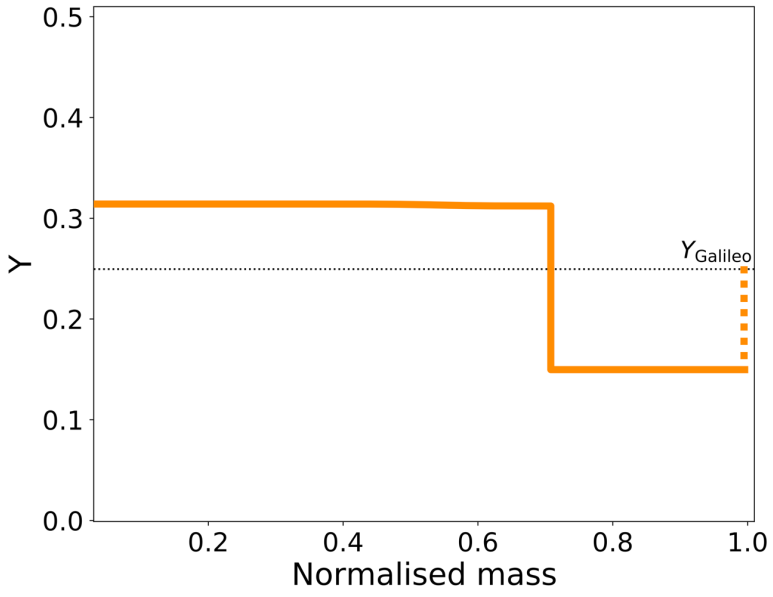

FIGURE 5.24: Mass fraction of helium as a function of normalised mass in a model with an inverted Y gradient.

To assess if it is a plausible solution, the first step is to check if models with an inverted Y gradient could fit the gravity data. I hence ran MCMC calculations. Figure 5.25 shows the results. We in fact find models that satisfy better the gravitational moments compared to models with an inverted Z gradient. The scenario of an inverted Y gradient may thus be promising from the point of view of the gravity data. Further work is needed. Nevertheless, homogeneous evolution models have been quite successful at predicting the age and luminosity of Jupiter, suggesting that He phase separation has not or just started in the planets. Investigating evolution models with such differentiation of helium would be required to assess the plausibility of the inverted Y gradient scenario.

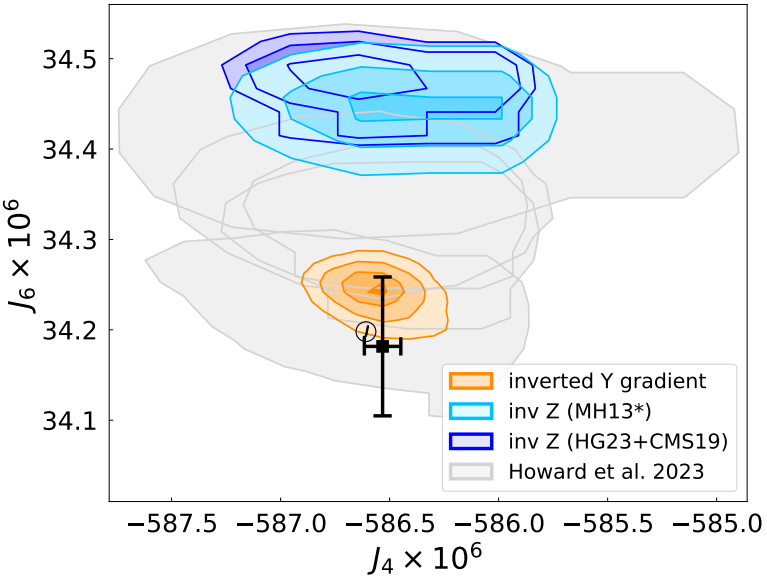

FIGURE 5.25: J_6 vs J_4 for models with an inverted Y gradient.

Chapter 6

Exoplanets

Contents

Throughout my thesis, while I mainly worked on Jupiter, I also ventured into the field of exoplanets. This was the opportunity for me to expand the scope of my research to encompass extra-solar systems. I tried to apply the work I carried out on Jupiter and see the consequences on exoplanets. In this chapter, I will present my contributions to several papers, in which I conducted calculations of evolution models of giant exoplanets.

6.1 Introduction

Exoplanets have been discovered only 30 years ago. These other worlds are far from the Earth, the closest being around Proxima Centauri, located at 4 light years from us. However, discoveries of exoplanets are now confirmed on a daily basis and interest keeps growing. While we have seen that we have very accurate observations on our giant planets (see Section 2.1), we have limited information about exoplanets. But with now more than 5 000 exoplanets discovered in our galaxy, statistical analyses may lead to a better understanding of their properties. So far, we have observed a diverse array of exoplanets, leading to the term "exoplanet zoo". While the initial discoveries were primarily dominated by hot Jupiters [Seager and Deming, 2010], the most common types nowadays appear to be super-Earths and sub-Neptunes [Howard et al., 2010, Mayor et al., 2011, Winn and Fabrycky, 2015]. Understanding the characteristics of these exoplanets, particularly the giant planets, was a subject of great interest in my thesis. These planets, although not the most numerous, are intriguing due to their composition, as they contain primordial gas within their envelopes or atmospheres, mainly composed of hydrogen and helium. The determination of their bulk composition will provide valuable insights into their formation processes. To determine their internal composition, we primarily rely on measurements of their radius and mass. It is through evolution models (see Section 2.4) that we can infer their composition. Additionally, knowledge of their age is crucial, which is obtained by measuring the age of the host star.

However, we now have the capability to measure the composition of exoplanet atmospheres through spectroscopy. Guillot et al. [2022] presents a list of 17 atoms and molecules detected in the atmospheres of about 40 planets and for which the detection can be considered as reliable. This list is growing steadily, as exemplified by JWST's recent detection of SO_2 [Tsai et al., 2023]. The three main methods are: transit spectroscopy, direct imaging, and Doppler spectroscopy (a detailed description of these methods can be found in Madhusudhan [2019]). In transit spectroscopy, light from the star passes through the exoplanet's atmosphere, and the resulting spectrum contains absorption features of the molecules present in the atmosphere. The properties of these atmospheres are then derived using atmospheric retrieval models [Madhusudhan, 2018], which depend on various parameters and factors such as composition, temperature-pressure profiles, presence of clouds. By employing these spectroscopic techniques, various molecules have been detected in exoplanet atmospheres, including

water [Sing et al., 2016] and even other molecules now, like carbon dioxide [JWST Transiting Exoplanet Community Early Release Science Team et al., 2023]. The importance of spectroscopy and atmospheric composition lies in its potential to provide information about the planet's formation, notably where these planets formed and how they migrated in their early stages. Nevertheless, it remains a challenge to link formation and atmosphere [Mordasini et al., 2016]. Different formation pathways (core accretion, pebble accretion, gravitational instability) may lead to variations in the carbon-oxygen (C/O) ratio, for instance. But obtaining measurements of different chemical components in exoplanet atmospheres is hard due to the diverse spectral signatures that occur at different wavelengths. Additionally, the present composition of the atmosphere may not exactly reflect its composition at the time of formation, planetary evolution is hence crucial to assess.

It is important to note that information obtained from spectroscopy of an exoplanet's atmosphere may not necessarily represent its interior composition. Knowledge gained from our solar system's gas giants should be applied when studying exoplanets. The inhomogeneity of Jupiter's atmosphere [Li et al., 2017] and its interior [Miguel et al., 2022] serve as guides. Measurements of the composition are essentially done in the upper atmosphere of exoplanets (between 10^{-2} and 10^{-4} bar [Gandhi et al., 2023]). Modellers have to bear in mind that such measurements are probably not representative of the bulk composition of a planet. Future measurements, in particular of atmospheric metallicities could help constrain the interiors (see also Müller and Helled [2023a]) and offer insights into the formation mechanisms.

Exoplanets models often simply consist of a compact core surrounded by a homogeneous envelope of hydrogen and helium. In Bloot et al. [2023], using the same MCMC approach that I used to study Jupiter's interior, we question whether we can distinguish between exoplanets with a homogeneous or an inhomogeneous structure, using a sample of 37 giant planets. We found that more massive planets have smaller core mass fractions and are less enriched in heavy elements. However, we cannot distinguish between homogeneous and inhomogeneous interiors at this stage. Further investigation is needed but Plato's future measurements (radii, masses, ages) in addittion to a better atmospheric characterization will help make progress in this area.

Another complication that has affected our comprehension of exoplanetary internal structures is the phenomenon of inflation, in particular for hot Jupiters. These highly irradiated planets ($T_{\rm eq} > 1\,000$ K) exhibit radii larger than those predicted by models [Thorngren and Fortney, 2018, Fortney et al., 2021]. The mechanisms behind this phenomenon can be attributed to either a reduction in the planets' cooling rates or an internal energy source. Notably, tidal dissipation [Bodenheimer et al., 2001], suggesting that strong periodic tides can heat the planet's interior, or ohmic dissipation [Batygin and Stevenson, 2010], where currents generated by interactions between atmospheric winds and the magnetic field dissipate, potentially serve as an internal heat source.

This inflation appears to be linked to the level of irradiation: less-irradiated planets ($T_{\rm eq} < 1\,000$ K) are not as inflated, whereas heavily irradiated ones ($T_{\rm eq} > 1\,500$ K) exhibit significant inflation. Guillot and Showman [2002] have hence modelled this mechanism by considering an internal heat source as a fraction ϵ of the irradiation. Thorngren and Fortney [2018] conducted a Bayesian analysis to quantify the fraction of irradiation involved in this process.

Improving our modelling to refine the characterization of exoplanetary systems is key. In a few years only, Plato [Rauer et al., 2014] will provide accurate measurements of the radii, masses and also ages of many planetary systems. Understanding the interior structure and evolution of giant planets enables us to infer their bulk compositions from these measurements. We showed in Howard and Guillot [2023] that including non-ideal mixing effects in the EOS can affect the calculated radii by up to 6%, therefore affecting the inferred composition potentially significantly. We will now detect warm giant planets [Müller and Helled, 2023b], with properties that are more similar to our solar system giants. The possibility to measure atmospheric properties and abundances for temperate transiting giant planets, i.e. with atmospheric properties closer to our own (including the presence of storm-driving condensing species like water) is extremely promising. This is becoming a reality with the discovery of more long-period transiting exoplanets, in particular thanks to the TESS mission [Ricker et al., 2015] helped with a large number of ground-based follow-up telescopes including ASTEP (Antarctica Search for Transiting ExoPlanets [Guillot et al., 2015]).

6.2 Case studies

In the following subsections, I used evolution models to constrain newly discovered transiting giant planets, observed by TESS and also ASTEP. Most of them are in multiple systems, where planets are sometimes in mean motion resonance, with TTV (transit-timing variation) observations which can allow to infer the mass of the planets. In multiple systems, the planets must have the same age. The constraints found for their composition depend on this age and are inherently linked [Havel et al., 2011]. We can therefore refine the relative compositions of the planets more precisely. This is important in order to understand their formation pathways. Here, I provide my contributions to several discoveries of exoplanets. The paragraphs have directly been taken from the text I have provided in the corresponding papers.

6.2.1 TOI-1130

This subsection has been taken from Korth et al. [2023]. The parameters of the star and the planets of the system are summarized in Table 6.1.

TABLE 6.1: Stellar and planetary parameters of the TOI-1130 system. Adapted from Korth et al. [2023].

Stellar parameters	TOI-1130
Spectral type	K6-K7
$M_\star$ $[M_\odot]$	0.71 ± 0.02
$R_\star$ $[R_\odot]$	0.68 ± 0.02
$T_{\rm eff}$ [K]	4350 ± 60
Age [Gyr]	3.2 – 5

Planetary parameters	TOI-1130 b	TOI-1130 c
P [days]	4.07445 ± 0.00046	8.350231 ± 0.000098
M_p $[M_\oplus]$	19.28 ± 0.97	325.69 ± 5.59
R_p $[R_\oplus]$	3.56 ± 0.13	$13.32^{+1.55}_{-1.41}$
ρ_p [g.cm^{-3}]	2.34 ± 0.26	$0.75^{+0.31}_{-0.21}$
a [AU]	0.04457 ± 0.00036	0.07191 ± 0.00058
$T_{\rm eq}$ [K]	632.17 ± 12.60	497.70 ± 9.92

Knowing the radii and masses of several planets in the same system is extremely useful because one can remove the age uncertainty when comparing the planets to each other, thereby providing important constraints for formation models [Havel et al., 2011]. Here we use CEPAM [Guillot and Morel, 1995] and a non-grey atmosphere [Parmentier et al., 2015] to model the evolution of both planets in the system. We assume simple structures consisting of a central dense core and a surrounding hydrogen and helium envelope of solar composition. The core is assumed to be made with 50% of ices and 50% of rocks. Figure 6.1 shows the resulting evolution models and observational constraints for both planets in the system. For guidance, we compare them to similarly simple models of Jupiter and Neptune (which have very similar masses as TOI-1130 c and TOI-1130 b, respectively), knowing that the ensemble of possibilities regarding their structure and composition is much wider [Helled and Fortney, 2020]. TOI-1130 c is found to have a small enrichment in heavy elements, with a core of less than 20 $M_\oplus$. This is lower to what was obtained for our simple model of Jupiter. We point out however that Jupiter's enrichment corresponds to a much wider range of possibilities, i.e. 8 - 46 $M_\oplus$ [Guillot et al., 2022]. TOI-1130 b is slightly more massive than Neptune but is found to contain less hydrogen and helium, assuming a similar composition core. With the same hypotheses, as shown in Fig. 6.1, the envelope of TOI-1130 b must be smaller than 0.5 $M_\oplus$ (i.e., less than 3% of the mass of TOI-1130 b compared to about 10% of the mass of Neptune). Determining atmospheric abundances and possibly ice-to-rock ratios in TOI-1130 b and TOI-1130 c will be key to understanding the structure of ice and gas giants and the formation of these planetary systems [Guillot et al., 2022].

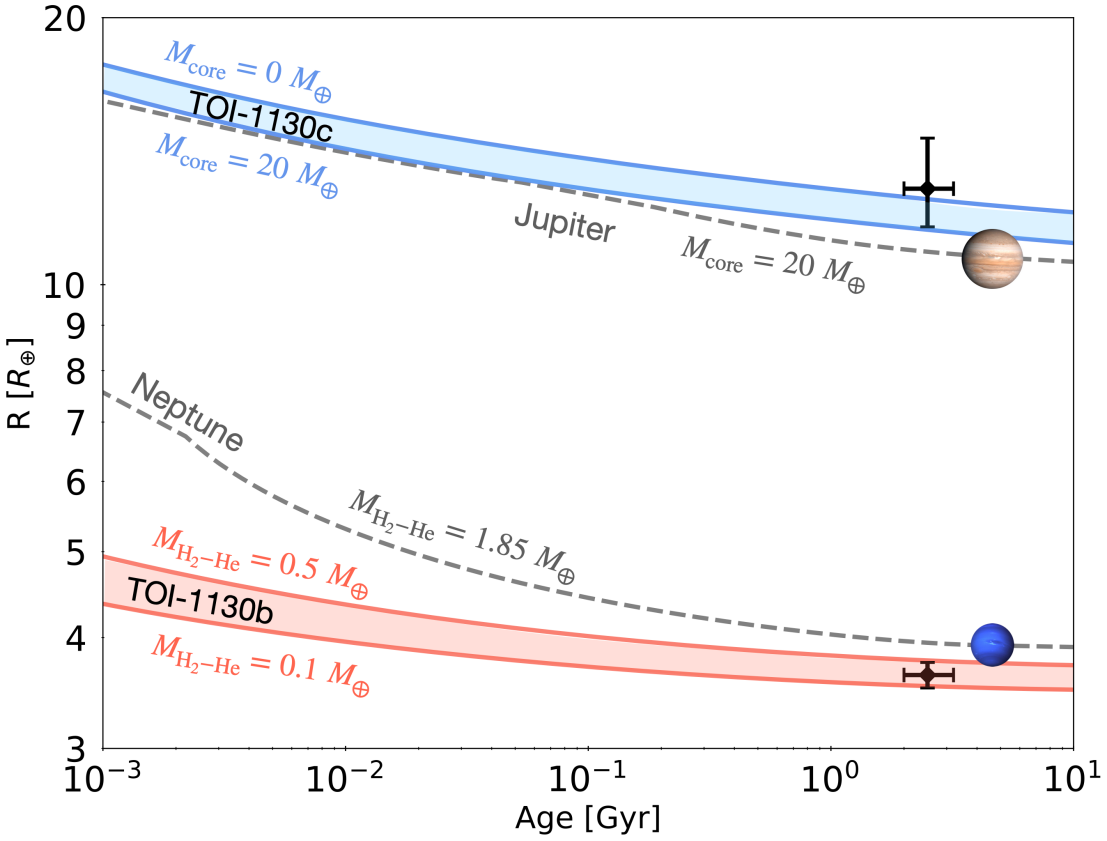

FIGURE 6.1: Evolution models of TOI-1130 b and TOI-1130 c, compared to Neptune and Jupiter, respectively. All models assume a central ice-rock core overlain by a solar composition hydrogen-helium envelope. The M_{core} value corresponds to the mass of the core while M_{env} corresponds to the mass of the envelope. The range of envelope mass compatible with the observational constraints is shown for TOI-1130 b and compared to a similarly simple model of Neptune. For TOI-1130 c, only an upper limit on the core mass can be derived. For all cases, additional uncertainties on the core and envelope masses arise due to the unknown interior composition, temperature structure, and EOS uncertainties. The black error bars correspond to observational constraints on the age and the radius of TOI-1130 b and TOI-1130 c. Taken from Korth et al. [2023].

6.2.2 TOI-2525

This subsection has been taken from Trifonov et al. [2023]. The parameters of the star and the planets of the system are summarized in Table 6.2.

We model the evolution of both planets in the system, using CEPAM [Guillot and Morel, 1995, Guillot et al., 2006] and a nongray atmosphere [Parmentier et al., 2015], to provide constraints on their interiors. We assume simple structures consisting of a central dense core surrounded by a hydrogen and helium envelope of solar composition. The core is assumed to be made of 50% ices and 50% rocks. Figure 6.2 shows the resulting evolution models. The core mass of TOI-2525 c is found to be between 20 and 43 $M_\oplus$. This indicates that the enrichment in heavy elements of TOI-2525 c could be comparable to Jupiter's, which is between 8 and 46 $M_\oplus$ [Guillot et al., 2022]. With a radius similar to Saturn's (1.08 times larger) but 3.4 times less massive than Saturn,

TABLE 6.2: Stellar and planetary parameters of the TOI-2525 system. Adapted from Trifonov et al. [2023].

Stellar parameters	TOI-2525
Spectral type	K8V
$M_\star$ $[M_\odot]$	0.849 ± 0.042
$R_\star$ $[R_\odot]$	0.785 ± 0.031
$T_{\rm eff}$ [K]	5096 ± 80
Age [Gyr]	$3.99^{+4.30}_{-2.60}$

Planetary parameters	TOI-2525 b	TOI-2525 c
P [days]	$23.288^{+0.001}_{-0.002}$	$49.260^{+0.001}_{-0.001}$
M_p $[M_{\rm Jup}]$	$0.088^{+0.005}_{-0.004}$	$0.709^{+0.034}_{-0.034}$
R_p $[R_{\rm Jup}]$	0.88 ± 0.02	0.98 ± 0.02
ρ_p [g.cm^{-3}]	$0.174^{+0.016}_{-0.015}$	$1.014^{+0.084}_{-0.076}$
a [AU]	$0.1511^{+0.0025}_{-0.0025}$	$0.2491^{+0.0041}_{-0.0042}$
$T_{\rm eq}$ [K]	513	399

TOI-2525 b is an uncommon example of a very low density and inflated planet with an equilibrium temperature close to 500 K. The H–He envelope of TOI-2525 b is found to be between 19 and 24 $M_\oplus$. The case of TOI-2525 b is challenging for the traditional core accretion formation scenario. With our simple modeling of TOI-2525 b, such a small envelope hints that the accretion of H–He has potentially been hindered. Characterizing the atmospheres of both planets of the system would be very useful to understand their structure and formation. Not many inflated Neptune-mass planets are known, making TOI-2525 b a useful addition to the sample of transiting planets with a measured mass. The low density, and thus large scale height, of TOI-2525 b makes it a good target for a future atmospheric investigation with transmission spectroscopy.

6.2.3 TOI-2000

This subsection has been taken from Sha et al. [2023]. The parameters of the star and the planets of the system are summarized in Table 6.3.

Measuring the atmospheric metallicity of both planets could help us understand their structure and origin. Using CEPAM [Guillot and Morel, 1995, Guillot et al., 2006] and a non-grey atmosphere [Parmentier et al., 2015], we model the evolution of both planets in the system assuming a simple structure consisting of a central rocky core surrounded by a H–He envelope of Solar composition. Figure 6.3 shows the results. The core mass of TOI-2000 c is between 36 and 46 $M_\oplus$, about twice as large as Saturn's total mass of heavy elements (16.5 to 21 $M_\oplus$; Mankovich and Fuller [2021]). The presumed H–He envelope of TOI-2000 b must be smaller than 0.1 $M_\oplus$ (1 per cent of the mass of the planet), in line with Figure 11 of Sha et al. [2023], which indicates that the radius of TOI-2000 b is up to 10 per cent smaller than the radius predicted by the theoretical

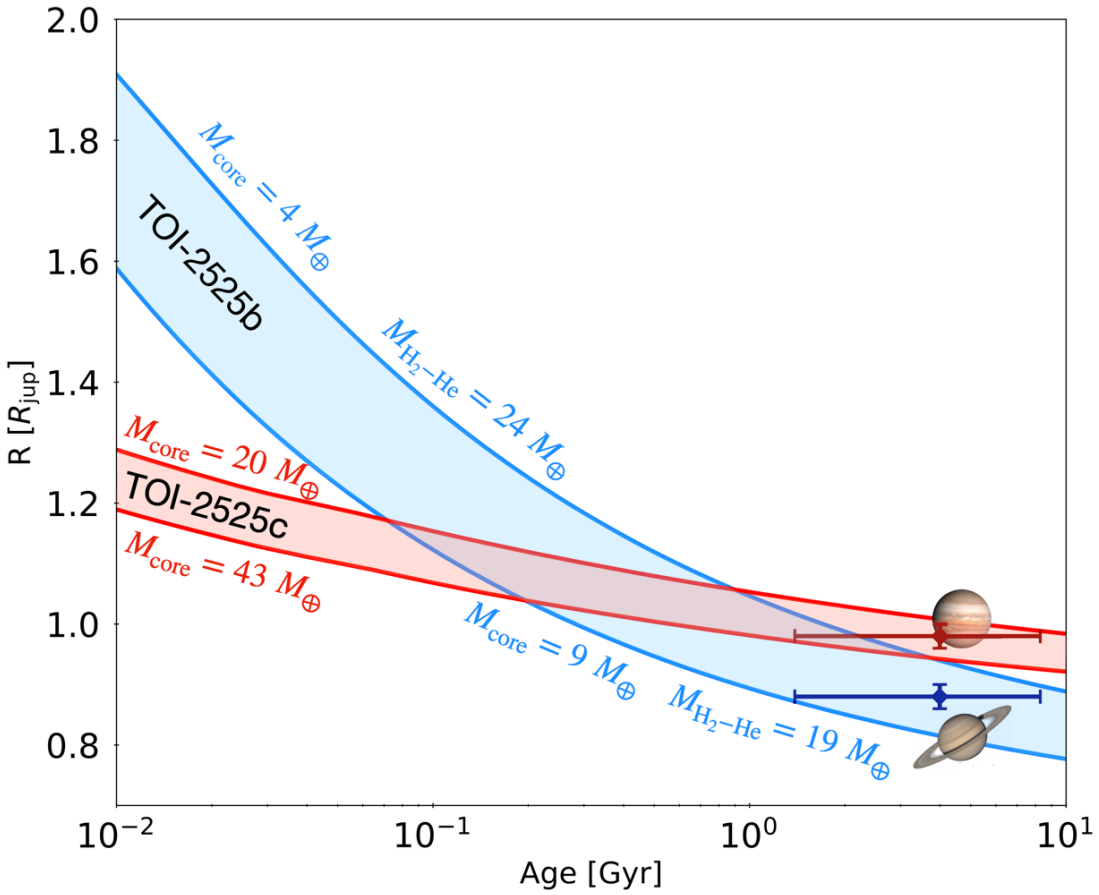

FIGURE 6.2: Evolution models of TOI-2525 b and c. All models assume a central ice–rock core surrounded by a hydrogen–helium envelope of solar composition. For both planets, the range of core masses is shown. For TOI-2525 b, the range of envelope masses is also shown. The error bars correspond to observational constraints on their age and radius compared to the ones of Jupiter and Saturn. Taken from Trifonov et al. [2023].

mass–radius curve of Zeng et al. [2019] for planets with 1 per cent H_2 envelope. Overall, this analysis implies that both planets likely contain a proportion of heavy elements that is significantly larger than that of planets with similar mass in the Solar System.

6.2.4 TOI-588

This subsection has been taken from Vowell et al. [2023]. The parameters of the star and the companion of the system are summarized in Table 6.4.

Using CEPAM [Guillot and Morel, 1995], we calculate evolutionary tracks of TOI-588 b. Our models are based on the same approach as in Bouchy et al. [2011], using the analytical atmospheric boundary conditions from Guillot [2010]. Our fiducial model has a solar metallicity interior ($Z^*_{\rm interior} = Z_\odot$) and thermal and visible mean opacities set to $\kappa^*_{\rm th} = 0.04\,{\rm g.cm^{-2}}$ and $\kappa^*_{\rm v} = 0.024\,{\rm g.cm^{-2}}$, respectively. As shown in Fig. 6.4, this model reproduces the observed radius for the age of TOI-588 b. Because of the brown

TABLE 6.3: Stellar and planetary parameters of the TOI-2000 system. Adapted from Sha et al. [2023].

Stellar parameters	TOI-2000
Spectral type	G5-G6
$M_\star$ $[M_\odot]$	$1.082^{+0.059}_{-0.050}$
$R_\star$ $[R_\odot]$	$1.134^{+0.037}_{-0.036}$
$T_{\rm eff}$ [K]	5611 ± 85
Age [Gyr]	5.3 ± 2.7

Planetary parameters	TOI-2000 b	TOI-2000 c
P [days]	$3.098330^{+0.000021}_{-0.000019}$	$9.1270550^{+0.0000073}_{-0.0000072}$
M_p $[M_{\rm Jup}]$	$0.0347^{+0.0077}_{-0.0075}$	$0.257^{+0.015}_{-0.014}$
R_p $[R_{\rm Jup}]$	0.241 ± 0.014	$0.727^{+0.028}_{-0.027}$
ρ_p [g.cm^{-3}]	$3.07^{+0.94}_{-0.78}$	$0.829^{+0.111}_{-0.096}$
a [AU]	$0.04271^{+0.00076}_{-0.00067}$	$0.0878^{+0.0016}_{-0.0014}$
$T_{\rm eq}$ [K]	1488^{+122}_{-160}	1038^{+84}_{-111}

TABLE 6.4: Stellar and brown dwarf parameters of the TOI-588 system. Adapted from Vowell et al. [2023].

Stellar parameters	TOI-588
Spectral type	B
$M_\star$ $[M_\odot]$	$2.383^{+0.10}_{-0.095}$
$R_\star$ $[R_\odot]$	$1.863^{+0.087}_{-0.082}$
$T_{\rm eff}$ [K]	10400 ± 800
Age [Gyr]	0.153 ± 0.024

Brown dwarf parameters	TOI-588 b
P [days]	39.471814 ± 0.000014
M_p $[M_{\rm Jup}]$	$68.0^{+7.4}_{-7.1}$
R_p $[R_{\rm Jup}]$	$1.580^{+0.074}_{-0.070}$
ρ_p [g.cm^{-3}]	$21.3^{+4.0}_{-3.4}$
a [AU]	$0.3058^{+0.0042}_{-0.0041}$
$T_{\rm eq}$ [K]	1237^{+73}_{-61}

dwarf's large mass and intrinsic luminosity ($L_{\rm int} = 4 \times 10^{30}$ erg.s^{-1}), we find that the interior is entirely convective and therefore its evolution is not affected by changes of the interior opacities. The energy supplied by tidal dissipation, $L_{\rm tides} \approx 10^{25}$ erg.s^{-1} for a tidal quality factor ($Q' = 10^6$) (e.g., Bodenheimer et al. [2001]), is also too low to affect the evolution, as is that due to internal dissipation $L_{\rm dissipation} \approx 10^{27}$ erg.s^{-1} (see Thorngren and Fortney [2018]). The radius of TOI-588 b is thus mainly affected by three factors: the initial formation entropy (here we assume a hot start initial entropy of $S = 13.4\,k_b$/baryon), the deep interior mean molecular weight and the atmospheric opacity (see Guillot [2005]). Figure 6.4 shows that the latter is by far the dominant effect: when multiplying the atmospheric opacities by 2 over their fiducial values, we obtain a theoretical radius that is 25% larger (at the measured age) than our fiducial

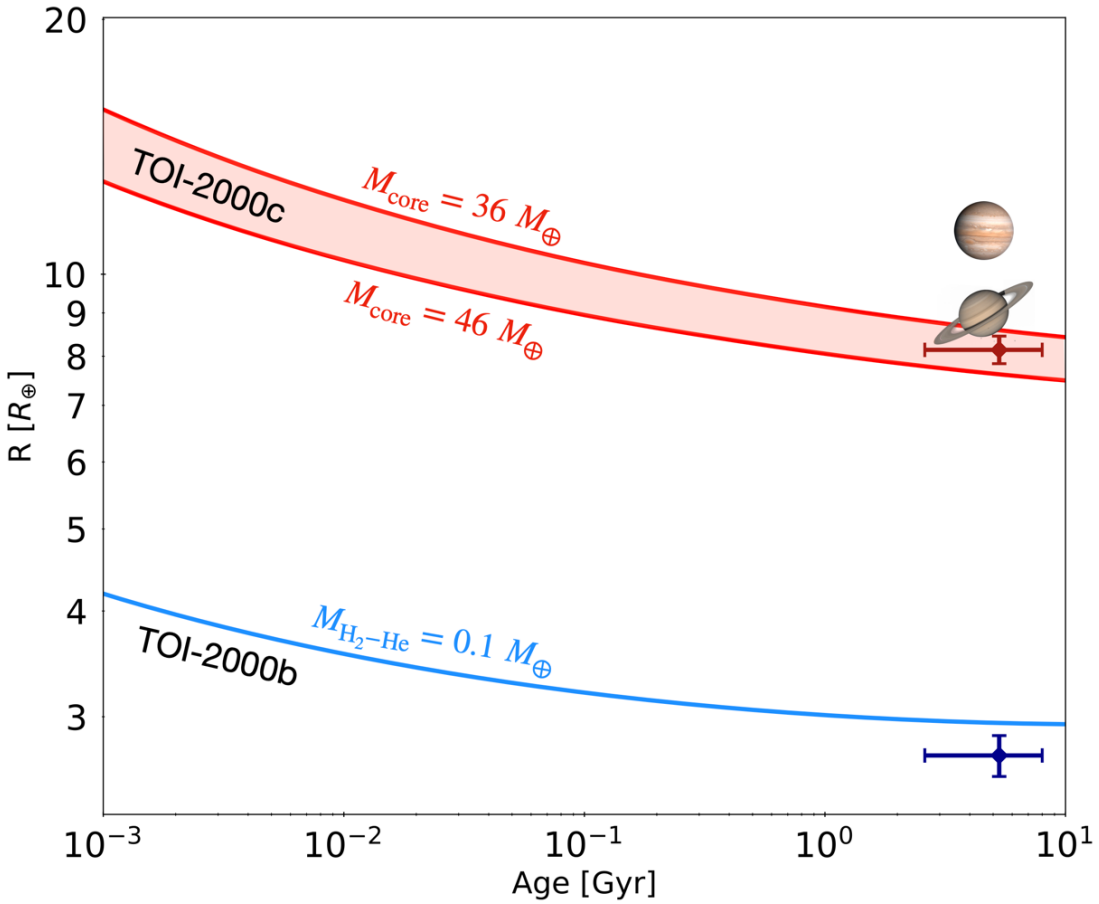

FIGURE 6.3: Evolution models of TOI-2000 b and c. All models assume a central ice–rock core surrounded by a hydrogen–helium envelope of solar composition. For TOI-2000 b, an upper limit for the mass of the envelope is given while for TOI-2000 c, the range of core masses is shown. The error bars correspond to observational constraints on their age and radius compared to the ones of Jupiter and Saturn.

model and clearly incompatible with the observations. On the other hand, when multiplying the interior metallicity by a factor 5 (equivalent to adding $4.2\,M_{\rm Jup}$ of heavy elements in its interior) the radius change remains limited. Although a wider ensemble of dedicated evolution models should be calculated, this already shows that observations of TOI-588 b with the James Webb Space Telescope would be extremely important, by independently yielding its atmospheric metallicity (that we predict should be solar) and intrinsic luminosity (our evolution models predict $T_{\rm eff} = 2630\,K$).

6.2.5 TOI-615, TOI-622, TOI-2641

This subsection has been taken from Psaridi et al. [2023]. The parameters of the star and the planet of the systems are summarized in Table 6.5.

Using CEPAM [Guillot and Morel, 1995] and a nongray atmosphere [Parmentier et al., 2015], we model the evolution of TOI-615 b, TOI-622 b, and TOI-2641 b. We assume

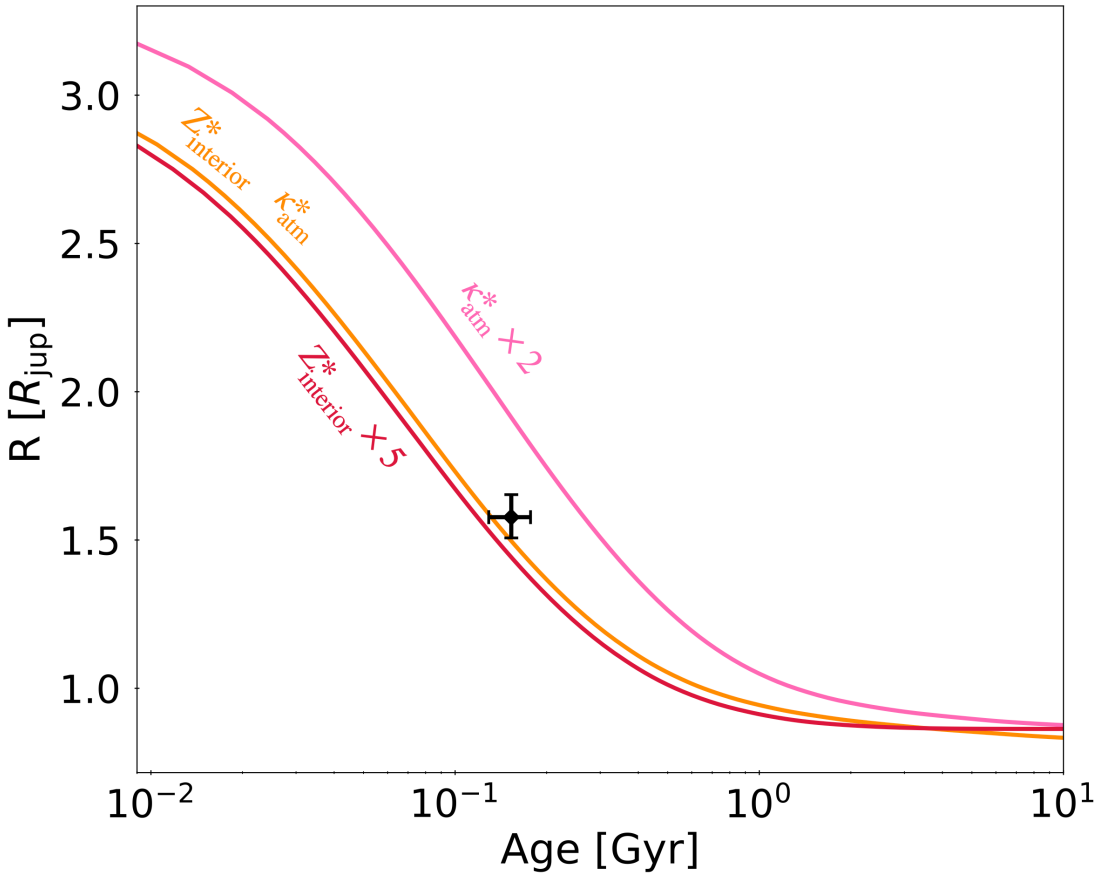

FIGURE 6.4: The radius evolution of TOI-588 b. The black point signifies the measured age and radius with 1 σ error bars. The orange line is our fiducial evolutionary model. The pink line multiplies the atmospheric opacities of the fiducial model by 2, and the red line multiplies the interior metallicity by 5. Taken from Vowell et al. [2023].

simple structures consisting of a central dense core surrounded by a hydrogen and helium envelope of solar composition. The core is assumed to be composed of 50% ices and 50% rocks, by mass. Since all these planets are highly irradiated, we account for the dissipation of energy in the interior, following the approach of Guillot and Showman [2002]: A fraction ϵ of the irradiation luminosity $L_\star$ is assumed to be dissipated at the bottom of the envelope and included in the evolution calculations.

The source and magnitude of this dissipation is still under investigation, but using a statistical approach, Thorngren and Fortney [2018] estimate for exoplanets with these irradiation levels that $\epsilon \sim 2\%$. This yields a luminosity due to internal dissipation $L^*_{\text{dissipation}} = 10^{28}$, 10^{27} and 5×10^{27} erg/s, for TOI-615 b, TOI-622 b, and TOI-2641 b respectively. In Fig. 6.5, we explore how observational constraints and uncertainties on dissipation affect what we can infer on the bulk composition of these planets. We show the results of calculations with our fiducial dissipation luminosity compared to models with $L^*_{\text{dissipation}}$ divided by 10 (for TOI-615 b and TOI-2641 b) or 100 (for TOI-622 b). After a few to hundred million years, our models predict that the planetary radii remain constant, due to internal heating that exceeds the planet's cooling luminosity.

TABLE 6.5: Stellar and planetary parameters of the TOI-615, TOI-622 and TOI-2641 systems. Adapted from Psaridi et al. [2023].

Stellar parameters	TOI-615	TOI-622	TOI-2641
Spectral type	F2V	F6V	F9V
$M_\star$ $[M_\odot]$	1.449 ± 0.087	1.313 ± 0.079	1.16 ± 0.07
$R_\star$ $[R_\odot]$	1.732 ± 0.055	1.415 ± 0.047	1.336 ± 0.055
$T_{\rm eff}$ [K]	6850 ± 100	6400 ± 100	6100 ± 100
Age [Gyr]	1.7 ± 0.3	0.9 ± 0.2	10.8 ± 9.0

Planetary parameters	TOI-615 b	TOI-622 b	TOI-2641 b
P [days]	$4.6615983^{+0.0000025}_{-0.0000016}$	$6.402513^{+0.000031}_{-0.000054}$	$4.880974^{+0.000023}_{-0.000037}$
M_p $[M_{\rm Jup}]$	$0.435^{+0.086}_{-0.082}$	$0.303^{+0.069}_{-0.072}$	$0.386^{+0.022}_{-0.036}$
R_p $[R_{\rm Jup}]$	$1.693^{+0.052}_{-0.057}$	$0.824^{+0.028}_{-0.029}$	$1.615^{+0.462}_{-0.640}$
ρ_p $[\rho_{\rm Jup}]$	$0.084^{+0.018}_{-0.018}$	$0.507^{+0.126}_{-0.126}$	$0.092^{+0.078}_{-0.109}$
a [AU]	$0.0678^{+0.0031}_{-0.0026}$	$0.0708^{+0.0052}_{-0.0059}$	$0.0607^{+0.0042}_{-0.0043}$
$T_{\rm eq}$ [K]	1666^{+24}_{-24}	1388^{+22}_{-22}	1387^{+23}_{-23}

We find that these planets tend to be significantly enriched in heavy elements. Defining an approximate bulk metallicity as $Z \approx M_{\rm core}/M_{\rm tot}$ and assuming $Z_\odot = 0.015$, we find $Z/Z_\odot = 17$ to 31 for TOI-615 b, 43 to 52 for TOI-622 b, and 7 to 29 for TOI-2641 b. For comparison, Jupiter and Saturn have bulk metallicities $Z/Z_\odot$ ranging from 4 to 14, depending on assumptions on interior models [Guillot et al., 2022]. For TOI-615 b, and to some extent for TOI-622 b, heat dissipation is found to be the dominant factor controlling the inferred composition. Spectroscopic observations of these planets (e.g., with JWST) would be highly valuable for the possibility to constrain the atmospheric metallicity and relate it to the bulk metallicity.

6.2.6 TOI-199

This subsection has been taken from Hobson et al. [2023]. The parameters of the star and the planets of the system are summarized in Table 6.6.

We model the evolution of both planets in the system using CEPAM [Guillot and Morel, 1995] and a non-grey atmosphere [Parmentier et al., 2015]. We assume simple structures consisting of a central dense core surrounded by a hydrogen and helium envelope of solar composition. The core is assumed to be composed of 50% ices and 50% rocks. The EOS used for hydrogen and helium accounts for non-ideal mixing effects [Howard and Guillot, 2023, Chabrier et al., 2019].

Figure 6.6 shows the resulting evolution models and the observational constraints. Defining an approximate bulk metallicity as $Z \approx M_{\rm core}/M_{\rm tot}$ and assuming $Z_\odot = 0.015$, we find $Z/Z_\odot = 7$ to 21 for TOI-199 b. This is comparable to what we obtain for a similarly simple model of Saturn although we stress that Saturn's enrichment corresponds to a wider range of possibilities [between 12 and 15 according to Mankovich and Fuller,

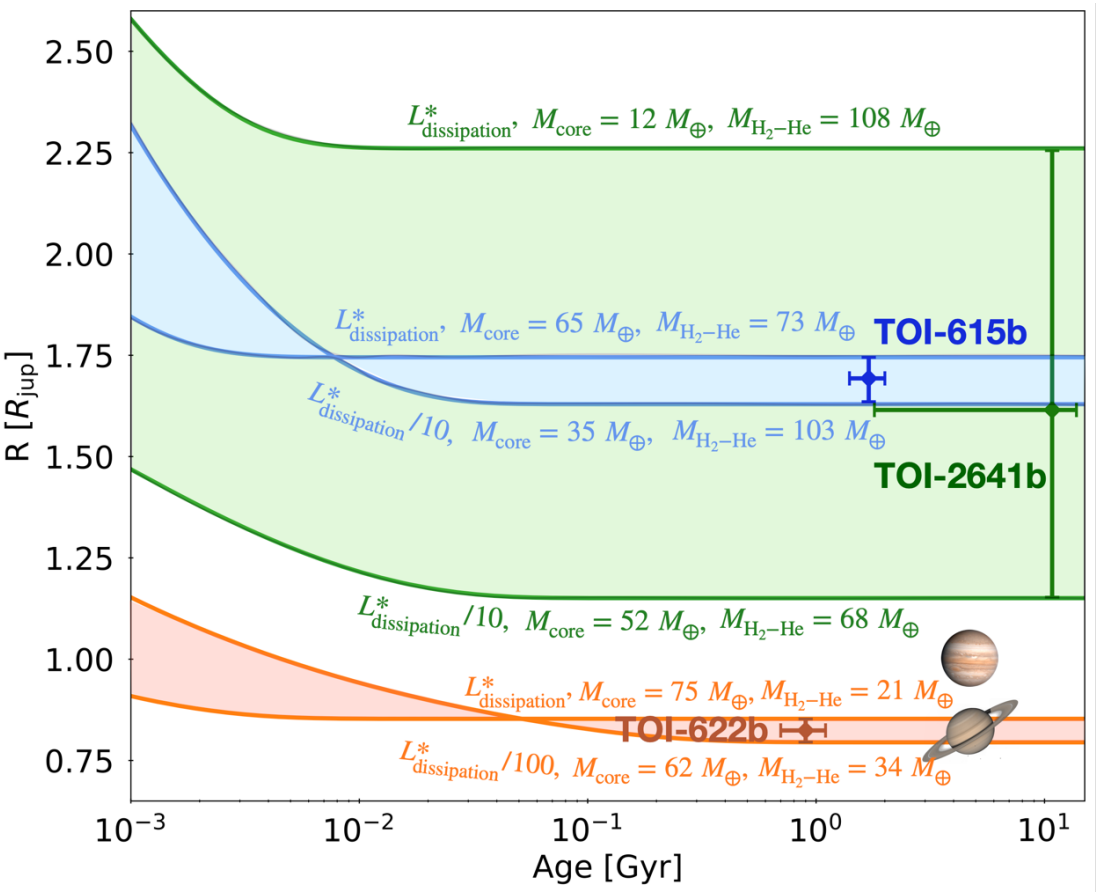

FIGURE 6.5: Evolution models of TOI-615 b, TOI-622 b, and TOI-2641 b. All models assume a central ice-rock core surrounded by a hydrogen-helium envelope of solar composition. Models account for dissipation of energy in the interior due to important irradiation and $L^*_{\text{dissipation}}$ corresponds to our fiducial dissipation luminosity. For each planet, the ranges of core masses and envelope masses are shown. The errorbars correspond to observational constraints on their age and radius, compared to the ones of Jupiter and Saturn. Taken from Psaridi et al. [2023].

2021]. However, most of the uncertainty comes from the poor constraint on the age of the system. An accurate determination of its age would thus greatly help to constrain the bulk metallicity of TOI-199 b [see also Müller and Helled, 2023a]. We unfortunately do not have a measurement of the radius of TOI-199 c. Using the same evolution models and a composition with cores between 5 and 60 $M_\oplus$ (bulk metallicity between 3 and 41), we obtain expected radii of TOI-199 c between 0.64 and 1.04 R_J.

The intrinsic luminosities of both planets are between a third to one time the present-day luminosity of Jupiter, implying that their atmospheric structure is mostly governed by the irradiation that they receive [see Parmentier et al., 2015]. With photospheric temperatures expected to range between 250 and 350 K, these planets are ideal for the observation of the consequence of condensation of water in giant planet atmospheres [see Guillot et al., 2022].

TABLE 6.6: Stellar and planetary parameters of the TOI-199 system. Adapted from Hobson et al. [2023].

Stellar parameters	TOI-199
Spectral type	G9V
$M_\star$ $[M_\odot]$	$0.936^{+0.003}_{-0.005}$
$R_\star$ $[R_\odot]$	0.820 ± 0.003
$T_{\rm eff}$ [K]	5255^{+12}_{-10}
Age [Gyr]	$0.8^{+1.2}_{-0.6}$

Planetary parameters	TOI-199 b	TOI-199 c
P [days]	$104.8589^{+0.0014}_{-0.0016}$	$271.67^{+0.36}_{-0.37}$
M_p $[M_{\rm Jup}]$	$0.1872^{+0.0287}_{-0.0274}$	$0.243^{+0.010}_{-0.011}$
R_p $[R_{\rm Jup}]$	0.83 ± 0.06	
ρ_p [g.cm^{-3}]	$3.07^{+0.94}_{-0.78}$	
a [AU]	0.4257 ± 0.015	
$T_{\rm eq}$ [K]	325	

6.3 Summary

I have studied several systems, that already show the diversity of exoplanetary systems. TOI-1130 hosts both a Neptune-like and a Jupiter-like planet. TOI-2525 contains a Jupiter-like planet and an inflated Neptune-like planet, larger than Saturn. Meanwhile, TOI-2000 possesses a Saturn-like and a Neptune-like planet. Interestingly, these three systems share a similar structure, featuring an inner planet with a mass of about a dozen Earth masses and an outer planet with a mass of the order of a hundred Earth masses. This could suggest similarities in their formation pathways. In contrast to these systems, TOI-588 has a companion that is a brown dwarf. Brown dwarfs are believed to form differently from planets. TOI-615, TOI-622, and TOI-2461 are systems where planets are highly irradiated by their star. Understanding the mechanisms responsible for the inflation of such planets is crucial, as it helps constrain their bulk composition. Finally, TOI-199 hosts two Saturn-like planets. Given their distance from the star and their temperature, they are warmer than other planets studied here, making them excellent candidates to investigate processes like cloud condensation.

From these systems, we have observed that it is possible to derive certain constraints on the internal structures of planets using evolution models and measurements of their radius, mass, and age. Our models rely on several assumptions, particularly the EOS. For most of my calculations, I used the SCvH95 EOS; however, in the case of TOI-199, I employed the more up-to-date HG23 EOS developed in Howard and Guillot [2023] which incorporates non-ideal mixing effects. For the case of TOI-2525 c, I show in Fig. 6.7 evolution models using the HG23+CMS19 EOS. The inferred bulk metallicity of the planet is significantly affected compared to what previously obtained with the SCvH95 EOS (Fig. 6.2). While the bulk metallicity $Z_{\rm planet}/Z_\odot$ was between 6 and 13, it

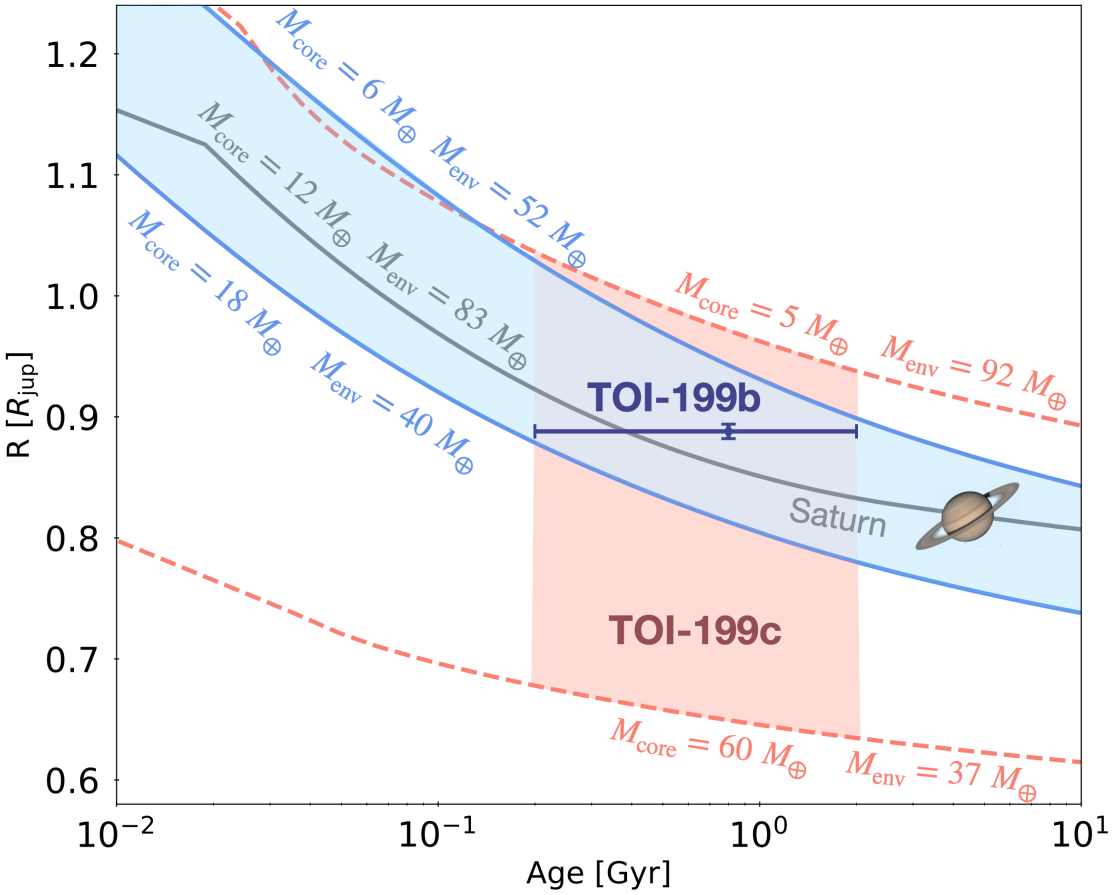

FIGURE 6.6: Evolution models of TOI-199 b and TOI-199 c compared to a simple model for Saturn. All models assume a central ice-rock core surrounded by a hydrogen and helium envelope of solar composition. M_{core} corresponds to the mass of the ice/rock core while M_{env} corresponds to the mass of the solar-composition envelope. The range of M_{core} and M_{env} compatible with the observational constraints is shown for TOI-199 b. The blue error bar corresponds to observational constraints on the age and the radius of TOI-199 b. We also show the range of radii expected for likely extreme compositions of TOI-199 c in red.

is now between 1 and 9. The effect on TOI-2525 b is less significant given the less massive hydrogen and helium envelope. The methodologies used to study Jupiter, including last generation EOSs, can hence be applied on exoplanets, leading to important implications for their inferred bulk composition.

Even if I studied only a few systems, it remains worthwhile to conduct a comparison and consider these works collectively. Of course, it is essential to acknowledge that these systems can have very different properties: some planets are highly irradiated, their host star can be different, they do not have the same ages. For 10 specific planets, I calculated the bulk metallicity $Z_{planet} = M_{core}/M_{planet}$ relative to the solar metallicity $Z_\odot = 0.015$. Figure 6.8 illustrates the bulk metallicity of the 10 chosen planets. Despite the limited sample size, a noticeable mass-metallicity relationship emerges, with more massive giant planets appearing less enriched than the less massive ones. This negative correlation is consistent with the core accretion model (see Section 5.1.1), where gas poor in heavy

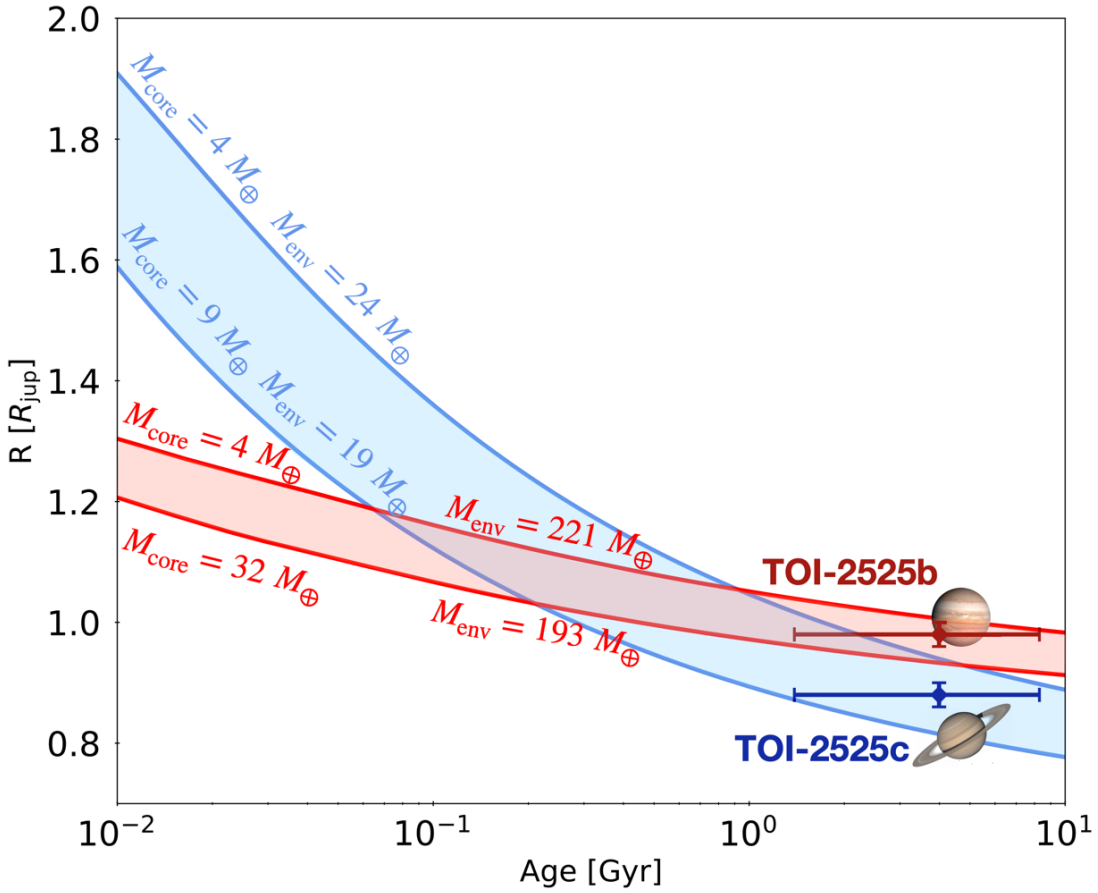

FIGURE 6.7: Evolution models of TOI-2525 b and c (same as in Fig. 6.2) but using the HG23+CMS19 EOS [Howard and Guillot, 2023].

elements is accreted around a pure heavy-element core. It has already been observed by Thorngren et al. [2016] but also in [Mordasini et al., 2014] using planetary population synthesis. Interestingly, the planets in our solar system seem to align well with this trend in the relationship. We see for TOI-2525 c the impact of using a new EOS on the calculated bulk metallicity, as previously mentioned. Müller and Helled [2023a] already stressed the influence of the EOS on the mass-metallicity relationship. Expanding the sample size would yield valuable insights, especially looking at planets more massive than Jupiter which are lacking here.

A strong assumption of our models is the use of an envelope of solar composition. Measuring the metallicity of the host stars would be important, as it may be connected to the planet's metallicity [Guillot et al., 2006]. But Thorngren et al. [2016] found only a weak correlation between the metallicity of the planet and the one of its parent star. Recently, Teske et al. [2019] did not find any correlation. Furthermore, the most massive giant planets still seem to be enriched, raising the issue that they should possess envelopes with a substantial amount of heavy elements. TOI-622 b is a good example (Fig. 6.8) but its host star has a rather high metallicity of 0.09 ± 0.07. One plausible

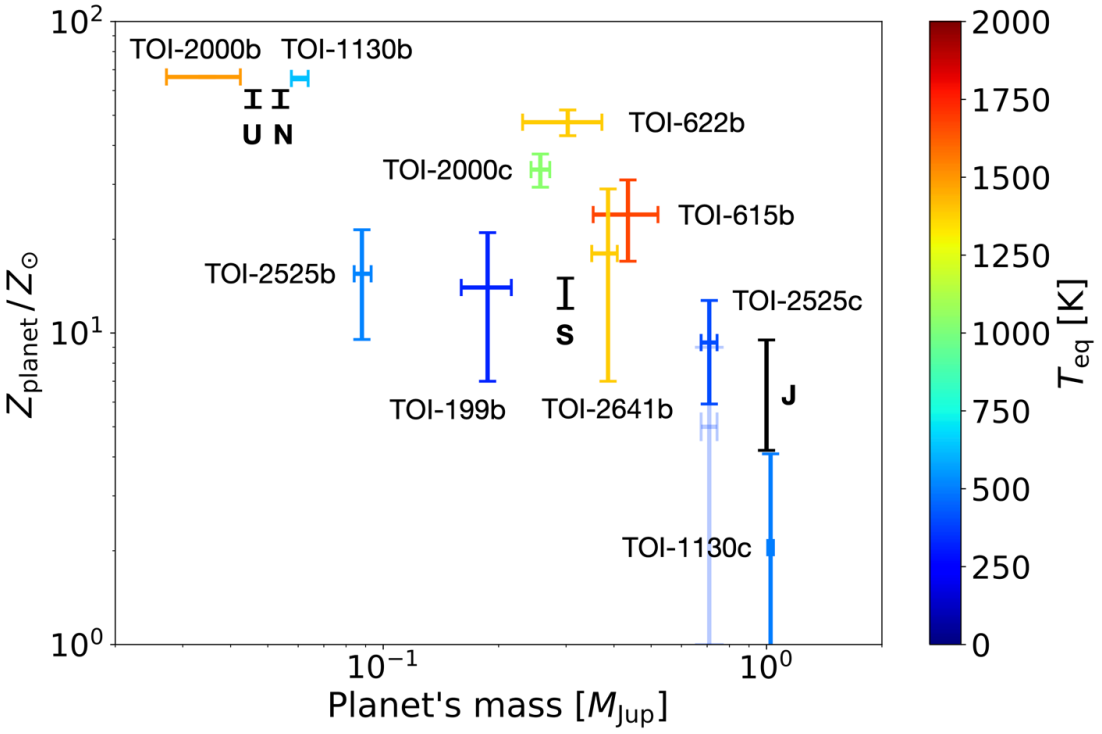

FIGURE 6.8: Heavy element enrichment (relative to the Sun's) as a function of mass, for 10 giant exoplanets I studied. Bulk metallicities for Jupiter [Guillot et al., 2022], Saturn [Mankovich and Fuller, 2021], Uranus and Neptune [Helled et al., 2020b] are shown in black. The bulk metallicity for TOI-2525 c using the HG23+CMS19 EOS is shown with transparency.

scenario for hot Jupiters is that they could enrich their envelopes by accreting dust-rich gas in proximity to their host stars [Morbidelli et al., 2023].

Measuring atmospheric metallicities (e.g., with JWST) will be helpful to improve the inferred compositions. Comparing metallicities of exoplanets and their host star will provide valuable information about their formation mechanisms. We should keep in mind that the star's atmospheric metallicity may not be similar to the one of the planets, as seen in our solar system. Furthermore, the measured metallicity of the planets may not fully represent their entire interior composition. Future missions like Plato, with more accurate measurements of radii, masses, and ages, will undoubtedly improve the constraints on many exoplanetary systems and lead to a better understanding of their formation.

Chapter 7

Conclusions

Contents

This thesis provided me with an excellent opportunity to dive into the field of planetary sciences. It was a dangerous dive as I spent three years exploring mostly Jupiter but also giant exoplanets. Throughout my research, I learnt how giant planets work, the methodologies to study them, and how important they are to study. I will summarize here the main aspects of this thesis and provide some future prospects.

7.1 Summary

The Juno mission has revealed the remarkable complexity of Jupiter's interior. Over the past few years, many models emerged to satisfy the extremely accurate measurements of the gravitational moments provided by the mission [Wahl et al., 2017, Debras and Chabrier, 2019, Ni, 2019, Nettelmann et al., 2021, Militzer et al., 2022]. In this context, while previous contributions focused on several models, my collaborators and I carried out Markov chain Monte Carlo calculations to explore a wider range of interior models of Jupiter.

In Miguel et al. [2022], we explored two types of structure: the traditional three-layer model and the dilute core paradigm which received a renewed interest since Juno. We conducted calculations using several H-He EOSs. By examining the heavy element distribution, we robustly demonstrated that the envelope of Jupiter is inhomogeneous, with a heavy-element enrichment in the interior relative to the outer envelope. This work has implications for formation and evolution models which should therefore be consistent with such present inhomogeneous interior structure. This may discriminate different formation pathways. Nevertheless, the models required invoking a warmer interior ($T_{1\mathrm{bar}}$ between 170 and 180 K) than expected (166 K from Galileo).

Another conclusion was the importance of the EOS. In particular, non-ideal mixing effects due to interactions between hydrogen and helium are non-negligible. Omitting these effects can lead to a relative error in density of up to 15% for Jupiter and Saturn. I thus developed an EOS table to incorporate the non-ideal mixing effects [Howard and Guillot, 2023]. This table, along with intrinsic uncertainties in the EOS, was then taken into account when calculating interior models. We allowed for modifications in the EOS which satisfied a thermodynamical constraint, while previous models were freely perturbing the EOS. However, if we impose a deep entropy in agreement or only modestly above the Galileo probe value, the modifications of the EOS found to reproduce Juno's gravity data are even more significant than suggested by comparisons of different EOSs and our work on non-ideal effects.

Specific emphasis was then placed on determining the extent of the dilute core [Howard et al., 2023]. The size of the dilute core holds major importance to understand the origin and evolution of Jupiter. Previous interior models [Debras and Chabrier, 2019, Militzer

et al., 2022] pointed to solutions with very extended dilute cores (up to 60% of Jupiter's mass), in tension with evolution models including mixing in the planetary interior. I have identified alternative solutions, featuring less extended dilute cores ($\sim$ 20% of the planet's mass), in better agreement with evolution models [Müller et al., 2020]. This implies a dilute core that represent no more than $\sim$ 60 $M_\oplus$, in agreement also with the encompassed mass in the dilute core found in Saturn [Mankovich and Fuller, 2021], suggesting a formation scenario consistent for both gas giants of our solar system. The results in Howard et al. [2023] are in line with what we found in Miguel et al. [2022]. We confirm that the interior of Jupiter may be warmer than expected. We find the compact core to be between 0 and 6 $M_\oplus$. The total mass of heavy elements is between 18 and 33 $M_\oplus$, which are lower limits given the possibility of superadiabatic regions [Guillot, 1995, Leconte and Chabrier, 2012, Leconte et al., 2017]. These numbers are important constraints in the context of the formation of the planet.

Despite the progress made, our models still struggle to match the measured supersolar abundance of heavy elements in Jupiter's atmosphere (about three times the protosolar value). In Miguel et al. [2022], the heavy element abundance in the atmosphere (assumed to be the same as in the outer envelope) was set to 1$\times$ protosolar; and in Howard et al. [2023], it was set to 1.3$\times$ protosolar. One potential solution is the presence of an inverted Z gradient, namely an inward decrease of the heavy element abundance. Such inverted Z gradient, at the location of helium rain ($\sim$ Mbar level), was already suggested by Debras and Chabrier [2019]. However, it requires to accrete an excessive amount of material and at a late stage which is not possible as it would bring material with the wrong isotopic composition. We hence investigated the hypothesis of an inverted Z gradient, due to a radiative zone, located at upper regions ($\sim$ kbar level) and established early. Nevertheless, the radiative zone being moved to deeper regions as Jupiter evolves, it implies a substantial enrichment in the early stages that cannot remain stable. We have concluded that the presence of an inverted Z gradient inside Jupiter is unlikely. An inverted Y gradient might be a solution. Still, the interior of Jupiter remains shrouded in mystery.

Furthermore, I had the opportunity to apply my findings on Jupiter to giant exoplanets. The knowledge gained from this research is valuable for understanding exoplanets. By using the newly developed HG23 EOS [Howard and Guillot, 2023] to include the non-ideal mixing effects, I showed that the calculated radii may be affected by up to 6%. The inferred bulk composition can hence be significantly impacted (see the case of TOI-2525 c). I have studied several systems, which showed the diversity of exoplanetary systems. Some of them (TOI-1130, TOI-2525, TOI-2000) featured an inner planet with a mass of about a dozen Earth masses and an outer planet with a mass of the order of a hundred Earth masses, suggesting potential similarities in their formation pathways. I also looked at highly irradiated planets (TOI-615 b, TOI-622 b, TOI-2641 b), warm

giant planets (TOI-199 b) and even brown dwarfs (TOI-588 b), which are opportunities to improve our understanding of the inflation of certain exoplanets, of processes like cloud condensation and of particular formation mechanisms, respectively. A comparison of these systems, despite the limited sample size, has confirmed the mass-metallicity relationship, with more massive giant planets being less enriched than the less massive ones [Thorngren et al., 2016].

Overall, this thesis has contributed to a better understanding of the internal structure of Jupiter. We confirmed its complexity, shed light to some important uncertainties and could provide some insights towards a better agreement with models of its evolution. This work is important as it can then be applied to the field of exoplanets.

7.2 Outlook

This thesis opens up promising avenues for future research and development. The interior of Jupiter is still not perfectly understood. Finding solutions in better agreement with the measurements of the atmospheric composition remains a challenge. This problem also arises in Saturn, potentially indicating that we may be missing an important physical ingredient. Different paths of research can be envisioned to make progress.

The EOS remains a source of uncertainty, with variations between different H-He EOSs that can reach up to 5%, in particular between 0.01 and a few Mbar. Ab initio simulations lead to slightly different predictions in this warm dense matter regime. This is due to different assumptions in the EOS calculations (e.g., choice of exchange correlation functional) but also due to interpolation methods in the EOS tables [Howard et al., 2023]. In order to account for this uncertainty, we allowed for modifications of the EOS by perturbing the adiabats. Comparing these modified EOSs to Hugoniot data to see if they still agree with experiments would be interesting. Looking back at our approach, we may have been too restrictive in modifying the EOS, especially at low and high pressures where we did not allow any perturbations. However, the EOS at these pressure levels is still uncertain at the percent level. Militzer et al. [2022] were able to reach supersolar abundances of heavy element by reducing the density by only a few percent but on a wide range of pressures (by 2% from 1 kbar or by 3% from 100 kbar, all the way to the center of the planet) and without using the thermodynamical constraint that we proposed in Howard et al. [2023]. It is imperative to continue investigating the EOS in the future, conducting more experiments and numerical calculations. Experiments would be highly valuable, even on a few pressure-temperature points, to check if the EOSs we are using are correct. My postdoc in Zürich with Ravit Helled and her group will be an opportunity to work on this topic. Guglielmo Mazzola is conducting QMC

simulations to study the hydrogen EOS. We plan to test these calculations in future models of giant planets. However, QMC calculations are predicting a denser EOS so far, which will probably not help Jupiter interior models. But this shows additional uncertainty on the EOS and should motivate further investigation.

In Howard et al. [2023], we found interior models in better agreement with evolution models. Continuing to work on reconciling formation, evolution and interior structure is important. Building models consistent with all these aspects but also with the potential constraints from the planet's oscillations as normal modes have been detected [Gaulme et al., 2011, Durante et al., 2022] would be valuable. Working on a better treatment of the composition in interior models would also be important. To model the dilute core, we used an error function in CEPAM but the Z profiles of the composition gradients are quite different in evolution calculations from Müller et al. [2020] using MESA. In my postdoc, I hope that I will be able to learn to handle this code and consider more realistic compositional distributions in interior models. Evolution models that include mixing in the planetary interior could also be improved by incorporating more physics (core erosion, helium rain). Furthermore, I would also like to expand the scope of my research by working on planets like Uranus and Neptune. In the context of such planets, it is necessary to have a better treatment of the composition in interior model calculations.

Finally, further work on applying the lessons learnt with Jupiter and other solar system planets to exoplanets is needed. Bloot et al. [2023] has started to apply composition gradients to exoplanets. But it appears that we still do not have the capabilities to distinguish between homogeneous and inhomogeneous interiors in exoplanets. With JWST that is now providing measurements of the atmospheric metallicities and future missions like Plato that will provide accurate measurements of radii, masses and ages, we will be able to refine the constraints on the bulk compositions. In this thesis, I studied only a dozen of exoplanetary systems. As demographics is key in this field, expanding the sample size would yield valuable insights, especially looking at planets more massive than Jupiter which were lacking here. Therefore, I would like to continue working on Jupiter, to expand my research to other giant planets of the solar system and to continue studying exoplanets.

References

M. M. Abbas, H. Kandadi, A. LeClair, R. K. Achterberg, F. M. Flasar, V. G. Kunde, B. J. Conrath, G. Bjoraker, J. Brasunas, R. Carlson, D. E. Jennings, and M. Segura. D/H ratio of Titan from Observations of the Cassini/Composite Infrared Spectrometer. ApJ, 708(1):342–353, Jan. 2010. doi: 10.1088/0004-637X/708/1/342.

J. Aléon. Multiple Origins of Nitrogen Isotopic Anomalies in Meteorites and Comets. ApJ, 722(2):1342–1351, Oct. 2010. doi: 10.1088/0004-637X/722/2/1342.

Y. Alibert, J. Venturini, R. Helled, S. Ataiee, R. Burn, L. Senecal, W. Benz, L. Mayer, C. Mordasini, S. P. Quanz, and M. Schönbächler. The formation of Jupiter by hybrid pebble-planetesimal accretion. Nature Astronomy, 2:873–877, Aug. 2018. doi: 10.1038/s41550-018-0557-2.

E. Anders and N. Grevesse. Abundances of the elements: Meteoritic and solar. Geochim. Cosmochim. Acta, 53(1):197–214, Jan. 1989. doi: 10.1016/0016-7037(89)90286-X.

B. A. Archinal, M. F. A'Hearn, E. Bowell, A. Conrad, G. J. Consolmagno, R. Courtin, T. Fukushima, D. Hestroffer, J. L. Hilton, G. A. Krasinsky, G. Neumann, J. Oberst, P. K. Seidelmann, P. Stooke, D. J. Tholen, P. C. Thomas, and I. P. Williams. Report of the IAU Working Group on Cartographic Coordinates and Rotational Elements: 2009. Celestial Mechanics and Dynamical Astronomy, 109(2):101–135, Feb. 2011. doi: 10.1007/s10569-010-9320-4.

M. Asplund, A. M. Amarsi, and N. Grevesse. The chemical make-up of the Sun: A 2020 vision. A&A, 653:A141, Sept. 2021. doi: 10.1051/0004-6361/202140445.

S. K. Atreya, P. R. Mahaffy, H. B. Niemann, M. H. Wong, and T. C. Owen. Composition and origin of the atmosphere of Jupiter - an update, and implications for the extrasolar giant planets. Planet. Space Sci., 51(2):105–112, Feb. 2003. doi: 10.1016/S0032-0633(02)00144-7.

H. H. Aumann, J. Gillespie, C. M., and F. J. Low. The Internal Powers and Effective Temperatures of Jupiter and Saturn. ApJ, 157:L69, July 1969. doi: 10.1086/180388.

J. N. Bahcall, M. H. Pinsonneault, and G. J. Wasserburg. Solar models with helium and heavy-element diffusion. Reviews of Modern Physics, 67(4):781–808, Oct. 1995. doi: 10.1103/RevModPhys.67.781.

I. Baraffe. Latest News on the Physics of Brown Dwarfs. In V. Joergens, editor, 50 Years of Brown Dwarfs, volume 401 of Astrophysics and Space Science Library, page 141, Jan. 2014. doi: 10.1007/978-3-319-01162-2_8.

B. Basillais and J. M. Huré. Nested spheroidal figures of equilibrium - III. Connection with the gravitational moments J_{2n}. MNRAS, 520(1):1504–1525, Mar. 2023. doi: 10.1093/mnras/stad151.

K. Batygin and D. J. Stevenson. Inflating Hot Jupiters with Ohmic Dissipation. ApJ, 714(2):L238–L243, May 2010. doi: 10.1088/2041-8205/714/2/L238.

M. Bazot, S. Bourguignon, and J. Christensen-Dalsgaard. A Bayesian approach to the modelling of α Cen A. MNRAS, 427(3):1847–1866, Dec. 2012. doi: 10.1111/j.1365-2966.2012.21818.x.

A. Becker, W. Lorenzen, J. J. Fortney, N. Nettelmann, M. Schöttler, and R. Redmer. Ab Initio Equations of State for Hydrogen (H-REOS.3) and Helium (He-REOS.3) and their Implications for the Interior of Brown Dwarfs. ApJS, 215(2):21, Dec. 2014. doi: 10.1088/0067-0049/215/2/21.

A. Bhattacharya, C. Li, S. K. Atreya, P. G. Steffes, S. M. Levin, S. J. Bolton, T. Guillot, P. Gupta, A. P. Ingersoll, J. I. Lunine, G. S. Orton, F. A. Oyafuso, J. H. Waite, A. Belloti, and M. H. Wong. Highly depleted alkali metals in Jupiter's deep atmosphere. arXiv e-prints, art. arXiv:2306.12546, June 2023. doi: 10.48550/arXiv.2306.12546.

Bibring J. P. La quête spatiale de l'émergence de la vie, 2019. URL https://youtu.be/QAIXHlKwlIY.

N. Biver, R. Moreno, D. Bockelée-Morvan, A. Sandqvist, P. Colom, J. Crovisier, D. C. Lis, J. Boissier, V. Debout, G. Paubert, S. Milam, A. Hjalmarson, S. Lundin, T. Karlsson, M. Battelino, U. Frisk, D. Murtagh, and Odin Team. Isotopic ratios of H, C, N, O, and S in comets C/2012 F6 (Lemmon) and C/2014 Q2 (Lovejoy). A&A, 589:A78, May 2016. doi: 10.1051/0004-6361/201528041.

S. Bloot, Y. Miguel, M. Bazot, and S. Howard. Exoplanet interior retrievals: core masses and metallicities from atmospheric abundances. MNRAS, 523(4):6282–6292, Aug. 2023. doi: 10.1093/mnras/stad1873.

D. Bockelée-Morvan. Cometary science with ALMA. Ap&SS, 313(1-3):183–189, Jan. 2008. doi: 10.1007/s10509-007-9641-2.

D. Bockelée-Morvan, U. Calmonte, S. Charnley, J. Duprat, C. Engrand, A. Gicquel, M. Hässig, E. Jehin, H. Kawakita, B. Marty, S. Milam, A. Morse, P. Rousselot,

S. Sheridan, and E. Wirström. Cometary Isotopic Measurements. Space Sci. Rev., 197(1-4):47–83, Dec. 2015. doi: 10.1007/s11214-015-0156-9.

P. Bodenheimer, D. N. C. Lin, and R. A. Mardling. On the Tidal Inflation of Short-Period Extrasolar Planets. ApJ, 548(1):466–472, Feb. 2001. doi: 10.1086/318667.

S. J. Bolton, J. Lunine, D. Stevenson, J. E. P. Connerney, S. Levin, T. C. Owen, F. Bagenal, D. Gautier, A. P. Ingersoll, G. S. Orton, T. Guillot, W. Hubbard, J. Bloxham, A. Coradini, S. K. Stephens, P. Mokashi, R. Thorne, and R. Thorpe. The Juno Mission. Space Sci. Rev., 213(1-4):5–37, Nov. 2017. doi: 10.1007/s11214-017-0429-6.

G. V. Boriskov, A. I. Bykov, R. I. Il'kaev, V. D. Selemir, G. V. Simakov, R. F. Trunin, V. D. Urlin, V. E. Fortov, and A. N. Shuikin. Shock-wave compression of solid deuterium at a pressure of 120 gpa. Doklady Physics, 48(10):553–555, Oct 2003. doi: 10.1134/1.1623535. URL https://doi.org/10.1134/1.1623535.

W. J. Borucki, D. Koch, G. Basri, N. Batalha, T. Brown, D. Caldwell, J. Caldwell, J. Christensen-Dalsgaard, W. D. Cochran, E. DeVore, E. W. Dunham, A. K. Dupree, T. N. Gautier, J. C. Geary, R. Gilliland, A. Gould, S. B. Howell, J. M. Jenkins, Y. Kondo, D. W. Latham, G. W. Marcy, S. Meibom, H. Kjeldsen, J. J. Lissauer, D. G. Monet, D. Morrison, D. Sasselov, J. Tarter, A. Boss, D. Brownlee, T. Owen, D. Buzasi, D. Charbonneau, L. Doyle, J. Fortney, E. B. Ford, M. J. Holman, S. Seager, J. H. Steffen, W. F. Welsh, J. Rowe, H. Anderson, L. Buchhave, D. Ciardi, L. Walkowicz, W. Sherry, E. Horch, H. Isaacson, M. E. Everett, D. Fischer, G. Torres, J. A. Johnson, M. Endl, P. MacQueen, S. T. Bryson, J. Dotson, M. Haas, J. Kolodziejczak, J. Van Cleve, H. Chandrasekaran, J. D. Twicken, E. V. Quintana, B. D. Clarke, C. Allen, J. Li, H. Wu, P. Tenenbaum, E. Verner, F. Bruhweiler, J. Barnes, and A. Prsa. Kepler Planet-Detection Mission: Introduction and First Results. Science, 327(5968): 977, Feb. 2010. doi: 10.1126/science.1185402.

W. Bottke, D. Vokrouhlicky, R. Marshall, D. Nesvorny, A. Morbidelli, R. Deienno, S. Marchi, L. Dones, and H. Levison. The Collisional Evolution of the Primordial Kuiper Belt, Its Destabilized Population, and the Trojan Asteroids. arXiv e-prints, art. arXiv:2307.07089, July 2023. doi: 10.48550/arXiv.2307.07089.

F. Bouchy, M. Deleuil, T. Guillot, S. Aigrain, L. Carone, W. D. Cochran, J. M. Almenara, R. Alonso, M. Auvergne, A. Baglin, P. Barge, A. S. Bonomo, P. Bordé, S. Csizmadia, K. de Bondt, H. J. Deeg, R. F. Díaz, R. Dvorak, M. Endl, A. Erikson, S. Ferraz-Mello, M. Fridlund, D. Gandolfi, J. C. Gazzano, N. Gibson, M. Gillon, E. Guenther, A. Hatzes, M. Havel, G. Hébrard, L. Jorda, A. Léger, C. Lovis, A. Llebaria, H. Lammer, P. J. MacQueen, T. Mazeh, C. Moutou, A. Ofir, M. Ollivier, H. Parviainen, M. Pätzold, D. Queloz, H. Rauer, D. Rouan, A. Santerne, J. Schneider, B. Tingley, and G. Wuchterl. Transiting exoplanets from the CoRoT space mission. XV. CoRoT-15b: a brown-dwarf transiting companion. A&A, 525:A68, Jan. 2011. doi: 10.1051/0004-6361/201015276.

Bruno G. De l'infinito universo et mondi. 1584.

S. Brygoo, P. Loubeyre, M. Millot, J. R. Rygg, P. M. Celliers, J. H. Eggert, R. Jeanloz, and G. W. Collins. Evidence of hydrogen−helium immiscibility at Jupiter-interior conditions. Nature, 593(7860):517–521, Jan. 2021. doi: 10.1038/s41586-021-03516-0.

G. Budde, C. Burkhardt, and T. Kleine. Molybdenum isotopic evidence for the late accretion of outer Solar System material to Earth. Nature Astronomy, 3:736–741, May 2019. doi: 10.1038/s41550-019-0779-y.

A. Burrows, M. Marley, W. B. Hubbard, J. I. Lunine, T. Guillot, D. Saumon, R. Freedman, D. Sudarsky, and C. Sharp. A Nongray Theory of Extrasolar Giant Planets and Brown Dwarfs. ApJ, 491(2):856–875, Dec. 1997. doi: 10.1086/305002.

L. Caillabet, S. Mazevet, and P. Loubeyre. Multiphase equation of state of hydrogen from ab initio calculations in the range 0.2 to 5 g/cc up to 10 ev. Phys. Rev. B, 83: 094101, Mar 2011. doi: 10.1103/PhysRevB.83.094101. URL https://link.aps.org/doi/10.1103/PhysRevB.83.094101.

J. K. Campbell and S. P. Synnott. Gravity field of the Jovian system from Pioneer and Voyager tracking data. AJ, 90:364–372, Feb. 1985. doi: 10.1086/113741.

T. Cavalié, J. Lunine, and O. Mousis. A subsolar oxygen abundance or a radiative region deep in Jupiter revealed by thermochemical modelling. Nature Astronomy, Mar. 2023. doi: 10.1038/s41550-023-01928-8.

P. M. Celliers, P. Loubeyre, J. H. Eggert, S. Brygoo, R. S. McWilliams, D. G. Hicks, T. R. Boehly, R. Jeanloz, and G. W. Collins. Insulator-to-conducting transition in dense fluid helium. Phys. Rev. Lett., 104:184503, May 2010. doi: 10.1103/PhysRevLett.104.184503. URL https://link.aps.org/doi/10.1103/PhysRevLett.104.184503.

G. Chabrier and F. Debras. A New Equation of State for Dense Hydrogen-Helium Mixtures. II. Taking into Account Hydrogen-Helium Interactions. ApJ, 917(1):4, Aug. 2021. doi: 10.3847/1538-4357/abfc48.

G. Chabrier and A. Y. Potekhin. Equation of state of fully ionized electron-ion plasmas. Phys. Rev. E, 58:4941–4949, Oct 1998. doi: 10.1103/PhysRevE.58.4941. URL https://link.aps.org/doi/10.1103/PhysRevE.58.4941.

G. Chabrier, D. Saumon, W. B. Hubbard, and J. I. Lunine. The Molecular-Metallic Transition of Hydrogen and the Structure of Jupiter and Saturn. ApJ, 391:817, June 1992. doi: 10.1086/171390.

G. Chabrier, S. Mazevet, and F. Soubiran. A New Equation of State for Dense Hydrogen-Helium Mixtures. ApJ, 872(1):51, Feb. 2019. doi: 10.3847/1538-4357/aaf99f.

M. E. Davies, V. K. Abalakin, M. Bursa, T. Lederle, J. H. Lieske, R. H. Rapp, P. K. Seidelman, A. T. Sinclair, V. G. Teifel, and Y. S. Tjuflin. Report of the Iau/iag COSPAR Working Group on Cartographic Coordinates and Rotational Elements of the Planets and Satellites - 1985. Celestial Mechanics, 39(1):103–113, May 1986. doi: 10.1007/BF01232291.

B. T. de Gregorio, R. M. Stroud, G. D. Cody, L. R. Nittler, A. L. David Kilcoyne, and S. Wirick. Correlated microanalysis of cometary organic grains returned by Stardust. 46(9):1376–1396, Sept. 2011. doi: 10.1111/j.1945-5100.2011.01237.x.

F. Debras and G. Chabrier. New Models of Jupiter in the Context of Juno and Galileo. ApJ, 872(1):100, Feb. 2019. doi: 10.3847/1538-4357/aaff65.

W. C. Demarcus. The constitution of Jupiter and Saturn. AJ, 63:2, Jan. 1958. doi: 10.1086/107672.

W. C. DeMarcus. Obituary Rupert Wildt (1905-1976) Gewidmet. Icarus, 30(2):441–445, Feb. 1977. doi: 10.1016/0019-1035(77)90182-8.

D. Durante, M. Parisi, D. Serra, M. Zannoni, V. Notaro, P. Racioppa, D. R. Buccino, G. Lari, L. Gomez Casajus, L. Iess, W. M. Folkner, G. Tommei, P. Tortora, and S. J. Bolton. Jupiter's Gravity Field Halfway Through the Juno Mission. Geophys. Res. Lett., 47(4):e86572, Feb. 2020. doi: 10.1029/2019GL086572.

D. Durante, T. Guillot, L. Iess, D. J. Stevenson, C. R. Mankovich, S. Markham, E. Galanti, Y. Kaspi, M. Zannoni, L. Gomez Casajus, G. Lari, M. Parisi, D. R. Buccino, R. S. Park, and S. J. Bolton. Juno spacecraft gravity measurements provide evidence for normal modes of Jupiter. Nature Communications, 13:4632, Aug. 2022. doi: 10.1038/s41467-022-32299-9.

A. Dörnbrack. Turbulent mixing by breaking gravity waves. Journal of Fluid Mechanics, 375:113–141, 1998. doi: 10.1017/S0022112098002833.

J. Eggert, S. Brygoo, P. Loubeyre, R. S. McWilliams, P. M. Celliers, D. G. Hicks, T. R. Boehly, R. Jeanloz, and G. W. Collins. Hugoniot data for helium in the ionization regime. Phys. Rev. Lett., 100:124503, Mar 2008. doi: 10.1103/PhysRevLett.100.124503. URL https://link.aps.org/doi/10.1103/PhysRevLett.100.124503.

J. L. Elliot, L. H. Wasserman, J. Veverka, C. Sagan, and W. Liller. The Occultation of Beta Scorpii by Jupiter. 11. the Hydrogen-Helium Abundance in the Jovian Atmosphere. ApJ, 190:719–730, June 1974. doi: 10.1086/152931.

C. Engrand, J. Lasue, D. H. Wooden, and M. E. Zolensky. Chemical and physical properties of cometary dust. arXiv e-prints, art. arXiv:2305.03417, May 2023. doi: 10.48550/arXiv.2305.03417.

Epicurus. Letter to Herodotus.

L. N. Fletcher, Y. Kaspi, T. Guillot, and A. P. Showman. How Well Do We Understand the Belt/Zone Circulation of Giant Planet Atmospheres? Space Sci. Rev., 216(2):30, Mar. 2020a. doi: 10.1007/s11214-019-0631-9.

L. N. Fletcher, G. S. Orton, T. K. Greathouse, J. H. Rogers, Z. Zhang, F. A. Oyafuso, G. Eichstädt, H. Melin, C. Li, S. M. Levin, S. Bolton, M. Janssen, H. J. Mettig, D. Grassi, A. Mura, and A. Adriani. Jupiter's Equatorial Plumes and Hot Spots: Spectral Mapping from Gemini/TEXES and Juno/MWR. Journal of Geophysical Research (Planets), 125(8):e06399, Aug. 2020b. doi: 10.1029/2020JE006399.

W. M. Folkner, L. Iess, J. D. Anderson, S. W. Asmar, D. R. Buccino, D. Durante, M. Feldman, L. Gomez Casajus, M. Gregnanin, A. Milani, M. Parisi, R. S. Park, D. Serra, G. Tommei, P. Tortora, M. Zannoni, S. J. Bolton, J. E. P. Connerney, and S. M. Levin. Jupiter gravity field estimated from the first two Juno orbits. Geophys. Res. Lett., 44(10):4694–4700, May 2017. doi: 10.1002/2017GL073140.

J. J. Fortney and W. B. Hubbard. Phase separation in giant planets: inhomogeneous evolution of Saturn. Icarus, 164(1):228–243, July 2003. doi: 10.1016/S0019-1035(03)00130-1.

J. J. Fortney and N. Nettelmann. The Interior Structure, Composition, and Evolution of Giant Planets. Space Sci. Rev., 152(1-4):423–447, May 2010. doi: 10.1007/s11214-009-9582-x.

J. J. Fortney, M. S. Marley, and J. W. Barnes. Planetary Radii across Five Orders of Magnitude in Mass and Stellar Insolation: Application to Transits. ApJ, 659(2):1661–1672, Apr. 2007. doi: 10.1086/512120.

J. J. Fortney, I. Baraffe, and B. Militzer. Giant Planet Interior Structure and Thermal Evolution. In S. Seager, editor, Exoplanets, pages 397–418. 2010.

J. J. Fortney, R. I. Dawson, and T. D. Komacek. Hot Jupiters: Origins, Structure, Atmospheres. Journal of Geophysical Research (Planets), 126(3):e06629, Mar. 2021. doi: 10.1029/2020JE006629.

N. Fray, A. Bardyn, H. Cottin, D. Baklouti, C. Briois, C. Engrand, H. Fischer, K. Hornung, R. Isnard, Y. Langevin, H. Lehto, L. Le Roy, E. M. Mellado, S. Merouane, P. Modica, F.-R. Orthous-Daunay, J. Paquette, J. Rynö, R. Schulz, J. Silén, S. Siljeström, O. Stenzel, L. Thirkell, K. Varmuza, B. Zaprudin, J. Kissel, and M. Hilchenbach. Nitrogen-to-carbon atomic ratio measured by COSIMA in the particles of comet 67P/Churyumov-Gerasimenko. MNRAS, 469:S506–S516, July 2017. doi: 10.1093/mnras/stx2002.

F. Fressin, G. Torres, D. Charbonneau, S. T. Bryson, J. Christiansen, C. D. Dressing, J. M. Jenkins, L. M. Walkowicz, and N. M. Batalha. The False Positive Rate of Kepler

and the Occurrence of Planets. ApJ, 766(2):81, Apr. 2013. doi: 10.1088/0004-637X/766/2/81.

J. R. Fuentes, E. H. Anders, A. Cumming, and B. W. Hindman. Rotation Reduces Convective Mixing in Jupiter and Other Gas Giants. ApJ, 950(1):L4, June 2023. doi: 10.3847/2041-8213/acd774.

E. Füri and B. Marty. Nitrogen isotope variations in the Solar System. Nature Geoscience, 8(7):515–522, July 2015. doi: 10.1038/ngeo2451.

E. Galanti and Y. Kaspi. An Adjoint-based Method for the Inversion of the Juno and Cassini Gravity Measurements into Wind Fields. ApJ, 820(2):91, Apr. 2016. doi: 10.3847/0004-637X/820/2/91.

E. Galanti, Y. Kaspi, K. Duer, L. Fletcher, A. P. Ingersoll, C. Li, G. S. Orton, T. Guillot, S. M. Levin, and S. J. Bolton. Constraints on the Latitudinal Profile of Jupiter's Deep Jets. Geophys. Res. Lett., 48(9):e92912, May 2021. doi: 10.1029/2021GL092912.

E. Galanti, Y. Kaspi, and T. Guillot. The Shape of Jupiter and Saturn Based on Atmospheric Dynamics, Radio Occultations and Gravity Measurements. Geophys. Res. Lett., 50(6):e2022GL102321, Mar. 2023. doi: 10.1029/2022GL102321.

G. Galilei. Sidereus nuncius magna, longeque admirabilia spectacula pandens lunae facie, fixis innumer 1610. doi: 10.3931/e-rara-695.

S. Gandhi, A. Kesseli, Y. Zhang, A. Louca, I. Snellen, M. Brogi, Y. Miguel, N. Casasayas-Barris, S. Pelletier, R. Landman, C. Maguire, and N. P. Gibson. Retrieval Survey of Metals in Six Ultrahot Jupiters: Trends in Chemistry, Rain-out, Ionization, and Atmospheric Dynamics. AJ, 165(6):242, June 2023. doi: 10.3847/1538-3881/accd65.

P. Gaulme, F. X. Schmider, J. Gay, T. Guillot, and C. Jacob. Detection of Jovian seismic waves: a new probe of its interior structure. A&A, 531:A104, July 2011. doi: 10.1051/0004-6361/201116903.

D. Gautier, B. Conrath, M. Flasar, R. Hanel, V. Kunde, A. Chedin, and N. Scott. The helium abundance of Jupiter from Voyager. J. Geophys. Res., 86(A10):8713–8720, Sept. 1981. doi: 10.1029/JA086iA10p08713.

J. Geiss and G. Gloeckler. Isotopic Composition of H, HE and NE in the Protosolar Cloud. Space Sci. Rev., 106(1):3–18, Apr. 2003. doi: 10.1023/A:1024651232758.

I. Gonçalves, F. X. Schmider, P. Gaulme, R. Morales-Juberías, T. Guillot, J.-P. Rivet, T. Appourchaux, P. Boumier, J. Jackiewicz, B. Sato, S. Ida, M. Ikoma, D. Mékarnia, T. A. Underwood, and D. Voelz. First measurements of Jupiter's zonal winds with visible imaging spectroscopy. Icarus, 319:795–811, Feb. 2019. doi: 10.1016/j.icarus.2018.10.019.

H. C. Graboske, D. J. Harwood, and F. J. Rogers. Thermodynamic Properties of Nonideal Gases. I. Free-Energy Minimization Method. Physical Review, 186(1):210–225, Oct. 1969. doi: 10.1103/PhysRev.186.210.

J. Graboske, H. C., J. B. Pollack, A. S. Grossman, and R. J. Olness. The structure and evolution of Jupiter: the fluid contraction stage. ApJ, 199:265–281, July 1975. doi: 10.1086/153689.

D. Grassi, A. Adriani, A. Mura, S. K. Atreya, L. N. Fletcher, J. I. Lunine, G. S. Orton, S. Bolton, C. Plainaki, G. Sindoni, F. Altieri, A. Cicchetti, B. M. Dinelli, G. Filacchione, A. Migliorini, M. L. Moriconi, R. Noschese, A. Olivieri, G. Piccioni, R. Sordini, S. Stefani, F. Tosi, and D. Turrini. On the Spatial Distribution of Minor Species in Jupiter's Troposphere as Inferred From Juno JIRAM Data. Journal of Geophysical Research (Planets), 125(4):e06206, Apr. 2020. doi: 10.1029/2019JE006206.

P. C. Gregory. Bayesian Logical Data Analysis for the Physical Sciences. Cambridge University Press, 2001.

T. Guillot. Condensation of Methane, Ammonia, and Water and the Inhibition of Convection in Giant Planets. Science, 269(5231):1697–1699, Sept. 1995. doi: 10.1126/science.7569896.

T. Guillot. A comparison of the interiors of Jupiter and Saturn. Planet. Space Sci., 47 (10-11):1183–1200, Oct. 1999. doi: 10.1016/S0032-0633(99)00043-4.

T. Guillot. THE INTERIORS OF GIANT PLANETS: Models and Outstanding Questions. Annual Review of Earth and Planetary Sciences, 33:493–530, Jan. 2005. doi: 10.1146/annurev.earth.32.101802.120325.

T. Guillot. On the radiative equilibrium of irradiated planetary atmospheres. A&A, 520:A27, Sept. 2010. doi: 10.1051/0004-6361/200913396.

T. Guillot. Uranus and Neptune are key to understand planets with hydrogen atmospheres. Experimental Astronomy, 54(2-3):1027–1049, Dec. 2022. doi: 10.1007/s10686-021-09812-x.

T. Guillot and D. Gautier. Giant Planets. In G. Schubert, editor, Treatise on Geophysics, pages 529–557. 2015. doi: 10.1016/B978-0-444-53802-4.00176-7.

T. Guillot and P. Morel. CEPAM: a code for modeling the interiors of giant planets. A&AS, 109:109–123, Jan. 1995.

T. Guillot and A. P. Showman. Evolution of "51 Pegasus b-like" planets. A&A, 385: 156–165, Apr. 2002. doi: 10.1051/0004-6361:20011624.

T. Guillot, D. Gautier, G. Chabrier, and B. Mosser. Are the Giant Planets Fully Convective? Icarus, 112(2):337–353, Dec. 1994. doi: 10.1006/icar.1994.1188.

T. Guillot, G. Chabrier, D. Gautier, and P. Morel. Effect of Radiative Transport on the Evolution of Jupiter and Saturn. ApJ, 450:463, Sept. 1995. doi: 10.1086/176156.

T. Guillot, D. Gautier, and W. B. Hubbard. NOTE: New Constraints on the Composition of Jupiter from Galileo Measurements and Interior Models. Icarus, 130(2): 534–539, Dec. 1997. doi: 10.1006/icar.1997.5812.

T. Guillot, D. J. Stevenson, W. B. Hubbard, and D. Saumon. The interior of Jupiter. In F. Bagenal, T. E. Dowling, and W. B. McKinnon, editors, Jupiter. The Planet, Satellites and Magnetosphere, volume 1, pages 35–57. 2004.

T. Guillot, N. C. Santos, F. Pont, N. Iro, C. Melo, and I. Ribas. A correlation between the heavy element content of transiting extrasolar planets and the metallicity of their parent stars. A&A, 453(2):L21–L24, July 2006. doi: 10.1051/0004-6361:20065476.

T. Guillot, L. Abe, A. Agabi, J. P. Rivet, J. B. Daban, D. Mékarnia, E. Aristidi, F. X. Schmider, N. Crouzet, I. Gonçalves, C. Gouvret, S. Ottogalli, H. Faradji, P. E. Blanc, E. Bondoux, and F. Valbousquet. Thermalizing a telescope in Antarctica - analysis of ASTEP observations. Astronomische Nachrichten, 336(7):638, Sept. 2015. doi: 10.1002/asna.201512174.

T. Guillot, Y. Miguel, B. Militzer, W. B. Hubbard, Y. Kaspi, E. Galanti, H. Cao, R. Helled, S. M. Wahl, L. Iess, W. M. Folkner, D. J. Stevenson, J. I. Lunine, D. R. Reese, A. Biekman, M. Parisi, D. Durante, J. E. P. Connerney, S. M. Levin, and S. J. Bolton. A suppression of differential rotation in Jupiter's deep interior. Nature, 555 (7695):227–230, Mar. 2018. doi: 10.1038/nature25775.

T. Guillot, C. Li, S. J. Bolton, S. T. Brown, A. P. Ingersoll, M. A. Janssen, S. M. Levin, J. I. Lunine, G. S. Orton, P. G. Steffes, and D. J. Stevenson. Storms and the Depletion of Ammonia in Jupiter: II. Explaining the Juno Observations. Journal of Geophysical Research (Planets), 125(8):e06404, Aug. 2020. doi: 10.1029/2020JE006404.

T. Guillot, L. N. Fletcher, R. Helled, M. Ikoma, M. R. Line, and V. Parmentier. Giant Planets from the Inside-Out. arXiv e-prints, art. arXiv:2205.04100, May 2022.

P. Gupta, S. K. Atreya, P. G. Steffes, L. N. Fletcher, T. Guillot, M. D. Allison, S. J. Bolton, R. Helled, S. Levin, C. Li, J. I. Lunine, Y. Miguel, G. S. Orton, J. Hunter Waite, and P. Withers. Jupiter's Temperature Structure: A Reassessment of the Voyager Radio Occultation Measurements. PSJ, 3(7):159, July 2022. doi: 10.3847/PSJ/ac6956.

R. Hanel, B. Conrath, M. Flasar, L. Herath, V. Kunde, P. Lowman, W. Maguire, J. Pearl, J. Pirraglia, R. Samuelson, D. Gautier, P. Gierasch, L. Horn, S. Kumar, and C. Ponnamperuma. Infrared Observations of the Jovian System from Voyager 2. Science, 206(4421):952–956, Nov. 1979a. doi: 10.1126/science.206.4421.952.

R. Hanel, B. Conrath, M. Flasar, V. Kunde, P. Lowman, W. Maguire, J. Pearl, J. Pirraglia, R. Samuelson, D. Gautier, P. Gierasch, S. Kumar, and C. Ponnamperuma. Infrared Observations of the Jovian System from Voyager 1. Science, 204(4396):972–976, June 1979b. doi: 10.1126/science.204.4396.972.

R. Hanel, B. Conrath, L. Herath, V. Kunde, and J. Pirraglia. Albedo, internal heat, and energy balance of Jupiter: preliminary results of the voyager infrared investigation. J. Geophys. Res., 86(A10):8705–8712, Sept. 1981. doi: 10.1029/JA086iA10p08705.

M. Havel, T. Guillot, D. Valencia, and A. Crida. The multiple planets transiting Kepler-9. I. Inferring stellar properties and planetary compositions. A&A, 531:A3, July 2011. doi: 10.1051/0004-6361/201116779.

R. Helled. The Interiors of Jupiter and Saturn. In Oxford Research Encyclopedia of Planetary Science, page 175. 2018. doi: 10.1093/acrefore/9780190647926.013.175.

R. Helled and J. J. Fortney. The interiors of Uranus and Neptune: current understanding and open questions. Philosophical Transactions of the Royal Society of London Series A, 378(2187):20190474, Dec. 2020. doi: 10.1098/rsta.2019.0474.

R. Helled and T. Guillot. Internal Structure of Giant and Icy Planets: Importance of Heavy Elements and Mixing. In H. J. Deeg and J. A. Belmonte, editors, Handbook of Exoplanets, page 44. 2018. doi: 10.1007/978-3-319-55333-7_44.

R. Helled and D. Stevenson. The Fuzziness of Giant Planets' Cores. ApJ, 840(1):L4, May 2017. doi: 10.3847/2041-8213/aa6d08.

R. Helled, P. Bodenheimer, M. Podolak, A. Boley, F. Meru, S. Nayakshin, J. J. Fortney, L. Mayer, Y. Alibert, and A. P. Boss. Giant Planet Formation, Evolution, and Internal Structure. In H. Beuther, R. S. Klessen, C. P. Dullemond, and T. Henning, editors, Protostars and Planets VI, pages 643–665, Jan. 2014. doi: 10.2458/azu_uapress_9780816531240-ch028.

R. Helled, G. Mazzola, and R. Redmer. Understanding dense hydrogen at planetary conditions. Nature Reviews Physics, 2(10):562–574, Sept. 2020a. doi: 10.1038/s42254-020-0223-3.

R. Helled, N. Nettelmann, and T. Guillot. Uranus and Neptune: Origin, Evolution and Internal Structure. Space Sci. Rev., 216(3):38, Mar. 2020b. doi: 10.1007/s11214-020-00660-3.

R. Helled, N. Movshovitz, and N. Nettelmann. The nature of gas giant planets. arXiv e-prints, art. arXiv:2202.10046, Feb. 2022a. doi: 10.48550/arXiv.2202.10046.

R. Helled, D. J. Stevenson, J. I. Lunine, S. J. Bolton, N. Nettelmann, S. Atreya, T. Guillot, B. Militzer, Y. Miguel, and W. B. Hubbard. Revelations on Jupiter's formation,

evolution and interior: Challenges from Juno results. Icarus, 378:114937, May 2022b. doi: 10.1016/j.icarus.2022.114937.

D. G. Hicks, T. R. Boehly, P. M. Celliers, J. H. Eggert, S. J. Moon, D. D. Meyerhofer, and G. W. Collins. Laser-driven single shock compression of fluid deuterium from 45 to 220 gpa. Phys. Rev. B, 79:014112, Jan 2009. doi: 10.1103/PhysRevB.79.014112. URL https://link.aps.org/doi/10.1103/PhysRevB.79.014112.

C. A. Higgins, T. D. Carr, F. Reyes, W. B. Greenman, and G. R. Lebo. A redefinition of Jupiter's rotation period. J. Geophys. Res., 102(A10):22033–22042, Sept. 1997. doi: 10.1029/97JA02090.

M. J. Hobson, T. Trifonov, and T. Henning. TOI-199 b: A well-characterized 100-day transiting warm giant planet with TTVs seen from Antarctica. 2023.

Homer. The Iliad.

A. W. Howard, G. W. Marcy, J. A. Johnson, D. A. Fischer, J. T. Wright, H. Isaacson, J. A. Valenti, J. Anderson, D. N. C. Lin, and S. Ida. The Occurrence and Mass Distribution of Close-in Super-Earths, Neptunes, and Jupiters. Science, 330(6004): 653, Oct. 2010. doi: 10.1126/science.1194854.

S. Howard and T. Guillot. Accounting for non-ideal mixing effects in the hydrogen-helium equation of state. A&A, 672:L1, Apr. 2023. doi: 10.1051/0004-6361/202244851.

S. Howard, T. Guillot, M. Bazot, Y. Miguel, D. J. Stevenson, E. Galanti, Y. Kaspi, W. B. Hubbard, B. Militzer, R. Helled, N. Nettelmann, B. Idini, and S. Bolton. Jupiter's interior from Juno: Equation-of-state uncertainties and dilute core extent. A&A, 672: A33, Apr. 2023. doi: 10.1051/0004-6361/202245625.

W. B. Hubbard. Thermal structure of Jupiter. ApJ, 152:745–754, June 1968. doi: 10.1086/149591.

W. B. Hubbard. Thermal Models of Jupiter and Saturn. ApJ, 155:333, Jan. 1969. doi: 10.1086/149868.

W. B. Hubbard. Interior of Jupiter and Saturn. Annual Review of Earth and Planetary Sciences, 1:85, Jan. 1973. doi: 10.1146/annurev.ea.01.050173.000505.

W. B. Hubbard. Gravitational field of a rotating planet with a polytropic index of unity. Soviet Ast., 18:621–624, Apr. 1975.

W. B. Hubbard. The Jovian Surface Condition and Cooling Rate. Icarus, 30(2):305–310, Feb. 1977. doi: 10.1016/0019-1035(77)90164-6.

W. B. Hubbard. Intrinsic luminosities of the Jovian planets. Reviews of Geophysics and Space Physics, 18:1–9, Feb. 1980. doi: 10.1029/RG018i001p00001.

W. B. Hubbard. Effects of differential rotation on the gravitational figures of Jupiter and Saturn. Icarus, 52(3):509–515, Dec. 1982. doi: 10.1016/0019-1035(82)90011-2.

W. B. Hubbard. NOTE: Gravitational Signature of Jupiter's Deep Zonal Flows. Icarus, 137(2):357–359, Feb. 1999. doi: 10.1006/icar.1998.6064.

W. B. Hubbard. High-precision Maclaurin-based Models of Rotating Liquid Planets. ApJ, 756(1):L15, Sept. 2012. doi: 10.1088/2041-8205/756/1/L15.

W. B. Hubbard. Concentric Maclaurin Spheroid Models of Rotating Liquid Planets. ApJ, 768(1):43, May 2013. doi: 10.1088/0004-637X/768/1/43.

W. B. Hubbard and B. Militzer. A Preliminary Jupiter Model. ApJ, 820(1):80, Mar. 2016. doi: 10.3847/0004-637X/820/1/80.

W. B. Hubbard and T. C. van Flandern. The Occultation of Beta Scorpii by Jupiter and Io. III. Astrometry. AJ, 77:65, Feb. 1972. doi: 10.1086/111246.

W. B. Hubbard, T. Guillot, M. S. Marley, A. Burrows, J. I. Lunine, and D. S. Saumon. Comparative evolution of Jupiter and Saturn. Planet. Space Sci., 47(10-11):1175–1182, Oct. 1999. doi: 10.1016/S0032-0633(99)00042-2.

D. G. Hummer and D. Mihalas. The Equation of State for Stellar Envelopes. I. an Occupation Probability Formalism for the Truncation of Internal Partition Functions. ApJ, 331:794, Aug. 1988. doi: 10.1086/166600.

B. Idini and D. J. Stevenson. The Lost Meaning of Jupiter's High-degree Love Numbers. PSJ, 3(1):11, Jan. 2022a. doi: 10.3847/PSJ/ac4248.

B. Idini and D. J. Stevenson. The Gravitational Imprint of an Interior-Orbital Resonance in Jupiter-Io. PSJ, 3(4):89, Apr. 2022b. doi: 10.3847/PSJ/ac6179.

L. Iess, W. M. Folkner, D. Durante, M. Parisi, Y. Kaspi, E. Galanti, T. Guillot, W. B. Hubbard, D. J. Stevenson, J. D. Anderson, D. R. Buccino, L. G. Casajus, A. Milani, R. Park, P. Racioppa, D. Serra, P. Tortora, M. Zannoni, H. Cao, R. Helled, J. I. Lunine, Y. Miguel, B. Militzer, S. Wahl, J. E. P. Connerney, S. M. Levin, and S. J. Bolton. Measurement of Jupiter's asymmetric gravity field. Nature, 555(7695):220–222, Mar. 2018. doi: 10.1038/nature25776.

A. P. Ingersoll. Atmospheric Dynamics of the Outer Planets. Science, 248(4953):308–315, Apr. 1990. doi: 10.1126/science.248.4953.308.

A. P. Ingersoll, R. F. Beebe, S. A. Collins, G. E. Hunt, J. L. Mitchell, P. Muller, B. A. Smith, and R. J. Terrile. Zonal velocity and texture in the jovian atmosphere inferred from Voyager images. Nature, 280(5725):773–775, Aug. 1979. doi: 10.1038/280773a0.

A. P. Ingersoll, R. F. Beebe, J. L. Mitchell, G. W. Garneau, G. M. Yagi, and J. P. Muller. Interaction of Eddies and mean zonal flow on Jupiter as inferred from Voyager 1 and 2 Images. J. Geophys. Res., 86(A10):8733–8743, Sept. 1981. doi: 10.1029/JA086iA10p08733.

R. C. Jacobson. Jupiter satellite ephemeris file Jup230. NASA Navigation and Ancillary Information Facility, 2003. URL https://naif.jpl.nasa.gov/pub/naif/generic_kernels/spk/satellites/a_old_versions/jup230l.cmt.

R. C. Jacobson. Jupiter satellite ephemeris file Jup310. NASA Navigation and Ancillary Information Facility, 2009. URL https://naif.jpl.nasa.gov/pub/naif/generic_kernels/spk/satellites/a_old_versions/jup310.cmt.

H. Jeffreys. On the internal constitution of Jupiter and Saturn. MNRAS, 84:534, May 1924. doi: 10.1093/mnras/84.7.534.

E. K. Jessberger, A. Christoforidis, and J. Kissel. Aspects of the major element composition of Halley's dust. Nature, 332(6166):691–695, Apr. 1988. doi: 10.1038/332691a0.

A. Johansen and M. Lambrechts. Forming Planets via Pebble Accretion. Annual Review of Earth and Planetary Sciences, 45(1):359–387, Aug. 2017. doi: 10.1146/annurev-earth-063016-020226.

JWST Transiting Exoplanet Community Early Release Science Team, E.-M. Ahrer, L. Alderson, N. M. Batalha, N. E. Batalha, J. L. Bean, T. G. Beatty, T. J. Bell, B. Benneke, Z. K. Berta-Thompson, A. L. Carter, I. J. M. Crossfield, N. Espinoza, A. D. Feinstein, J. J. Fortney, N. P. Gibson, J. M. Goyal, E. M. R. Kempton, J. Kirk, L. Kreidberg, M. López-Morales, M. R. Line, J. D. Lothringer, S. E. Moran, S. Mukherjee, K. Ohno, V. Parmentier, C. Piaulet, Z. Rustamkulov, E. Schlawin, D. K. Sing, K. B. Stevenson, H. R. Wakeford, N. H. Allen, S. M. Birkmann, J. Brande, N. Crouzet, P. E. Cubillos, M. Damiano, J.-M. Désert, P. Gao, J. Harrington, R. Hu, S. Kendrew, H. A. Knutson, P.-O. Lagage, J. Leconte, M. Lendl, R. J. MacDonald, E. M. May, Y. Miguel, K. Molaverdikhani, J. I. Moses, C. A. Murray, M. Nehring, N. K. Nikolov, D. J. M. Petit dit de la Roche, M. Radica, P.-A. Roy, K. G. Stassun, J. Taylor, W. C. Waalkes, P. Wachiraphan, L. Welbanks, P. J. Wheatley, K. Aggarwal, M. K. Alam, A. Banerjee, J. K. Barstow, J. Blecic, S. L. Casewell, Q. Changeat, K. L. Chubb, K. D. Colón, L.-P. Coulombe, T. Daylan, M. de Val-Borro, L. Decin, L. A. Dos Santos, L. Flagg, K. France, G. Fu, A. García Muñoz, J. E. Gizis, A. Glidden, D. Grant, K. Heng, T. Henning, Y.-C. Hong, J. Inglis, N. Iro, T. Kataria, T. D. Komacek, J. E. Krick, E. K. H. Lee, N. K. Lewis, J. Lillo-Box, J. Lustig-Yaeger, L. Mancini, A. M. Mandell, M. Mansfield, M. S. Marley, T. Mikal-Evans, G. Morello, M. C. Nixon, K. Ortiz Ceballos, A. A. A. Piette, D. Powell, B. V. Rackham, L. Ramos-Rosado, E. Rauscher, S. Redfield, L. K. Rogers, M. T. Roman, G. M. Roudier, N. Scarsdale, E. L. Shkolnik, J. Southworth, J. J. Spake, M. E. Steinrueck, X. Tan, J. K. Teske, P. Tremblin, S.-M.

Tsai, G. S. Tucker, J. D. Turner, J. A. Valenti, O. Venot, I. P. Waldmann, N. L. Wallack, X. Zhang, and S. Zieba. Identification of carbon dioxide in an exoplanet atmosphere. Nature, 614(7949):649–652, Feb. 2023. doi: 10.1038/s41586-022-05269-w.

Y. Kaspi. Inferring the depth of the zonal jets on Jupiter and Saturn from odd gravity harmonics. Geophys. Res. Lett., 40(4):676–680, Feb. 2013. doi: 10.1029/2012GL053873.

Y. Kaspi, W. B. Hubbard, A. P. Showman, and G. R. Flierl. Gravitational signature of Jupiter's internal dynamics. Geophys. Res. Lett., 37(1):L01204, Jan. 2010. doi: 10.1029/2009GL041385.

Y. Kaspi, E. Galanti, W. B. Hubbard, D. J. Stevenson, S. J. Bolton, L. Iess, T. Guillot, J. Bloxham, J. E. P. Connerney, H. Cao, D. Durante, W. M. Folkner, R. Helled, A. P. Ingersoll, S. M. Levin, J. I. Lunine, Y. Miguel, B. Militzer, M. Parisi, and S. M. Wahl. Jupiter's atmospheric jet streams extend thousands of kilometres deep. Nature, 555 (7695):223–226, Mar. 2018. doi: 10.1038/nature25793.

J. F. Kerridge. Carbon, hydrogen and nitrogen in carbonaceous chondrites: Abundances and isotopic compositions in bulk samples. Geochim. Cosmochim. Acta, 49(8):1707–1714, Aug. 1985. doi: 10.1016/0016-7037(85)90141-3.

R. Kippenhahn, A. Weigert, and A. Weiss. Stellar Structure and Evolution. 2013. doi: 10.1007/978-3-642-30304-3.

W. J. Klepczynski, P. K. Seidelmann, and R. L. Duncombe. The Masses of the Principal Planets. Celestial Mechanics, 4:253, Oct. 1971. doi: 10.1007/BF01228829.

M. D. Knudson and M. P. Desjarlais. High-precision shock wave measurements of deuterium: Evaluation of exchange-correlation functionals at the molecular-to-atomic transition. Phys. Rev. Lett., 118:035501, Jan 2017. doi: 10.1103/PhysRevLett.118.035501. URL https://link.aps.org/doi/10.1103/PhysRevLett.118.035501.

D. Kong, K. Zhang, G. Schubert, and D. Anderson, John. Origin of Jupiter's cloud-level zonal winds remains a puzzle even after Juno. Proceedings of the National Academy of Science, 115(34):8499–8504, Aug. 2018. doi: 10.1073/pnas.1805927115.

J. Korth, D. Gandolfi, J. Šubjak, S. Howard, S. Ataiee, K. A. Collins, S. N. Quinn, A. J. Mustill, T. Guillot, N. Lodieu, A. M. S. Smith, M. Esposito, F. Rodler, A. Muresan, L. Abe, S. H. Albrecht, A. Alqasim, K. Barkaoui, P. G. Beck, C. J. Burke, R. P. Butler, D. M. Conti, K. I. Collins, J. D. Crane, F. Dai, H. J. Deeg, P. Evans, S. Grziwa, A. P. Hatzes, T. Hirano, K. Horne, C. X. Huang, J. M. Jenkins, P. Kabáth, J. F. Kielkopf, E. Knudstrup, D. W. Latham, J. Livingston, R. Luque, S. Mathur, F. Murgas, H. L. M. Osborne, E. Pallé, C. M. Persson, J. E. Rodriguez, M. Rose, P. Rowden, R. P. Schwarz, S. Seager, L. M. Serrano, L. Sha, S. A. Shectman, A. Shporer, G. Srdoc, C. Stockdale, T. G. Tan, J. K. Teske, V. Van Eylen, A. Vanderburg, R. Vanderspek, S. X. Wang,

and J. N. Winn. TOI-1130: A photodynamical analysis of a hot Jupiter in resonance with an inner low-mass planet. arXiv e-prints, art. arXiv:2305.15565, May 2023. doi: 10.48550/arXiv.2305.15565.

M. Lambrechts and A. Johansen. Rapid growth of gas-giant cores by pebble accretion. A&A, 544:A32, Aug. 2012. doi: 10.1051/0004-6361/201219127.

J. Leconte and G. Chabrier. A new vision of giant planet interiors: Impact of double diffusive convection. A&A, 540:A20, Apr. 2012. doi: 10.1051/0004-6361/201117595.

J. Leconte, F. Selsis, F. Hersant, and T. Guillot. Condensation-inhibited convection in hydrogen-rich atmospheres . Stability against double-diffusive processes and thermal profiles for Jupiter, Saturn, Uranus, and Neptune. A&A, 598:A98, Feb. 2017. doi: 10.1051/0004-6361/201629140.

C. Li, A. Ingersoll, M. Janssen, S. Levin, S. Bolton, V. Adumitroaie, M. Allison, J. Arballo, A. Bellotti, S. Brown, S. Ewald, L. Jewell, S. Misra, G. Orton, F. Oyafuso, P. Steffes, and R. Williamson. The distribution of ammonia on Jupiter from a preliminary inversion of Juno microwave radiometer data. Geophys. Res. Lett., 44(11): 5317–5325, June 2017. doi: 10.1002/2017GL073159.

C. Li, A. Ingersoll, S. Bolton, S. Levin, M. Janssen, S. Atreya, J. Lunine, P. Steffes, S. Brown, T. Guillot, M. Allison, J. Arballo, A. Bellotti, V. Adumitroaie, S. Gulkis, A. Hodges, L. Li, S. Misra, G. Orton, F. Oyafuso, D. Santos-Costa, H. Waite, and Z. Zhang. The water abundance in Jupiter's equatorial zone. Nature Astronomy, 4: 609–616, Feb. 2020. doi: 10.1038/s41550-020-1009-3.

L. Li, X. Jiang, R. A. West, P. J. Gierasch, S. Perez-Hoyos, A. Sanchez-Lavega, L. N. Fletcher, J. J. Fortney, B. Knowles, C. C. Porco, K. H. Baines, P. M. Fry, A. Mallama, R. K. Achterberg, A. A. Simon, C. A. Nixon, G. S. Orton, U. A. Dyudina, S. P. Ewald, and R. W. Schmude. Less absorbed solar energy and more internal heat for jupiter. Nature Communications, 9:3709, 2018. ISSN 2041-1723. doi: 10.1038/s41467-018-06107-2. URL https://doi.org/10.1038/s41467-018-06107-2.

G. F. Lindal, G. E. Wood, G. S. Levy, J. D. Anderson, D. N. Sweetnam, H. B. Hotz, B. J. Buckles, D. P. Holmes, P. E. Doms, V. R. Eshleman, G. L. Tyler, and T. A. Croft. The atmosphere of Jupiter: an analysis of the Voyager radio occulation measurements. J. Geophys. Res., 86(A10):8721–8727, Sept. 1981. doi: 10.1029/JA086iA10p08721.

D. C. Lis, D. Bockelée-Morvan, R. Güsten, N. Biver, J. Stutzki, Y. Delorme, C. Durán, H. Wiesemeyer, and Y. Okada. Terrestrial deuterium-to-hydrogen ratio in water in hyperactive comets. A&A, 625:L5, May 2019. doi: 10.1051/0004-6361/201935554.

S.-F. Liu, Y. Hori, S. Müller, X. Zheng, R. Helled, D. Lin, and A. Isella. The formation of Jupiter's diluted core by a giant impact. Nature, 572(7769):355–357, Aug. 2019. doi: 10.1038/s41586-019-1470-2.

K. Lodders, H. Palme, and H. P. Gail. Abundances of the Elements in the Solar System. Landolt Börnstein, 4B:712, Jan. 2009. doi: 10.1007/978-3-540-88055-4_34.

W. Lorenzen, B. Holst, and R. Redmer. Demixing of hydrogen and helium at megabar pressures. Phys. Rev. Lett., 102:115701, Mar 2009. doi: 10.1103/PhysRevLett.102.115701. URL https://link.aps.org/doi/10.1103/PhysRevLett.102.115701.

W. Lorenzen, B. Holst, and R. Redmer. Metallization in hydrogen-helium mixtures. Phys. Rev. B, 84:235109, Dec 2011. doi: 10.1103/PhysRevB.84.235109. URL https://link.aps.org/doi/10.1103/PhysRevB.84.235109.

P. Loubeyre, J. M. Besson, J. P. Pinceaux, and J. P. Hansen. High-pressure melting curve of ^{4}He. Phys. Rev. Lett., 49:1172–1175, Oct 1982. doi: 10.1103/PhysRevLett.49.1172. URL https://link.aps.org/doi/10.1103/PhysRevLett.49.1172.

P. Loubeyre, R. Letoullec, and J. P. Pinceaux. A new determination of the binary phase diagram of h2-he mixtures at 296 k. Journal of Physics: Condensed Matter, 3(18): 3183, may 1991. doi: 10.1088/0953-8984/3/18/012. URL https://dx.doi.org/10.1088/0953-8984/3/18/012.

P. Loubeyre, F. Occelli, and R. LeToullec. Optical studies of solid hydrogen to 320 gpa and evidence for black hydrogen. Nature, 416(6881):613–617, Apr 2002. doi: 10.1038/416613a. URL https://doi.org/10.1038/416613a.

P. Loubeyre, S. Brygoo, J. Eggert, P. M. Celliers, D. K. Spaulding, J. R. Rygg, T. R. Boehly, G. W. Collins, and R. Jeanloz. Extended data set for the equation of state of warm dense hydrogen isotopes. Phys. Rev. B, 86:144115, Oct 2012. doi: 10.1103/PhysRevB.86.144115. URL https://link.aps.org/doi/10.1103/PhysRevB.86.144115.

F. J. Low. Observations of Venus, Jupiter, and Saturn at $\lambda 20$ μ. AJ, 71:391, Feb. 1966. doi: 10.1086/110110.

M. Lozovsky, R. Helled, E. D. Rosenberg, and P. Bodenheimer. Jupiter's Formation and Its Primordial Internal Structure. ApJ, 836(2):227, Feb. 2017. doi: 10.3847/1538-4357/836/2/227.

S. P. Lyon and J. D. Johnson. SESAME: The Los Alamos national laboratory equation of state database. LANL Report, LA-UR-92-3407, 1992.

N. Madhusudhan. Atmospheric Retrieval of Exoplanets. In H. J. Deeg and J. A. Belmonte, editors, Handbook of Exoplanets, page 104. 2018. doi: 10.1007/978-3-319-55333-7_104.

N. Madhusudhan. Exoplanetary Atmospheres: Key Insights, Challenges, and Prospects. ARA&A, 57:617–663, Aug. 2019. doi: 10.1146/annurev-astro-081817-051846.

J. A. Magalhães, A. Seiff, and R. E. Young. The Stratification of Jupiter's Troposphere at the Galileo Probe Entry Site. Icarus, 158(2):410–433, Aug. 2002. doi: 10.1006/icar.2002.6891.

P. R. Mahaffy, T. M. Donahue, S. K. Atreya, T. C. Owen, and H. B. Niemann. Galileo Probe Measurements of D/H and 3He/4He in Jupiter's Atmosphere. Space Sci. Rev., 84:251–263, Apr. 1998.

P. R. Mahaffy, H. B. Niemann, A. Alpert, S. K. Atreya, J. Demick, T. M. Donahue, D. N. Harpold, and T. C. Owen. Noble gas abundance and isotope ratios in the atmosphere of Jupiter from the Galileo Probe Mass Spectrometer. J. Geophys. Res., 105(E6):15061–15072, June 2000. doi: 10.1029/1999JE001224.

J. Manfroid, E. Jehin, D. Hutsemékers, A. Cochran, J. M. Zucconi, C. Arpigny, R. Schulz, J. A. Stüwe, and I. Ilyin. The CN isotopic ratios in comets. A&A, 503(2):613–624, Aug. 2009. doi: 10.1051/0004-6361/200911859.

C. R. Mankovich and J. J. Fortney. Evidence for a Dichotomy in the Interior Structures of Jupiter and Saturn from Helium Phase Separation. ApJ, 889(1):51, Jan. 2020. doi: 10.3847/1538-4357/ab6210.

C. R. Mankovich and J. Fuller. A diffuse core in Saturn revealed by ring seismology. Nature Astronomy, 5:1103–1109, Aug. 2021. doi: 10.1038/s41550-021-01448-3.

B. Marty. The origins and concentrations of water, carbon, nitrogen and noble gases on Earth. Earth and Planetary Science Letters, 313:56–66, Jan. 2012. doi: 10.1016/j.epsl.2011.10.040.

B. Marty, M. Chaussidon, R. C. Wiens, A. J. G. Jurewicz, and D. S. Burnett. A ^{15}N-Poor Isotopic Composition for the Solar System As Shown by Genesis Solar Wind Samples. Science, 332(6037):1533, June 2011. doi: 10.1126/science.1204656.

S. T. Massie and D. M. Hunten. Stratospheric eddy diffusion coefficients from tracer data. Journal of Geophysical Research: Oceans, 86(C10):9859–9868, 1981. doi: https://doi.org/10.1029/JC086iC10p09859. URL https://agupubs.onlinelibrary.wiley.com/doi/abs/10.1029/JC086iC10p09859.

K. J. Mathew and K. Marti. Early evolution of Martian volatiles: Nitrogen and noble gas components in ALH84001 and Chassigny. J. Geophys. Res., 106(E1):1401–1422, Jan. 2001. doi: 10.1029/2000JE001255.

A. Matter, T. Guillot, and A. Morbidelli. Calculation of the enrichment of the giant planet envelopes during the "late heavy bombardment". Planet. Space Sci., 57(7):816–821, June 2009. doi: 10.1016/j.pss.2009.01.010.

M. Mayor and D. Queloz. A Jupiter-mass companion to a solar-type star. Nature, 378(6555):355–359, Nov. 1995. doi: 10.1038/378355a0.

M. Mayor, M. Marmier, C. Lovis, S. Udry, D. Ségransan, F. Pepe, W. Benz, J. L. Bertaux, F. Bouchy, X. Dumusque, G. Lo Curto, C. Mordasini, D. Queloz, and N. C. Santos. The HARPS search for southern extra-solar planets XXXIV. Occurrence, mass distribution and orbital properties of super-Earths and Neptune-mass planets. arXiv e-prints, art. arXiv:1109.2497, Sept. 2011. doi: 10.48550/arXiv.1109.2497.

S. Mazevet, A. Licari, and F. Soubiran. Benchmarking the ab initio hydrogen equation of state for the interior structure of Jupiter. A&A, 664:A112, Aug. 2022. doi: 10.1051/0004-6361/201935764.

G. Mazzola, R. Helled, and S. Sorella. Phase Diagram of Hydrogen and a Hydrogen-Helium Mixture at Planetary Conditions by Quantum Monte Carlo Simulations. Phys. Rev. Lett., 120(2):025701, Jan. 2018. doi: 10.1103/PhysRevLett.120.025701.

J. M. McMahon, M. A. Morales, C. Pierleoni, and D. M. Ceperley. The properties of hydrogen and helium under extreme conditions. Rev. Mod. Phys., 84:1607–1653, Nov 2012. doi: 10.1103/RevModPhys.84.1607. URL https://link.aps.org/doi/10.1103/RevModPhys.84.1607.

R. S. McWilliams, D. A. Dalton, M. F. Mahmood, and A. F. Goncharov. Optical properties of fluid hydrogen at the transition to a conducting state. Phys. Rev. Lett., 116:255501, Jun 2016. doi: 10.1103/PhysRevLett.116.255501. URL https://link.aps.org/doi/10.1103/PhysRevLett.116.255501.

P. J. Michael. The concentration, behavior and storage of H $_2$O in the suboceanic upper mantle: Implications for mantle metasomatism. Geochim. Cosmochim. Acta, 52(2):555–566, Feb. 1988. doi: 10.1016/0016-7037(88)90110-X.

Y. Miguel and A. Vazan. Interior and Evolution of the Giant Planets. Remote Sensing, 15(3):681, Jan. 2023. doi: 10.3390/rs15030681.

Y. Miguel, T. Guillot, and L. Fayon. Jupiter internal structure: the effect of different equations of state. A&A, 596:A114, Dec. 2016. doi: 10.1051/0004-6361/201629732.

Y. Miguel, M. Bazot, T. Guillot, S. Howard, E. Galanti, Y. Kaspi, W. B. Hubbard, B. Militzer, R. Helled, S. K. Atreya, J. E. P. Connerney, D. Durante, L. Kulowski, J. I. Lunine, D. Stevenson, and S. Bolton. Jupiter's inhomogeneous envelope. A&A, 662:A18, June 2022. doi: 10.1051/0004-6361/202243207.

B. Militzer. Equation of state calculations of hydrogen-helium mixtures in solar and extrasolar giant planets. Phys. Rev. B, 87:014202, Jan 2013. doi: 10.1103/PhysRevB.87.014202. URL https://link.aps.org/doi/10.1103/PhysRevB.87.014202.

B. Militzer and W. B. Hubbard. Comparison of Jupiter interior models derived from first-principles simulations. Ap&SS, 322(1-4):129–133, Aug. 2009. doi: 10.1007/s10509-008-9958-5.

B. Militzer and W. B. Hubbard. Ab Initio Equation of State for Hydrogen-Helium Mixtures with Recalibration of the Giant-planet Mass-Radius Relation. ApJ, 774(2): 148, Sept. 2013. doi: 10.1088/0004-637X/774/2/148.

B. Militzer, W. B. Hubbard, J. Vorberger, I. Tamblyn, and S. A. Bonev. A Massive Core in Jupiter Predicted from First-Principles Simulations. ApJ, 688(1):L45, Nov. 2008. doi: 10.1086/594364.

B. Militzer, F. Soubiran, S. M. Wahl, and W. Hubbard. Understanding Jupiter's interior. Journal of Geophysical Research (Planets), 121(9):1552–1572, Sept. 2016. doi: 10.1002/2016JE005080.

B. Militzer, W. B. Hubbard, S. Wahl, J. I. Lunine, E. Galanti, Y. Kaspi, Y. Miguel, T. Guillot, K. M. Moore, M. Parisi, J. E. P. Connerney, R. Helled, H. Cao, C. Mankovich, D. J. Stevenson, R. S. Park, M. Wong, S. K. Atreya, J. Anderson, and S. J. Bolton. Juno Spacecraft Measurements of Jupiter's Gravity Imply a Dilute Core. PSJ, 3(8):185, Aug. 2022. doi: 10.3847/PSJ/ac7ec8.

P. J. Mohr, B. N. Taylor, and D. B. Newell. Codata recommended values of the fundamental physical constants: 2010. Rev. Mod. Phys., 84:1527–1605, Nov 2012. doi: 10.1103/RevModPhys.84.1527. URL https://link.aps.org/doi/10.1103/RevModPhys.84.1527.

M. A. Morales, E. Schwegler, D. Ceperley, C. Pierleoni, S. Hamel, and K. Caspersen. Phase separation in hydrogen-helium mixtures at Mbar pressures. Proceedings of the National Academy of Science, 106(5):1324, Feb. 2009. doi: 10.1073/pnas.0812581106.

M. A. Morales, C. Pierleoni, E. Schwegler, and D. M. Ceperley. Evidence for a first-order liquid-liquid transition in high-pressure hydrogen from ab initio simulations. Proceedings of the National Academy of Sciences, 107(29):12799–12803, 2010. doi: 10.1073/pnas.1007309107. URL https://www.pnas.org/doi/abs/10.1073/pnas.1007309107.

M. A. Morales, S. Hamel, K. Caspersen, and E. Schwegler. Hydrogen-helium demixing from first principles: From diamond anvil cells to planetary interiors. Phys. Rev. B, 87:174105, May 2013. doi: 10.1103/PhysRevB.87.174105. URL https://link.aps.org/doi/10.1103/PhysRevB.87.174105.

A. Morbidelli, K. Batygin, and E. Lega. In situ enrichment in heavy elements of hot Jupiters. A&A, 675:A75, July 2023. doi: 10.1051/0004-6361/202346868.

C. Mordasini, Y. Alibert, and W. Benz. Destruction of planetesimals in protoplanetry atmospheres. In L. Arnold, F. Bouchy, and C. Moutou, editors, Tenth Anniversary of 51 Peg-b: Status of and prospects for hot Jupiter studies, pages 84–86, Feb. 2006.

C. Mordasini, Y. Alibert, H. Klahr, and T. Henning. Characterization of exoplanets from their formation. I. Models of combined planet formation and evolution. A&A, 547:A111, Nov. 2012. doi: 10.1051/0004-6361/201118457.

C. Mordasini, H. Klahr, Y. Alibert, N. Miller, and T. Henning. Grain opacity and the bulk composition of extrasolar planets. I. Results from scaling the ISM opacity. A&A, 566:A141, June 2014. doi: 10.1051/0004-6361/201321479.

C. Mordasini, R. van Boekel, P. Mollière, T. Henning, and B. Benneke. The Imprint of Exoplanet Formation History on Observable Present-day Spectra of Hot Jupiters. ApJ, 832(1):41, Nov. 2016. doi: 10.3847/0004-637X/832/1/41.

S. Müller. 2023.

S. Müller and R. Helled. Towards a new era in giant exoplanet characterisation. A&A, 669:A24, Jan. 2023a. doi: 10.1051/0004-6361/202244827.

S. Müller and R. Helled. Warm giant exoplanet characterisation: current state, challenges and outlook. Frontiers in Astronomy and Space Sciences, 10:1179000, May 2023b. doi: 10.3389/fspas.2023.1179000.

S. Müller, R. Helled, and A. Cumming. The challenge of forming a fuzzy core in Jupiter. A&A, 638:A121, June 2020. doi: 10.1051/0004-6361/201937376.

Naor Movshovitz. Personal notes of Naor Movshovitz - Concentric Maclaurin Spheroids: theory and practice. University of California, Santa Cruz, 2017. URL https://github.com/nmovshov/CMS-planet.

N. Nettelmann. Matter under extreme conditions: modelling giant planets. PhD dissertation, Universität Rostock, 2011.

N. Nettelmann. Low- and high-order gravitational harmonics of rigidly rotating Jupiter. A&A, 606:A139, Oct. 2017. doi: 10.1051/0004-6361/201731550.

N. Nettelmann and D. Valencia. Exoplanetary Interiors. In N. Madhusudhan, editor, ExoFrontiers; Big Questions in Exoplanetary Science, pages 16–1. 2021. doi: 10.1088/2514-3433/abfa8fch16.

N. Nettelmann, B. Holst, A. Kietzmann, M. French, R. Redmer, and D. Blaschke. Ab Initio Equation of State Data for Hydrogen, Helium, and Water and the Internal Structure of Jupiter. ApJ, 683(2):1217–1228, Aug. 2008. doi: 10.1086/589806.

N. Nettelmann, A. Becker, B. Holst, and R. Redmer. Jupiter Models with Improved Ab Initio Hydrogen Equation of State (H-REOS.2). ApJ, 750(1):52, May 2012. doi: 10.1088/0004-637X/750/1/52.

N. Nettelmann, N. Movshovitz, D. Ni, J. J. Fortney, E. Galanti, Y. Kaspi, R. Helled, C. R. Mankovich, and S. Bolton. Theory of Figures to the Seventh Order and the Interiors of Jupiter and Saturn. PSJ, 2(6):241, Dec. 2021. doi: 10.3847/PSJ/ac390a.

D. Ni. Understanding Jupiter's deep interior: the effect of a dilute core. A&A, 632:A76, Dec. 2019. doi: 10.1051/0004-6361/201935938.

H. B. Niemann, S. K. Atreya, G. R. Carignan, T. M. Donahue, J. A. Haberman, D. N. Harpold, R. E. Hartle, D. M. Hunten, W. T. Kasprzak, P. R. Mahaffy, T. C. Owen, and S. H. Way. The composition of the Jovian atmosphere as determined by the Galileo probe mass spectrometer. J. Geophys. Res., 103(E10):22831–22846, Sept. 1998. doi: 10.1029/98JE01050.

H. B. Niemann, S. K. Atreya, J. E. Demick, D. Gautier, J. A. Haberman, D. N. Harpold, W. T. Kasprzak, J. I. Lunine, T. C. Owen, and F. Raulin. Composition of Titan's lower atmosphere and simple surface volatiles as measured by the Cassini-Huygens probe gas chromatograph mass spectrometer experiment. Journal of Geophysical Research (Planets), 115(E12):E12006, Dec. 2010. doi: 10.1029/2010JE003659.

G. W. Null. Gravity field of Jupiter and its satellites from Pioneer 10 and Pioneer 11 tracking data. AJ, 81:1153–1161, Dec. 1976. doi: 10.1086/111999.

E. J. Öpik. Jupiter: Chemical composition, structure, and origin of a giant planet. Icarus, 1(1):200–257, Jan. 1962. doi: 10.1016/0019-1035(62)90022-2.

G. Orton, J. L. Ortiz, K. Baines, G. Bjoraker, U. Carsenty, F. Colas, A. Dayal, D. Deming, P. Drossart, E. Frappa, J. Friedson, J. Goguen, W. Golisch, D. Griep, C. Hernandez, W. Hoffmann, D. Jennings, C. Kaminski, J. Kuhn, P. Laques, S. Limaye, H. Lin, J. Lecacheux, T. Martin, G. McCabe, T. Momary, D. Parker, R. Puetter, M. Ressler, G. Reyes, P. Sada, J. Spencer, J. Spitale, S. Stewart, J. Varsik, J. Warell, W. Wild, P. Yanamandra-Fisher, G. Fazio, J. Hora, and L. Deutsch. Earth-Based Observations of the Galileo Probe Entry Site. Science, 272(5263):839–840, May 1996. doi: 10.1126/science.272.5263.839.

T. Owen, P. R. Mahaffy, H. B. Niemann, S. Atreya, and M. Wong. Protosolar Nitrogen. ApJ, 553(1):L77–L79, May 2001. doi: 10.1086/320501.

V. Parmentier, T. Guillot, J. J. Fortney, and M. S. Marley. A non-grey analytical model for irradiated atmospheres. II. Analytical vs. numerical solutions. A&A, 574:A35, Feb. 2015. doi: 10.1051/0004-6361/201323127.

J. C. Pearl and B. J. Conrath. The albedo, effective temperature, and energy balance of Neptune, as determined from Voyager data. J. Geophys. Res., 96:18921–18930, Oct. 1991. doi: 10.1029/91JA01087.

P. J. E. Peebles. The Structure and Composition of Jupiter and Saturn. ApJ, 140:328, July 1964. doi: 10.1086/147922.

C. Pierleoni, M. A. Morales, G. Rillo, M. Holzmann, and D. M. Ceperley. Liquid–liquid phase transition in hydrogen by coupled electron–ion monte carlo simulations. Proceedings of the National Academy of Sciences, 113(18):4953–4957, 2016. doi: 10.1073/pnas.1603853113. URL https://www.pnas.org/doi/abs/10.1073/pnas.1603853113.

J. B. Pollack, O. Hubickyj, P. Bodenheimer, J. J. Lissauer, M. Podolak, and Y. Greenzweig. Formation of the Giant Planets by Concurrent Accretion of Solids and Gas. Icarus, 124(1):62–85, Nov. 1996. doi: 10.1006/icar.1996.0190.

C. C. Porco, R. A. West, A. McEwen, A. D. Del Genio, A. P. Ingersoll, P. Thomas, S. Squyres, L. Dones, C. D. Murray, T. V. Johnson, J. A. Burns, A. Brahic, G. Neukum, J. Veverka, J. M. Barbara, T. Denk, M. Evans, J. J. Ferrier, P. Geissler, P. Helfenstein, T. Roatsch, H. Throop, M. Tiscareno, and A. R. Vasavada. Cassini Imaging of Jupiter's Atmosphere, Satellites, and Rings. Science, 299(5612):1541–1547, Mar. 2003. doi: 10.1126/science.1079462.

A. Psaridi, F. Bouchy, M. Lendl, B. Akinsanmi, K. G. Stassun, B. Smalley, D. J. Armstrong, S. Howard, S. Ulmer-Moll, N. Grieves, K. Barkaoui, J. E. Rodriguez, E. M. Bryant, O. Suárez, T. Guillot, P. Evans, O. Attia, R. A. Wittenmyer, S. W. Yee, K. A. Collins, G. Zhou, F. Galland, L. Parc, S. Udry, P. Figueira, C. Ziegler, C. Mordasini, J. N. Winn, S. Seager, J. M. Jenkins, J. D. Twicken, R. Brahm, M. I. Jones, L. Abe, B. Addison, C. Briceño, J. T. Briegal, K. I. Collins, T. Daylan, P. Eigmüller, G. Furesz, N. M. Guerrero, J. Hagelberg, A. Heitzmann, R. Hounsell, C. X. Huang, A. Krenn, N. M. Law, A. W. Mann, J. McCormac, D. Mékarnia, D. Mounzer, L. D. Nielsen, A. Osborn, Y. Reinarz, R. R. Sefako, M. Steiner, P. A. Strøm, A. H. M. J. Triaud, R. Vanderspek, L. Vanzi, J. I. Vines, C. A. Watson, D. J. Wright, and A. Zapata. Three Saturn-mass planets transiting F-type stars revealed with TESS and HARPS. arXiv e-prints, art. arXiv:2303.15080, Mar. 2023. doi: 10.48550/arXiv.2303.15080.

H. Rauer, C. Catala, C. Aerts, T. Appourchaux, W. Benz, A. Brandeker, J. Christensen-Dalsgaard, M. Deleuil, L. Gizon, M. J. Goupil, M. Güdel, E. Janot-Pacheco, M. Mas-Hesse, I. Pagano, G. Piotto, D. Pollacco, Ċ. Santos, A. Smith, J. C. Suárez, R. Szabó, S. Udry, V. Adibekyan, Y. Alibert, J. M. Almenara, P. Amaro-Seoane, M. A.-v. Eiff, M. Asplund, E. Antonello, S. Barnes, F. Baudin, K. Belkacem, M. Bergemann, G. Bihain, A. C. Birch, X. Bonfils, I. Boisse, A. S. Bonomo, F. Borsa, I. M. Brandão, E. Brocato, S. Brun, M. Burleigh, R. Burston, J. Cabrera, S. Cassisi, W. Chaplin, S. Charpinet, C. Chiappini, R. P. Church, S. Csizmadia, M. Cunha, M. Damasso, M. B. Davies, H. J. Deeg, R. F. Díaz, S. Dreizler, C. Dreyer, P. Eggenberger, D. Ehrenreich, P. Eigmüller, A. Erikson, R. Farmer, S. Feltzing, F. de Oliveira Fialho, P. Figueira, T. Forveille, M. Fridlund, R. A. García, P. Giommi, G. Giuffrida, M. Godolt, J. Gomes da Silva, T. Granzer, J. L. Grenfell, A. Grotsch-Noels, E. Günther, C. A. Haswell, A. P. Hatzes, G. Hébrard, S. Hekker, R. Helled,

K. Heng, J. M. Jenkins, A. Johansen, M. L. Khodachenko, K. G. Kislyakova, W. Kley, U. Kolb, N. Krivova, F. Kupka, H. Lammer, A. F. Lanza, Y. Lebreton, D. Magrin, P. Marcos-Arenal, P. M. Marrese, J. P. Marques, J. Martins, S. Mathis, S. Mathur, S. Messina, A. Miglio, J. Montalban, M. Montalto, M. J. P. F. G. Monteiro, H. Moradi, E. Moravveji, C. Mordasini, T. Morel, A. Mortier, V. Nascimbeni, R. P. Nelson, M. B. Nielsen, L. Noack, A. J. Norton, A. Ofir, M. Oshagh, R. M. Ouazzani, P. Pápics, V. C. Parro, P. Petit, B. Plez, E. Poretti, A. Quirrenbach, R. Ragazzoni, G. Raimondo, M. Rainer, D. R. Reese, R. Redmer, S. Reffert, B. Rojas-Ayala, I. W. Roxburgh, S. Salmon, A. Santerne, J. Schneider, J. Schou, S. Schuh, H. Schunker, A. Silva-Valio, R. Silvotti, I. Skillen, I. Snellen, F. Sohl, S. G. Sousa, A. Sozzetti, D. Stello, K. G. Strassmeier, M. Švanda, G. M. Szabó, A. Tkachenko, D. Valencia, V. Van Grootel, S. D. Vauclair, P. Ventura, F. W. Wagner, N. A. Walton, J. Weingrill, S. C. Werner, P. J. Wheatley, and K. Zwintz. The PLATO 2.0 mission. Experimental Astronomy, 38(1-2):249–330, Nov. 2014. doi: 10.1007/s10686-014-9383-4.

G. R. Ricker, J. N. Winn, R. Vanderspek, D. W. Latham, G. Á. Bakos, J. L. Bean, Z. K. Berta-Thompson, T. M. Brown, L. Buchhave, N. R. Butler, R. P. Butler, W. J. Chaplin, D. Charbonneau, J. Christensen-Dalsgaard, M. Clampin, D. Deming, J. Doty, N. De Lee, C. Dressing, E. W. Dunham, M. Endl, F. Fressin, J. Ge, T. Henning, M. J. Holman, A. W. Howard, S. Ida, J. M. Jenkins, G. Jernigan, J. A. Johnson, L. Kaltenegger, N. Kawai, H. Kjeldsen, G. Laughlin, A. M. Levine, D. Lin, J. J. Lissauer, P. MacQueen, G. Marcy, P. R. McCullough, T. D. Morton, N. Narita, M. Paegert, E. Palle, F. Pepe, J. Pepper, A. Quirrenbach, S. A. Rinehart, D. Sasselov, B. Sato, S. Seager, A. Sozzetti, K. G. Stassun, P. Sullivan, A. Szentgyorgyi, G. Torres, S. Udry, and J. Villasenor. Transiting Exoplanet Survey Satellite (TESS). Journal of Astronomical Telescopes, Instruments, and Systems, 1:014003, Jan. 2015. doi: 10.1117/1.JATIS.1.1.014003.

A. C. Riddle and J. W. Warwick. Redefinition of System III Longitude. Icarus, 27(3): 457–459, Mar. 1976. doi: 10.1016/0019-1035(76)90025-7.

E. Rosenblum, P. Garaud, A. Traxler, and S. Stellmach. Turbulent Mixing and Layer Formation in Double-diffusive Convection: Three-dimensional Numerical Simulations and Theory. ApJ, 731(1):66, Apr. 2011. doi: 10.1088/0004-637X/731/1/66.

M. Rubin, K. Altwegg, H. Balsiger, J.-J. Berthelier, M. R. Combi, J. De Keyser, M. Drozdovskaya, B. Fiethe, S. A. Fuselier, S. Gasc, T. I. Gombosi, N. Hänni, K. C. Hansen, U. Mall, H. Rème, I. R. H. G. Schroeder, M. Schuhmann, T. Sémon, J. H. Waite, S. F. Wampfler, and P. Wurz. Elemental and molecular abundances in comet 67P/Churyumov-Gerasimenko. MNRAS, 489(1):594–607, Oct. 2019. doi: 10.1093/mnras/stz2086.

Z. Rustamkulov, D. K. Sing, S. Mukherjee, E. M. May, J. Kirk, E. Schlawin, M. R. Line, C. Piaulet, A. L. Carter, N. E. Batalha, J. M. Goyal, M. López-Morales,

J. D. Lothringer, R. J. MacDonald, S. E. Moran, K. B. Stevenson, H. R. Wakeford, N. Espinoza, J. L. Bean, N. M. Batalha, B. Benneke, Z. K. Berta-Thompson, I. J. M. Crossfield, P. Gao, L. Kreidberg, D. K. Powell, P. E. Cubillos, N. P. Gibson, J. Leconte, K. Molaverdikhani, N. K. Nikolov, V. Parmentier, P. Roy, J. Taylor, J. D. Turner, P. J. Wheatley, K. Aggarwal, E. Ahrer, M. K. Alam, L. Alderson, N. H. Allen, A. Banerjee, S. Barat, D. Barrado, J. K. Barstow, T. J. Bell, J. Blecic, J. Brande, S. Casewell, Q. Changeat, K. L. Chubb, N. Crouzet, T. Daylan, L. Decin, J. Désert, T. Mikal-Evans, A. D. Feinstein, L. Flagg, J. J. Fortney, J. Harrington, K. Heng, Y. Hong, R. Hu, N. Iro, T. Kataria, E. M. R. Kempton, J. Krick, M. Lendl, J. Lillo-Box, A. Louca, J. Lustig-Yaeger, L. Mancini, M. Mansfield, N. J. Mayne, Y. Miguel, G. Morello, K. Ohno, E. Palle, D. J. M. Petit dit de la Roche, B. V. Rackham, M. Radica, L. Ramos-Rosado, S. Redfield, L. K. Rogers, E. L. Shkolnik, J. Southworth, J. Teske, P. Tremblin, G. S. Tucker, O. Venot, W. C. Waalkes, L. Welbanks, X. Zhang, and S. Zieba. Early Release Science of the exoplanet WASP-39b with JWST NIRSpec PRISM. Nature, 614(7949):659–663, Feb. 2023. doi: 10.1038/s41586-022-05677-y.

H. Saito and K. Kuramoto. D/H Ratio in the Interiors of Rocky Protoplanets Accreting in the Solar Nebula. ApJ, 889(1):40, Jan. 2020. doi: 10.3847/1538-4357/ab5f11.

E. E. Salpeter. On Convection and Gravitational Layering in Jupiter and in Stars of Low Mass. ApJ, 181:L83, Apr. 1973. doi: 10.1086/181190.

D. Saumon and T. Guillot. Shock Compression of Deuterium and the Interiors of Jupiter and Saturn. ApJ, 609(2):1170–1180, July 2004. doi: 10.1086/421257.

D. Saumon, W. B. Hubbard, G. Chabrier, and H. M. van Horn. The Role of the Molecular-metallic Transition of Hydrogen in the Evolution of Jupiter, Saturn, and Brown Dwarfs. ApJ, 391:827, June 1992. doi: 10.1086/171391.

D. Saumon, G. Chabrier, and H. M. van Horn. An Equation of State for Low-Mass Stars and Giant Planets. ApJS, 99:713, Aug. 1995. doi: 10.1086/192204.

M. Schöttler and R. Redmer. Simulations of H-He mixtures using the van der Waals density functional. Journal of Plasma Physics, 84(4):755840401, Aug. 2018a. doi: 10.1017/S0022377818000685.

M. Schöttler and R. Redmer. Ab Initio Calculation of the Miscibility Diagram for Hydrogen-Helium Mixtures. Phys. Rev. Lett., 120(11):115703, Mar. 2018b. doi: 10.1103/PhysRevLett.120.115703.

S. Seager and D. Deming. Exoplanet Atmospheres. ARA&A, 48:631–672, Sept. 2010. doi: 10.1146/annurev-astro-081309-130837.

P. K. Seidelmann and N. Divine. Evaluation of Jupiter longitudes in System III (1965). Geophys. Res. Lett., 4(2):65–68, Feb. 1977. doi: 10.1029/GL004i002p00065.

A. Seiff, D. B. Kirk, T. C. D. Knight, R. E. Young, J. D. Mihalov, L. A. Young, F. S. Milos, G. Schubert, R. C. Blanchard, and D. Atkinson. Thermal structure of Jupiter's atmosphere near the edge of a 5-μm hot spot in the north equatorial belt. J. Geophys. Res., 103(E10):22857–22890, Sept. 1998. doi: 10.1029/98JE01766.

A. M. Serenelli and S. Basu. Determining the Initial Helium Abundance of the Sun. ApJ, 719(1):865–872, Aug. 2010. doi: 10.1088/0004-637X/719/1/865.

L. Sha, A. M. Vanderburg, C. X. Huang, D. J. Armstrong, R. Brahm, S. Giacalone, M. L. Wood, K. A. Collins, L. D. Nielsen, M. J. Hobson, C. Ziegler, S. B. Howell, P. Torres-Miranda, A. W. Mann, G. Zhou, E. Delgado-Mena, F. I. Rojas, L. Abe, T. Trifonov, V. Adibekyan, S. G. Sousa, S. B. Fajardo-Acosta, T. Guillot, S. Howard, C. Littlefield, F. Hawthorn, F.-X. Schmider, J. Eberhardt, T.-G. Tan, A. Osborn, R. P. Schwarz, P. Strøm, A. Jordán, G. Wang, T. Henning, B. Massey, N. Law, C. Stockdale, E. Furlan, G. Srdoc, P. J. Wheatley, D. Barrado Navascués, J. J. Lissauer, K. G. Stassun, G. R. Ricker, R. K. Vanderspek, D. W. Latham, J. N. Winn, S. Seager, J. M. Jenkins, T. Barclay, L. G. Bouma, J. L. Christiansen, N. Guerrero, and M. E. Rose. TESS spots a mini-neptune interior to a hot saturn in the TOI-2000 system. MNRAS, June 2023. doi: 10.1093/mnras/stad1666.

C. L. Shaw, D. J. Gulledge, R. Swindle, S. M. Jefferies, and N. Murphy. PMODE I: Design and Development of an Observatory for Characterizing Giant Planet Atmospheres and Interiors. Frontiers in Astronomy and Space Sciences, 9:768452, Mar. 2022. doi: 10.3389/fspas.2022.768452.

Y. Shinnaka, H. Kawakita, E. Jehin, A. Decock, D. Hutsemékers, J. Manfroid, and A. Arai. Nitrogen isotopic ratios of NH_2 in comets: implication for ^{15}N-fractionation in cometary ammonia. MNRAS, 462:S195–S209, Nov. 2016. doi: 10.1093/mnras/stw2410.

D. K. Sing, J. J. Fortney, N. Nikolov, H. R. Wakeford, T. Kataria, T. M. Evans, S. Aigrain, G. E. Ballester, A. S. Burrows, D. Deming, J.-M. Désert, N. P. Gibson, G. W. Henry, C. M. Huitson, H. A. Knutson, A. Lecavelier Des Etangs, F. Pont, A. P. Showman, A. Vidal-Madjar, M. H. Williamson, and P. A. Wilson. A continuum from clear to cloudy hot-Jupiter exoplanets without primordial water depletion. Nature, 529(7584):59–62, Jan. 2016. doi: 10.1038/nature16068.

M. Smirnova, E. Galanti, and Y. Kaspi. Studying the dynamics of Jupiter using a 3D general circulation model constrained by radio occultation measurements. In European Planetary Science Congress, pages EPSC2022–932, Sept. 2022. doi: 10.5194/epsc2022-932.

R. Smoluchowski. Internal Structure and Energy Emission of Jupiter. Nature, 215 (5102):691–695, Aug. 1967. doi: 10.1038/215691a0.

L. Spilker. Cassini-Huygens' exploration of the Saturn system: 13 years of discovery. Science, 364(6445):1046–1051, June 2019. doi: 10.1126/science.aat3760.

D. J. Stevenson. Interiors of the Giant Planets. Annual Review of Earth and Planetary Sciences, 10:257, Jan. 1982. doi: 10.1146/annurev.ea.10.050182.001353.

D. J. Stevenson. Cosmochemistry and structure of the giant planets and their satellites. Icarus, 62(1):4–15, Apr. 1985. doi: 10.1016/0019-1035(85)90168-X.

D. J. Stevenson. Jupiter's Interior as Revealed by Juno. Annual Review of Earth and Planetary Sciences, 48:465–489, May 2020. doi: 10.1146/annurev-earth-081619-052855.

D. J. Stevenson and E. E. Salpeter. The dynamics and helium distribution in hydrogen-helium fluid planets. ApJS, 35:239–261, Oct. 1977a. doi: 10.1086/190479.

D. J. Stevenson and E. E. Salpeter. The phase diagram and transport properties for hydrogen-helium fluid planets. ApJS, 35:221–237, Oct. 1977b. doi: 10.1086/190478.

D. J. Stevenson, P. Bodenheimer, J. J. Lissauer, and G. D'Angelo. Mixing of Condensable Constituents with H-He during the Formation and Evolution of Jupiter. PSJ, 3 (4):74, Apr. 2022. doi: 10.3847/PSJ/ac5c44.

I. Tamblyn and S. A. Bonev. Structure and phase boundaries of compressed liquid hydrogen. Phys. Rev. Lett., 104:065702, Feb 2010. doi: 10.1103/PhysRevLett.104.065702. URL https://link.aps.org/doi/10.1103/PhysRevLett.104.065702.

J. K. Teske, D. Thorngren, J. J. Fortney, N. Hinkel, and J. M. Brewer. Do Metal-rich Stars Make Metal-rich Planets? New Insights on Giant Planet Formation from Host Star Abundances. AJ, 158(6):239, Dec. 2019. doi: 10.3847/1538-3881/ab4f79.

D. P. Thorngren and J. J. Fortney. Bayesian Analysis of Hot-Jupiter Radius Anomalies: Evidence for Ohmic Dissipation? AJ, 155(5):214, May 2018. doi: 10.3847/1538-3881/aaba13.

D. P. Thorngren, J. J. Fortney, R. A. Murray-Clay, and E. D. Lopez. The Mass-Metallicity Relation for Giant Planets. ApJ, 831(1):64, Nov. 2016. doi: 10.3847/0004-637X/831/1/64.

T. Trifonov, R. Brahm, A. Jordán, C. Hartogh, T. Henning, M. J. Hobson, M. Schlecker, S. Howard, F. Reichardt, N. Espinoza, M. H. Lee, D. Nesvorny, F. I. Rojas, K. Barkaoui, D. Kossakowski, G. Boyle, S. Dreizler, M. Kürster, R. Heller, T. Guillot, A. H. M. J. Triaud, L. Abe, A. Agabi, P. Bendjoya, N. Crouzet, G. Dransfield, T. Gasparetto, M. N. Günther, W. Marie-Sainte, D. Mékarnia, O. Suarez, J. Teske, R. P. Butler, J. D. Crane, S. Shectman, G. R. Ricker, A. Shporer, R. Vanderspek, J. M. Jenkins, B. Wohler, K. A. Collins, K. I. Collins, D. R. Ciardi, T. Barclay, I. Mireles, S. Seager, and J. N. Winn. TOI-2525 b and c: A Pair of Massive Warm Giant Planets

with Strong Transit Timing Variations Revealed by TESS. AJ, 165(4):179, Apr. 2023. doi: 10.3847/1538-3881/acba9b.

S.-M. Tsai, E. K. H. Lee, D. Powell, P. Gao, X. Zhang, J. Moses, E. Hébrard, O. Venot, V. Parmentier, S. Jordan, R. Hu, M. K. Alam, L. Alderson, N. M. Batalha, J. L. Bean, B. Benneke, C. J. Bierson, R. P. Brady, L. Carone, A. L. Carter, K. L. Chubb, J. Inglis, J. Leconte, M. Line, M. López-Morales, Y. Miguel, K. Molaverdikhani, Z. Rustamkulov, D. K. Sing, K. B. Stevenson, H. R. Wakeford, J. Yang, K. Aggarwal, R. Baeyens, S. Barat, M. de Val-Borro, T. Daylan, J. J. Fortney, K. France, J. M. Goyal, D. Grant, J. Kirk, L. Kreidberg, A. Louca, S. E. Moran, S. Mukherjee, E. Nasedkin, K. Ohno, B. V. Rackham, S. Redfield, J. Taylor, P. Tremblin, C. Visscher, N. L. Wallack, L. Welbanks, A. Youngblood, E.-M. Ahrer, N. E. Batalha, P. Behr, Z. K. Berta-Thompson, J. Blecic, S. L. Casewell, I. J. M. Crossfield, N. Crouzet, P. E. Cubillos, L. Decin, J.-M. Désert, A. D. Feinstein, N. P. Gibson, J. Harrington, K. Heng, T. Henning, E. M. R. Kempton, J. Krick, P.-O. Lagage, M. Lendl, J. D. Lothringer, M. Mansfield, N. J. Mayne, T. Mikal-Evans, E. Palle, E. Schlawin, O. Shorttle, P. J. Wheatley, and S. N. Yurchenko. Photochemically produced SO_2 in the atmosphere of WASP-39b. Nature, 617(7961):483–487, May 2023. doi: 10.1038/s41586-023-05902-2.

A. Vazan, R. Helled, A. Kovetz, and M. Podolak. Convection and Mixing in Giant Planet Evolution. ApJ, 803(1):32, Apr. 2015. doi: 10.1088/0004-637X/803/1/32.

A. Vazan, R. Helled, M. Podolak, and A. Kovetz. The Evolution and Internal Structure of Jupiter and Saturn with Compositional Gradients. ApJ, 829(2):118, Oct. 2016. doi: 10.3847/0004-637X/829/2/118.

A. Vazan, R. Helled, and T. Guillot. Jupiter's evolution with primordial composition gradients. A&A, 610:L14, Feb. 2018. doi: 10.1051/0004-6361/201732522.

U. von Zahn, D. M. Hunten, and G. Lehmacher. Helium in Jupiter's atmosphere: Results from the Galileo probe helium interferometer experiment. J. Geophys. Res., 103(E10): 22815–22830, Sept. 1998. doi: 10.1029/98JE00695.

J. Vorberger, I. Tamblyn, B. Militzer, and S. A. Bonev. Hydrogen-helium mixtures in the interiors of giant planets. Phys. Rev. B, 75:024206, Jan 2007. doi: 10.1103/PhysRevB.75.024206. URL https://link.aps.org/doi/10.1103/PhysRevB.75.024206.

W. L. Vos, M. G. E. van Hinsberg, and J. A. Schouten. High-pressure triple point in helium: The melting line of helium up to 240 kbar. Phys. Rev. B, 42:6106–6109, Oct 1990. doi: 10.1103/PhysRevB.42.6106. URL https://link.aps.org/doi/10.1103/PhysRevB.42.6106.

N. Vowell, J. E. Rodriguez, S. N. Quinn, G. Zhou, A. Vanderburg, A. W. Mann, M. J. Hooton, K. G. Stassun, S. Howard, A. Bieryla, D. W. Latham, S. B. Howell, T. Guillot, C. Ziegler, K. A. Collins, T. W. Carmichael, J. M. Jenkins, A. Shporer, L. ABE,

P. Bendjoya, J. L. Bush, M. Buttu, K. I. Collins, J. D. Eastman, M. J. Fields, T. Gasparetto, M. N. Günther, V. B. Kostov, A. L. Kraus, K. V. Lester, A. M. Levine, C. Littlefield, W. Marie-Sainte, D. Mékarnia, H. P. Osborn, D. Rapetti, G. R. Ricker, S. Seager, R. Sefako, G. Srdoc, O. Suarez, G. Torres, A. H. M. J. Triaud, R. Vanderspek, and J. N. Winn. HIP 33609 b: An Eccentric Brown Dwarf Transiting a V = 7.3 Rapidly Rotating B Star. AJ, 165(6):268, June 2023. doi: 10.3847/1538-3881/acd197.

S. M. Wahl, W. B. Hubbard, B. Militzer, T. Guillot, Y. Miguel, N. Movshovitz, Y. Kaspi, R. Helled, D. Reese, E. Galanti, S. Levin, J. E. Connerney, and S. J. Bolton. Comparing Jupiter interior structure models to Juno gravity measurements and the role of a dilute core. Geophys. Res. Lett., 44(10):4649–4659, May 2017. doi: 10.1002/2017GL073160.

H. R. Wakeford, D. K. Sing, D. Deming, N. K. Lewis, J. Goyal, T. J. Wilson, J. Barstow, T. Kataria, B. Drummond, T. M. Evans, A. L. Carter, N. Nikolov, H. A. Knutson, G. E. Ballester, and A. M. Mandell. The Complete Transmission Spectrum of WASP-39b with a Precise Water Constraint. AJ, 155(1):29, Jan. 2018. doi: 10.3847/1538-3881/aa9e4e.

K. J. Walsh, A. Morbidelli, S. N. Raymond, D. P. O'Brien, and A. M. Mandell. A low mass for Mars from Jupiter's early gas-driven migration. Nature, 475(7355):206–209, July 2011. doi: 10.1038/nature10201.

C. R. Webster, P. R. Mahaffy, G. J. Flesch, P. B. Niles, J. H. Jones, L. A. Leshin, S. K. Atreya, J. C. Stern, L. E. Christensen, T. Owen, H. Franz, R. O. Pepin, A. Steele, and aff9. Isotope Ratios of H, C, and O in CO_2 and H_2O of the Martian Atmosphere. Science, 341(6143):260–263, July 2013. doi: 10.1126/science.1237961.

E. Wigner and H. B. Huntington. On the possibility of a metallic modification of hydrogen. The Journal of Chemical Physics, 3(12):764–770, 1935.

R. Wildt. The Constitution of the planets (Council Report on the progress of astronomy). MNRAS, 107:84, Jan. 1947. doi: 10.1093/mnras/107.1.84.

A. S. Williams. on the drift of the surface material of Jupiter in different latitudes. MNRAS, 56:143, Jan. 1896. doi: 10.1093/mnras/56.3.143.

H. F. Wilson and B. Militzer. Sequestration of Noble Gases in Giant Planet Interiors. Phys. Rev. Lett., 104(12):121101, Mar. 2010. doi: 10.1103/PhysRevLett.104.121101.

J. N. Winn and D. C. Fabrycky. The Occurrence and Architecture of Exoplanetary Systems. ARA&A, 53:409–447, Aug. 2015. doi: 10.1146/annurev-astro-082214-122246.

J. Wisdom and W. B. Hubbard. Differential rotation in Jupiter: A comparison of methods. Icarus, 267:315–322, Mar. 2016. doi: 10.1016/j.icarus.2015.12.030.

M. H. Wong, P. R. Mahaffy, S. K. Atreya, H. B. Niemann, and T. C. Owen. Updated Galileo probe mass spectrometer measurements of carbon, oxygen, nitrogen, and sulfur on Jupiter. Icarus, 171(1):153–170, Sept. 2004. doi: 10.1016/j.icarus.2004.04.010.

M. H. Wong, S. K. Atreya, P. N. Mahaffy, H. B. Franz, C. Malespin, M. G. Trainer, J. C. Stern, P. G. Conrad, H. L. K. Manning, R. O. Pepin, R. H. Becker, C. P. McKay, T. C. Owen, R. Navarro-González, J. H. Jones, B. M. Jakosky, and A. Steele. Isotopes of nitrogen on Mars: Atmospheric measurements by Curiosity's mass spectrometer. Geophys. Res. Lett., 40(23):6033–6037, Dec. 2013. doi: 10.1002/2013GL057840.

M. Zaghoo, A. Salamat, and I. F. Silvera. Evidence of a first-order phase transition to metallic hydrogen. Phys. Rev. B, 93:155128, Apr 2016. doi: 10.1103/PhysRevB.93.155128. URL https://link.aps.org/doi/10.1103/PhysRevB.93.155128.

L. Zeng, S. B. Jacobsen, D. D. Sasselov, M. I. Petaev, A. Vanderburg, M. Lopez-Morales, J. Perez-Mercader, T. R. Mattsson, G. Li, M. Z. Heising, A. S. Bonomo, M. Damasso, T. A. Berger, H. Cao, A. Levi, and R. D. Wordsworth. Growth model interpretation of planet size distribution. Proceedings of the National Academy of Science, 116(20): 9723–9728, May 2019. doi: 10.1073/pnas.1812905116.

V. N. Zharkov and V. P. Trubitsyn. Determination of the equation of state of the molecular envelopes of Jupiter and Saturn from their gravitational moments. Icarus, 21(2):152–156, Feb. 1974. doi: 10.1016/0019-1035(74)90131-6.

V. N. Zharkov and V. P. Trubitsyn. Physics of planetary interiors. 1978.

Appendix A

Appendix of Howard & Guillot 2023

A.1 Comparisons of the entropy of mixing

Figure A.1 shows a comparison of the entropies obtained from our work and by SR18 (SM Fig.1). For $T = 10000\ K$, $r_s = 1.4\,a_0$ and $1.25\,a_0$, and various helium fractions x_{He}, we calculated the total entropy (using Eq. (3.3), with CMS19-H, CMS19-He, and our table of the mixing terms to compute S_H, S_{He} and S_{mix}, respectively). We also show the entropy resulting from the ideal mixing of only the pure terms ($XS_H + YS_{He}$). The difference between the two curves represents the entropy of mixing ΔS. First, we note some important differences on the pure H and He EOSs between CMS19 and the work of SR18. Typically, for $r_s = 1.4\,a_0$, the entropy of CMS19-H is 0.2 k_b/atom lower than the pure H EOS from SR18, while the entropy of CMS19-He is 0.53 k_b/atom higher than the pure He EOS from SR18. In H-He mixtures, the entropy we calculate (where the mixing entropy is initially based on the MH13 EOS) is always higher than the entropy from SR18 (0.58 k_b/atom greater at most).

These intrinsic differences in the pure EOSs and also in the entropies yielded for H-He mixtures lead to discrepancies between the entropy of mixing that we obtain and the one from SR18. In this parameter space ($T = 10000\ K$, $r_s = 1.4\,a_0$ or $1.25\,a_0$), while the entropy of mixing of SR18 ranges from 0.23 to 0.66 k_b/atom, our entropy of mixing ranges from 0.26 to 1.2 k_b/atom. The entropy of mixing that we obtain is hence 1.1 to 2.2 times higher than the entropy of mixing of SR18. (Similar results would be obtained using the Morales et al. [2009] calculations because their entropies of mixing are similar to those of SR18). This highlights the fact that the EOSs for pure hydrogen, pure helium, and mixtures of hydrogen and helium obtained by the different groups still differ; this is particularly obvious for the pure helium EOS used here (CMS19-He)

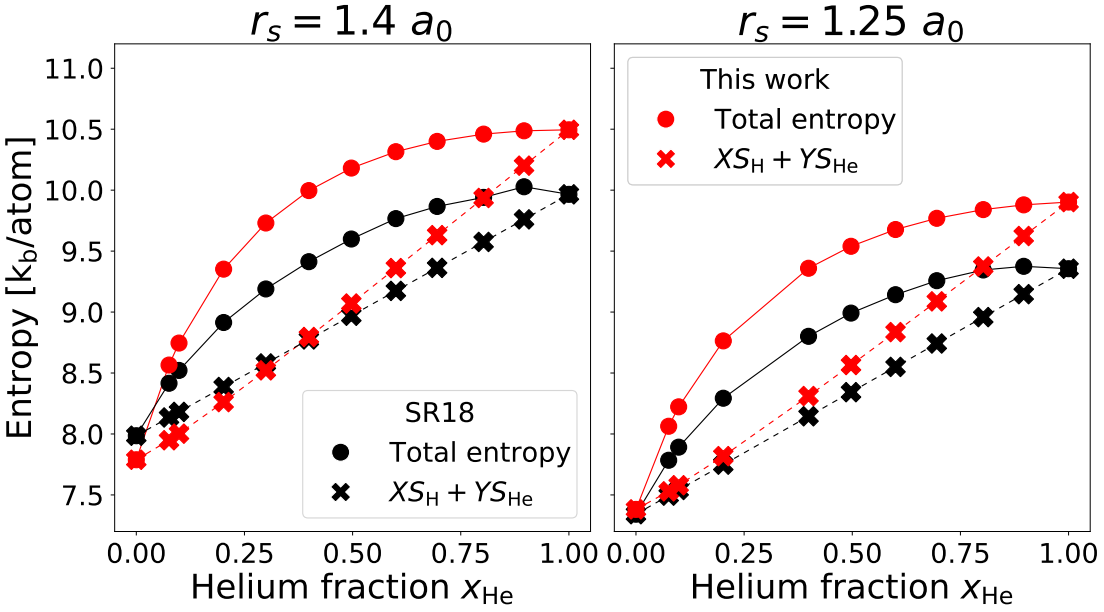

FIGURE A.1: Comparison of our entropy with the one calculated by SR18 (from Fig.1 of their supplemental material) for $T = 10000\ K$ and various helium fractions x_{He}. The two panels show results for values of Wigner-Seitz radii of $r_s = 1.4\,a_0$ and $r_s = 1.25\,a_0$ respectively. Each panel displays our calculations (*red*) of the total entropy (computed using Eq. 3.3 with CMS19-H, CMS19-He and our table for ΔS) and also the entropy without including the entropy of mixing ΔS (hence corresponding to $XS_H + YS_{He}$). Results from SR18 are shown in *black*.

and the one obtained by SR18. While CMS19 have used the Perdew–Burke–Ernzerhof (PBE) exchange-correlation functional in their simulations, SR18 applied the van der Waals density functional (vdW-DF) exchange-correlation functional. Both exchange-correlation functionals support different experiments and have their own benefits and limitations (see SR18 for a more detailed discussion). A consistent, homogeneous exploration of EOSs in this regime of pressures and temperature and for different compositions is crucial.

In spite of these uncertainties, we believe that using the table of non-ideal mixing effects that we provide in addition to the CMS19 EOS is an improvement for two reasons: (i) It includes non-ideal mixing effects that are otherwise ignored, and for low helium abundances ($Y < 0.3$), it yields total entropies that differ from those of SR18 by less than 4%. (ii) It enables calculations in the high-temperature regions spanned by massive planets and brown dwarfs, which are otherwise not possible with the CD21 EOS.

A.2 Table of the non-ideal mixing effects

The derivation of V_{mix} and S_{mix} is described in Sect. 3.5.2. The table had to be slightly adjusted in order to avoid spurious interpolation issues and to be directly usable for interior and evolution models of giant planets and brown dwarfs. V_{mix} displayed an

TABLE A.1: Table of the mixing terms. A full version of the electronic table is available at the CDS via anonymous ftp to cdsarc.cds.unistra.fr (130.79.128.5) or via https://cdsarc.cds.unistra.fr/cgi-bin/qcat?J/A+A/; or via https://doi.org/10.5281/zenodo.7346181.

$\log(P)$ [dyn/cm^2]	$\log(T)$ [K]	$V_{\rm mix}$ [cm^3/g]	$S_{\rm mix}$ [erg/g/K]
10.5	2.5	0.21972032499215227	145270983.02864826
10.5	2.55	-1.6752656793119542	97266054.24784786
10.5	2.6	-0.5750688394019108	19976893.840987258
10.5	2.65	-0.20048821618796142	114994434.5574714
10.5	2.7	0.013568193301054745	157590130.69068393
10.5	2.75	0.1328211678295867	153264410.38666478
10.5	2.8	0.21204647603740195	153310129.47913098
10.5	2.85	0.24501465036396686	156237499.56270728

alternation of positive and negative values with very low amplitude that jeopardised the interpolation through the table. Hence $V_{\rm mix}$ was set to 0 when $\Delta V \times \rho_{\rm H-He}$ was lower than 0.01%. Thirteen isolated outliers, located in a region of the table where $11.1 < \log(P) < 12.5$ (with pressure in dyn/cm^2) and $2.45 < \log(T) < 2.85$ (with temperature in K), were smoothed with a median over the contiguous points of the table. $S_{\rm mix}$ presented strong outliers at the edges of the table both at low ($\log(P) < 6$) and high pressure ($\log(P) > 15$), with values that could differ by several orders of magnitudes. Hence, for regions of the table where $6 < \log(P) < 15$, we set the values of $S_{\rm mix}$ so that ΔS is equal to the ideal entropy of mixing. Furthermore, when we used the table to model the evolution of massive brown dwarfs ($\sim 60\ M_{\rm J}$) using our planetary evolution code, we ran into convergence issues. We found that the CD21 entropy table caused this at high temperatures ($\log(T) > 5$). We therefore multiplied $\Delta S(\tilde{Y}) - \Delta S_{\rm ideal}(\tilde{Y})$ by $\{1 - {\rm erf}[({\rm T} - {\rm T}_{\rm ref})/\ \delta T]\}/2$ with $T_{\rm ref} = 4.9$ and $\delta T = 0.1$: At higher temperatures, the entropy of mixing smoothly converges to the ideal value.

A fragment of the final version is presented in Table A.1. The table may be used both in the low- (giant planets) and in the high-mass regime (brown dwarfs). We recall that this table is valid in the same domain as the EOS from Chabrier et al. [2019], whose limitations concern the regions in which molecular hydrogen and ionised hydrogen become solid, as well as in the region in which ion quantum effects become important, namely at low T and high P (see Fig.1 and Fig.16 of Chabrier et al. [2019] for the precise locations in the phase diagrams).

Appendix B

Corner plots of models in Miguel et al. 2022

We display in Figs. B.1 (dilute core models) and B.2 (three-layer models) the corner plots corresponding to the models presented in Section 5.2.

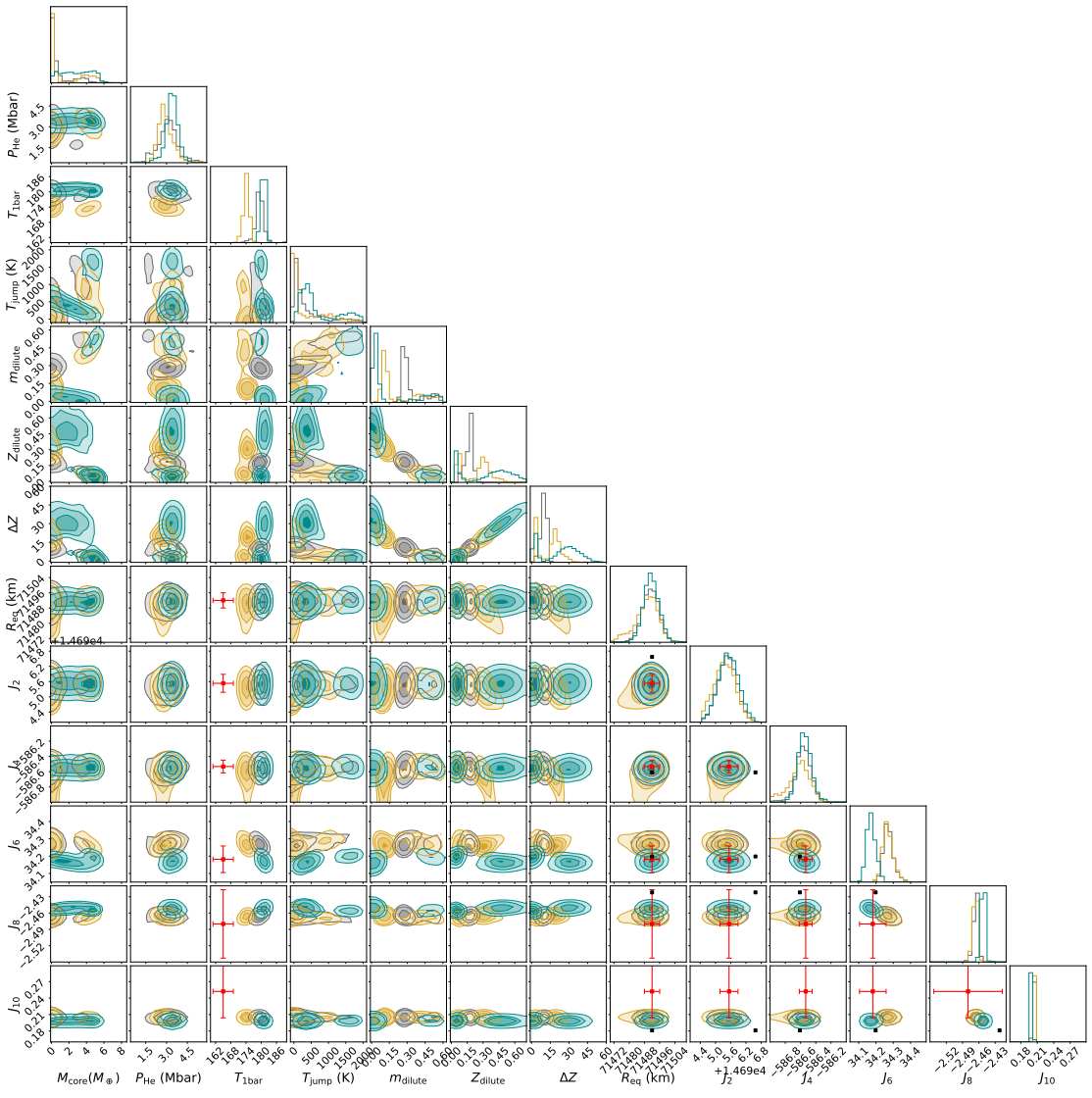

FIGURE B.1: Posterior distributions obtained for dilute core models, where $T_{\rm 1bar}$ is a free parameter and $Z_1 = 1\times$ protosolar. Colours corresponds to results from different EOSs: *grey* for MGF16+MH13, *yellow* for MLS22 and *green* for CMS19. The black points correspond to the measured J_{2n} by Juno. The red error bars correspond to Juno's measurements accounting for differential rotation for the J_{2n} and Galileo's measurement for $T_{\rm 1bar}$.

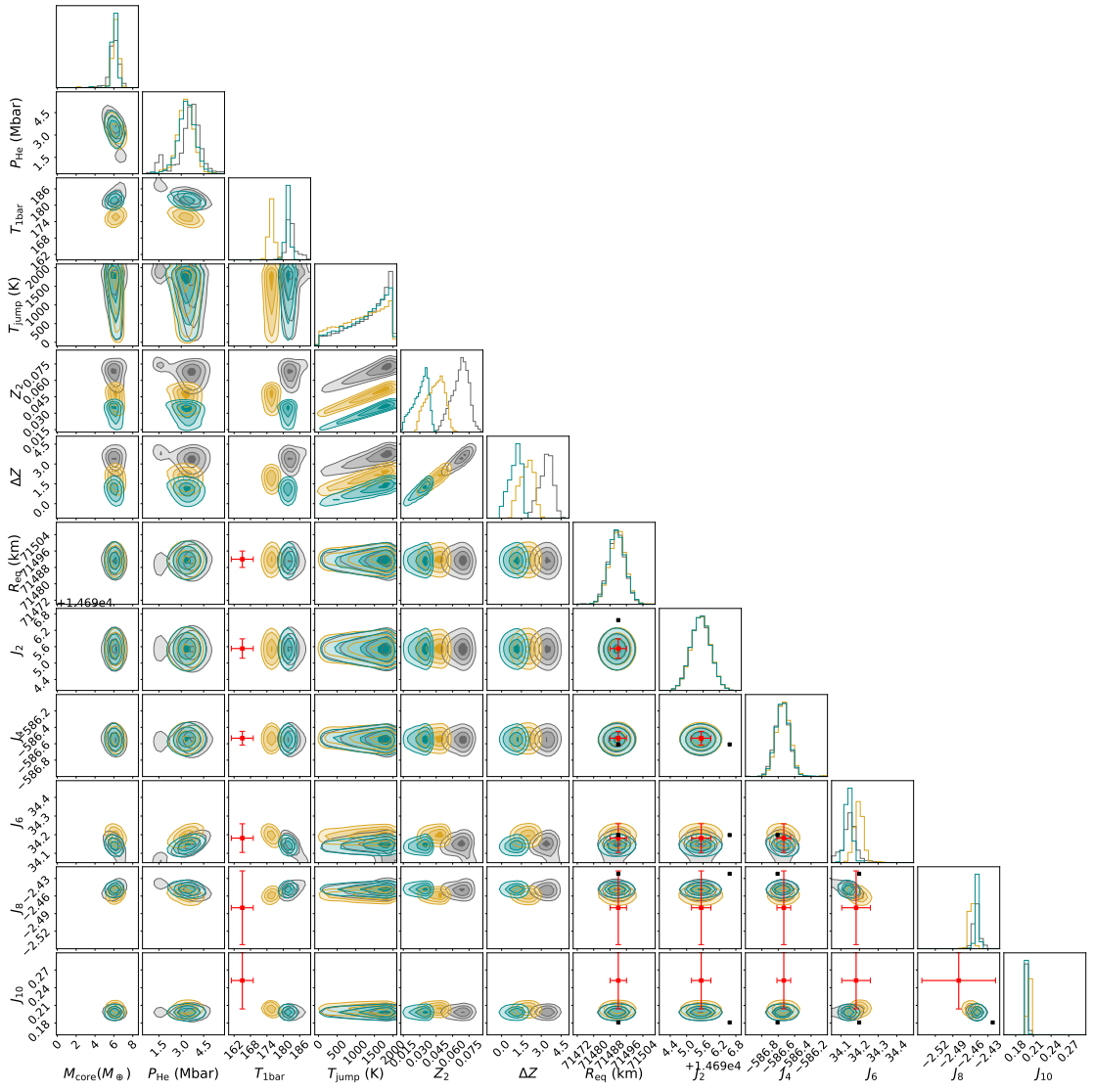

FIGURE B.2: Same as Fig. B.1 but for three-layer models.

Appendix C

Unconstrained modification of EOS: results

We display in Figs. C.1 and C.2 the corner plots corresponding to the models presented in Subsection 5.3.1, respectively for three-layer and dilute core models.

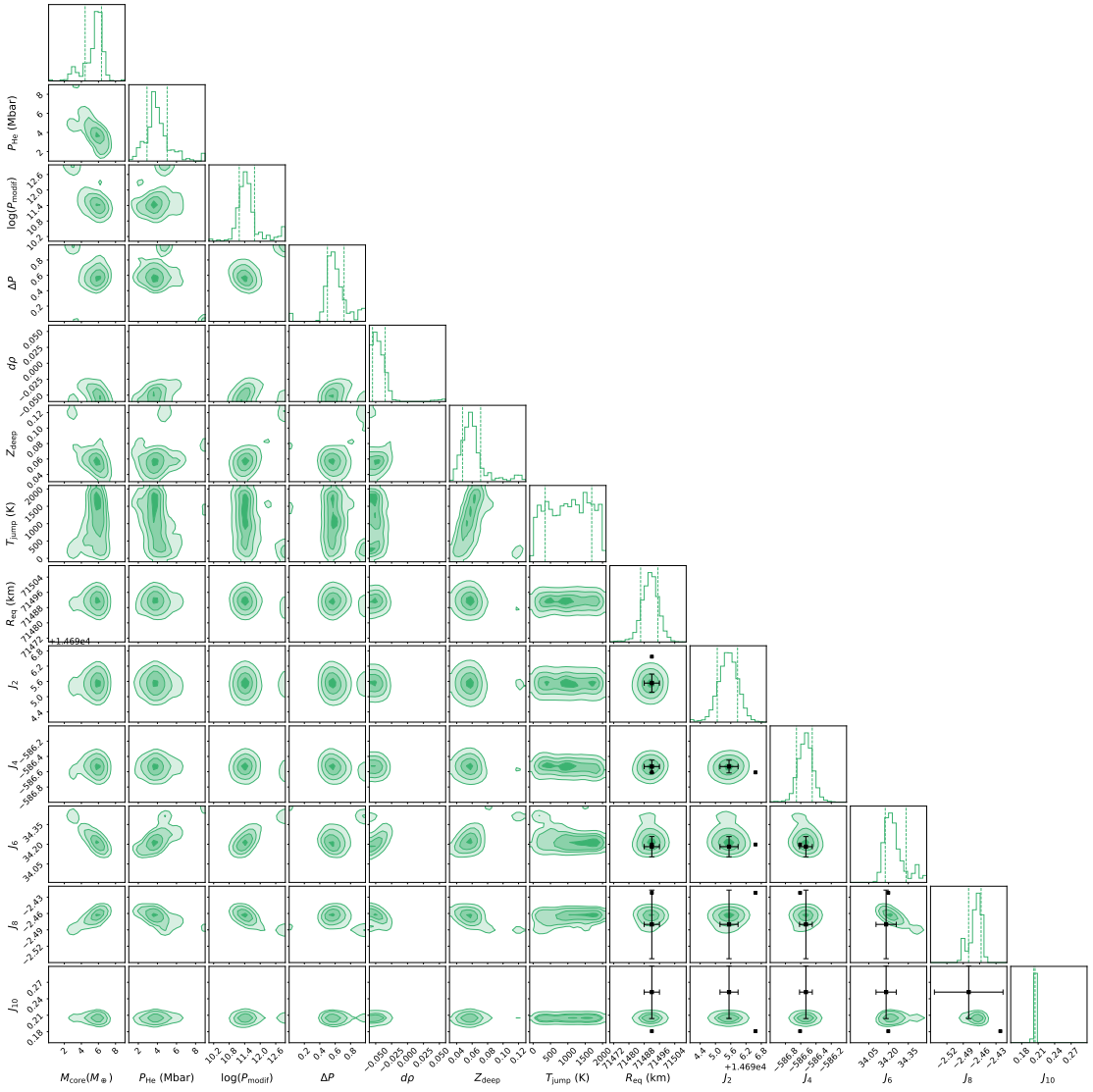

FIGURE C.1: Posterior distributions obtained for three-layer models, where $T_{1\rm bar} = 166.1$ K, $Z_1 = 1\times$ protosolar and where the EOS has been modified. The black points correspond to the measured J_{2n} by Juno. The black error bars correspond to Juno's measurements accounting for differential rotation for the J_{2n}.

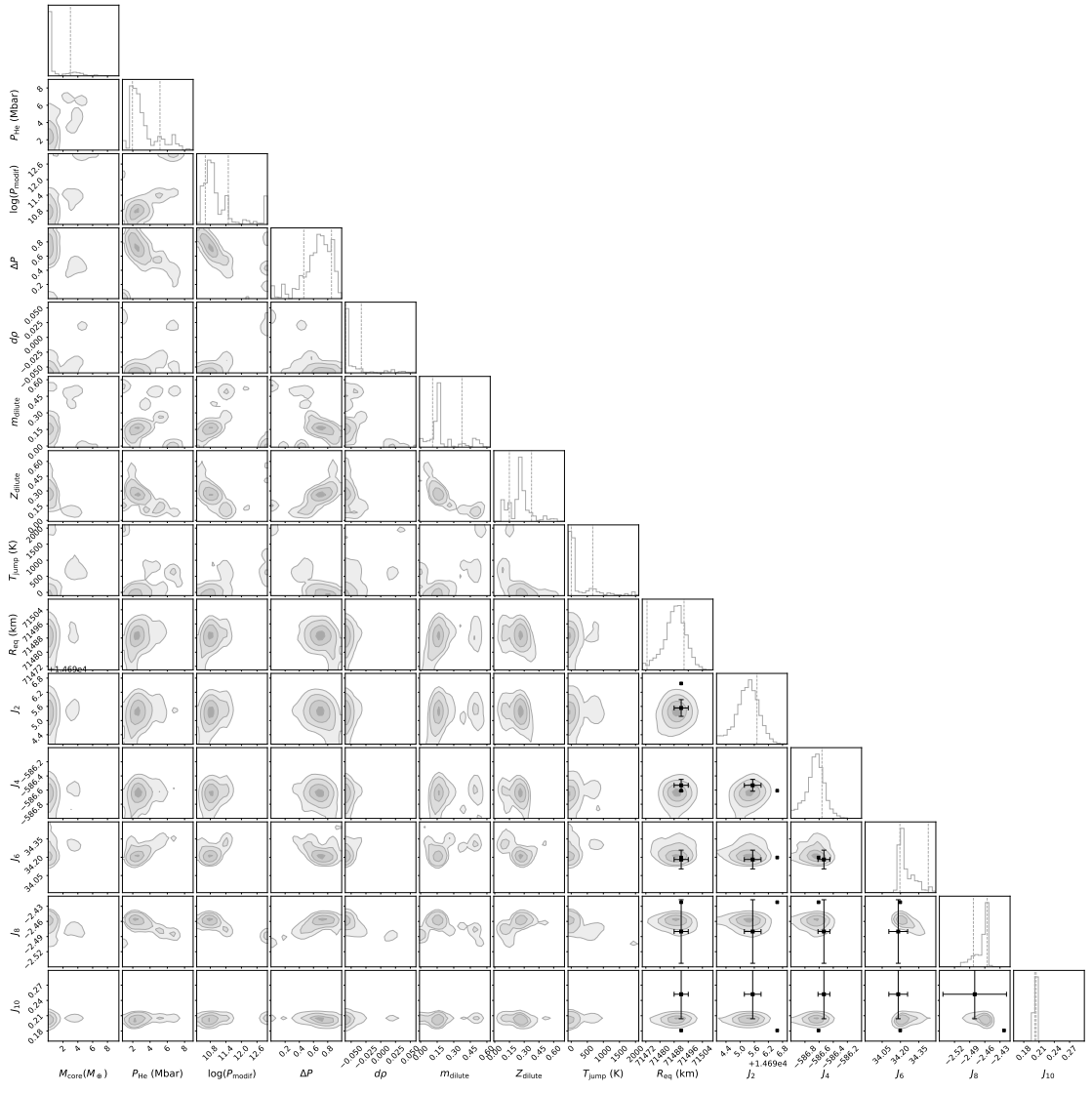

FIGURE C.2: Same as Fig. C.1 but for dilute core models.

Appendix D

Appendix of Howard et al. 2023

D.1 Comparison between runs with Gaussian and uniform priors

Figure D.1 compares the posterior distributions of two MCMC simulations: using Gaussian or uniform priors on the parameters to modify the EOS (see Section 5.3.4).

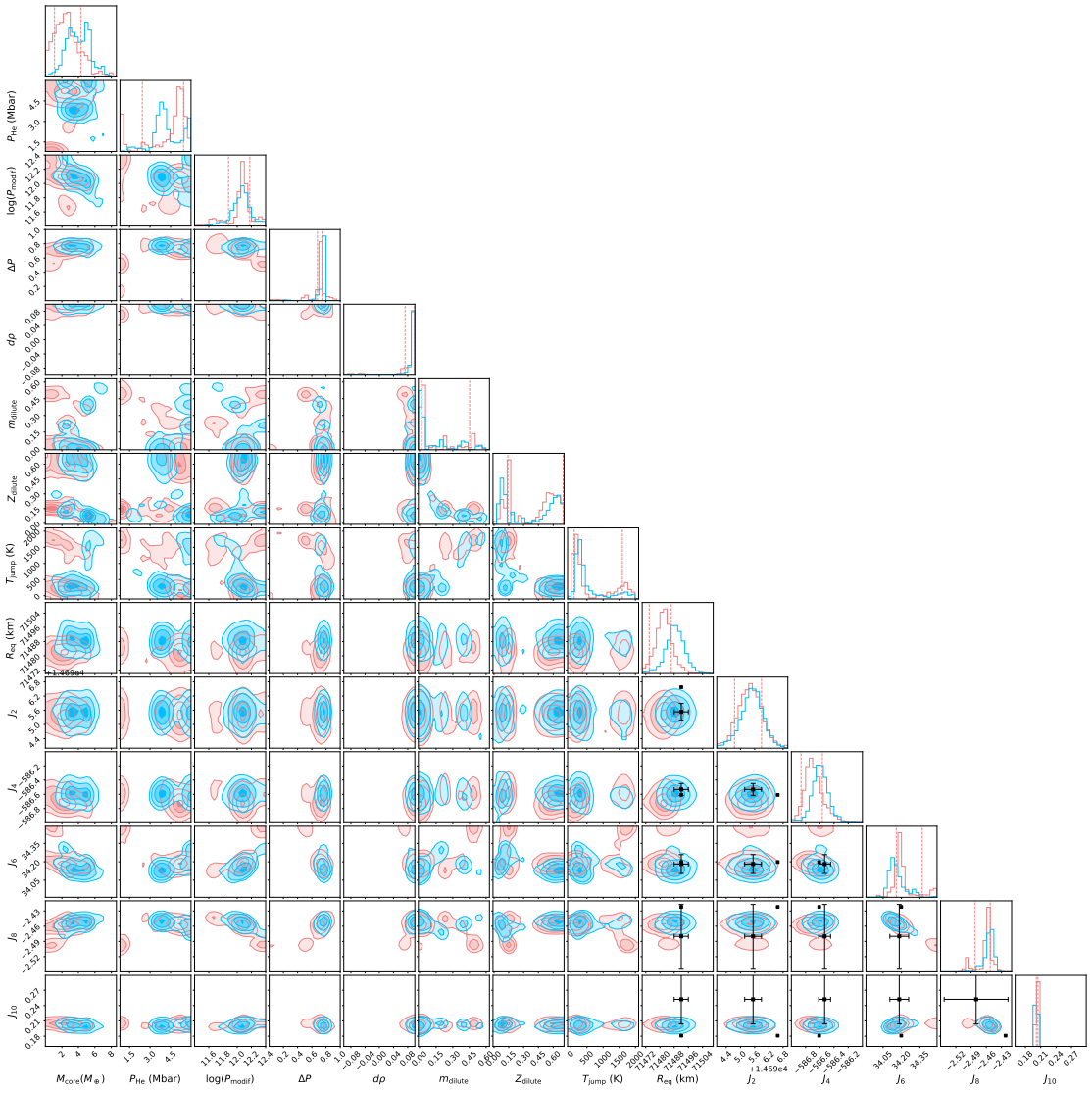

FIGURE D.1: Posterior distributions obtained with a modification of the EOS. Red shows results obtained with Gaussian priors. Blue shows results obtained with uniform priors. $T_{1\text{bar}}$ is fixed at 166.1 K and $Z_1 = 0.02$. The black points correspond to the measured J_{2n} by Juno. The black error bars correspond to Juno's measurements accounting for differential rotation for the J_{2n}.

D.2 Corner plots of models with and without modification of the EOS

Figures D.2, D.3, D.4, D.5, and D.6 show the posterior distributions of the MCMC simulations using original EOSs, respectively, MGF16+MH13, MH13*, CD21, HG23+CMS19, and HG23+MLS22.

Figures D.7 and D.8 show the posterior distributions of the MCMC simulations using modified EOS, with $T_{1\mathrm{bar}} = 166.1$ K and respectively for $Z_1 = 0.02$ and $Z_1 = 0.0286$. Figures D.9 and D.10 show the posterior distributions of the MCMC simulations using modified EOS, with $T_{1\mathrm{bar}} = 174.1$ K and respectively for $Z_1 = 0.02$ and $Z_1 = 0.035$.

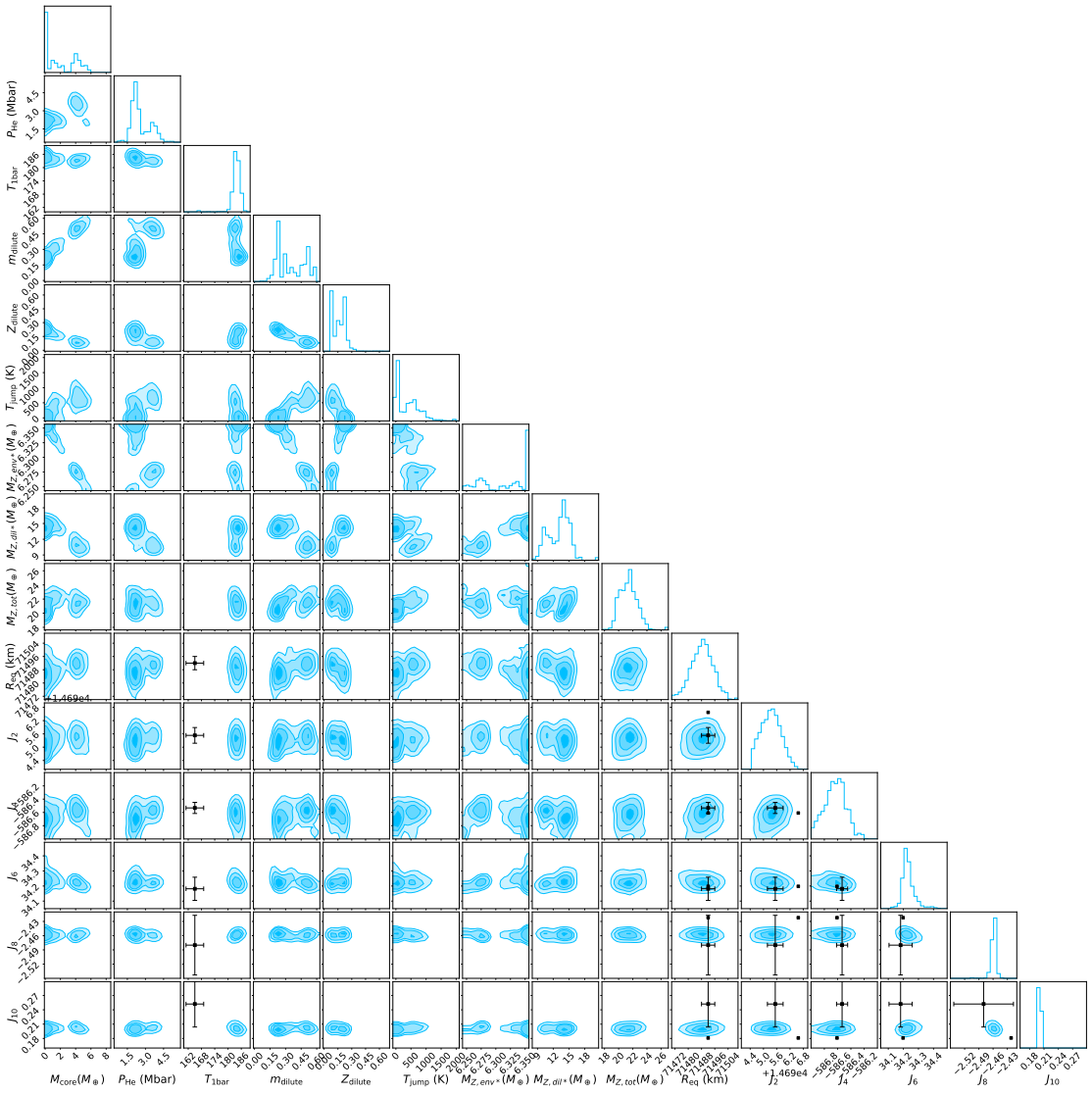

FIGURE D.2: Posterior distributions obtained with the MGF16+MH13 EOS, where $T_{1\mathrm{bar}}$ is a free parameter, $Z_1 = 0.02$ (1.3 $\times$ the protosolar value). The black points correspond to the measured J_{2n} by Juno. The black error bars correspond to Juno's measurements accounting for differential rotation for the J_{2n} and Galileo's measurement for $T_{1\mathrm{bar}}$.

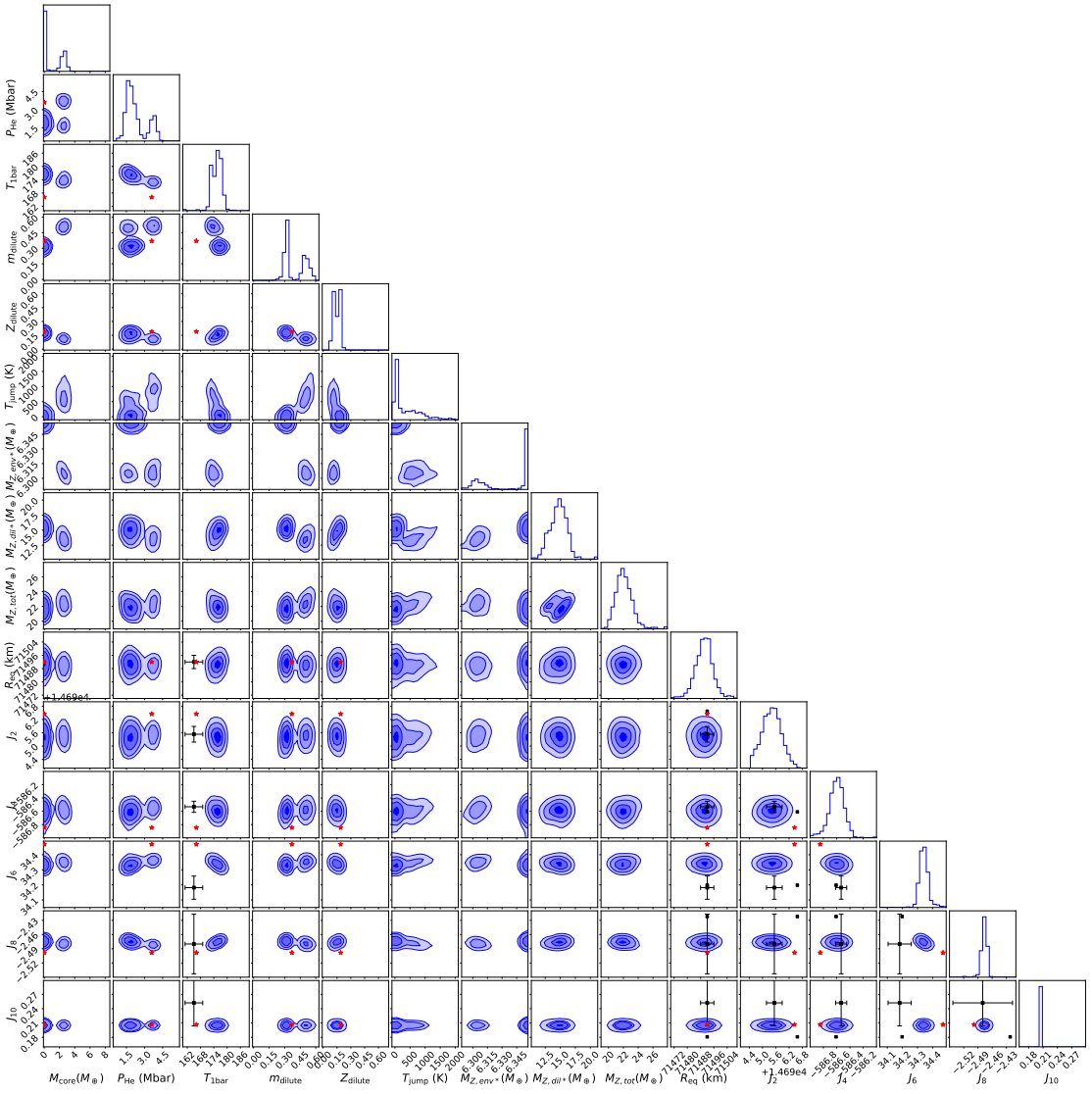

FIGURE D.3: Same as Fig. D.2 but with the MH13* EOS. The red star shows the Militzer et al. [2022] preferred (static) model.

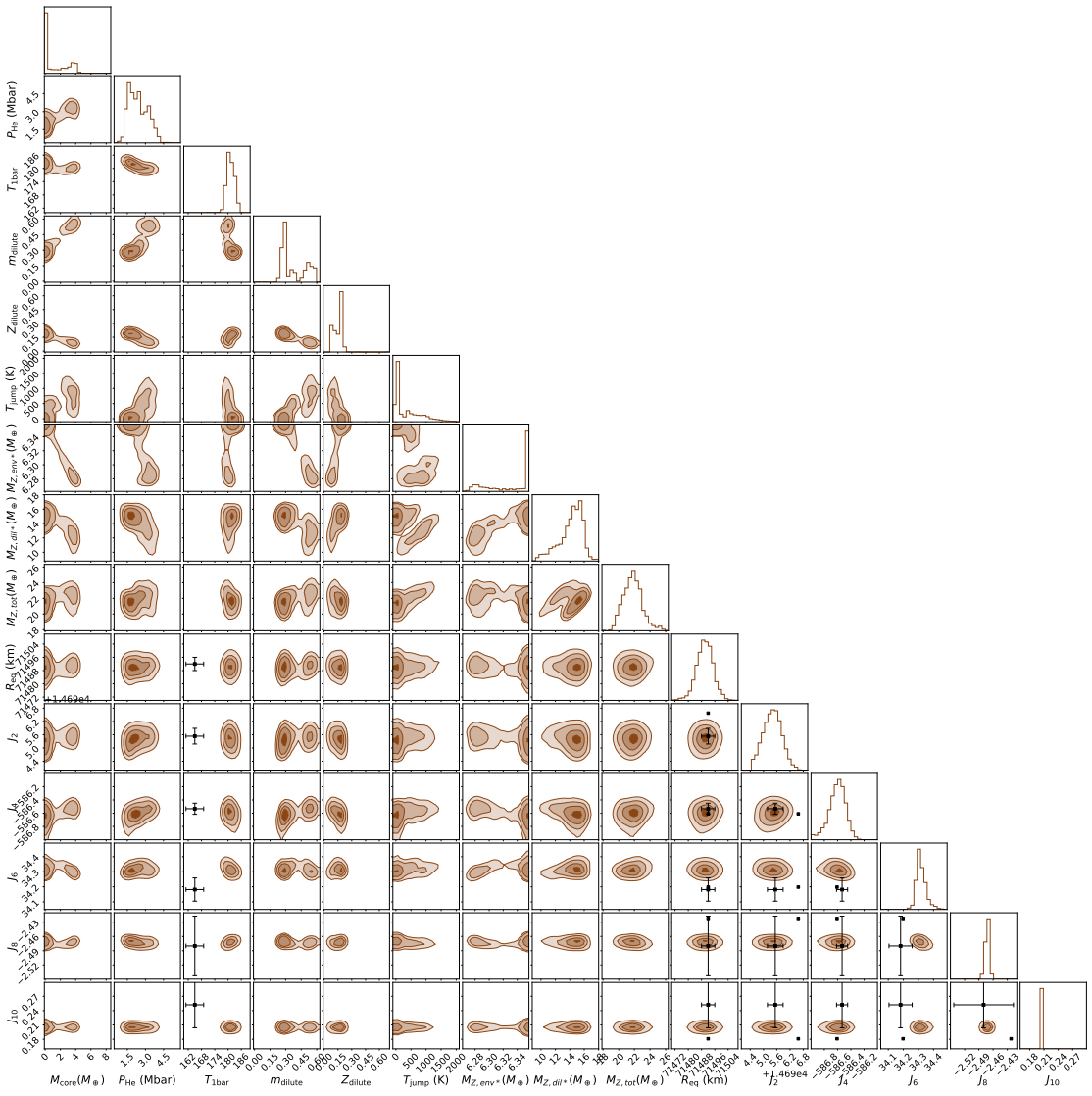

FIGURE D.4: Same as Fig. D.2 but with the CD21 EOS.

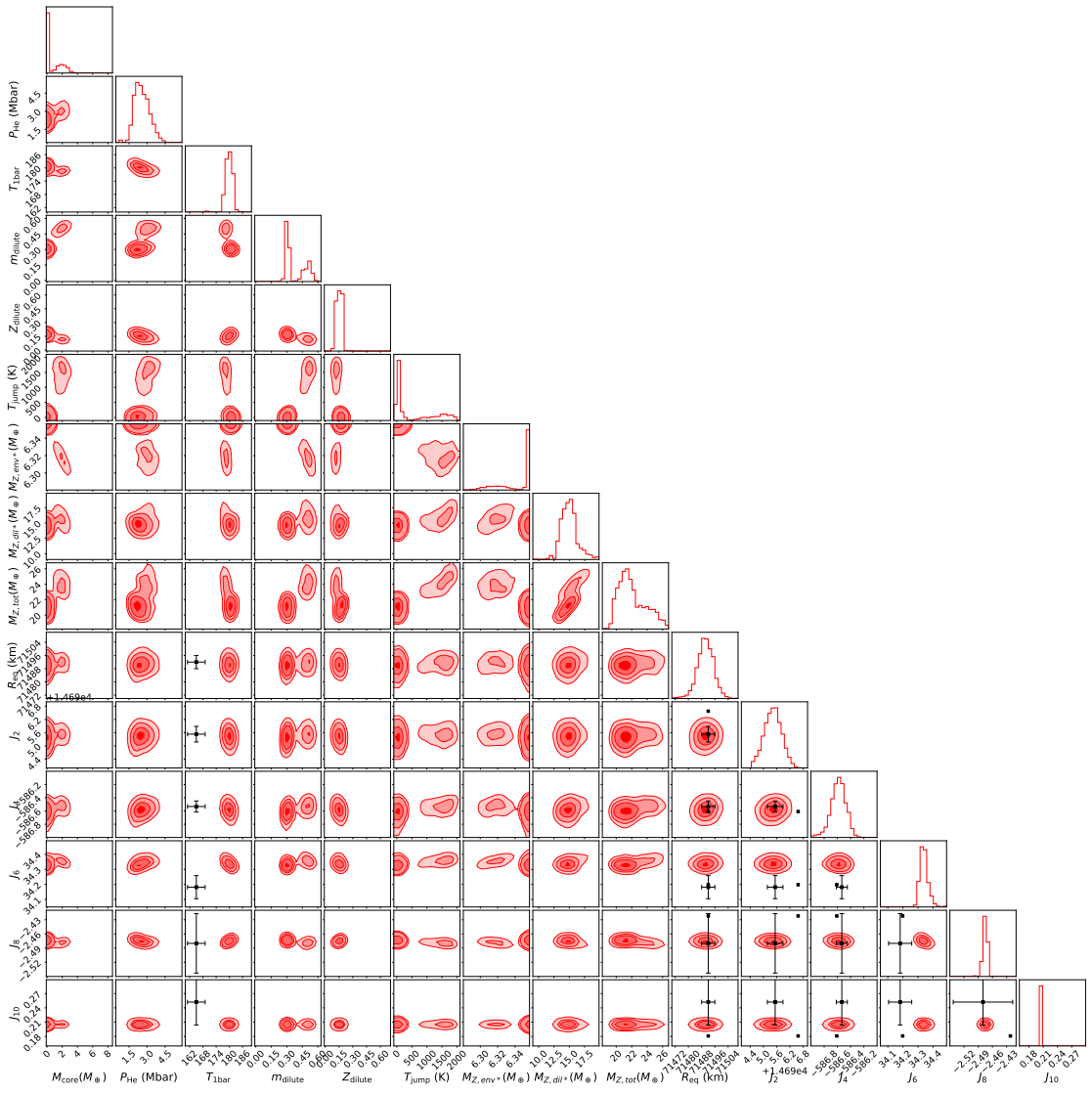

FIGURE D.5: Same as Fig. D.2 but with the HG23+CMS19 EOS.

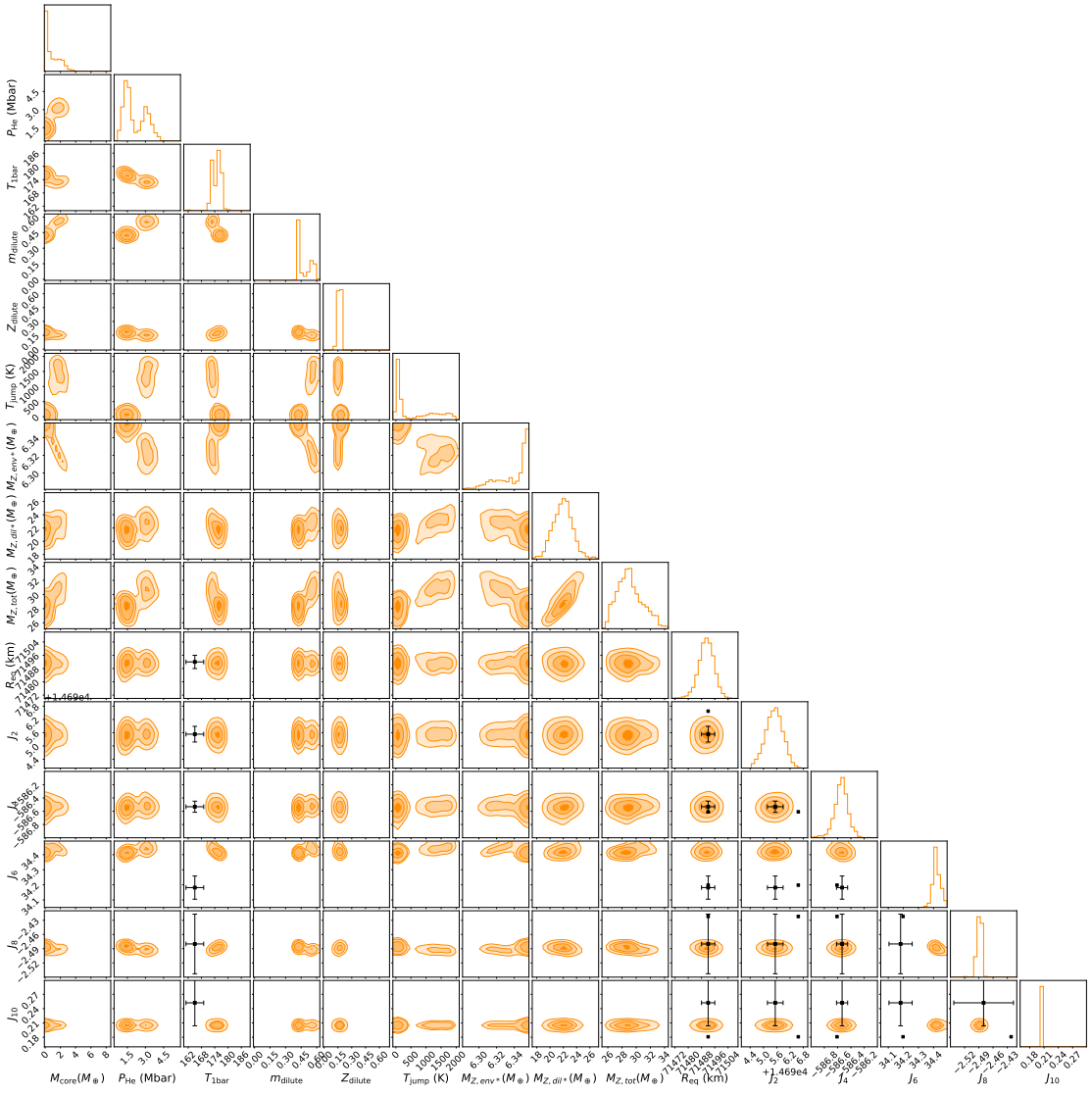

FIGURE D.6: Same as Fig. D.2 but with the HG23+MLS22 EOS.

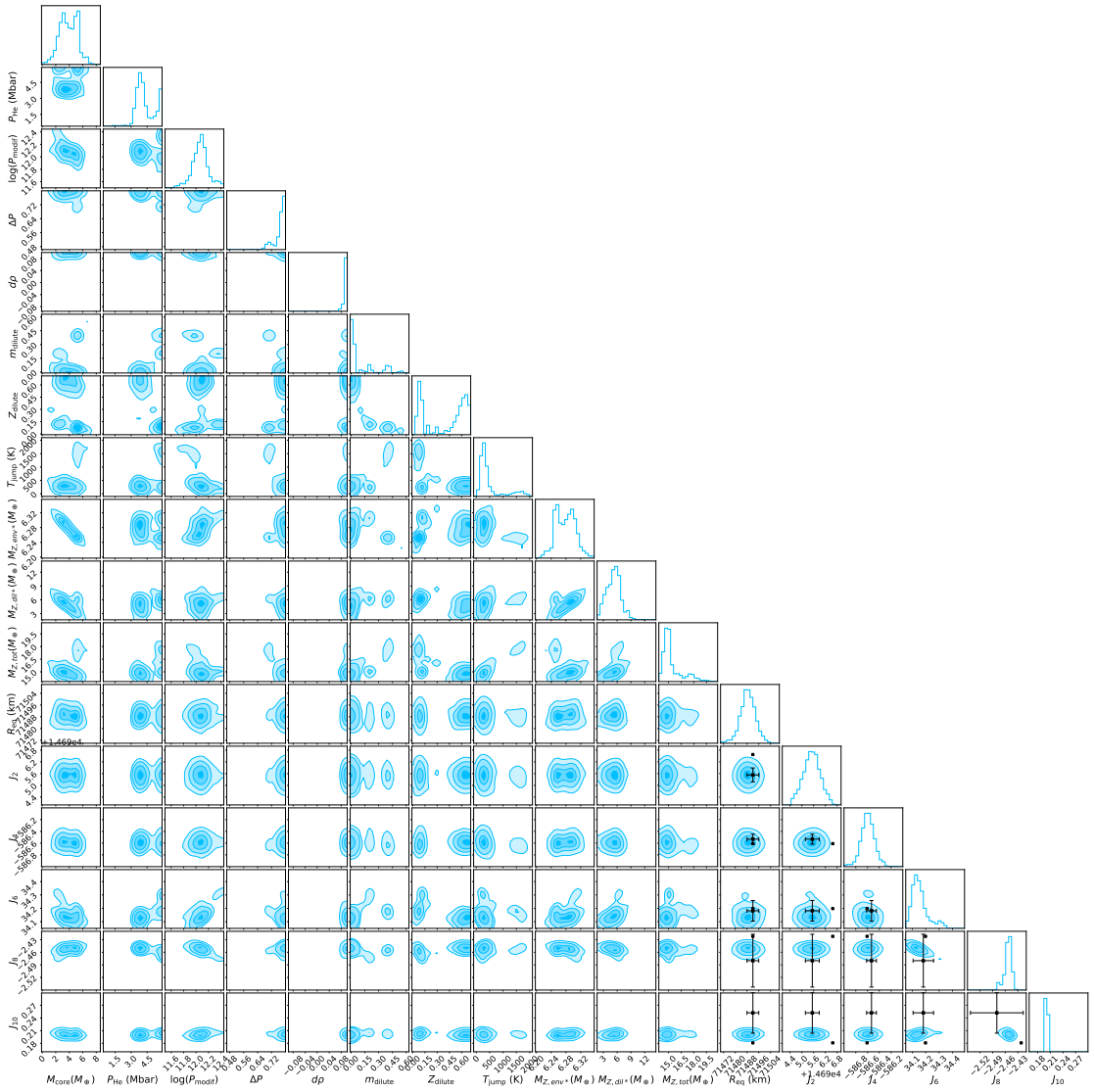

FIGURE D.7: Posterior distributions obtained with a modification of the EOS, where $T_{\rm 1bar}$ is fixed at 166.1 K, $Z_1 = 0.02$ (1.3 $\times$ the protosolar value). The black points correspond to the measured J_{2n} by Juno. The black error bars correspond to Juno's measurements accounting for differential rotation for the J_{2n}.

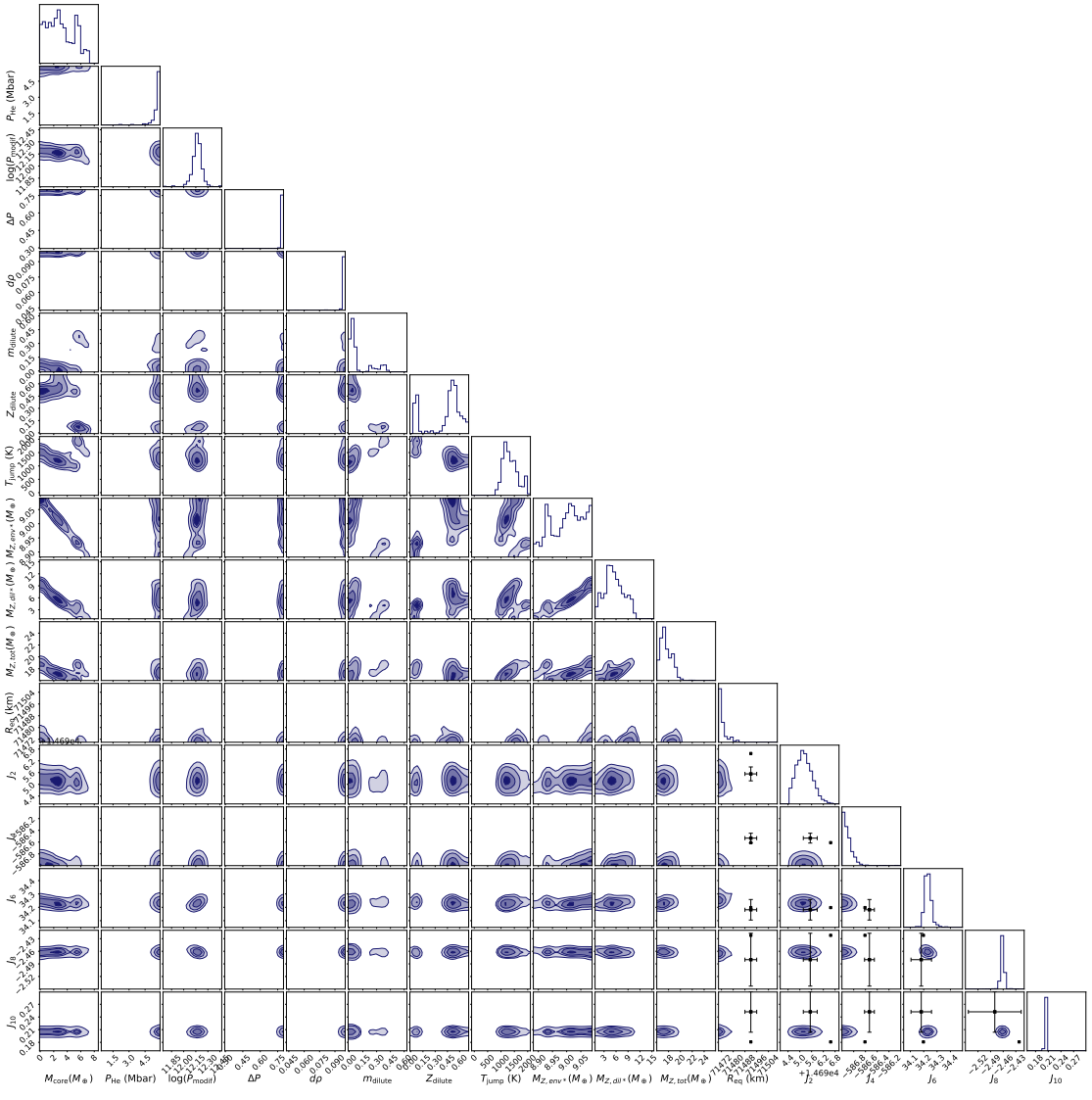

FIGURE D.8: Same as Fig. D.7 but with $Z_1 = 0.0286$ (1.9 $\times$ the protosolar value)

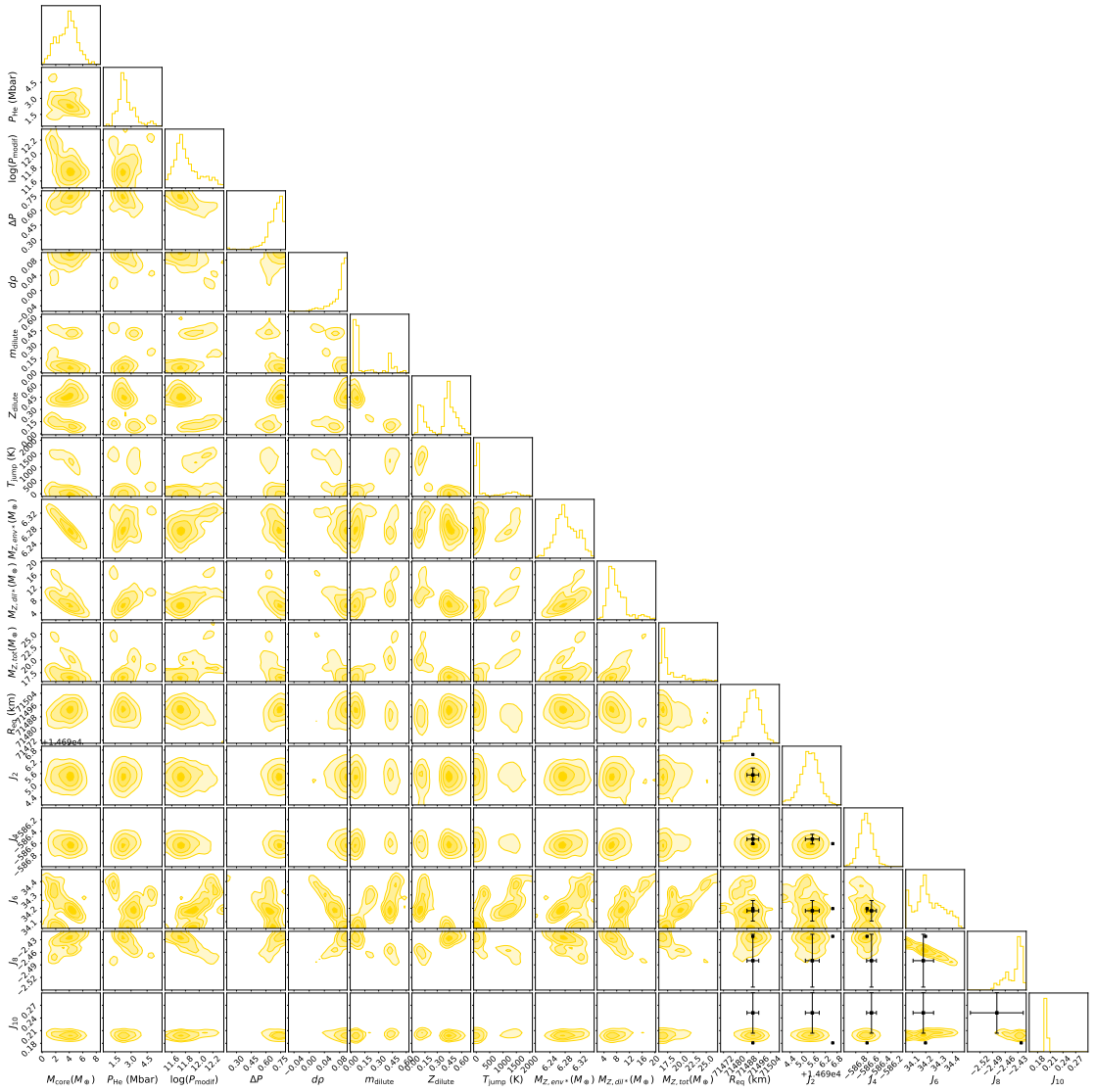

FIGURE D.9: Posterior distributions obtained with a modification of the EOS, where $T_{1\text{bar}}$ is fixed at 174.1 K, $Z_1 = 0.02$ (1.3 $\times$ the protosolar value). The black points correspond to the measured J_{2n} by Juno. The black error bars correspond to Juno's measurements accounting for differential rotation for the J_{2n}.

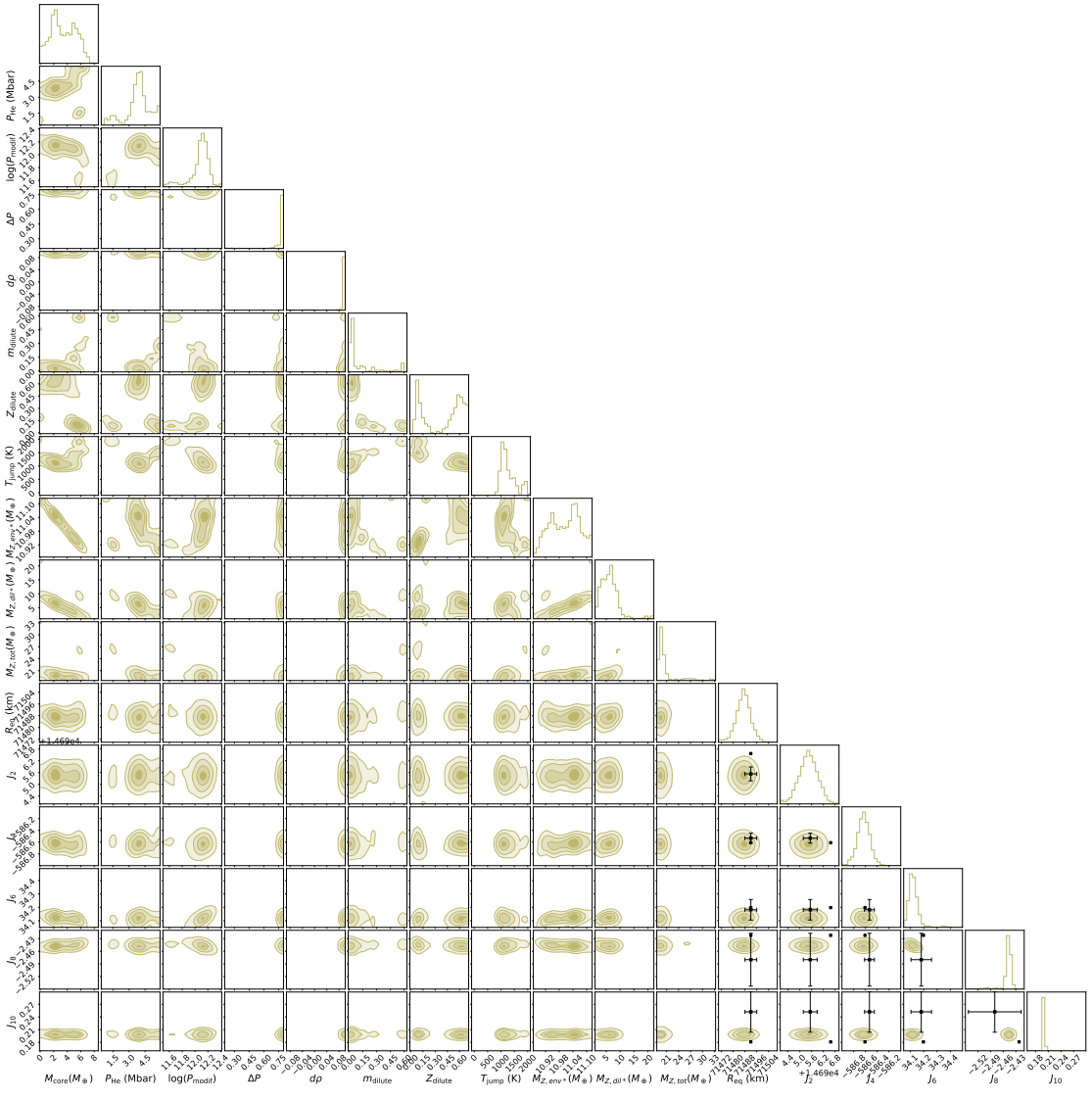

FIGURE D.10: Same as Fig. D.9 but with $Z_1 = 0.035$ (2.3 $\times$ the protosolar value)

D.3 Comparison with Militzer et al. 2022

We ran MCMC simulations to reproduce the results obtained by Militzer et al. [2022]. To do so, we changed the values of the gravitational moments around which the MCMC is sampling models. We used the gravitational moments of the interior model of Militzer et al. [2022] (see their Table 1). We used the same properties: no compact core, $Z_1 = 0.0153$, $T_{1\text{bar}} = 166.1$ K, and the MH13* EOS. Figure D.11 shows the posterior distributions we obtain. We find models with similar properties to Model A from Militzer et al. [2022]: the same gravitational moments, the same P_{He}, and comparable characteristics for the dilute core.

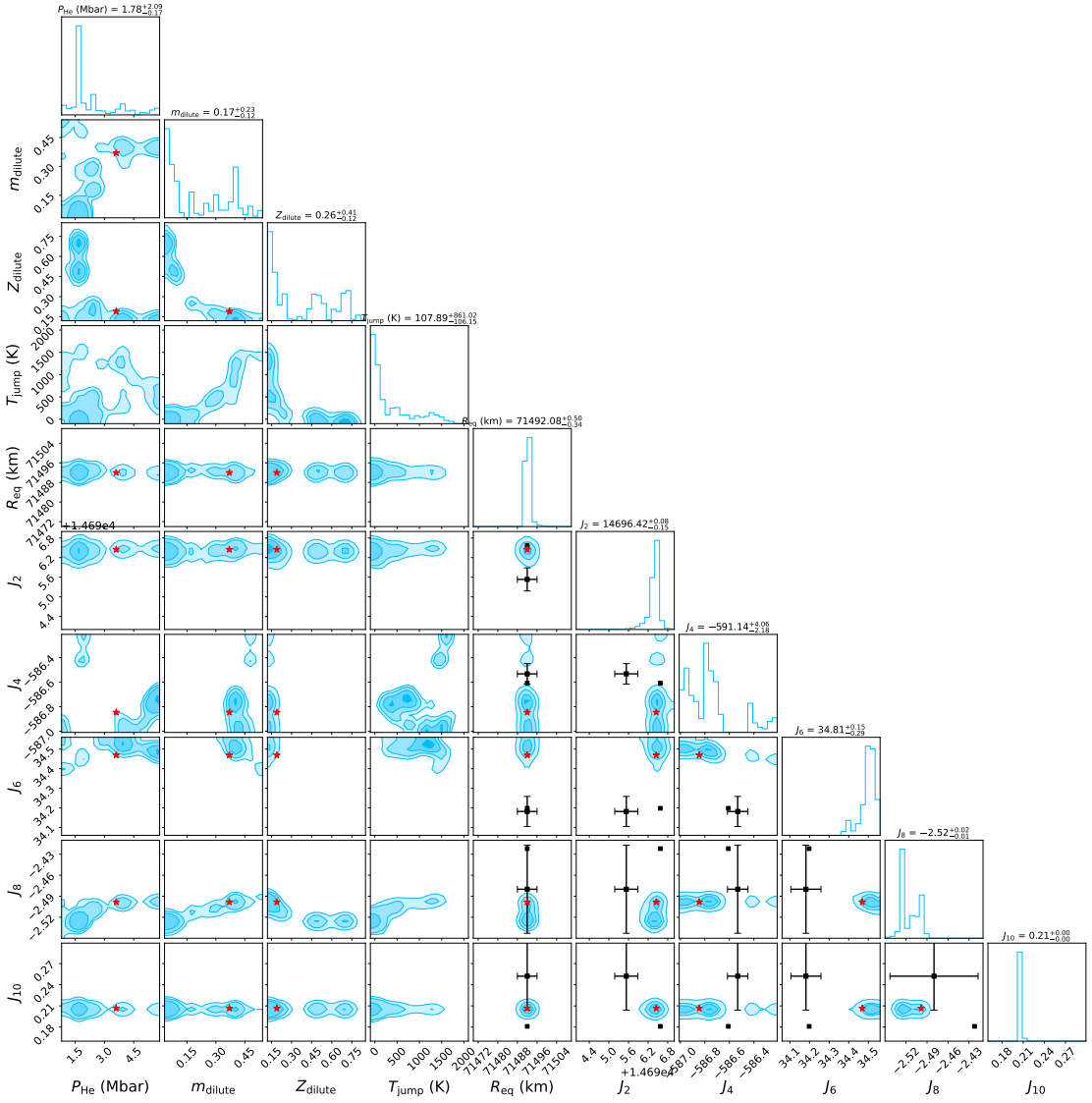

FIGURE D.11: Posterior distributions obtained with MH13*. The red star shows the Militzer et al. [2022] preferred (static) model. $M_{\text{core}} = 0$, $T_{1\text{bar}}$ is fixed at 166.1 K and $Z_1 = 0.0153$. The black error bars correspond to Juno's measurements accounting for differential rotation for the J_{2n}.

D.4 Subsample of models

We extracted one single model from each MCMC simulation using original EOSs (see Fig. D.2, D.3, D.4, D.5, D.6) and list them in Table D.1 and Table D.2.

TABLE D.1: Comparison of the parameters of selected models extracted from MCMC simulations using original EOSs. The full table can be found in Howard et al. [2023]. Models are available at the CDS via anonymous ftp to cdsarc.cds.unistra.fr (130.79.128.5) or via https://cdsarc.cds.unistra.fr/cgi-bin/qcat?J/A+A/ and at https://doi.org/10.5281/zenodo.7598377.

EOS	$M_{\rm core}$ ($M_\oplus$)	$P_{\rm He}$ (Mbar)	$m_{\rm dilute}$	$Z_{\rm dilute}$	$T_{\rm jump}$ (K)	$T_{\rm 1bar}$ (K)
MGF16+MH13	0.0305	2.12	0.237	0.214	60.3	185.3
MH13*	0.0288	2.05	0.317	0.175	82.3	176.1
CD21	0.0115	1.64	0.280	0.186	16.1	183.3
HG23+CMS19	0.231	1.66	0.324	0.177	9.10	182.1
HG23+MLS22	0.466	2.06	0.441	0.180	60.0	174.6

TABLE D.2: Comparison of the equatorial radius and the gravitational moments of the same models as in Table D.1.

EOS	$R_{\rm eq}$ (km)	$J_2 \times 10^6$	$J_4 \times 10^6$	$J_6 \times 10^6$	$J_8 \times 10^6$	$J_{10} \times 10^6$
MGF16+MH13	71487.6	14695.42	-586.649	34.211	-2.4548	0.2011
MH13*	71492.1	14695.62	-586.622	34.339	-2.4750	0.2035
CD21	71491.8	14695.57	-586.611	34.291	-2.4676	0.2027
HG23+CMS19	71491.4	14695.53	-586.559	34.309	-2.4704	0.2030
HG23+MLS22	71491.2	14695.65	-586.625	34.436	-2.4904	0.2054

Appendix E

Corner plot for models with an inverted Z gradient

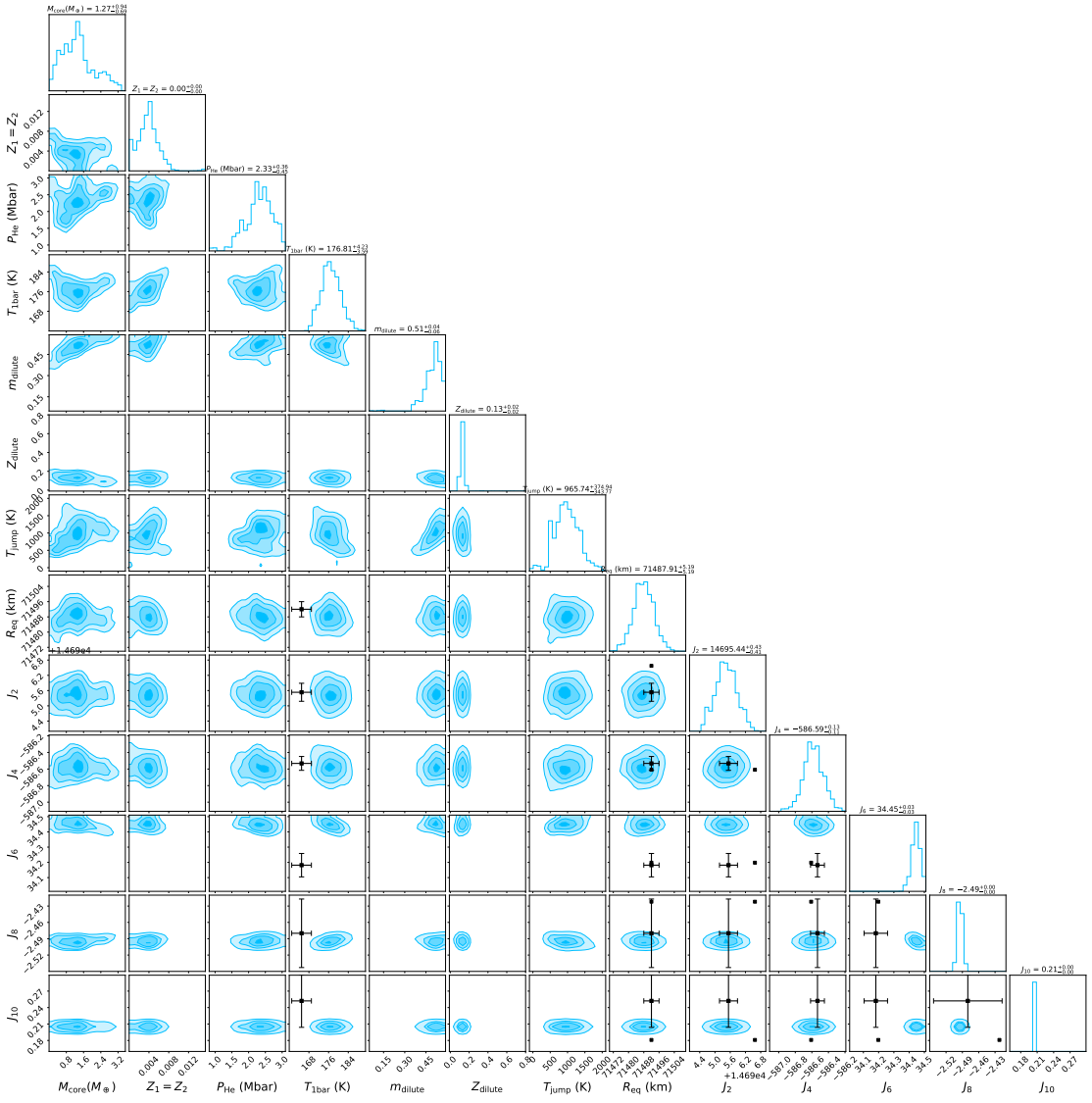

FIGURE E.1: Posterior distributions obtained with the MH13* EOS [Militzer and Hubbard, 2013], including a radiative zone (opacities multiplied by 5). The black points correspond to the measured J_{2n} by Juno. The black error bars correspond to Juno's measurements accounting for differential rotation for the J_{2n} and Galileo's measurement for $T_{1\text{bar}}$.